Muscle Impedance Signal Processing for biomarker development in Amyotrophic Lateral Sclerosis

Chlöe Natasha Schooling

Supervisors: Dr J.J.P. Alix, Prof V. Kadirkamanathan, Dr. T. J. Healey

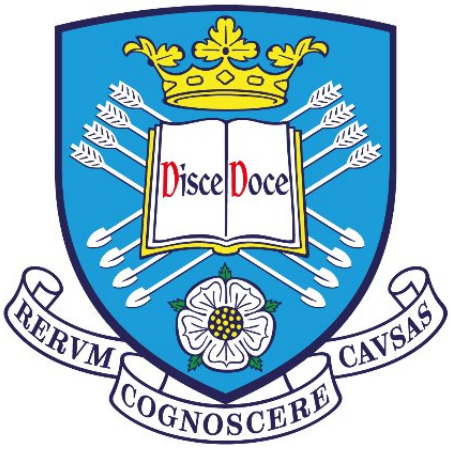

Sheffield Institute for Translational Neuroscience
The University of Sheffield

Thesis submitted for the degree of doctor of philosophy (PhD)

October 2019 - June 2023

Acknowledgements

I would like to extend a huge thank you to my supervisors Dr James Alix, Prof. Visakan Kadirkamanathan, and Dr Jamie Healey for providing me with the opportunity to join such an interesting project. Our regular group meetings were always full of thought provoking discussions, and I have greatly expanded my skill set and grown in confidence over the past four years we have worked together. Thank you so much to James, for your constant enthusiasm and all the support you have provided me throughout this project. I so appreciate how you always made my work a top priority, replied to emails at an impressive speed, and encouraged me to take breaks as well as constantly keeping me inspired with new ideas for the project. Thank you to Visakan, for all of your support on the technical side of the project, your input on my analyses was invaluable, and I learnt a lot from our conversations. Thank you Jamie, for all your help in the lab, where your expertise in the instrumentation of the devices was always so beneficial. And an extra thank you for building me a set of electrodes at the last minute, for use in the porcine study. I would also like to extend my gratitude to Dr. Alex Rothman for his accommodation in allowing me to join him and his team during their pig experiment, and providing me with ex vivo porcine tissue to study.

A very big thank you to my family for their constant support and love. Thank you for providing me with a peaceful place to write my thesis in these final weeks, looking after me, bringing me cups of coffee and peppermint tea, and joining me for walks in the woods and swims in the river when I needed a break. I would also like to extend thanks to all my lovely supportive friends for always being there, and checking in when times were hard. And finally, thank you so much to Jenny for your shared understanding of going through a PhD, supporting me through the stress of these final few months and for always encouraging me and believing in me.

Abstract

Amyotrophic Lateral Sclerosis (ALS) is a progressive neurodegenerative disease that affects motor neurons, leading to muscle weakness and ultimately death. Early and accurate diagnosis of ALS is crucial specifically given the common occurrence of misdiagnosis due to overlapping symptoms with mimic diseases. Electrical Impedance Myography (EIM) is a non-invasive and promising technique for assessing the electrical properties of muscle. In this thesis, multidimensional EIM data were assessed as a potential biomarker for ALS, with a focus on two sections: EIM analysis of the tongue to assess ALS bulbar disease, and EIM analysis of multiple muscles in the limbs to address the contribution of the subcutaneous fat layer and how this effects the biomarker capabilities for the assessment of a range of neurodegenerative disorders.

The first section of the thesis involved EIM analysis of the tongue, where a finite element method (FEM) based model of the tongue was optimised to fit the measurement dataset. This work revealed the underlying differences in the dielectric properties of healthy muscle compared to ALS patient groups of different severities. The model also established that lateral measurements on the edge of the tongue were viable. Additionally, a novel analysis framework, termed tensor EIM, was developed for dimensionality reduction of the multi-dimensional EIM dataset. Tensor EIM was able to characterise the direction of the spectral shift associated with worsening disease, which can be attributed to an increase in the centre frequency. The methodology successfully improved classification and correlation with the bulbar disease burden. Additionally, tensor EIM was found to be more sensitive to longitudinal disease changes than other biomarkers. Furthermore, complex multi-directional spectral shifts were identified throughout progression, where preliminary findings suggest these differences may pertain to acute and chronic denervation.

The second section addressed the challenge of subcutaneous fat contribution to limb EIM data. Initial assessment of the dataset found that the subcutaneous fat thickness had a significant correlation with the EIM data as well as with the disease severity, suggesting a causal relationship between EIM and the disease state. Through a sophisticated optimisation algorithm, an FEM model of the human limb was refined and demonstrated clear agreement with measured data. With use of the optimised FEM model, a methodology was developed to separate the signal of the skin-subcutaneous fat layer from the muscle in limb EIM measurement data. Following signal separation the dominance of the subcutaneous fat was considerably reduced, and the biomarker performance of the data improved in some areas. Furthermore, the tensor EIM framework was used to identify the spectral pattern associated with neurodegenerative disease, with some preliminary findings indicating differences in the spectral pattern for myopathic compared to neurogenic disease.

Overall, this thesis provides valuable insights into the use of multidimensional EIM data as a biomarker for ALS. The findings from the tongue and limb EIM analysis, combined with the development of optimised FEM models and a signal separation procedure, contribute to the understanding of the diagnostic and prognostic potential of EIM in ALS. These results have implications for clinical practice and may aid in early and accurate diagnosis of ALS, as well as improving clinical trial design, enabling the development of more effective therapies.

Contents

List of Figures

List of Tables

Acronyms

ALS amyotrophic lateral sclerosis

ALSFRS-R amyotrophic lateral sclerosis rating scale-revised

AUROC area under the receiver operating characteristic

BDBS bulbar disease burden score

BOBYQA bound optimisation by quadratic approximation

CMAP compound muscle action potential

CSF cerebrospinal fluid

DMD Duchenne nuscular dystrophy

EIM electrical impedance myography

EIS electrical impedance spectroscopy

EMG electromyography

fALS familial ALS

FAS flail arm syndrome

FDR false discovery rate

FEM finite element method

FLS flail leg syndrome

HHD hand-held dynamometry

L-BFGS-B limited-memory Broyden-Fletcher-Goldfarb-Shanno with bound constraint

LMN lower motor neurones

MMA method of moving asymptotes

MND motor neurone disease

MRC medical research council

MRI magnetic resonance imaging

MUNE motor unit number estimation

MUNIX motor unit number index

Nfl neurofilament light chain

NI neurophysiological index

NMF non-negative matrix factorisation

NRMSE normalised root mean squared error

NTF non-negative tensor factorisation

PARAFAC parallel factor analysis

PBP progressive bulbar palsy

PCA principal component analysis

PET positron emission tomography

PLS primary lateral sclerosis

PMA progressive muscular atrophy

RMSD root mean squared deviation

S-SFL skin-subcutaneous fat layer

S-SFT skin-subcutaneous fat thickness

SFL subcutaneous fat layer

SFT subcutaneous fat thickness

SIP surface interference pattern

TA tibialis anterior

TMS transcranial magnetic stimulation

UMN upper motor neurones

1 Chapter 1: General introduction

1.1 Amyotrophic lateral sclerosis

Amyotrophic lateral sclerosis (ALS), the most common form of motor neurone disease (MND), is a neurodegenerative disease characterised by the degeneration of both upper motor neurones (UMN) and lower motor neurones (LMN) (Hardiman et al., 2017). The disorder is relentlessly progressive, ultimately causing respiratory failure from paralysis of the diaphragm (Kwan et al., 2020). The average time of survival is generally reported in the range of 2-4 years (Hobson and McDermott, 2016; Hardiman et al., 2011; Verber et al., 2019). Although there is some evidence of this being even more relentless, where a median life expectancy of 11 months following diagnosis was reported for patients attending a general neurology clinic (Aridegbe et al., 2013). ALS is considered to be a complex genetic disorder with the aetiology of the disease not fully understood (Hardiman et al., 2017).

For the majority of ALS cases, the cause of disease is unknown and termed sporadic. However, 5-20% of ALS patients have familial ALS (fALS), with strong evidence of the disorder in the immediate family (Byrne et al., 2011; Hardiman et al., 2017). Approximately two-thirds of familial cases can be attributed to mutations of four genes, C9orf72, SOD1, TARDBP, and FUS (Chiò et al., 2012; Millecamps et al., 2012). Additionally, there is some evidence of disease caused by lifestyle, but no strong environmental factors have been identified (Hardiman et al., 2017; Chiò et al., 2014). Patients can manifest with a variety of symptoms. Limb-onset disease is the most common and is seen in around two-thirds of patients (Wijesekera and Nigel Leigh, 2009), while bulbar-onset tends to make up the remaining third (Masrori and Van Damme, 2020), although a small proportion will onset with respiratory difficulties (Sennfält et al., 2023). Additionally, the affected motor neurons will manifest in UMN, LMN or a combination of both (Goutman et al., 2022). This heterogeneity is further confounded by poorly predictable rates of disease progression, overall compounding to delays in diagnosis, generally seen at 9 to 12 months from symptom onset (Van Es et al., 2017; Kwan et al., 2020).

UMN disease causes spasticity, weakness and brisk deep tendon reflexes in the limbs and spastic dysarthria in the bulbar segment. In contrast, LMN features include fasciculations, muscle wasting and weakness as well as flaccid dysarthria and later dysphagia (Kiernan et al., 2011). In more than 40% of cases patients also display cognitive impairment, which is primarily dysexecutive in nature (Phukan et al., 2012). Overall the prognosis is better for patients who display no cognitive abnormality at baseline (Elamin et al., 2013).

1.1.1 Muscle denervation

The degeneration of motor neurones in ALS is characterised by the death of the respective axons. One specific characteristic of LMN degeneration is muscle denervation, which occurs when the axon of the LMN dies, resulting in the loss of nerve supply to the affected muscles. Denervation results in the detachment of muscle fibres from their motor neurons, depriving them of the necessary signals for contraction and proper function. Muscle fasciculations often occur in the early stages of degeneration, where damage to the motor neurons caused by subacute partial denervation leads to spontaneous and uncontrolled firing of the motor units (Daroff and Aminoff, 2014). Following acute denervation the muscle will atrophy, with shrinkage and weakening of the muscle fibres (Carlson, 2014; Daroff and Aminoff, 2014). Functioning muscle tissue is eventually largely replaced by fat and fibrous connective tissue. This fibrosis within the muscle tissue disrupts the normal architecture and functionality of the muscle (Rebolledo et al., 2019). The changes in muscle architecture, including muscle cell size, cell number and the intra-muscular presence of increased fat and glycogen, underpin why impedance myography

can be used to study disease progression in ALS. This will be discussed in detail in Section 1.2.3.

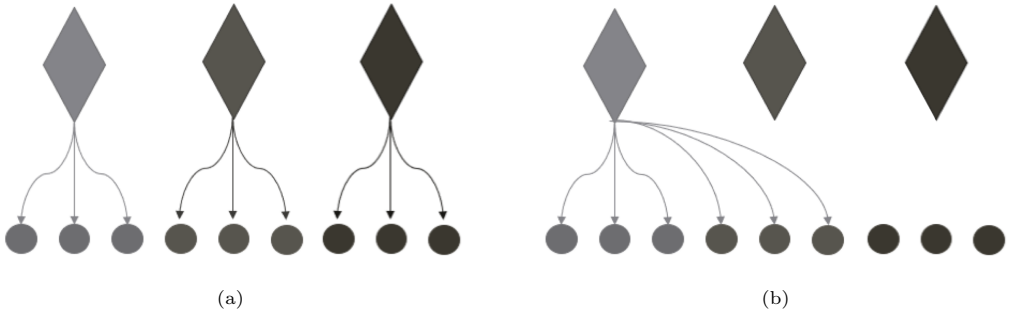

Figure 1.1: Diagram showing denervation and reinnervation of muscle. The diamonds represent axons and the circles represent muscle cells. (a) shows a healthy motor unit, while (b) shows reinnervation of the centre axon and complete denervation of the right axon.

Active denervation may not be immediately clinically apparent in the early stages of disease. This is due to the reinnervation of the degenerated neurones via collateral sprouting (Figure 1.1), by which the surviving axons grow intramuscular axon branches to synapse with the denervated muscle fibres (Wohlfart, 1957). Collateral sprouting results in the reorganisation of the motor unit, expansion of the motor unit territory, and an increased number of muscle fibres per motor unit (Daroff and Aminoff, 2014). During this process, neighbouring muscle fibres that are innervated by the same axon will cluster. This process is commonly referred to as chronic denervation. In ALS the denervation process is progressive meaning the reinervated axons are eventually lost causing atrophy of these clustered muscle fibres, known as 'grouped atrophy'. Interestingly muscle fibres of mixed type have been observed in individual regions of grouped atrophy (Baloh et al., 2007).

1.1.2 Other forms of MND and ALS mimics

While sporadic and familial ALS are the most common forms of adult-onset neurodegenerative MND, there are other forms of MND which include primary lateral sclerosis (PLS); progressive muscular atrophy (PMA); progressive bulbar palsy (PBP); flail arm syndrome (FAS); and flail leg syndrome (FLS) (Pinto et al., 2019). PLS involves UMN only degeneration and represents only 3-5% of all MND patients (Masrori and Van Damme, 2020). Most patients initially diagnosed with the PLS variant eventually develop signs of LMN involvement within four years and are reclassified as UMN-predominant ALS (Pinto et al., 2019). Conversely, PMA is a form of MND with only LMN dysfunction, where again substantial numbers of patients initially diagnosed with this disease will go on to develop UMN symptoms and will be reconsidered as LMN-predominant ALS (Pinto et al., 2019). In addition, PBP is a form of MND defined by bulbar dysfunction and can be attributed to either UMN and/or LMN disease (Pinto et al., 2019). Clearly, the primary differential diagnosis is bulbar-onset ALS, however, there is scarce literature that separates the two. Finally, FAS and FLS present as predominantly LMN patterns of weakness in the upper and lower limbs, respectively, these subtypes of ALS tend to progress more slowly compared to typical limb-onset ALS (Masrori and Van Damme, 2020).

Additionally, there exists a heterogeneous group of conditions called ALS mimics, which while distinct from MND do resemble ALS in their presentation and clinical features. Population-based studies have shown that over 50% of patients with initial ALS, presentation turn out to

have an alternative disease (Jenkins et al., 2016). Certain mimic syndromes will have potentially curative treatments available, therefore it is important to rule these out as early as possible.

Predominant signs	MND	Mimic disorder
LMN	Progressive muscular atrophy (PMA) Flail arm syndrome (FAS) Flail leg syndrome (FLS)	Benign cramp fasciculation syndrome (BCFS) multifocal motor neuropathy (MMN) Kennedy disease with conduction block (spinobulbar muscular atrophy) Spinal muscular atrophy (SMA) Neuralgic amyotrophy Motor-predominant CIDP Inclusion body myositis
UMN	Primary lateral sclerosis (PLS)	Hereditary spastic paraparesis (HSP) Multiple sclerosis (MS) Metabolic myelopathies
Mixed	Familial ALS Sporadic ALS Progressive bulbar palsy (PBP)	Cervical myeloradiculopathy

CIDP = chronic inflammatory demyelinating polyneuropathy

Table 1.1: Different forms of MND and ALS mimic syndromes can be categorised based on the predominant signs of the disease, classified as LMN, UMN or a combination of both. Adapted from Turner and Talbot (2013).

The main ALS mimic syndromes are outlined in Table 1.1, separated into those presenting with exclusively LMN signs, UMN signs, or a combination of both. Here the greatest diagnostic difficulty comes from LMN presentations (Turner and Talbot, 2013). The most important signs to suggest alternative diagnosis are an evolution of atypical symptoms and a lack of progression of typical symptoms. Thorough clinical examination along with electrophysiological assessment, neuroimaging and laboratory studies should be conducted to enhance diagnostic understanding (Andersen et al., 2012). ALS mimics provide a useful group through which to test the diagnostic potential of EIM.

1.1.3 Diagnosis

Despite the lack of curative treatment for the disease, prompt diagnosis is important in preventing prolonged diagnostic uncertainty in patients. Similarly, it allows for quicker access to multi-disciplinary care, which is essential for increasing the quality of life and prolonging survival (Aridegbe et al., 2013). Unfortunately, diagnosis is not always easy and many patients are initially misdiagnosed at rates of 27% to 44% (Sennfält et al., 2023).

The diagnosis of ALS requires demonstration of a combination of UMN and LMN abnormalities (de Carvalho et al., 2008). These abnormalities are identified via both clinical assessment and needle electromyography (EMG) (Krarup, 2011). LMN dysfunction is clinically assessed by identifying signs of muscle weakness, atrophy, reduced muscle tone, and fasciculations (Masrori and Van Damme, 2020). However, due to the effects of collateral sprouting over half of the motor unit pool may be lost before clinical signs of wasting and weakness become apparent (de Carvalho and Swash, 2016). Overall, EMG assessment is essential for confirming LMN affection in weak muscles. During EMG a combination of evidence for active and chronic denervation is required in several muscles that do not share common anatomical pathways. Active muscle denervation is confirmed through the observation of positive sharp waves and fibrillation potentials, which represent the spontaneous discharge of individual muscle fibres; as well as fasciculation potentials that arise from the spontaneous discharge of part or all of the motor unit (Krarup, 2011; Whittaker, 2012). Chronic denervation is typically assessed by qualitative judgement on the size of the motor unit potentials, which enlarge due to collateral reinnervation.

Here, the EMG will develop a prolonged duration, increased amplitude, and often a polyphasic configuration (Daroff and Aminoff, 2014), where the waveform exhibits complex morphology and consists of multiple deflections or peaks.

The identification of UMN abnormalities is a more difficult process, primarily relying on clinical examination (Verber et al., 2019). Signs of UMN abnormalities include hyperreflexia with pathological reflex spread; preserved reflexes in weak wasted limbs; spasticity associated with increased muscle tone; clonus; and impairment in motor control (Huynh et al., 2016; Masrori and Van Damme, 2020). There are a number of emerging methods for the assessment of UMN lesions, including transcranial magnetic stimulation (TMS) and advanced neuroimaging techniques; however, they are not yet standardised clinical tools for diagnosis (de Carvalho et al., 2008).

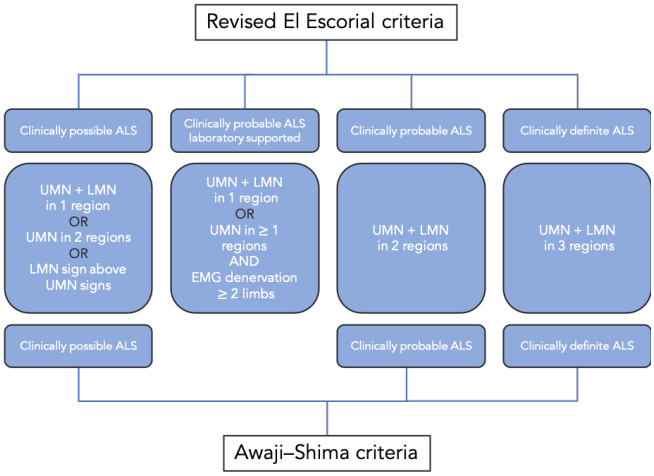

Figure 1.2: Revised El Escorial criteria and Awaji-Shima criteria. Adapted from Douglass et al. (2010).

Given the lack of a single diagnostic tool, the revised El Escorial and Awaji-Shima criteria for the diagnosis of ALS are widely accepted (Kiernan et al., 2011; Al-Chalabi et al., 2016). These criteria describe algorithms to determine the degree of diagnostic certainty in any patient using evidence of both UMN and LMN abnormalities (Figure 1.2). The Awaji-Shima, proposed in 2008 (de Carvalho et al., 2008), advises equal weight be given to both clinical and electrophysiological signs of LMN degeneration, with the addition of fasciculation potentials used as evidence for active denervation in electrophysiological assessment. The diagnostic specificity was reported as 97.9% for either set of criteria. While the sensitivity in early diagnosis was 79% and 77.6% for Awaji-Shima and the revised El Escorial, respectively (Pugdahl et al., 2021). Clearly, the Awaji-Shima slightly increases specificity without affecting the sensitivity; however, it is recognised that both these criteria have limitations as they are complex to apply and do not give much diagnostic certainty.

In 2020, a new diagnostic criteria, known as the Gold Coast Criteria was proposed (Shefner et al., 2020) (table 1.2). Here, the previous diagnostic categories of Definite, Probable, and Possible were abandoned, with an aim to improve diagnostic clarity and facilitate easier and earlier diagnosis (Kiernan, 2021). Assessment of the diagnostic accuracy found these criteria improved both the sensitivity and specificity of diagnosis to 88.2% and 98.9%, respectively (Pugdahl et al., 2021). Overall the introduction of this new simplified criteria aimed to enhance the recruitment process of ALS patients for clinical trials and to facilitate more targeted patient management (Kiernan, 2021).

Criteria for diagnosis of ALS.
1. Progressive motor impairment documented by history or repeated clinical assessment, preceded by normal motor function, **and**
2. Presence of upper and lower motor neurone dysfunction in at least 1 body region, (with upper and lower motor neurone dysfunction noted in the same body region if only one body region is involved) or lower motor neurone dysfunction in at least 2 body regions, **and**
3. Investigations excluding other disease processes

Table 1.2: Gold Coast diagnostic criteria presented in (Shefner et al., 2020).

1.1.4 Clinical biomarkers of disease

Characteristics of ALS that can be objectively measured and evaluated are known as biomarkers. The current clinical and functional measures of disease progression include the amyotrophic lateral sclerosis rating scale-revised (ALSFRS-R) (Cedarbaum et al., 1999), which is a questionnaire-based tool used to assess the functional status of patients carrying out activities of daily living. This method correlates well with survival (Kaufmann et al., 2005) and is easily reproducible but is limited by its subjective nature and limited sensitivity in slow disease progression (Rutkove, 2015).

Since muscle weakness is a major clinical feature of LMN dysfunction, another assessment tool is a measurement of muscle strength. Manual muscle testing (MMT) gives a qualitative measure of muscle strength but is limited by its subjectivity (Rutkove, 2015; Shefner, 2017). Alternatively, hand-held dynamometry (HHD) quantitatively assesses voluntary isometric strength and gives improved reproducibility and sensitivity to disease progression (Shefner, 2017). However, the detection of disease progression is limited in the presence of collateral reinnervation and reproducibility is restricted since patient performance can depend on mood, effort, and cognitive status (Rutkove, 2015). Measurement of body weight can also be an informative biomarker where $> 5\%$ weight loss at baseline has an adverse effect on life expectancy (Verber et al., 2019).

Respiratory dysfunction remains the usual cause of death in ALS, hence an important clinical assessment and determinant of survival is a measure of the respiratory muscle weakness (Bourke et al., 2006; Radunovic et al., 2017). Forced vital capacity (FVC) assesses inspiratory muscle strength and is established as a recommended test in clinical trials (Czaplinski et al., 2006). However, FVC recording is limited in patients with significant bulbar muscle weakness and it lacks sensitivity in earlier stages of the disease (Morgan et al., 2005; Verber et al., 2019). An alternative measure is sniff nasal-inspiratory force (SNIF), which allows for assessment of the global respiratory function and is a more sensitive tool giving important prognostic information (Morgan et al., 2005). Both assessments of respiratory function are non-invasive; however, effort-dependent (Verber et al., 2019).

There are a growing number of biomarkers for the monitoring of LMN-specific disease. These include electrophysiology biomarkers to directly assess the motor units, such as motor unit number estimation (MUNE), which provides a reproducible and quantitative measure of the number of functional motor units within a nerve (Benatar et al., 2016). This is achieved by stimulating a peripheral nerve with an electrical impulse and recording the electrical response from the muscle, which is known as the compound muscle action potential (CMAP) (Mccomas et al., 1971; Gooch et al., 2014). Additonally, the motor unit number index (MUNIX) is a surface-based EMG technique, which provides an easier to perform and less invasive alternative to MUNE. Here, the number of motor units is indirectly measured through a mathematical model applied to the CMAP evoked by supramaximal nerve stimulation and the EMG surface interference pattern (SIP) for different voluntary activation levels (Gaweł, 2019). An additional metric calculated from the CMAP is the neurophysiological index (NI), which provides a quan-

titative measure of the overall peripheral disease burden (Verber et al., 2019), and has been found to be highly sensitive to disease progression (Benatar et al., 2016). All of these methods give valuable insight into pre-clinical LMN loss.

Identifying biomarkers specifically for assessing UMN degeneration presents a greater challenge; however, there have been growing advancements in neurophysiological and neuroimaging techniques (Huynh et al., 2016). An increasingly promising neurophysiological method for UMN assessment at earlier stages of disease is TMS (Vucic and Kiernan, 2006, 2017; Verber et al., 2019). TMS involves using a handheld device that contains a coil, which generates a rapidly changing magnetic field, applying magnetic pulses to the scalp (Vucic and Kiernan, 2017). Threshold tracked TMS techniques utilising paired-pulse TMS protocols, such as short-interval intracortical inhibition, are considered the most effective methods for assessing UMN dysfunction (Vucic and Kiernan, 2006; Turner et al., 2009; Tankisi et al., 2021). TMS studies have confirmed dysfunction in the motor cortex and corticospinal pathway in ALS, with early evidence indicating cortical hyperexcitability (Vucic and Kiernan, 2006; Turner et al., 2009). Additionally, there is evidence for the use of advanced neuroimaging techniques, including magnetic resonance imaging (MRI) and positron emission tomography (PET) for the assessment of UMN dysfunction (Huynh et al., 2016; Verber et al., 2019). MRI stands out for its ability to simultaneously evaluate brain structure and function, offering a comprehensive understanding of the in vivo progression of cerebral pathology, which provides valuable insights into the dynamic changes occurring within the brain (Menke et al., 2017). Additionally, fluorodeoxyglucose (FDG) PET has demonstrated a clear pattern of hypometabolism in the frontal and occipital cortex as well as successful discrimination of ALS and healthy brains (Pagani et al., 2014). Furthermore, these imaging techniques can be applied to LMN assessment; where, for example, the stages of muscle denervation can be identified through distinct signal intensity patterns observed in MRI scans of muscle (Kamath et al., 2008).

Biofluid markers make up another set of candidate biomarkers, including cerebrospinal fluid (CSF), blood, and urine biomarkers. Neurofilament proteins are a promising marker of ALS, where neurofilament light chain (Nfl) levels in both CSF and blood have been found to be significantly higher in ALS (Verber et al., 2019). Additionally, proteomic and metabolomic profiles, oxidative stress markers in CSF, as well as neuroinflammatory mediators, and genetic markers present in both CSF and blood show promise for assessing disease (Poesen et al., 2017; Verber et al., 2019). Finally, spontaneous Raman spectroscopy offers a quick and label-free method to obtain a highly specific molecular fingerprint of tissue and has shown potential as an attractive biomarker (Plesia et al., 2021; Alix et al., 2022e).

The search for biomarkers in ALS is a crucial and ongoing field of research. Identifying a sensitive and objective tool for accurate assessment of disease would significantly impact the diagnosis, monitoring, and treatment of ALS. A successful biomarker provides clear indications of disease presence, progression, and response to therapies. Specifically, when biomarkers are sensitive to early therapeutic effects, our reliance on animal models would reduce (Turner et al., 2009). Overall they can help with early detection; prognosis prediction; tracking disease progression; evaluating treatment efficacy; and highlighting potential therapeutic targets for novel therapies (Verber et al., 2019). Additionally, sensitive biomarkers can aid clinical trial design and contribute to more efficient and effective clinical trials (Benatar et al., 2016). As ALS is a highly heterogeneous disease, there are significant challenges in clinical trial design, often with a large number of participants and long trial duration required. Thus reliable biomarkers associated with ALS can help researchers to more precisely select suitable participants for study within clinical trials. This can lead to a more homogeneous study cohort, thus improving the statistical power of the study (Turner et al., 2009). Overall, biomarkers have the potential to improve patient care, accelerate research advancements, and ultimately contribute to the

development of effective treatments for ALS.

1.2 Electrical impedance

1.2.1 Scientific background

Current flow (I) is dependent upon the voltage (V) and resistance (R) as described by Ohm's law (Halliday et al., 2000):

$$V = IR \tag{1.1}$$

In other words, the voltage, measured in volts, drives the current flow and the resistance, measured in ohms (Ω), opposes it (Holder, 2004). Electrical impedance, Z, is analogous to resistance for alternating current (AC) circuits where current flow varies in a sinusoidal pattern. Unlike resistance, the impedance varies with the frequency of the current as it takes into account the effects of capacitance and inductance. (Holder, 2004; Williams et al., 2011)

Capacitors and inductors are devices which store energy in the form of an electric and magnetic field respectively. The capacitance (C), measured in farads (F), describes the capacitor's effectiveness in storing charge. The opposition to the flow of current resulting from the internal impedance of a capacitor is known as capacitive reactance (X_c):

$$X_c = \frac{1}{2\pi f C} \tag{1.2}$$

where X_c=capacitive reactance (Ω), C=capacitance (F), f=frequency (Hz) (Halliday et al., 2000). The inductor's ability to store energy is described by inductance L, measured in henries (H). Where the internal impedance of an inductor or inductive reactance (X_L) is described by:

$$X_L = 2\pi f L \tag{1.3}$$

where X_L=inductive reactance (Ω), L=inductance (H), f=frequency (Hz) (Halliday et al., 2000).

In a purely resistive circuit, the voltage drop across the resistor will be in phase with the applied alternating current. While a purely capacitive circuit exhibits a phase lag of -90° and a purely inductive circuit exhibits a phase lead of +90°. Thence for a more complex circuit the overall phase depends on the relative contributions of each group (Holder, 2004).

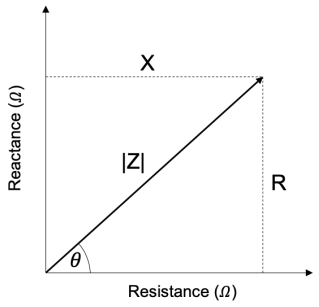

Figure 1.3: Complex impedance plane showing resistance (R), reactance (X = $X_L - X_C$), magnitude ($|Z|$) and phase (θ). Adapted from Sanchez and Rutkove (2017).

The total complex impedance, Z, of a circuit containing capacitors and/or inductors, is given by:

$$Z = R + i(X_L - X_C) \tag{1.4}$$

where i is the imaginary unit, and Ohm's law becomes: (Rutkove, 2009)

$$V = IZ \tag{1.5}$$

Figure 1.3 gives a graphical representation of the complex impedance where the corresponding magnitude ($|Z|$) and phase (θ) are given by:

$$|Z| = \sqrt{R^2 + (X_L - X_C)^2} \qquad \theta = arctan\left(\frac{X_L - X_C}{R}\right) \tag{1.6}$$

1.2.2 Impedance in muscle

Electrical impedance spectroscopy (EIS) is a technique used to measure the electrical impedance of a system as a function of frequency. This technique can be used to directly assess the impedance of muscle, which is commonly referred to as electrical impedance myography (EIM). It is based on the concept that muscle can be modelled as a network of resistors and capacitors (Bayford, 2006; Holder, 2004). The inductive effects in muscle are taken to be negligible, which means eq. 1.4 becomes:

$$Z = R + iX \tag{1.7}$$

where X is the conductive reactance. Note there is some discrepancy in the literature in how the sign of the reactance (X) (and consequently the phase, θ) is defined. My team (Alix et al., 2020) set the reactance as X=X_C, giving majoritively negative reactance values in muscle recordings. While others (Rutkove et al., 2002; Esper et al., 2006; Mcilduff et al., 2017) define the reactance as X=-X_C, yielding a majority of positive reactance values in muscle. This has no effect on the performance of the biomarker and simply reflects how the direction of imaginary space has been defined. For direct comparison between impedance measurements, the sign can be flipped where necessary, although care must be taken when interpreting directional changes of reactance and how this relates to specific muscle changes.

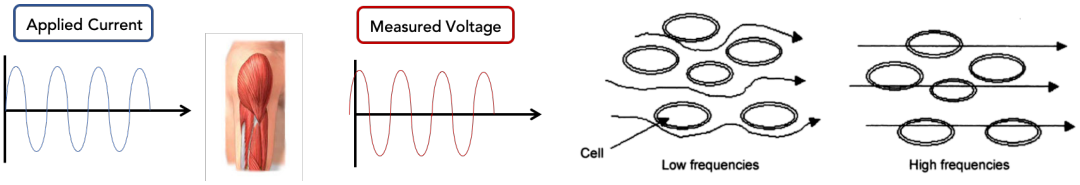

(a) (b)

Figure 1.4: (a) The underlying principles of muscle EIM are shown. The intrinsic properties of the tissue impact the corresponding amplitude and phase of the measured voltage. (b) The current flow through cells at low and high frequencies. Taken from Holder (2004).

Figure 1.4a demonstrates the basis to muscle EIM where an AC current is applied across the muscle and a voltage measurement is taken in order to calculate the respective impedance (i.e. eq. 1.5). This provides a non-invasive, painless method for evaluating muscle with an objective quantitative output (Sanchez and Rutkove, 2017). For surface impedance measurements electrodes are placed on the surface of the skin, over the muscle of interest, where a pair of electrodes are used for injecting the current (excitation electrodes) and a pair of electrodes are used for reading out the voltage (sense electrodes). These four electrodes can be arranged into different configurations in order to measure in different directions through the tissue. This can be useful for making assessments of tissue anisotropy for example.

Simple three and five-element circuit diagrams are used to illustrate the basic sources of impedance in muscle (Figure 1.4b). The tissue is described as having resistances coming from the extracellular (r_1) and intracellular (r_2) components as well as capacitance (c_1) arising from the cell membrane. The additional branch in the five-element circuit (r_3, c_2) describes the internal fluids and membranes of the organelles within a cell (Shiffman et al., 2008; Rutkove, 2009).

For low frequencies, the membrane impedes current flow and the current passes between cells, or entirely across the extracellular resistive component (r_1). As shown in figure 1.5a, when the frequency is increased the current will increasingly flow inside the cells due to reducing capacitive reactance (eq. 1.2) (Holder, 2004; Bayford, 2006; Rutkove, 2009). A graphical representation of the variation of impedance with frequency is demonstrated by a Cole-Cole plot (Figure 1.5b) (Cole and Cole, 1941; Holder, 2004). When the current enters the intracellular space the reactive part of impedance increases, while the overall magnitude decreases. This is because access to ions in both the extracellular and intracellular spaces increases the conductivity. For high enough frequencies membrane capacitance becomes negligible and the impedance is again purely resistive. The high frequency resistance is a result of the parallel intracellular and extracellular resistances (Holder, 2004).

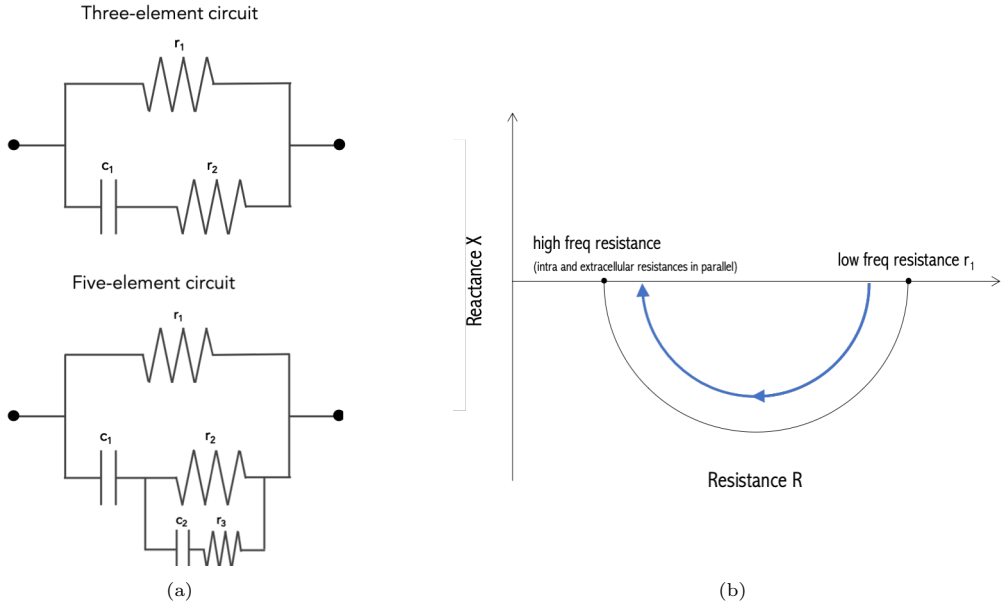

Figure 1.5: (a) The simple equivalent three and five-element circuits of bioelectrical impedance. Adapted from Rutkove (2009); Shiffman and Rutkove (2013a). (b) Cole-Cole plot of the three-element circuit, adapted from Holder (2004).

Generally healthy skeletal muscle is reportedly most reactive around 50 kHz current and therefore most EIM studies so far have made assessments at this single frequency (Rutkove et al., 2012a, 2014). It is hypothesised that as disease progression affects the underlying cellular structure of the muscle, the impedance relationship with frequency will change accordingly, hence analysis of a full spectrum of data can provide more detailed insights. The impedance phase is most commonly employed as the chosen parameter in EIM analyses and has been reported as the most disease sensitive metric (Rutkove et al., 2007). Another benefit is that both resistance and reactance vary with the tissue size and shape, while the phase, which is

calculated using the ratio of the two (eq. 1.6), is resilient to these changes (Rutkove et al., 2007, 2016). However, a simple transformation of the impedance ($Z = R + iX$) data can be performed to remove the volume dependence:

$$z = \frac{Z}{K}, \quad \rho = \frac{R}{K}, \quad \chi = \frac{X}{K} \tag{1.8}$$

where K is the cell constant of the specific geometrical arrangement of measurement electrodes, and z, ρ and χ are the apparent impedivity (or specific impedance), apparent resistivity and apparent reactivity, respectively. These quantities are all independent of the volume of tissue under measurement and are only dependent on the intrinsic electrical properties of the tissue. Eq.1.8 relies on the assumption that the tissue is locally homogeneous around the area of measurement, which is evidenced following the assessment of the measurement dataset in Section 2.3.4. The cell constant, K can be determined for a given electrode configuration by performing calibration in saline of known conductivity, which can be further validated using simulation data.

To make further insights into the direct electrical properties of the muscle from the impedance dataset, the conductivity (σ) and relative permittivity ($\mathcal{E}_r$) can be calculated as:

$$\sigma = KG = K\frac{R}{R^2 + X^2} \tag{1.9}$$

$$\mathcal{E}_r = K\frac{C}{\mathcal{E}_0} = K\frac{X}{\mathcal{E}_0\omega(R^2 + X^2)} \tag{1.10}$$

where G is the conductance, C is the capacitance, ω is the applied, or angular frequency ($\omega = 2\pi f$), and $\mathcal{E}_0$ is the permittivity of free space (Duck, 1990; Wang et al., 2011). This can be done for a full spectrum of frequencies, thence giving a spectrum of dielectric properties for the muscle under measurement. These physical properties of the bulk of the muscle have been termed volume conduction properties (VCPs) by Sanchez et al. (2021); Luo and Sanchez (2021). When impedance measurements are taken for a given arrangement of electrodes over what is realistically non-homogeneous and anisotropic tissue, the outputs here would be the apparent dielectric properties. This refers to the overall conductivity and permittivity of the composite material (which may well include additional biological tissue, such as epithelial tissue, skin, fat, or bone). The output would be some combination of the dielectric properties in multiple directions through the tissue dependent on the path of current flow. Through the use of an inverse model and validated using simulation data, a new multi-electrode probe has been optimised to calculate the VCPs in a 2D plane, in the longitudinal and transverse directions (Luo et al., 2021a,b; Luo and Sanchez, 2021).

1.2.3 EIM in application to ALS

It has been three decades since EIM was first pioneered for neuromuscular evaluation through an initial study in Duchenne dystrophy (Noshiro et al., 1993), and two decades since the technique was first assessed in ALS specifically (Rutkove et al., 2002). In subsequent years, EIM in application to a range of neuromuscular disorders has been a growing area of study, and the technique has been demonstrated to be highly reproducible; to have capabilities at separating healthy and diseased muscle; have prognostic potential with significant correlations found between EIM and measures of disease severity; as well as being sensitive to progression of disease over time.

Initial work began with an interest in EIM applied to the limbs, with most assessments made at a single 50 kHz frequency with analysis focused on the impedance phase (Rutkove et al.,

2002, 2005, 2006, 2007; Garmirian et al., 2009; Rutkove et al., 2012a, 2014; Offit et al., 2020). There seems to be limited physiological evidence for this frequency choice, most likely being dictated by impedance work by Nyboer et al. (1950), as well as the availability of relatively inexpensive impedance instruments. However, some assessments have been made on multi-frequency spectra (Esper et al., 2006; Shefner et al., 2018). It is worth mentioning that there is a limit to the range of frequencies that are viable for surface impedance recordings in the limbs, below 8-10 kHz electrode contact artefacts relating to keratinised skin appear, while high frequencies, above 1000 kHz, see distortion due to inductive effects from the wires and parasitic capacitance artefacts in the hardware (Martisnen et al., 1997; Pandeya et al., 2021, 2022). All these studies have made impedance measurements using commercial systems, including the Imp SFB7 (Impedimed, Inc., Sydney Austrailia) and the mView (Myolex, Inc., San Francisco, CA). Multiple studies have demonstrated that the impedance phase exhibits some disease related change (Rutkove et al., 2007; Rutkove, 2009; Shellikeri et al., 2015; Mcilduff et al., 2017); with a significance of less than 5% in identifying differences in healthy and ALS datasets. However, the potential utility of impedance magnitude should not necessarily be discounted; particularly as it has been used in other applications of impedance spectroscopy (Murdoch et al., 2014; **?**).

Throughout the course of ALS numerous complex changes occur to the muscle structure. In previous literature we see some description of the expected changes to the underlying electrical properties at a 50 kHz frequency. For example, it is hypothesised that resulting atrophy of both the muscle and the individual cells, along with an increase in the amount of endomysial connective tissue and fat are expected to increase the resistance (Rutkove, 2009). This is a result of the decreasing cross-sectional area of the muscle and the change in the current path. Alternatively, the reducing surface area of the cell membrane will decrease C, and as capacitors in series sum as the inverse of the individual components (Halliday et al., 2000) then overall capacitance is expected to increase. Hence the capacitive reactance X_C - being inversely proportional to C (Section 1.2.1) - should decrease. While this is a useful start to hypothesising the impedance response to the physical changes occurring in muscle with degenerative disease, this is somewhat an oversimplification. The direction of change will vary depending on the dominant disease process, such as acute versus chronic changes, which will be explored throughout this thesis. Additionally, the directions of change will vary across the frequency spectrum, hence a full paramterisation of multi-frequency data is likely to give deeper insights into the disease processes. The cellular structure of skeletal muscle is also intrinsically anisotropic, with current preferentially flowing along the direction of muscle fibres (Garmirian et al., 2009). This anisotropy is expected to change with the disease, where the loss of muscle structure will lead to a more isotropic medium. Alternatively, chronic reinnervation and type grouping may increase anisotropy (Rutkove, 2009). Assessment of such anisotropy can be made by measuring the impedance spectrum in multiple directions across the muscle.

Initial studies made use of hydrogel electrodes (Rutkove et al., 2002, 2005; Esper et al., 2006), which were manually placed meaning that accurate positioning is very important. To begin with the current electrodes were placed on the dorsum of both hands or both feet for measurement of the biceps or tibialis anterior/quadriceps. Although this has the advantage of large spatial resolution and a reduction in the contribution of subcutaneous fat, it is not muscle-specific and differences in joint position and/or electrode placement have large effects on the data output (Sanchez and Rutkove, 2017). Hence the standard method is now to perform localised measurements with all electrodes arranged around a particular muscle of interest (Rutkove, 2009; Schwartz et al., 2015; Li et al., 2016b; Rutkove et al., 2016, 2017). The majority of EIM studies in the limbs have recorded in a single electrode configuration, however, some systems have been developed to record in multiple orientations with respect to muscle fibres to make rapid assessments of anisotropic properties of the muscle (Ogunnika et al., 2008,

2010; Garmirian et al., 2009; Li et al., 2012; Rutkove et al., 2016; Li et al., 2017b,a). For further assessment of EIM's biomarker capability specific to ALS, a number of studies have also been undertaken in the ALS SOD1 G93A Mouse (Li et al., 2013; Sanchez et al., 2016a; Li et al., 2016a; Kapur et al., 2018; Pandeya et al., 2022; Nagy et al., 2022).

A large barrier to the assessment of limb EIM is the large contribution the subcutaneous fat layer (SFL) has on measurements. Surface impedance measurements in the limbs could be argued to be deviating from the concept of EIM, as this is not isolated impedance myography (relating to muscle), but rather a superposition of impedances from the layers of skin and fat, as well as the muscle. Despite this, analysis to account for subcutaneous fat has been largely limited, often avoided with the argument that phase is said to cancel out the volume dependence of the impedance measurements. However, one study reported that the reactance data is the least impacted by subcutaneous fat thickness, with phase seeing a significant correlation with the subcutaneous fat thickness (SFT) (Sung et al., 2013). This is contradictory to that reported by Schwartz et al. (2015); Li et al. (2016b); Rutkove et al. (2017), who found minimal contribution from the SFL by employing a two-frequency phase ratio. Some work has been put into fine-tuning the electrode configurations to optimise for the least contribution from the SFL layer (Jafarpoor et al., 2013; Li et al., 2016b). However, this only reduces rather than removes the effects of the subcutaneous fat, hence work to determine an algorithm for removal of this contribution would be an invaluable advancement in this field. One such procedure termed Model Component Analysis (MCA), has been introduced and some initial simulation work suggests it could be successful in separating the impedance of subcutaneous fat and muscle (Kwon et al., 2019). However, there has been limited validation of this approach, so clearly more work is needed in this area.

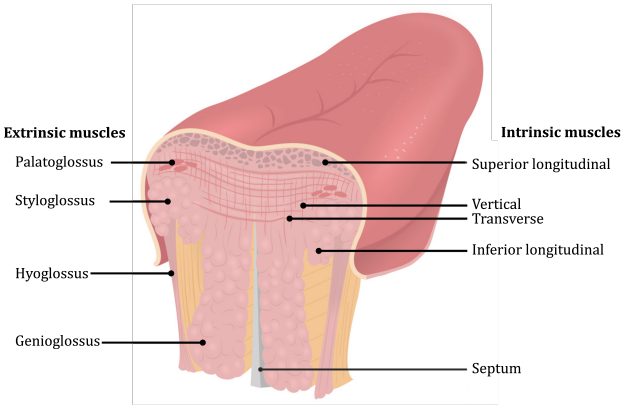

Figure 1.6: Posterior view of the tongue, demonstrating the varied orientations of muscle fibres. Adapted from Iwanaga and Tubbs (2021).

In recent years EIM has been applied to bulbar function measurement in ALS and has several advantages compared with other methods (Figure 1.7). One particular advantage of EIM of the tongue compared to the limbs is that the tongue surface is mucosal with limited keratinisation on the epithelial layer, therefore much lower frequency impedance assessment is possible (Murdoch et al., 2014). Additionally, the tongue is a unique muscle in the human body, characterized by its isolated location within the oral cavity. Unlike other muscles in the body, the tongue lacks subcutaneous fat and a thick layer of skin covering its surface, meaning the surface impedance is not obstructed or attenuated by the layers of fat or skin. Furthermore, the tongue possesses a much more complex myofibre arrangement than limb muscles. Figure 1.6 depicts the diverse

orientations of muscle fibres within the body of the tongue. The fibres pertaining to the central body of the tongue blade primarily align in vertical and transverse directions, while the peripheral regions are dominated by fibres aligned in a longitudinal direction.

Prior to the commencement of this project, a handful of studies had been presented in EIM of the bulbar region (Shellikeri et al., 2015; Mcilduff et al., 2015, 2017), making use of custom 4-electrode 2D arrays designed for tongue application with the Imp SFB7 bioimpedance system. Assessments here found high reproducibility for a 50 kHz assessment only (Shellikeri et al., 2015; Mcilduff et al., 2015), as well as for a number of frequencies in the range 50-500 kHz (Mcilduff et al., 2017). The 50 kHz study found a significant difference ($p<0.05$) in ALS and healthy tongue EIM datasets for R, X and θ, as well as correlation with tongue endurance (Shellikeri et al., 2015). Mcilduff et al. made assessments on a smaller electrode array to reduce gag reflexes in participants (Mcilduff et al., 2015). The multi-frequency study presented a visual of the phase spectral differences between healthy and ALS patients and determined an optimal 100 kHz frequency, which gave maximum separation of patients ($p=0.0015$) (Mcilduff et al., 2017). Additionally, the development of a finite element model by Pacheck et al. (2016) demonstrated how the impedance differences in diseased tissue come from the inherent changes in electrical material properties of the tongue muscle, rather than simply as a consequence of reducing muscle volume.

	ALSFRS-R bulbar subscore	Video fluoroscopy	IOPI	Standard EMG	EIM
Painless	✓	✓	✓		✓
Non-invasive	✓		✓		✓
Quantitative			✓		✓
Objective			✓		✓
Portable	✓		✓	✓	✓
Minimal training required to perform	✓		✓		✓
Independent of patient cooperation, strength					✓

ALSFRS-R, Amyotrophic Lateral Sclerosis Functional Rating Scale—Revised. EIM, electrical impedance myography; EMG, electromyography; IOPI, Iowa Oral Performance Instrument.

Figure 1.7: Comparison of EIM with the measures of bulbar function commonly used in ALS. Taken from (Mcilduff et al., 2017).

Some prior analysis work has been performed on the EIM tongue dataset, by my supervisors and previous students and is presented in Alix et al. (2020). The study is the first to present a novel impedance system designed to measure the impedance of the tongue in both 2D and 3D electrode configurations. In this study, the full spectrum (76 Hz-625 kHz) of intraoral impedance (tongue relaxed) measured in the central region of the tongue was analysed for 6 months of longitudinal data. Machine learning was employed to select the most relevant information from the high-dimensional dataset. Overall the device was found to produce reliable data (overall ICC=0.836), with the ability to differentiate between patients and healthy controls (maximum AUROC=0.96). The phase was found to correlate significantly ($p< 0.001$) with established measures of disease severity (bulbar ALSFRS-R subscore, max r =-0.526; tongue strength; max r=-0.454). Finally, the EIM recordings revealed a group level significant longitudinal change over 6 months. This a comprehensive first analysis, however, there is still further work to do. By the time I began this project measurements had been performed for up to 12 months of follow up. Additionally, extraoral (tongue protruded) measurements have been taken, as well as lateral measurements on the left and right sides of the tongue. The efficacy of these new measurement types must be established, including an exploration of the impact of edge effects for lateral recordings. If it is possible to use, the amount of data to analyse would

increase considerably, and further insights may become possible. Additionally, although multi-frequency and multi-configuration data have been assessed, a more comprehensive method for dimensionality reduction could massively enhance the interpretability and performance of the results. This will be discussed in more detail below (Section 1.3.2).

Recent developments in bulbar EIM, published throughout the course of this project, have included spectral recordings over a range of input frequencies and increasingly complex electrode arrays capable of interrogating tissue with multiple electrode configurations (Luo et al., 2021b). These studies have applied a forward and inverse theoretical modelling framework to eestimate the VCPs of the tongue in the longitudinal and transverse directions (Luo et al., 2021a,c; Luo and Sanchez, 2021; Luo et al., 2023). This is an interesting approach giving a direct understanding of the anisotropy of the tissue.

One note of importance is that outliers and artefacts in EIM recordings can occur due to issues with poor electrode contact, or movement of the probe during measurement. Poor electrode contact can result in inconsistent electrical impedance measurements, leading to erroneous data points (Martinsen and Grimnes, 2011). Particularly in surface impedance applied to limbs, appropriate skin preparation is vital to reduce artefacts due to skin contact, additionally, electrode gels are suggested to help (Farinha et al., 2006; Martinsen and Grimnes, 2011). However, even with such preparation and a thorough monitoring of electrode contact throughout recording, outliers and artefacts can still arise. Despite this most previous studies have not undertaken any sophisticated outlier removal or pre-processing procedures, but have simply removed single data points where resistance values become negative. Looking to the wider area of impedance work, some studies in Electrical Impedance Tomography (EIT) have made use of noise filters to remove 'bad' patterns from the dataset (Murphy et al., 2017, 2018a,b).

1.3 Data analysis techniques

A summary of the data analysis techniques that have been applied to EIM datasets in application to a range of neuromuscular disorders are presented below. The standard techniques that have been undertaken so far are explored, and a compilation of the significant results that have been presented through a range of studies is provided. In order to consider how the comprehensive analysis of high-dimensional EIM data can be improved and fine-tuned, analysis methods from other forms of medical spectroscopy techniques are also assessed.

1.3.1 Reproducibility and measurement comparison

In order to assess the test-retest reproducibility of EIM measurements, the intra-class correlation coefficient (ICC) is a widely used tool. The ICC is a statistical measure that assesses the degree of agreement or reliability among multiple measurements, with values ranging from 0 (no agreement) to 1 (perfect agreement). The rater-rater ICC can also be determined, which assesses the reproducibility between measures to compare measurements taken by multiple observers (i.e. experienced and inexperienced clinicians). A summary of previous work in assessing the reproducibility of EIM is presented in Table 1.3.

An additional method for assessing and visualising the reproducibility between measurements is the use of Bland-Altman plots (Bland and Altman, 1999). These plots provide a visual representation of the differences between the two measurement methods on the y-axis and the average of the measurements on the x-axis. Assessing the mean difference between the two measurements, which is indicated by a horizontal line on the plot, is used to determine the average bias or systematic difference between the methods. "The limits of agreement, which represent the region for which 95% of measurements lie, are marked on the plot and can be calculated using parametric or non-parametric methods. Additionally, any patterns or trends

can be identified by examining the distribution of the differences around the mean. A handful of previous EIM studies have made use of Bland-Altman plots for reproducibility assessment (Mcilduff et al., 2015; Geisbush et al., 2015; Alix et al., 2020).

Measure	Frequency	Muscle	Intra-rater ICC	Inter-rater ICC	Reference
θ	50 kHz	biceps	0.970		(Rutkove et al., 2006)
θ	50 kHz	quadriceps	0.971		
θ	50 kHz	tibialis anterior	0.938		
θ	50 kHz	tongue	0.790		(Shellikeri et al., 2015)
R	50 kHz	tongue	0.733		
X	50 kHz	tongue	0.911		
θ	50 kHz	tongue	0.76	0.78	(Mcilduff et al., 2015)
θ	50 kHz	tongue	0.73	0.60	(Mcilduff et al., 2017)
θ	100 kHz	tongue	0.82	0.79	
θ	200 kHz	tongue	0.82	0.73	
θ	300 kHz	tongue	0.80	0.71	
θ	400 kHz	tongue	0.75	0.69	
θ	100 kHz	tongue	0.77	0.65	
θ	76 Hz-625kHz	tongue	0.841	0.788	(Alix et al., 2020)
θ	50 kHz	quadriceps	0.998	0.982	(Martinez-Gonzalez et al., 2020)
R	50 kHz	quadriceps	0.998	0.973	
X	50 kHz	quadriceps	0.979	0.903	

Table 1.3: ICC for intra-rater and inter-rater comparison of repeat EIM measurements reported in previous studies.

Finally, in order to assess the similarity between multi-frequency impedance spectra, the normalised root mean square error (NRMSE) can be used. For the NRMSE between two spectra Z_1 and Z_2, it is calculated as:

$$\frac{\sqrt{\sum_{f=1}^{N}(Z_1(f) - Z_2(f))^2}}{N \times Range(Z_1)} \tag{1.11}$$

where N is the number of frequencies measured.

While this method has not previously been used in EIM assessments, it is a widely used tool for assessing differences in spectral data, including for Raman and infrared spectroscopy (Lin et al., 2021; Gao et al., 2022; Vries et al., 2023), EMG (Youn and Kim, 2010; Qiu et al., 2015), and magnetic resonance spectroscopy (Song et al., 2022).

1.3.2 Dimensionality reduction

High-dimensional data is defined as datasets that contain a large number of features relative to the number of samples (Lederer, 2022). The datasets analysed within this thesis are very high-dimensional, more so than any EIM data previously presented in studies of biomarker assessment for neurodegenerative disease. This is due to multi-frequency impedance spectra being recorded in many different directions through the tissue, or electrode configurations; multiple positions of device placement; and in the case of the limb dataset, multiple different muscles. Overall, this gives a large number of complex data points per patient to undergo comprehensive analysis. Dimensionality reduction techniques offer many benefits including; better visualisation; improved predictive performance; increased interpretability; improved computational efficiency; and reduced likelihood of overfitting (Van Der Maaten et al., 2009). In the case where the number of features significantly surpasses the sample size, dimensionality reduction is a crucial stage of the analysis. Due to the nature of previous EIM work in this field of study,

there is a limited range of dimensionality reduction performed on such impedance datasets, however, an overview on the work that has been done is presented below.

A large majority of work presented in EIM in application to the assessment of muscle health in ALS have utilised just a single frequency (50kHz) impedance measurement (despite data often collected over a full spectrum of frequencies). This is the case when both studying animal models (e.g. ALS SOD1 G93A Mouse) (Li et al., 2013; Nagy et al., 2022), as well as studies in human limbs (Rutkove et al., 2002, 2005, 2006, 2007; Tarulli et al., 2005, 2009; Garmirian et al., 2009; Rutkove et al., 2012a, 2014; Offit et al., 2020) and tongue (Shellikeri et al., 2015; Mcilduff et al., 2015). The majority of these studies only consider a single arrangement of electrodes, and many only assess the performance of the impedance phase metric; giving a single dimension of data to analyse, hence dimensionality reduction is not usually necessary. Sometimes multiple frequencies are measured, but the full spectra are not combined into an analysis, rather individual analyses (e.g. significance tests) are performed on each frequency in turn (Li et al., 2012; Mcilduff et al., 2017; Luo et al., 2021b). Similarly, if we extend to EIM work in all medical applications, while again measurements are usually recorded over a spectrum of frequencies, many studies only assess on a single frequency; for example work in Duchenne nuscular dystrophy (DMD) (Schwartz et al., 2015; Rutkove et al., 2016; Rutkove and Darras, 2013); stroke (Li et al., 2017b; Hu et al., 2019); cervical dysonia (Lungu et al., 2011); Inclusion Body Myositis (IBM) (Roy et al., 2020); spinal cord injury (Li et al., 2017a); muscle mass prediction (Cheng et al., 2022); and hand-grip force prediction (Pan et al., 2023).

Some EIM studies incorporate multiple electrode arrangements, these have been compared (not combined) as individual analyses (Alix et al., 2020; Luo et al., 2021b); or in some scenarios an average is taken over multiple directions of measurement (Hu et al., 2019). However, there have been a number of studies where data from measurements taken both parallel and transverse to muscle fibres have been combined to calculate an anisotropy ratio. This has been done in ALS and other diseases in mouse models and human subjects (Garmirian et al., 2009; Li et al., 2012; Rutkove et al., 2016; Li et al., 2017b,a).

Most studies in the limbs take measurements over multiple muscles of interest. However, there is limited work that incorporates multiple muscles into a combined analysis, despite the fact that for diagnosis and assessment of complex neurodegenerative diseases such as ALS, it is necessary to consider multiple muscles since the site of onset of the disease is varied (Sennfält et al., 2023). Sometimes each muscle is analysed in turn with performance compared (Garmirian et al., 2009), or multiple muscle measurements are simply averaged to reduce the dimension down to a single value; done over all muscles, and/or splitting into upper limbs and lower limbs (Rutkove et al., 2007, 2012a, 2014; Shefner et al., 2018; Offit et al., 2020). Additionally, all muscles have been analysed and that with the most significant slope of change is chosen (Shefner et al., 2018; Offit et al., 2020). A more sophisticated approach to combining multiple muscles, rather than taking averages (where information is lost) or simply selecting the best performer (likelihood of overfitting), may help improve the diagnostic and prognostic capability of EIM.

In cases where analysis is made over multiple frequencies or frequency spectra, some simple attempts at dimensionality reduction have been applied. This includes taking the average phase over multiple frequencies (Esper et al., 2006); calculation of the L2 (Euclidean) norm (Alix et al., 2020); calculation of 2-frequency phase ratios (Schwartz et al., 2015; Li et al., 2016b; Rutkove et al., 2017; Shefner et al., 2018; Roy et al., 2020; Rutkove et al., 2017); determining the peak phase (Jafarpoor et al., 2011, 2013); or calculating the average impedance slope of change in a given frequency range (Srivastava et al., 2012; Rutkove et al., 2012b, 2017; Semple et al., 2020). These methods have shown promise in giving some clinically significant metrics of disease (p values <0.05 in separating patients and healthy and correlating with other biomarkers of disease

severity). However, they are limited in over-simplifying a complex dataset; losing potentially vital information, and having little or no physical interpretability. For example, the ratio of two phases is rather mathematically confusing, since the ratio of two complex numbers should be represented by subtraction of the phase. Hence what this ratio physically represents for a deeper clinical understanding of the muscle is unclear. Parameterising the slopes of change is a step towards getting a more detailed picture of the spectral shapes, but would generally be an oversimplification in understanding such spectral patterns, where gradients change rapidly throughout the frequency range of measurement.

More sophisticated attempts to parameterise the full impedance spectra include Cole-Cole models. The Cole-Cole model (Cole and Cole, 1941) is a mathematical model that is often used to describe the impedance behavior of biological tissues, over a range of frequencies. The model assumes that the tissue is a mixture of electrical components, such as resistors and capacitors, which respond to changes in the frequency of the applied electric field. The Cole-Cole model is a deviation from Randle's model (Randles, 1947), which considers the impedance spectra ($\mathrm{Z}(\omega)$) of a capacitor (C) and resistor (R) in series:

$$Z(\omega) = \frac{R+1}{i\omega C} \tag{1.12}$$

where ω is angular frequency ($\omega = 2\pi\mathrm{f}$). The Cole-Cole model introduces an additional parameter, α (range from 0 to 1), which can be interpreted as the distribution of relaxation times in tissue, as well as a characteristic relaxation time τ, the high frequency asymptotic value of permittivity $\mathcal{E}_\infty$ and the change in permittivity at small frequencies, $\Delta\mathcal{E}$. The original model, describes the complex permittivity, $\mathcal{E}^*(\omega)$, spectral changes with frequency:

$$\mathcal{E}^*(\omega) = \mathcal{E}_\infty + \frac{\Delta\mathcal{E}}{1 + (i\omega\tau)^\alpha} \tag{1.13}$$

(Cole and Cole, 1941; Martinsen and Grimnes, 2011). Alternatively, this can be expressed in terms of the complex impedance, $Z^*(\omega)$:

$$Z^*(\omega) = R_\infty + \frac{\Delta R}{1 + (i\omega\tau)^\alpha} \tag{1.14}$$

where here R_∞ and ΔR are the high frequency resistance and small frequency change in resistance, respectively. Often real-world biological tissues will exhibit more complex dielectric behaviour than can be adequately described by a single pole Cole-Cole model. Hence, this model can be extended to include multiple relaxation processes, each characterised by its own relaxation time (τ_n) and amplitude ($\Delta\mathcal{E}_n$). This is done by using the fractional derivative approach, which takes the dielectric response as a superposition of several (N) dispersion models (Jonscher, 1999):

$$\mathcal{E}^*(\omega) = \mathcal{E}_\infty + \sum_{n=1}^{N} \frac{\Delta\mathcal{E}_n}{1 + (i\omega\tau_n)^\alpha} \tag{1.15}$$

Such models have been applied to animal impedance measurements, where the model parameters - particularly centre frequency, f_c - have been found to show significant differences with disease in the ALS SOD1 G93A mouse (Sanchez et al., 2016a; Li et al., 2016a); the polG mouse to assess premature ageing (Clark-Mattot et al., 2019); the DMD mdx mouse (Sanchez et al., 2017); and aged Casper and Tübingen zebrafish (Rutkove et al., 2023). Similarly, such parameterisations have been made on the dielectric spectra of biological tissue (which can be inferred directly from impedance measurements, as in eq. 1.9 and 1.10), done so on a large

range of biological tissues (including muscle) in a combination of excised animal tissue, and human tissue both ex vivo and in vivo, using a four pole Cole-Cole dispersion (1.15, with N=4) in the Hz to GHz frequency range (Gabriel et al., 1996b,c), as well as in a comparison of slow and fast twitch muscle in rats, fitted to a single pole Cole-Cole model (1.13) in the 1kHz-10MHz range (Sanchez et al., 2014). This demonstrates a clearly successful way of reducing high-dimensional spectra of impedance measurements, to a decreased number of parameters, without losing information. However, there are limitations to such modelling, particularly if the frequency range of the data is small, and the number of parameters required to describe the impedance increases. Hence, there may be more parameters required than can be reliably estimated from the data leading to overfitting a decrease in predictive power (Malmivuo and Plonsey, 1995), additionally, for very low frequencies simpler models with fewer parameters may be more appropriate (Malmivuo and Plonsey, 1995).

In a similar vein, impedance spectra have been parameterised using lumped circuit modelling (Shiffman et al., 2008; Shiffman and Rutkove, 2013a,b); figure 1.4b shows the 5-element circuit model used. It is shown that multi-frequency EIM in a frequency range of 3kHz - 2MHz taken in the quadriceps of healthy and ALS participants can be successfully characterised by this circuit model (Shiffman et al., 2008), and such a paramterisation has been shown to give features which are highly reproducible in healthy participants over time (Shiffman and Rutkove, 2013b), as well as demonstrate well-defined changes between healthy and ALS, as well as consistent directional change with time in ALS disease progression (Shiffman and Rutkove, 2013a). This is another comprehensive way of reducing the dimension of multi-frequency impedance datasets, where the parameters can be physically interpreted to give a more detailed understanding of the changes to cellular structure occurring in different disease processes. For example, the elements in figure 1.4b can be understood as r1 being the extracellular space current path; r2 as the intracellular fluid current path; and C1, being the cell membranes. Additionally, the cell interior is considered to include intracellular organelles (Schwan, 1994), which have their own membranes, C2 and internal fluids, r3 (Shiffman and Rutkove, 2013a). There are certain limitations to this when the frequency range is small, as reliably estimating the parameters becomes harder and the issue of multiple local optima may arise (e.g. as in Deasy (1997)), where hence it is not possible to give a meaningful interpretation of the data (McAdams and Jossinet, 1996). Conversely, for a large frequency range, an increased number of circuit elements may be required to capture all dispersion processes within the anatomically complex muscle tissue, including, but not limited to, the effect of proteins, tubular systems, membrane relaxation, surface charge and organelles (Schwan, 1994). Realistically, capturing all these processes within a circuit with a minimal number of elements is hard, but increasing the number of elements not only limits the power of the dimensionality reduction, but the relevance of such a circuit is difficult to establish, particularly as equivalent circuits are seldom, if ever, unique (McAdams and Jossinet, 1996). Overall, while this is a useful technique, the specific model must be chosen with care and limitations of the physical interpretation should be considered.

Additionally, dimensionality reduction has been applied to EIM datasets using machine learning techniques with feature selection in classification and regression problems (Srivastava et al., 2012; Khan et al., 2016; Anumba et al., 2020; Cheng et al., 2022; Pandeya et al., 2022), as well as in the previous analysis on the bulbar dataset of this project (Alix et al., 2020). The issue with such analyses is the likelihood of biased selection, particularly in such studies of neurodegenerative diseases, like ALS, where the participant numbers are low (Loughrey and Cunningham, 2005; Salam et al., 2021), and additionally feature selection processes can be slow and computationally expensive with very high-dimensional data, so consideration of dimensionality reduction processes prior to the use of machine learning algorithms can be advantageous (Salam et al., 2021). Further discussion of the specifics of classification and

regression analysis are discussed in the following sections.

A summary of the benefits and drawbacks of all the previous dimensionality reduction work that has been applied to EIM datasets is given in table 1.4. Here, it is clear that while some successful attempts have been made to reduce the dimension of multi-frequency impedance spectra, most methods are too simple and lose frequency specific information. While both Cole-Cole and lumped circuit modelling give a more comprehensive parameterisation of the whole spectra, the parameter estimation involved is computationally expensive and not easy to implement on a large scale with model fitting needing to be applied to each individual spectra in turn. Hence, this may not be a realistic method for use in the assessment of biomarkers for neurodegenerative disease, where data analysis needs to be relatively quick and easy to implement for use in clinical trials as well as for clinicians in everyday medical assessment.

Procedure	Equation	Benefits	Drawbacks	References
Average	$\frac{\sum_{f=1}^{N} Z_f}{N}$	Simple to implement, can reduce noise, single metric output	Over-simplification, lose frequency specific information, equal weight given to all frequencies	Esper et al. (2006)
L2 norm	$\sqrt{\sum_{f=1}^{N}(Z_f)^2}$	Simple to implement, robust to outliers, takes into account the magnitude of impedance and is transnational invariant, single metric output	Over-simplification, lose frequency specific information, equal weight given to all frequencies, sensitive to scaling	Alix et al. (2020)
Phase ratio	θ_{f1}/θ_{f2}	Simple to implement, relative comparison of phases, single metric output	Ambiguous physical meaning, oversimplification, only considering 2 frequencies, lose absolute phase information	(Schwartz et al., 2015; Li et al., 2016b; Rutkove et al., 2017; Shefner et al., 2018; Roy et al., 2020; Rutkove et al., 2017)
Peak phase	$\max(\theta_f)$	Identify dominant frequency, gives insight into electrical properties, clear and interpretable single metric	Neglects multi-frequency insights, sensitive to noise, dependence on data quality	(Jafarpoor et al., 2011, 2013)
Average slope	$\frac{\sum_{n=1}^{N-1} \frac{\theta_{n+1}-\theta_n}{f_{n+1}-f_n}}{N-1}$	Captures overall trend in spectra, robust to noise, relates to physical properties of the muscle, single metric output	Simplified representation, doesn't account for changes in direction of gradient, dependent on frequency range, lose frequency specific information	(Srivastava et al., 2012; Rutkove et al., 2012b, 2017; Semple et al., 2020)
Cole-Cole modelling	$R_\infty + \frac{\Delta R}{1+(i\omega\tau)^\alpha}$	Comprehensive representation capturing both magnitude and phase information, frequency specific parameters, captures non-linear behaviour	Parameter estimation is complex and computationally expensive, interpreting parameters in terms of physical processes is challenging, assumptions about the linearity and homogeneity of the system, loss of Fine-grained Information	(Sanchez et al., 2016a; Li et al., 2016a; Sanchez et al., 2017; Rutkove et al., 2023)
Lumped circuit modelling		Physically interpretable parameters related to specific electrical properties or phenomena, models can be adapted and customised to fit system of interest, comprehensive representation capturing both magnitude and phase information	Assumptions and simplifications about the system, choice of circuit is not obvious, parameter estimation is complex and computationally expensive, prone to overfitting, interpreting the circuit model parameters in terms of specific physiological phenomena is challenging	(Shiffman et al., 2008; Shiffman and Rutkove, 2013a,b)
Feature selection		Reduce impact of redundant features, faster model training	Biased selection where certain important features may be overlooked, computationally expensive process, sensitive to feature selection method used	(Srivastava et al., 2012; Khan et al., 2016; Anumba et al., 2020; Cheng et al., 2022; Pandeya et al., 2022)

Table 1.4: A summary of the benefits and drawbacks of the range of dimensionality reduction techniques that have so far been applied to multi-frequency EIM datasets

Feature selection is certainly a useful tool to be applied to high-dimensional complex datasets, however, there is place for an additional more detailed and comprehensive method of dimensionality reduction, which captures the complexity of the multi-frequency spectra and provides physically meaningful outputs.

Looking to different types of spectroscopy based medical data where dimensionality reduction analysis is commonly used, other approaches are considered. For example, principal component analysis (PCA), is widely used in the analysis of both Raman and Infrared spectroscopy data (Salzer, 2014; Mozhaeva et al., 2022), as well as mass spectrometry (Brereton, 2003). PCA is a procedure used to identify the directions in the data space along which the data points exhibit the highest variance. These directions, called principal components are orthogonal to each other and, hence are independent and uncorrelated. The first principal component accounts for the largest variance in the data, followed by subsequent components that explain decreasing amounts of variance (Jolliffe, 2005). For classification work using spectroscopy data, it is very common for PCA to be used in tandem with Linear Discriminant Analysis (LDA) applied to different muscle disease including ALS (Plesia et al., 2021), DMD (Alix et al., 2022a), myopathies (Alix et al., 2022b), and mitochondrial muscle disease (Alix et al., 2022d). LDA is a supervised technique that aims to find linear combinations of features that maximize the separation between different classes (Hastie et al., 2009). PCA is a useful technique for effectively reducing the dimension of large datasets and can be beneficial for feature extraction and noise reduction (Jolliffe, 2005). However, when the sample size is small it can become harder to obtain stable estimates of the covariance matrix, the procedure can be prone to overfitting and the potential of limited variability within smaller datasets can lead to less informative principal components. Additionally, the procedure is very sensitive to outliers (which are often present in impedance datasets), and a PCA reduced representation of data does not provide any interpretable components in the original feature space (Jolliffe, 2005; Brodlie et al., 2005).

Another alternative dimensionality reduction technique applied to spectral based medical data is Partial-Least-Squares Discriminant Analysis (PLS-DA) (Salzer, 2014; Alix et al., 2022b,d). This is a supervised technique which identifies latent variables to maximise the covariance between two classes, this can be applied to regression problems where the explained variance in the response variables are maximised, or to classification problems where separation between the classes is maximised (Pomerantsev and Rodionova, 2018). This method combines feature selection and prediction into a single framework, leading to efficient and effective modelling. However, as with PCA, the method is sensitive to outliers, can be prone to overfitting and requires careful consideration of proper validation with test sets (Pomerantsev and Rodionova, 2018). There are also challenges to interpreting the PLS-DA models and understanding the contribution of individual features.

An additional effective method for dimensionality reduction used in medical signal processing techniques is non-negative matrix factorisation (NMF). Applications of NMF including biomedical spectroscopy, EMG, and MRI. Like PCA, NMF is an unsupervised learning algorithm, here the non-negativity constraint allows data to be decomposed as a parts-based representation (Lee and Seung, 2000), providing an interpretable and meaningful output. In the analysis of data with more than two dimensions, NMF can be extended to non-negative tensor factorisation (NTF), which is an analogous technique that can be used to capture complex interactions in large multi-dimensional datasets. This method of dimensionality reduction allows for constructive feature extraction from complex datasets, is a form of unsupervised clustering providing an insight into the dominant patterns within the dataset (Ding et al., 2008), and can be a useful tool for noise reduction and artefact removal (Cichocki et al., 2009). Hence, it has many attractive features for the analysis of high-dimensional impedance datasets and is

chosen as one of the primary analysis frameworks used throughout this thesis.

For NMF, consider a dataset of m, multivariate n-dimensional non-negative vectors. These vectors are then placed in the columns of an $N \times M$ matrix, V. The NMF factorisation is given by:

$$\mathbf{V} = \mathbf{WH} + \mathbf{E} \tag{1.16}$$

where $\mathbf{W}$ and $\mathbf{H}$ are the non-negative factor matrices of size $N \times R$ and $R \times M$ respectively(Lee and Seung, 2000). Additionally, $\mathbf{E}$ is the $N \times M$ error matrix and represents the difference between the original dataset and the factorised approximation. R is the rank of the decomposition, which is generally chosen to be smaller than N or M, so a reduction in dimension is achieved (Lee and Seung, 2000). The decomposition is solved using an alternating least squares algorithm (Cichocki and Zdunek, 2007), which minimises the error, $\mathbf{E}$.

$$Minimize\, \|\mathbf{V} - \mathbf{WH}\|^2 \quad with\, respect\, to\, \mathbf{W}\, and\, \mathbf{H},\, subject\, to\, the\, constraints\, \mathbf{W}, \mathbf{H} \geq 0 \tag{1.17}$$

Lee and Seung (2000). The function we minimise here is the square of the Euclidean distance, which is defined by:

$$\|\mathbf{V} - \mathbf{WH}\|^2 = \sum_{ij} (V_{ij} - (WH)_{ij})^2 \tag{1.18}$$

This can be extended to NTF if we consider an N-dimensional dataset, in the form of an N^{th} order tensor, $T \in \mathbb{R}^{I_1 \times I_2 \ldots \times I_N}$. Thence the tensor decomposition is formed of a set of N unknown matrices, $\mathbf{U}^{(n)} = [\mathbf{u}_1^{(n)}, \mathbf{u}_2^{(n)}, ..., \mathbf{u}_R^{(n)}] \in \mathbb{R}^{I_n \times R}$. The tensor decomposition is then given as:

$$\mathbf{T} = \sum_{r=1}^{R} \mathbf{u}_r^{(1)} \circ \mathbf{u}_r^{(2)} \circ ... \circ \mathbf{u}_r^{(N)} + \mathbf{E} \tag{1.19}$$

(Cichocki and Phan, 2009), where $\circ$ is the outer product of vectors. Again, generally algorithms for the NTF model are based on a minimisation of the Euclidean distance:

$$\begin{gathered} Minimize\, \|\mathbf{T} - \sum_{r=1}^{R} \mathbf{u}_r^{(1)} \circ \mathbf{u}_r^{(2)} \circ ... \circ \mathbf{u}_r^{(N)}\|^2\ with\, respect\, to\, \mathbf{U}^{(n)} \\ subject\, to\, the\, constraints\ \mathbf{U}^n \geq 0,\ n = 1, ..., N \end{gathered} \tag{1.20}$$

The procedure for NTF decomposition is known as a PARAFAC (parallel factor) decomposition (Harshman et al., 1970), also known as a CANDECOMP/PARAFAC (CP) decomposition. Various optimisation procedures can be applied to a PARAFAC problem, including alternative least squares, where each matrix is updated in turn (Harshman and Lundy, 1994); simultaneous least squares, where all factor matrices are updated simultaneously (Nion and De Lathauwer, 2008; Kolda and Bader, 2009); and gradient based optimisation, where gradients of the objective function with respect to the factor matrices are computed iteratively to minimize the decomposition error (Kolda and Bader, 2009; Cichocki et al., 2009). In order to perform the optimisation, the unknown matrices, $\mathbf{U}^{(n)}$ must be initialised. This can be done randomly, or using singular value decomposition (SVD), where the singular vectors determined from the SVD of the given tensor, $\mathbf{T}$, are used for initialisation (Bro, 2001). This can provide a starting point that is close to the optimal solution and therefore enhance the efficiency and accuracy of the decomposition process.

While the non-negativity constraint within both NMF and NTF has the advantage of providing an easy to interpret parts-based representation of our data, it also leads to non-convexity of the optimisation problem, which can result in multiple local optima. The presence of multiple solutions can mean it is hard to determine the 'best' factorisation and also means these

decompositions can be highly sensitive to the initialisation, which must be carefully considered. One advantage of considering factorisations of higher order tensors is that their rank decompositions are often unique (Kolda and Bader, 2009). Another consideration is selecting the appropriate rank (R) for the NMF/NTF, which is somewhat of a balancing act. A higher rank can capture more detailed information and will generally give a more accurate decomposition (smaller error, **E**), it can lead to overfitting and may capture noise or unimportant information. Conversely, a lower rank gives increased dimensionality reduction but can underfit the dataset and lose important features (Kolda and Bader, 2009).

This study is the first to present the application of NMF or NTF in EIM data, although semi-NMF (which loosens the constraints on non-negativity in the decomposition) has been used in application to electrical impedance tomography (EIT) (Hentze et al., 2018). Overall NMF is relatively well established for its use in wider applications of medical imaging including MRI (Sauwen et al., 2016), CT scans (Liu et al., 2007; Hosseini-Asl et al., 2014) and PET scans (Lee et al., 2001; Ahn et al., 2004). Additionally, some promise has previously been shown in the application of NMF to several studies of biomedical spectral based data including Raman spectroscopy (Yakimov et al., 2021; Alix et al., 2022c,e), and mass spectrometry imaging (Aram et al., 2015). The analysis of time-series surface EMG data has been undertaken using both NMF (Jiang et al., 2009; Gallina et al., 2018; Kim et al., 2020; Li et al., 2023), as well as NTF (Xie, 2014; Akmal et al., 2019; Ebied et al., 2020).

Factorisation of Raman data in the application of neuromuscular disease finds that classification is improved with the use of NMF (Alix et al., 2022c), and longitudinal change can be well described for the serial study of serum in ALS, where the use of Bounded Simplex-Structured Matrix Factorization (BSSMF) helps with the physical interpretability of the factorised dataset (Alix et al., 2022e). In the application of EMG muscle signals, NMF is found to provide effective dimensionality reduction (Kim et al., 2020) where the signals obtained in the factor matrices have physical significance (Li et al., 2023). A comparison of PCA and NMF applied to EMG found that the outputs of the two procedures are highly comparable, and the non-negative nature of the factor matrices is considered easier to interpret (Gallina et al., 2018). The application of NTF to EMG signals demonstrates the effectiveness of this procedure at extracting multi-domain features from complex high-dimensional signals (Xie, 2014; Ebied et al., 2020), additionally NTF was proven effective at completing missing values in signals, where segments of EMG data are missing or corrupted (Akmal et al., 2019). EIM datasets, like surface EMG, are made up of complex electrical spectral patterns, hence this suggests that NTF has the potential to also enrich signal processing techniques of high-dimensional spectral EIM datasets.

1.3.3 Group comparison and classification

The majority of work presented in the assessment of EIM as a diagnostic tool for neuromuscular disease has investigated the differences in EIM between healthy and diseased cohorts using statistical testing, such as t-tests or the Mann-Whitney U test (Field, 2013), where some statistically significant differences have been reported. For example, a significant splitting ($p<0.05$) between healthy controls and ALS patients has been found in the 50 kHz phase and 50 kHz resistance in the tongue (Shellikeri et al., 2015), as well as for phase in 13 frequencies between 76kHz and 625 kHz in the tongue (Alix et al., 2020). Additionally, significant splitting between normal and the ALS SOD1 G93A mice was reported for EIM in the hind leg at 50 kHz phase (Li et al., 2012, 2016a), as well as for Multifrequency Cole impedance parameters, alpha and R_0/R_∞ (Li et al., 2016a).

When looking at significance across multiple features in high-dimensional data it is important to control for the rate of false positives (Bühlmann et al., 2014). This can be achieved by

employing a false discovery rate (FDR) correction, which adjusts the p-values obtained from statistical tests by taking into account the number of tests performed simultaneously. Being cautious with p-values is crucial because they are influenced by various factors, including sample size, effect size, and statistical assumptions. A p-value represents the probability of observing the data or a more extreme result under the assumption that the null hypothesis is true. However, it does not provide direct information about the magnitude or practical significance of the observed effect. It is always important to interpret p-values in the context of the study design, statistical assumptions, and the overall body of evidence (Greenland et al., 2016). Therefore, employing FDR correction and exercising caution with p-values is crucial to ensure that significant findings are robust and reproducible. FDR has been employed in a handful of previous EIM studies in this field (Rutkove et al., 2017; Alix et al., 2020; Pandeya et al., 2022; Rutkove et al., 2023), however, most work has simply made assessments on single EIM features (despite multiple frequencies being recorded on), hence have neglected to make use of such procedures.

Throughout the analysis in this thesis, the Benjamin-Hochberg procedure for false discovery rate will be employed (Benjamini and Hochberg, 1995). Specifically, when dealing with a set of p-values obtained from m features, the p-values will be sorted in ascending order and assigned ranks ranging from 1 for the smallest p-value to m for the largest. The FDR-corrected p-value for each feature is then calculated as:

$$\text{p-value}^{FDR} = \text{p-value} \cdot \frac{m}{k} \,. \tag{1.21}$$

In order to gain deeper insight into the diagnostic potential of EIM the use of machine learning (ML) based classification models is potentially necessary. Such models have prediction capability; not only determining the significance of differences between groups but also providing predictions for new, unseen instances. Additionally, they can incorporate multiple variables, handle non-linear relationships, provide insights into the relative importance of different features and have built in robustness to noise and outliers (Frenay and Verleysen, 2014; Rajula et al., 2020). ML is particularly suited when there are few observations and many predictors(Rajula et al., 2020). A handful of previous studies have employed ML based classification techniques in application to disease diagnosis with the use of EIM data. This includes work in spinal muscular atrophy (SMA) introduced a combination of 50 kHz impedance (R, X and θ) and multi-frequency impedance slopes as features alongside quantitative muscle ultrasound (QMU) data (Srivastava et al., 2012). Using a support vector machine (SVM) classifier, Srivastava et al. produced a mean AUROC of 0.952 for normal vs SMA classification. A further study in prostate cancer, explored the classification of malignant vs benign tissue using EIS features recorded in 28 frequencies (1kHz-1MHz) across 8 different electrode patterns (Khan et al., 2016). Through a leave-one-patient-out (LOPO) cross-validation, a benign/malignant classification was successful, with AUROC=0.86.

Moving to specific classifications of ALS disease, a study in ALS SOD1 G93A mice, which assessed the performance of an ML random forest classifier (RF) incorporating multi-frequency (8-1027kHz) R, X and θ values measured on the mouse gastrocnemius (Pandeya et al., 2022). The question is of the necessity of including the phase data as input features since this is a function of both R and X, which are already included. However, using 10-fold cross-validation the classification of ALS vs healthy performed very highly with the RF classifier (AUROC=0.99) compared to just 50 kHz phase (AUROC=0.79). Finally, previous analysis performed on the multi-frequency (76 Hz-625 kHz) EIM tongue dataset, shows a promising performance of healthy vs ALS classification (Alix et al., 2020). Alix et al. employed 4-fold cross-validation with a 3-nearest neighbour classifier and an exhaustive wrapper for feature selection, and reported AUROC values between 0.81-0.96 in 3D configurations, and between 0.77-0.86 in 2D configurations. One thing to note is that classification has not been applied to the splitting of severe,

compared to mild or asymptomatic ALS. Neither has it been applied to the separation of ALS patients with mimic disease, nor been used to classify between myopathic and neurogenic muscle (which can be evaluated using needle EMG). Clearly, such analysis would be of great importance for assessing the biomarker capability of EIM for neurodegenerative disease on the whole.

In machine learning data are split into "training" and "test" sets which are utilised for training the classifiers and evaluating the performance of the model respectively. Overfitting is a common challenge in ML classification, particularly when dealing with high-dimensional data and a relatively small sample size. This occurs when a classifier models the training data too closely and is unable to give accurate predictions on new data, such models are said to have a low bias (fits the training data very well) and a high variance (very sensitive to fluctuations in the training data) (Loughrey and Cunningham, 2005). In order to provide a more reliable estimate of the model's generalisation ability cross-validation can be utilised, for example, k-fold cross-validation or leave-one-out cross-validation (Hastie et al., 2009). Doing so will give a more robust estimate of the model's performance and can help identify potential overfitting issues (Hawkins, 2004; Cawley and Talbot, 2010). When sample size is small, the available data for training becomes limited therefore complex models can find spurious correlations or fit noise, leading to poor generalization (Hawkins, 2004), hence careful model selection and use of cross-validation techniques becomes crucial. Another consideration is that high-dimensional data often suffer from the "curse of dimensionality". As the number of dimensions (features) increases, the available data becomes sparse, making it difficult to identify meaningful patterns and relationships. The sparsity of data leads to increased complexity in learning algorithms and can result in overfitting (Debie and Shafi, 2019). To overcome this appropriate dimensionality reduction procedures should be considered (see Section 1.3.2).

Additionally, feature selection can help address this issue of dimensionality, improve model performance, and reduce over-fitting models. Feature selection approaches include filters and wrapper methods. Filters assess the relevance of features by ranking them based on statistical properties such as correlation coefficients, done independently of the classification algorithm (Guyon and Elisseeff, 2003). While wrapper methods assess subsets of features within the classifier, and use the performance of the classifier as a criterion for feature selection (Guyon and Elisseeff, 2003). Generally, wrapper methods give improved performance as they can consider feature interactions and have direct feedback from the classifier, while filter methods may still select irrelevant features that are statistically correlated with the target variable but do not provide meaningful information for the classification task (Bolón-Canedo et al., 2015). On the other hand wrapper methods are much more computationally expensive, especially when considering an exhaustive search on high-dimensional data, although forward selection or backward elimination can improve this (Wah et al., 2018). Furthermore, wrapper methods are more prone to overfitting (Loughrey and Cunningham, 2005).

Finally, when building a classification model, the choice of the appropriate classifier must be carefully considered. A number of different classifiers have been selected throughout the analysis work of this project. Table 1.5 gives an overview of the different types of classifiers and their benefits, drawbacks, and considerations to be made.

In order to ensure robust classification of the high-dimensional impedance datasets analysed throughout this thesis, classification models will be carefully selected, with performances compared for deeper insight. Feature selection will be employed using wrapper selection techniques in tandem with dimensionality reduction. Finally, cross-validation will be carefully utilised in order to mitigate the effects of overfitting.

Classifier	Benefits	Drawbacks and considerations
K nearest neighbours (KNN)	Easy to understand and implement, can handle binary and multi-class problems, robust to outliers, can handle non-linear relationships between features	Sensitive to redundant features, may be outperformed on more difficult classification tasks, computationally expensive, selection of k may require cross-validation
Support vector machine (SVM)	Effective in high-dimensional spaces, works when the number of dimensions exceeds the number of samples, solution of the optimisation problem is relatively straightforward, versatile with the specification of custom kernels to consider non-linear relationships, robust to outliers	Computationally expensive, choice of kernel functions is crucial to avoid overfitting, sensitive to regularization parameter (C) which must be appropriately chosen, selection of kernel and C may require cross-validation, struggles with overlapping classes
Random Forest (RF)	Perform well with high-dimensional data, robust to overfitting and noise, provides a measure of feature importance, efficient computation suited for large-scale datasets	Lack of interpretability, sensitive to the number of trees and number of features, cross-validation may be required to find optimal values of these hyperparameters, cannot extrapolate classification outside the range of test data
Naive Bayes	Simple algorithm and low computational cost, fast to train, effectively handles high-dimensional feature space, robust to redundant features, provides insights into the importance of different features	Assumes feature independence and Gaussian feature distribution, if data deviates from assumptions of the performance may suffer, unable to capture non-linear boundaries as effectively as other algorithms

Table 1.5: Information on the advantages and disadvantages of different ML classifiers, collated from a number of sources (Zhang, 2004; Cunningham and Delany, 2007; Breiman, 2001; Pedregosa et al., 2011; Bishop, 2006).

1.3.4 Correlation and regression analysis

One important assessment to make when looking at the capability of a specific biomarker is its prognostic potential for capturing disease specific information. In order to do this it is common to perform statistical tests of correlation with our impedance biomarker with other markers of disease severity. For ALS severity assessment these markers usually include muscle strength and the ALSFRS-R. As impedance data are not typically assumed to be normally distributed, and hence Spearman's rank is often used as a non-parametric measure of the correlation between two measures. This is a statistical analysis, which tests for monotonicity in the data with rank value varying between -1 and 1 (Kendall and Stuart, 1979). The corresponding p-value roughly indicates the probability of an uncorrelated system producing datasets that have a Spearman correlation at least as extreme as the one computed. Previous EIM studies have found significant Spearman correlations between EIM metrics and the total ALSFRS-R (Rutkove et al., 2014; Offit et al., 2020) and ALSFRS-R subscores for bulbar (Mcilduff et al., 2017; Alix et al., 2020) and upper/lower extremities (Rutkove et al., 2014; Offit et al., 2020). Additionally, various forms of muscle strength testing have shown significant Spearman correlation with EIM data, this includes grip strength in the ALS SOD1G93A Mouse (Li et al., 2016a), as well as HHD (Rutkove et al., 2014), medical research council (MRC) strength testing (Rutkove et al., 2002; Offit et al., 2020), tongue endurance (Shellikeri et al., 2015) and tongue strength (Alix et al., 2020) in human participants. Table 1.6 gives an overall summary of all statistically significant results previously reported in the correlation between EIM metrics and measures of ALS severity.

Additionally, statistical tests of correlation can be extended to more complex regression techniques, which are particularly useful for high-dimensional datasets. Regression analysis can be used for predictive modelling, can quantify the impact of individual predictor variables

EIM metric	Muscle(s)	Comparison	Spearman rank (p-value)	Reference
50 kHz θ	Quadriceps	Quadricep MRC	0.64 (p<0.05)	(Rutkove et al., 2002)
50 kHz θ	Whole body	HHD (whole body)	0.47 (<0.001)	(Rutkove et al., 2014)
50 kHz θ	Lower limbs	HHD UE	0.65 (<0.001)	
50 kHz θ	Upper limbs	HHD LE	0.52 (<0.001)	
50 kHz θ	Lower limbs	ALSFRS-R UE	0.31 (0.018)	
50 kHz θ	Upper limbs	ALSFRS-R LE	0.45 (<0.001)	
50 kHz θ	Whole body	ALSFRS-R (total)	0.38 (0.039)	(Offit et al., 2020)
50 kHz θ	Whole body	MRC-8 muscle	0.53 (0.003)	
50 kHz θ	Upper limbs	ALSFRS-R UE	0.49 (0.006)	
50 kHz θ	Lower limbs	ALSFRS-R LE	0.39 (0.03)	
50 kHz θ	Tongue	Tongue endurance	0.457 (0.046)	(Shellikeri et al., 2015)
100 kHz θ	Tongue	ALSFRS-R bulbar	0.62 (0.044)	(Mcilduff et al., 2017)
3D L2 norm θ	Tongue	ALSFRS-R bulbar	-0.526 (<0.001)	(Alix et al., 2020)
2D L2 norm θ	Tongue	ALSFRS-R bulbar	-0.464 (<0.001)	
3D L2 norm θ	Tongue	Tongue strength	-0.454 (<0.001)	
2D L2 norm θ	Tongue	Tongue strength	-0.403 (0.001)	

UE= upper extremity, LE = lower extremity

Table 1.6: Summary of correlation assessment results between EIM metrics and other biomarkers of disease severity in ALS studies

on the outcome measure, and can be used to test for more complex hypotheses between variables (Field, 2013). There has been some application of regression techniques applied to EIM studies in ALS. This includes the use of Cox Proportional Hazards regression (Rutkove et al., 2012a), which is a statistical method used for analysing survival data (Cox, 1972). Here Rutkove et al. computed the Cox Hazard's ratio in order to assess the relationship between rate of decline and survival across patients and compared this for EIM data along with HHD and the ALSFRS-R. Regression has also been used as an estimation tool for myofibre size in ALS mice (Kapur et al., 2018). Using a standard multiple regression technique called least absolute shrinkage and selection operator (LASSO), the myofibre size in muscle was predicted with an error of 12% using multi-frequency EIM data measured in two directions (longitudinal and transverse) (Kapur et al., 2018). Looking to wider applications of EIM datasets, one study shows the comparison of two regression techniques, ridge regression (RR) and support vector regression (SVR), to predict muscle mass using 50 kHz EIM data recorded at multiple lower limb placement positions (Cheng et al., 2022). A separate study in cervical EIM employed multivariate linear and non-linear logistic regression analyses to study the power of impedance spectral data in predicting preterm birth in asymptomatic women (Anumba et al., 2020).

Regression and correlation techniques have also been used to specifically explore the impact of the skin-subcutaneous fat layer (S-SFL) thickness on EIM measurement data in the limbs. A multivariate regression analysis was performed on 50 kHz EIM data and SFT measurements in a healthy cohort, with age introduced as an independent variable. Here no significant correlation was found between EIM 50 kHz phase and SFL thickness in men or women (Tarulli et al., 2007). Another study in Spinal Muscular Atrophy used multivariate regression analysis to explore the correlations between EIM measurements, skin-subcutaneous fat thickness and strength (Rutkove et al., 2010). Additionally, correlation tests using Spearman's analysis on healthy cohort data have compared the correlation between resistance, reactance, and phase at 50 kHz with SFT (Sung et al., 2013); and comparison between different electrode configurations at 50 kHz as well as the 50/100kHz phase ratio (Li et al., 2016b). A comparison of the correlation coefficients reported between SFT and EIM resistance, reactance and phase recorded for different electrode configurations is shown in table 1.7. An argument is made for the use of impedance metrics which do not correlate significantly with the thickness of the fat layer;

those are reactance (at 50 kHz) (Sung et al., 2013) or the use of the 50kHz/100kHz phase ratio with a wide longitudinal electrode configuration (Li et al., 2016b). Clearly, there is still room for further assessment over a wider range of frequencies and muscles.

Frequency	Muscle(s)	Configuration	R^2 correlation coefficient (p-value)			Reference
			R	θ	X	
50 kHz	Gastroc	Narrow Long	0.64 (p<0.001)	0.7 (p<0.001)	0.07 (ns)	(Sung et al., 2013)
50 kHz	Biceps	Narrow Tran	0.74 (p<0.001)	0.64 (p<0.001)	0.43 (p=0.029)	(Li et al., 2016b)
50 kHz	Biceps	Narrow Long	0.74 (p<0.001)	0.53 (p<0.001)	0.42 (p<0.001)	
50 kHz	Biceps	Wide Long	0.68 (p<0.001)	0.56 (p<0.001)	0.35 (p=0.003)	
50/100kHz	Biceps	Narrow Tran		0.12 (ns)		
50/100kHz	Biceps	Narrow Long		0.24 (p=0.01)		
50/100kHz	Biceps	Wide Long		0.01 (ns)		

Table 1.7: Summary of correlation assessment results between EIM metrics recorded at different configurations and the SFT in healthy cohort studies.

Overall, while multiple regression analyses are a useful tool for gaining deeper insights into the relationship between different variables, several difficulties arise when there is collinearity and high correlations among variables (Mela and Kopalle, 2002). Issues pertaining to unreliable coefficient estimates, inflated standard error and model overfitting are likely. When assessing multi-dimensional EIM datasets regression based methods are not always appropriate, as significant collinearity is often seen across the dimensions.

1.3.5 Finite element modelling

A number of studies have employed finite element method (FEM) based modelling in order to gain deeper insights into multidimensional EIM datasets. This is done using the Comsol Multiphysics® software (COMSOL, 2023), which is a powerful tool for simulating and analysing complex physical systems, using an FEM approach to solve partial differential equations (PDEs). FEM is an effective tool as it takes into account both intrinsic and geometric properties of biological tissue, can account for anisotropy of dielectric properties in 3D and introduces changes in muscle volume and shape and in the case of limb measurements incorporate the SFL.

One hurdle with such modelling is that it is considerably difficult to obtain human tissue, in order to perform direct measurements of the conductivity and permittivity, for both practical and ethical reasons (Jafarpoor et al., 2011). Therefore, generally, the dielectric properties of the muscle are input from data collected through ex vivo studies in rat and mouse gastrocnemius tissue (Wang et al., 2011; Jafarpoor et al., 2011, 2013; Pacheck et al., 2016). While properties of other tissues have been obtained from recordings made in a study that extensively investigated the dielectric properties of various biological tissues (Gabriel et al., 1996a,b,c). This has been applied to modelling of the limbs with inputs for skin-subcutaneous fat, fascia, bone, and marrow (Wang et al., 2011; Jafarpoor et al., 2011, 2013), as well as for modelling of the tongue with inputs for the epithelial layer (Pacheck et al., 2016). A more recent study, (Heath et al., 2022), describes the development of a more intricate model of the electrical impedance of the tongue epithelium, providing further insight into frequency-dependent keratin properties, and the confounding effects of thicker keratinised layers.

However, there are clear limitations to the use of animal data for models of human tissue, firstly while in general the dielectric properties of mouse and human muscle tissues are expected to be largely comparable, there are also apparent differences. These include muscle architecture, fibre type composition, fibre length, and collagen content (Mathewson et al., 2012). In the case of the work in building an FEM model of the tongue completed by Pacheck et al.,

we would expect that using data recorded in the mouse gastrocnemius as a model input would give significant deviation from surface impedance measurements made in the human tongue. This is because the tongue is made up of a highly complicated muscle fibre arrangement with complex myo-architecture (Gaige et al., 2007), hence it can not be easily parameterised using a homogeneous muscle fibre direction with transverse and parallel dielectric properties input in the same architecture as the limbs. Additionally, the source of dielectric spectra presented by Gabriel et al. demonstrates a large variation in conductivity and permittivity values presented across the literature, with up to one order of magnitude variation in bone, two orders of magnitude variation in fat, up to four orders of magnitude variation in skin (Gabriel et al., 1996a). This clearly represents limitations with such measurements, which could be due to inter-subject variability, accuracy in the probe calibration, and the assumption of homogeneity of the tissue. Gabriel et al. used an open-ended coaxial probe for recording the dielectric spectra, which can be sensitive to environmental interference, as well as the size and contact area of the probe.

As expected, the modelling work that has been undertaken, described above, has failed to achieve good agreement between surface EIM recordings in human participants and FEM model data. One such study modelling the limbs in Spinal Muscular Atrophy (SMA), did not achieve agreement between the EIM and FEM resistance, reactance and peak values, but did capture a consistent trend in decreasing phase when moving from healthy to disease (Jafarpoor et al., 2011). A further study applying FEM to the tongue in ALS, also found large offsets in the resistance, reactance, and peak values when comparing EIM to the model. However, there was some agreement in the general spectral shapes as well as the same trend of decreasing phase when moving from healthy to disease (Pacheck et al., 2016), although it must be noted that a scaling factor was applied to the modelled data here in order to effectively plot this data side by side. Overall, although these models are clearly not perfectly parameterised, the results do conclude that the changes identified in EIM due to neuromuscular disease are seemingly the result of intrinsic changes in electrical properties of the tissue rather than simply loss of muscle volume.

Further FEM work has explored determining an optimal electrode configuration for recording EIM in the limbs with minimal contribution from the S-SFL (Jafarpoor et al., 2013). They determined firstly that the reactance was the impedance parameter least susceptible to changes in the thickness of the SFL. Additionally, using a configuration with the sense and excitation electrodes all in parallel and a fixed 30 mm separation between the sense electrodes, an 80 mm separation between the excitation electrodes gave the optimal configuration for minimal sensitivity to SFT. Another study explored the edge effects of EIM measurements, which refers to the distortion of measurements when one or more electrode(s) are placed near the boundaries of the area being examined (Li et al., 2019). Using a saline-tank phantom they provided results that demonstrated the ability of FEM models as a tool for optimising the EIM electrode configuration design in order to minimise the prevalence of such edge effects. Finally, some further work has applied FEM to validate a new approach using two concentric needles for intramuscular EIM recordings, termed needle EIM (Cardoner et al., 2021; Luo et al., 2023). A sophisticated computational algorithm has been determined using FEM to reverse engineer dielectric properties of the tongue in two dimensions and has been validated with ex vivo porcine tongue measurements (Luo et al., 2023). The inverse method is based on a number of assumptions, including infinitely large tissue and the electrode's linear axis oriented parallel to the anisotropic direction of the tissue.

A final study, which employs an FEM approach, proposed a method for the separation of subcutaneous fat from muscle in surface EIM measurements (Kwon et al., 2019). They introduced a new technique, termed Model Component Analysis (MCA), this methodology imposes a relationship between the frequency measured and the impedivity of the tissues by

means of a physical model implemented within the signal separation. Using FEM simulations the mixing matrices for the fat and muscle layers were determined, which were assumed to take a constant value. However, there are immediate limitations to this as the true mixing would be dependent on the characteristics of the electrodes, the frequency measured, and the (unknown) impedivity values of the muscle (Kwon et al., 2019). Other limitations of this model include the fact that the contribution of skin was neglected, and the dielectric spectra of biological tissues were parameterised by the Fricke-Morse model, which utilises only three parameters and may not capture the full complexity of these tissue's spectra. Additionally, the experimental impedivity values were obtained from Andreuccetti et al. (1997), which is an online resource based on the data published by Gabriel et al. Hence, the model is also affected by the limitations of this dataset as discussed above. Finally, although this signal separation was applied to three healthy subjects, there is no way of validating if this gives accurate results. Therefore, direct measurements of muscle impedivity measured ex vivo in patients undergoing muscle biopsy are needed in order to validate this approach.

1.3.6 Change over time

In order to assess the capability of a specific biomarker for detecting disease it is very common to perform longitudinal studies with measurements taken repeatedly over a given period of time. Such longitudinal studies enable the assessment of how well a biomarker reflects disease changes over time, allow for assessment of the individual variability in biomarker characteristics, and provide data to aid in the design of clinical trials for further study of the disease (Brody, 2012). Overall, longitudinal studies in EIM have undertaken analysis using one of two analysis procedures. Firstly, using linear mixed modelling to test for significant changes over time on a group level and to make comparisons of the slopes of change in diseased vs healthy cohorts. Secondly, in regard to the design of hypothetical clinical trials, power analysis is utilised to determine the sample size requirements in order to detect specific treatment effects.

A number of studies assessing limb EIM as a biomarker for ALS have undertaken power analysis on longitudinal data (Rutkove et al., 2007, 2012a; Shefner et al., 2018). The first study by Rutkove et al. considered a hypothetical clinical trial with a sample size of 100 patients receiving a drug and 100 receiving a placebo. Utilising a 50 kHz phase averaged over five limb muscles, they determined the power of such a study under the assumption of a specific treatment effect. For a 10% treatment effect, a power of 73% was achieved with EIM compared to 28% with MMT (Rutkove et al., 2007). Conversely, the work following this used power analysis to estimate the sample size required to detect a 20% treatment effect at a set power of 80%. Again utilising the 50 kHz phase, they assessed the mean phase across muscles, as well as the muscle, which has the steepest slope, based on the knowledge that the site of disease progression varies largely across patients. A sample size of 95 and 182 were determined for the EIM steepest and EIM mean respectively, in comparison assessment of HHD gave a value of 266 and ALSFRS-R gave 220 (Rutkove et al., 2012a). The work by Shefner et al. compared the sample size requirements across different frequencies, making assessments at 50 kHz, 100 kHz, as well as the 50kHz/200kHz phase ratio, which has been previously suggested to help reduce contributions of subcutaneous fat (Schwartz et al., 2015). This study utilised a random-slopes linear mixed model to run a power analysis, determining the sample size required to detect a 30% reduction in progression rate at 80% power. Again the EIM mean and EIM steepest were assessed, and a 5.2-fold reduction in sample size requirements was determined for EIM steepest compared to the ALSFRS-R at 50 kHz (Shefner et al., 2018).

Assessment of longitudinal change through linear mixed modelling to determine the significance of changes detected have been applied to DMD (Rutkove et al., 2017; Kapur et al., 2019),

as well as ALS for both a limb and tongue EIM dataset (Offit et al., 2020; Alix et al., 2020). Offit et al. employed a random regression coefficient model to evaluate the change of 50 kHz EIM phase measurements over 30 months. Significance testing indicated that the slope in the ALS group was different from that in the non-ALS group ($p<0.05$ for 8 muscle average), and the slope in the ALS group was significantly different than zero ($p<0.01$ for 8 muscle average) (Offit et al., 2020). For bulbar assessment, Alix et al. used linear mixed modelling, with the L2-norm of multi-frequency impedance spectra (76 Hz-625kHz) averaged over 8 different electrode configurations. Significant changes over time were found for the ALS (but not the healthy) group ($p=0.04$ at 3 months, $p=0.002$ at 6 months), compared to only insignificant changes ($p>0.05$) in tongue strength and the ALSFRS-R (Alix et al., 2020).

1.4 Gaps in the literature

Overall, while there have been numerous efforts to demonstrate the potential of EIM as a viable candidate biomarker for neurodegenerative disorders such as ALS in the past three decades, there are still areas of analysis that need further focus. Thus far, assessment of EIM has largely been limited to single frequency (50 kHz) studies, where measurements are often only recorded in a single direction or configuration of electrodes. However, EIM is capable of capturing impedance data at multiple frequencies and through many variations of electrode configurations, where 3D configurations in particular are a novel technique. Yet effectively utilising this information for classification and prognostic purposes remains an ongoing challenge. In cases where multi-frequency spectra have been studied, the dimensionality reduction procedures are often too simplistic and lose frequency specific information. Therefore the development of an effective dimensionality reduction procedure for the assessment of high-dimensional EIM datasets is crucial.

FEM-based modelling has been explored as a useful tool for a deeper understanding of EIM. However, thus far potential inaccuracies in the expected dielectric properties of biological tissue have led to modelled data presenting significant deviations from real life measurements. Therefore, work to optimise and refine these dielectric inputs in order to improve the agreement between modelled and measured EIM data would be extremely valuable. Furthermore, while EIM in the limbs has been demonstrated to be heavily influenced by the layers of skin and subcutaneous fat, the development and validation of an effective methodology to separate the contribution of the S-SFL from the muscle impedance information has yet to be produced. Therefore, this is a clear gap in the research that needs addressing. Finally, there is a lack of work in the comparison of EIM spectral changes to specific disease changes, such as acute compared to chronic denervation. Further work to corroborate the EIM signal to a more detailed picture of the muscle state would be highly beneficial.

1.5 Aims and objectives

1.5.1 Aims

The aim of this work was to develop novel methods for the robust analysis of multi-dimensional EIM data with the intention of enhancing the identification of ALS and other neurodegenerative diseases, as well as improving data interpretation.

1.5.2 Objectives

The main objective of utilising multiple frequencies is that EIM can capture a wider range of information on the underlying tissue characteristics, such as cell membrane integrity, tissue

composition, and muscle fibre structure. Different frequencies can probe specific aspects of tissue behaviour, where low frequencies are more sensitive to extracellular changes, such as extracellular fluid and connective tissue, while higher frequencies can provide information about intracellular properties and membrane integrity. Through a detailed assessment of dimensionality reduction techniques in application to EIM data and other spectroscopy based medical datasets, I have determined that NTF is an appropriate method which will aid in the dimensionality reduction and assessment of the high-dimensional impedance datasets under analysis, without losing important frequency specific spectral information. Additionally, other methods including PCA and lumped circuit modelling will be employed to further reduce dimension down to a single metric and to give insights into deeper physical interpretation of results.

Specifically in regards to bulbar EIM analysis, an assessment of the viability of lateral measurements on the tongue will be made by considering the impact of edge effects. Such measurements can then be assessed in comparison to central measurement data as well as used to assess for bulbar disease asymmetry. Additionally, comprehensive dimensionality reduction will be applied to the impedance spectrum over the multiple 2D and 3D electrode configurations, providing a novel assessment tool for the complex architecture of the tongue muscle. Sophisticated classification algorithms and assessments of longitudinal changes with disease progression will be made on these outputs. Additionally, disease changes will be assessed in patients with different EMG findings to make an assessment of how different directions of spectral change can characterise different disease processes. Overall, this will provide a much more thorough analysis than has previously been made in this area, with an in depth assessment of the complex EIM changes that occur in the tongue as a result of ALS.

Concerning limb EIM, the influence of the S-SFL on these data is a critical element that needs to be addressed. The majority of work in limb data analysis will focus on determining a sophisticated and effective method for separating the signal of the muscle impedivity from the combined skin-subcutaneous fat-muscle recordings. Ex vivo measurements in animal tissue as well as FEM work will be used to aid the development of such an algorithm. The signal separation procedure will be applied to a high-dimensional multi-muscle EIM dataset and the effectiveness of the approach will be accessed. EIM data post-subcutaneous-fat removal will be assessed for its capability of correlating with disease severity as well as classifying diseased and healthy muscle. Further to this, a separation of myopathy compared to neurogenic disease will be assessed, with the aim of evaluating the ability of limb EIM as a tool for distinguishing ALS from other mimic diseases.

1.6 Hypotheses

i. Multi-frequency and multi-configuration EIM measurements will produce reproducible data.

ii. Multi-frequency and multi-configuration EIM datasets will provide a more comprehensive understanding of muscle health than single frequency data.

iii. Multi-frequency and multi-configuration EIM datasets will improve the biomarker capability of EIM.

iv. NTF will provide an interpretable framework to decompose multi-dimensional EIM datasets with performance comparable, if not better, than traditional approaches.

v. The EIM spectral pattern will change over time in line with the progression of ALS but, owing to the complex changes in muscle, the change will not be unidirectional.

vi. Optimising FEM models for agreement with EIM measurement data will reveal information about the underlying dielectric changes that occur in muscle.

vii. Limb EIM data will be highly correlating to skin and fat thickness and FEM models will provide a framework for reducing their contribution.

viii. Signal separation procedures will reveal muscle specific impedance information in limb EIM.

2 Chapter 2: Bulbar data preprocessing and initial analyses

Parts of the analyses presented in this chapter have been published in Schooling et al. (2020).

2.1 Introduction

Prior to the commencement of this project, some initial analyses of the dataset had been made (Alix et al., 2020). In summary, this included an assessment of reproducibility, classification performance and longitudinal change with time (up to 6 months), of the central intraoral measurements. In this study, the analysis has been expanded to include all measurement data (including the extraoral and laterally recorded measurements, and the full 12 months of follow up visits).

This chapter outlines a general overview of the dataset under analysis, including a detailed description given of the study cohort, the EIM measurement procedure and additional measurement data. As well as a description of the updated outlier removal method and calibration procedure for the EIM data. A comprehensive reproducibility analysis was made on the whole dataset, as well as for various subsections of the data. An assessment of measurement paradigm similarities was made to give a robust understanding of the independent features within the dataset. Finally, an examination of the spectral patterns recorded across the multiple electrode configurations was made, with a visual inspection of the spectral changes that occur with the progression of disease severity.

2.2 Methods

2.2.1 Data collection

Impedance spectra of the tongue were recorded from 41 patients with ALS and 30 healthy controls. Informed consent was obtained and the study was approved by an NHS research ethics committee (reference 15/YH/0121). The data collection was undertaken 2015-2019 (prior to the commencement of this PhD). Demographics of the participant cohort (patient and healthy groups, respectively) can be seen in Table 2.1.

Measurement	**Patients** N = 41	**Healthy controls** N = 30	**P value** (Statistical test)
Mean age in years (range)	62 (30-83)	56 (22-86)	P = 0.12 (t-test)
Male: Female, n (%)	22:19 (54:46)	14:16 (47:53)	P = 0.63 (Fisher's test)
Maximum tongue strength in N (SD)	8.7 (4.8)	16.2 (2.4)	p<0.0001 (Unpaired t-test)

Table 2.1: Demographics (age, gender, tongue strength) of the participant cohort and the respective p-value for the statistical test comparing the patient and healthy control groups. This data is taken from Alix et al. (2020).

Measurements were recorded using a bespoke, handheld bioimpedance tongue device designed and constructed by the Department of Clinical Engineering at Sheffield Teaching Hospitals NHS Foundation Trust (Alix et al., 2020) (figure 2.1a). This novel tongue EIM system allowed for measurements in both 2D and (for the first time) 3D electrode configurations (figure 2.1b). The underlying hypothesis is that in order to capture all the relevant information, a 3D configuration or a combination of configurations will be needed, due to the complex nature of the tongue muscle fibre arrangement (Gaige et al., 2007). The upper and lower electrode

plates contain four, 1.5 mm diameter circular gold electrodes arranged in a square with a 5 mm centre inter-electrode distance and 7 mm plate separation distance (figure 2.1). A sinusoidal current (5μA root mean square) was injected between pairs of electrodes in the device for 14 AC frequencies (76Hz-625kHz). The potential difference between a second pair of electrodes in the configuration was also recorded, where the impedance output is then calculated as the ratio of this voltage to the injected current (eq. 1.5).

(a)

Configuration name	Picture	Current source	Current sink	Potential Sense +	Potential Sense -
2D *Current and potential sensing electrodes on the same surface*					
2D1		E2	E0	E4	E6
2D2		E6	E0	E4	E2
2D3		E3	E1	E5	E7
2D4		E7	E1	E5	E3
3D *Current electrodes on opposing surfaces, potential sensing electrodes on opposing surfaces*					
3D1		E6	E7	E4	E5
3D2		E0	E1	E2	E3
3D3		E4	E7	E2	E1
3D4		E5	E6	E3	E0

(b)

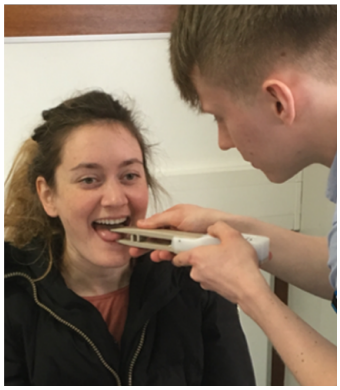

(c)

Figure 2.1: (a) The novel EIM tongue device with eight electrodes in a cuboidal arrangement. (b) The eight electrode configurations used; separated into 2D and 3D groups, utilising the electrode labels employed in (a). (c) Image showing central placement of the device on the participant's tongue. This figure has been collated from Alix et al. (2020) and Schooling et al. (2020).

We can denote the dataset for each measurement as $\mathcal{D} = \{Z(f_i)|i = 1, \cdots, N_f\}$, where N_f is the number of frequencies (14) and the i^{th} frequency is defined as $f_i = f_1 2^{i-1}$ with $f_1 = 76Hz$. The impedance in complex form is split as, $Z(f_i) = R(f_i) + iX(f_i)$ (eq. 1.7). Then impedance magnitude, $|Z(f_i)|$ and impedance phase, $\theta(f_i)$ at each frequency were calculated (from eq. 1.6) as:

$$\theta(f_i) = \arctan \frac{X(f_i)}{R(f_i)}, \ |Z(f_i)| = \sqrt{R(f_i)^2 + X(f_i)^2}. \tag{2.1}$$

Recordings were repeated for eight different electrode configurations, each of which defined a specific pair of electrodes for the current injection and a pair for the voltage reading. These multiple measurements allowed for recordings to be made for different directions through the tongue, which provides insight into the anisotropy of the tissue. The different configurations (see figure 2.1b) are split into 2D, which measured across the tongue surface, and 3D, which measured through the bulk of the tissue.

In addition to the eight electrode configurations, the impedance readings were taken for a number of different measurement paradigms. This included taking central measurements at the midline of the tongue as well as laterally on both the left and right sides, aiming to

investigate the variability of bulbar degeneration across different tongue regions. Additionally, measurements were repeated with the tongue relaxed inside the mouth (intraoral) and tongue protruding (extraoral). Generally, intraoral measurements may provide an easier and more comfortable position for patients, while a protruded tongue may give the clinician better visibility for full electrode contact. By taking recordings for both measurement sites, it can be determined if there is any difference in the data validity and the patient's experience. For each participant visit, recordings were made in turn for left, right, and then central placement; first in the extraoral configuration followed by the intraoral configuration. To assess for reproducibility, a second set of measurements was taken (trial 2), in which this whole process was repeated. Thus the probe was removed and replaced several times during a recording session.

In order to assess the longitudinal change in EIM over time, data was collected in patients at 3 monthly intervals for up to a year (where possible), while healthy controls had a single follow up visit 6 months from the baseline recording. Not all participants were able to complete the full study, due to patient death, progress in the severity of disease (i.e. complete tongue paresis, severe atrophy or respiratory failure), or an inability to attend due to personal reasons. The number of participants with an available measurement dataset at each time mark is presented in table 2.2. Note that for some of the recruited participants, the EIM recordings made were unsuccessful (see section 2.2.2 for reasons). Hence, while 41 patients were recruited only 39 had baseline data available due to failure to record in 2 of these patients.

Month	**Patients**	**Healthy**
Baseline	39	30
3 Months	28	-
6 Months	22	26
9 Months	20	-
12 Months	10	-

Table 2.2: Amount of participants data available across the full 12 months of follow up in the study.

Overall, the impedance dataset is high-dimensional in nature, where each participant had measurements recorded on 6 measurement paradigms (intraoral and extraoral, for central, left, and right placement); 8 electrode configurations; and 14 frequencies. Impedance is also a complex quantity so each value contains two data points (R and X). Together this gave 1,344 data points per participant for each time point. Clearly, the dimension was significantly larger than the sample size, meaning dimensionality reduction techniques were a key tenant to the analysis work. It should be noted, that not all of the different measurement types necessarily contain independent information. Therefore, this chapter will present work in similarity assessments between the different measurement paradigms, which concluded certain data types could be combined.

In addition to the EIM measurements, further data was collected to assess the severity of symptoms in the patient cohort. Tongue strength recordings were undertaken (for both the patient and healthy group) using the Quantitative Muscle Testing system (Averil Medical), coupled to the Iowa Oral Performance Instrument (Shellikeri et al., 2015). For these measurements, the participants were instructed to maximally push the small rubber balloon of the IOPI against their hard palate for 10 seconds. The maximum force (Newtons, N) achieved in this time frame was recorded. A single repeat recording was conducted with a short rest period between measurements; the highest recorded strength value was then used for analysis. There was a significant decrease in tongue strength observed in the patient group (table 2.1). Additionally, for the ALS group, the amyotrophic lateral sclerosis functional rating scale-revised (ALSFRS-R) as well as the bulbar specific subscore (scored from 0-12) were recorded. A thorough clinical bulbar examination was performed by an experienced clinician, and clinical signs

of disease (wasting, weakness and fasciculations) were quantified by a simple scoring system (see table 2.3). Additionally, the site of onset of disease (limb or bulbar), the length of time patients have experienced symptoms (symptom duration), the Awaji-Shima classification at baseline, and clinical evidence of LMN pathology were recorded for the cohort. Table 2.4 summarises the clinical characteristics of our patient cohort at the time of enrolment to the study. Finally, a number of patients also had data available from needle EMG assessment, from which evidence of acute and/or chronic denervation was inferred.

Clinical Sign	**Description and corresponding score**			
Tongue Wasting	None: 0	Minimal: 1	Moderate: 2	Severe: 3
Tongue Weakness	None: 0	Movement inside and outside mouth: 1	Movement only inside mouth: 2	Paresis: 3
Fasciculations:	Absent: 0	Present: 1		

Table 2.3: Description of scoring system for clinical signs of bulbar disease. The overall clinical score was calculated as a sum of all three signs giving a score between 0-7.

Characteristic	
Site of disease onset, n (%)	Limb: 24 (59%)
	Bulbar: 17 (41%)
Median symptom duration in months (range)	24 (5-204)
Awaji-Shima classification at time of enrolment, n	Possible: 14
	Probable: 17
	Definite: 10
Clinical examination, n (%):	
Dystharia	28 (68%)
Tongue atrophy	21 (51%)
Tongue fasciculations	28 (68%)
Normal	11 (27%)
Clinical evidence of LMN tongue pathology, n (%)	30 (73%)
Mean total ALSFRS-R score (range)	31 (4-45)
Mean bulbar ALSFRS-R subscore (range)	8 (0-12)

Table 2.4: Disease characteristics of the patient cohort. This data is taken from Alix et al. (2020).

2.2.2 Data preprocessing

Prior to the commencement of this project, the impedance values were calibrated to give the volume independent impedivity values (as in eq. 1.8, Section 1.2.2). These impedivity values provide a standardised measure of the passive electrical properties of tissue, independent of the volume of tissue recorded. This offered the advantage of direct comparison of data from different electrode configurations, and in theory different impedance devices (Luo et al., 2021b; Sanchez et al., 2021). For our measurement dataset, each electrode configuration (shown in figure 2.1b) recorded over a different volume of tissue and hence required a different calibration.

Initially, a base calibration of the probe was made, to account for internal errors within the device. Specifically, it is suggested to calibrate the resistance both between the potential unit electrodes and between the current-carrying electrodes (Gerzhik et al., 2020). This base calibration was made by taking electrical measurements against a network of resistors. Following this, a saline bath was used to determine the calibration cell constants, K, for each of the electrode configurations measured by the device. Salt was added to the bath in a titration process until the desired conductivity was reached, where the conductivity of the saline was measured using an Orion Star™A322 conductivity meter. The probe was placed in each saline

bath and the impedance data was recorded. With a rearrangement of eq 1.9, the cell constant for each configuration was determined as:

$$K^c = \sigma \frac{R^2 + X^2}{R} \tag{2.2}$$

This was repeated for a number of solutions in the range 0.1 S/m to 2 S/m, and an average value for K^c was computed using the gradient of the best fit line, for each configuration, c. The resulting cell constants were determined to be $18.6\,m^{-1}$ for the 2D configurations, $15.6\,m^{-1}$ for 3D1/2 and $24.8\,m^{-1}$ for 3D3/4.

Measurement errors can be caused by poor tongue to electrode contact, which produces artefacts (Martinsen and Grimnes, 2011). In order to minimise the chance of this, constant observation of electrode contact was made by the clinician during measurement. If electrodes became visible during measurement, then the recording was aborted. However, despite this, some measurements still produced invalid data, with features that clearly indicate artefacts. Clearly, before undergoing analysis of the data performance, efforts should be made to remove all erroneous spectra from the dataset by applying an outlier removal procedure. The tongue is a passive system thus it should behave as a positive real system, therefore data comprising negative resistance is a good indication that the measurements are artefactual. Therefore, as a first step in outlier removal, all spectra are removed if any of the impedance data contain negative real parts. Additionally, impedance with a large positive phase, at low frequency (<100kHz) or high frequency (>500MHz), is not a feature one would expect to see in the impedance of biological tissue. Therefore spectra with a phase value greater than 30°, at the first or last frequency are also removed as outliers. Next, the remaining outlier spectra were removed using a root-mean-squared deviation based outlier detection algorithm (see appendix A). This was developed from the algorithm presented in Alix et al. (2020), with some modifications. These adjustments are outlined and explained in the Discussion section of this chapter.

2.3 Results

2.3.1 Categorising patient severity

In order to assess the overall severity of disease in the patient cohort, the participants were manually split into four levels of symptom severity (no symptom, mild, moderate and severe). This was completed by an experienced physician (JJPA); the no symptom group was determined by a maximum (12/12) score on the ALS functional rating scale bulbar subscore and the absence of any abnormal clinical signs. The other groups were obtained by assessing the combination of ALSFRS bulbar subscore, tongue strength and clinical examination. Histograms showing the distribution of these symptom biomarkers across these four patient subgroups can be seen in figure 2.2. From this, it is clear how symptom severity progresses through the groups. When looking at the individual biomarkers in turn there is obvious overlap between the groups, but when all three are plotted together (figure 2.2d) the subgroups become more visually distinct. In the distribution of tongue strength values, the healthy control subgroup is also shown - here it is obvious that while as an overall trend patients have weaker tongues, there is significant overlap between the healthy group with the no/mild symptom subgroups. This is a simple demonstration of the lack of effectiveness of strength measurements as suitable standalone diagnostic tools in ALS.

In order to directly quantify the severity of disease in each patient, a comprehensive bulbar disease burden score (BDBS) was calculated by combining the ALSFRS-R Bulbar Subscore (BS), tongue strength (TS) and clinical score (CS) into a score out of 36, with a lower value

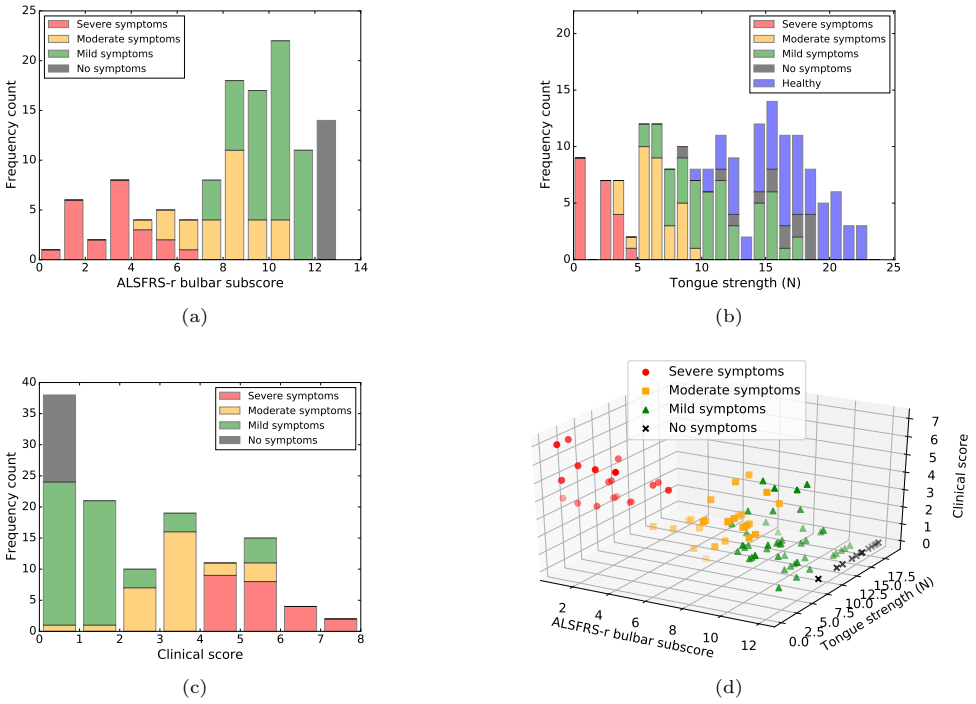

Figure 2.2: Histograms showing the distribution over the four symptom groups (plus healthy controls in tongue strength) for (a) the ALSFRS-r bulbar score, (b) tongue strength and (c) the clinical score. By plotting all three scores the different patient groups become visually distinct (d).

representing more severe disease. This was calculated as follows:

$$BDBS = BS - \frac{12}{7} \times CS + \frac{12}{MAX(TS)} \times TS \tag{2.3}$$

where both tongue strength and clinical signs were normalised to have a range of 0-12. This burden score was a simple and effective way to combine all the quantitative information on the severity of the patient's symptoms into a single score, which was used in my further analyses of the prognostic potential of tongue impedance data.

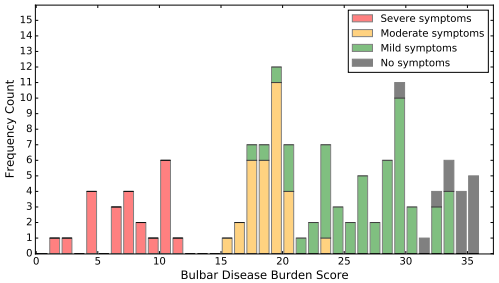

Figure 2.3: Histogram showing the bulbar disease burden score (BDBS) for all patients split into the four symptom groups.

A histogram showing the distribution of the BDBS is depicted in figure 2.3, again split into the four sub-groups of symptoms. The severe symptom subgroup was clearly distinct from the others. While there was some overlap between moderate/mild and mild/no disease groups, the trend of decreasing BDBS is in general agreement with the groupings. There are advantages of splitting into these sub-groups based on the clinician's expertise and knowledge of the subtleties of the disease, which will always be missed with the use of a limited number of absolute biomarkers. However, the BDBS has the strong advantage of providing us with quantitative data to include in more complex analyses.

2.3.2 Outlier identification

The amount of data identified as an outlier for the different participant cohorts is shown in Table 2.5. The proportion of data identified as outliers increased marginally with the severity of the disease.

Cohort	Percentage outliers
All Data	3.1%
Severe Symptoms	4.0%
Mild / No Symptoms	3.3%
Healthy	2.5%

Table 2.5: The number of outliers removed across the different cohorts within the dataset.

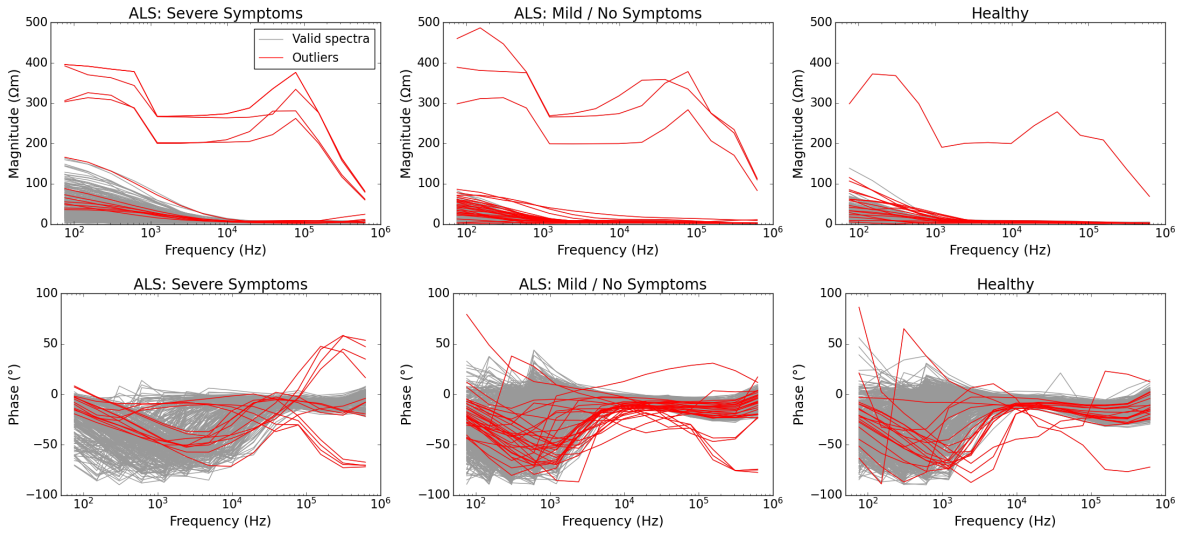

Figure 2.4: All recorded spectra (impedance magnitude and phase) shown for the ALS cohort split into two categories of disease severity, and for the healthy cohort. Red spectra show the artefactual spectra identified via the root-mean-squared deviation algorithm, and the grey spectra are the remaining data. Note this shows data for all measurement paradigms combined, including the different electrode configurations and device placements. Note that spectra are rejected due to the criteria met on either the magnitude or phase spectral patterns. For example, an outlier measurement may contain reasonable magnitude spectra but clear deviations in phase spectra or vice versa.

Figure 2.4 shows all the measurement data, with the identified outliers shown in red. Visually it is clear that the outlier spectra made up erroneous data with obvious spectral artefacts,

while all 'normal' looking spectra remained within the dataset. Both the impedance magnitude and impedance phase saw a number of distinct outliers across patients of different symptom severities and within the healthy cohort.

The longitudinal participant drop off, as seen in table 2.2, comes about partially due to participants lost to follow up; unable to attend the study visit, significantly worsened symptoms, or death. In addition, some patients are not available due to the fact that all measurement data was lost in outlier removal, meaning that no viable data were obtained. Note, that this did not occur for any of the participants within the healthy controls and is impacted by the increased difficulty of recording when severe bulbar symptoms are present. The breakdown of participants lost to follow up and to unsuccessful recording are shown in figure 2.5.

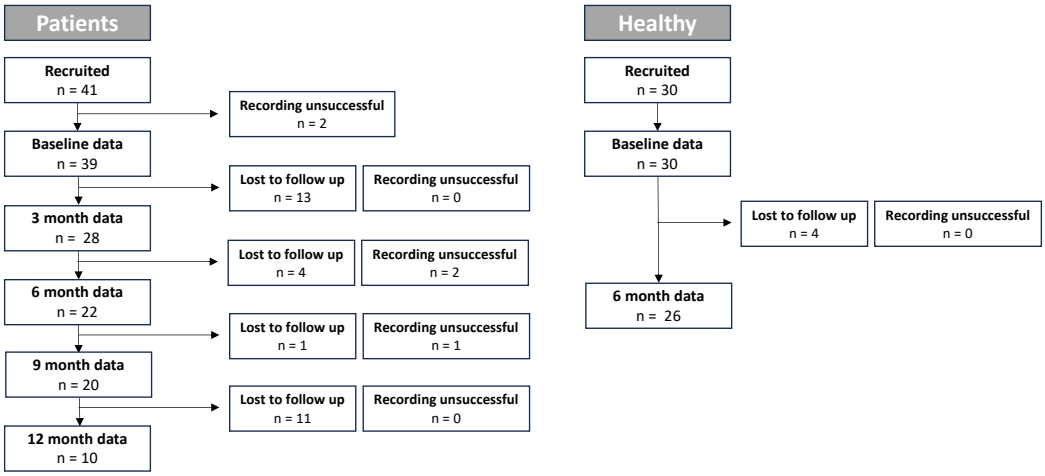

Figure 2.5: Participant drop-off over time, lost to follow up and due to completely unsuccessful recordings. Note that participants lost due to unsuccessful recording had lost all measurement paradigms within the dataset in the outlier removal stage.

2.3.3 Reproducibility

The ICC was calculated to determine the test-retest reproducibility of EIM measurements using the novel tongue probe. This was performed on the resistance, reactance, and phase impedance metrics. Previously, it has been shown that this dataset has high reproducibility (ICC>0.7) across both 2D and 3D configurations; longitudinally across repeat visits; and for an inter- and intra-rater analysis, compared between different examiner combinations including both experienced and inexperienced clinicians (Alix et al., 2020). To extend this assessment, the ICC was compared for the healthy cohort and ALS patients split into the different levels of disease severity. Additionally, comparisons were made for the different types of measurement including intraoral/extraoral, and central/left/right positions on the tongue. Finally, values were calculated at each frequency in the spectrum. These results are displayed in Figure 2.6.

From this, it is clear that the tongue EIM probe produced reproducible data (ICC>0.7) across the full dataset. This was consistent across the different severities of disease, even in severe patients where maintaining good electrode contact throughout recording can be more difficult. The placement position on the tongue had no impact on the reproducibility, while protrusion of the tongue (extraoral measurements) did slightly reduce this, but not significantly as an ICC greater than 0.8 was maintained. Finally, observing the full spectra of frequencies, it

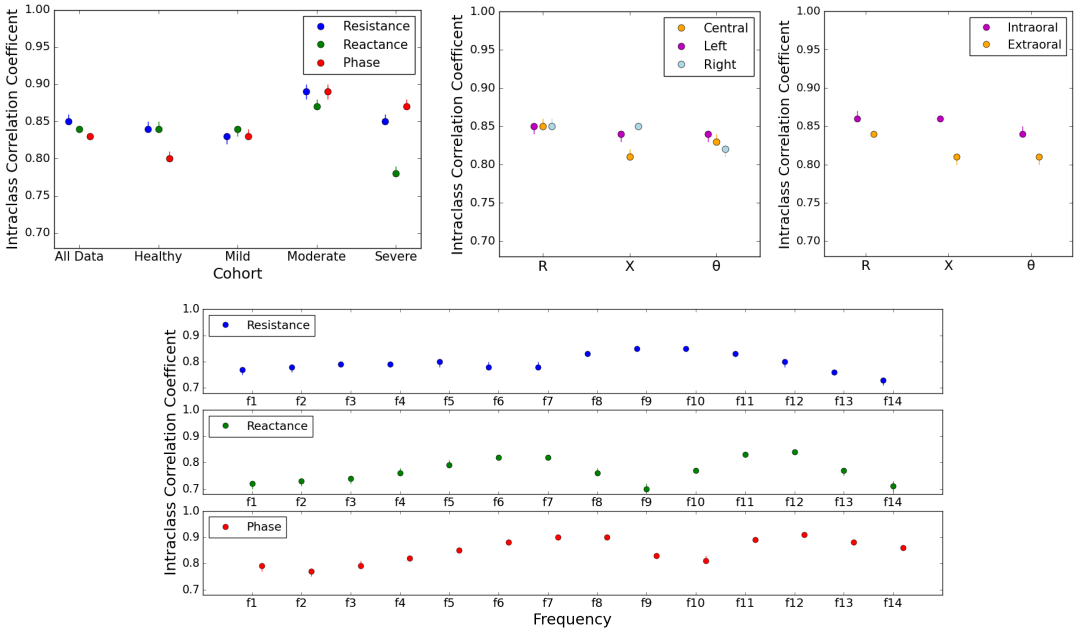

Figure 2.6: Intraclass correlation coefficients for different subsets of the data, presented for impedance resistance (R), reactance (X) and phase (θ). This data is also presented in the appendix, table C1.1.

is clear that reproducibility tended to be higher for the middle frequencies and slightly less at the low and high frequency ends. However, clearly, all frequencies gave acceptable reproducibility and hence it was deemed suitable to conduct an analysis encompassing the entire spectrum of 14 frequencies.

2.3.4 Measurement paradigm similarity assessments

There are a number of measurement paradigms that were hypothesised to be similar. Since extraoral measurement involved protrusion, which is achieved via contraction of the genioglossus, and not the tongue blade from which recordings are made, it was expected that minimal difference would be seen between the intra- and extraoral measurement types. Additionally, the two configurations 3D1 and 3D2 are geometrically identical apart from a 5mm lateral shift in the measurement area. Thus, any differences seen here would be due to local variation in the structure of the tissue, so again these measurements were expected to produce highly similar data.

In order to assess this similarity, Bland-Altman plots were used and the differences were compared to those in two repeat measurements. These are presented in Figure 2.7, where a table showing the Bland-Altman bias and 95% quantile range, as well as the mean NRMSE between the two measurement types, is also shown. This analysis demonstrated that both intraoral-extraoral and 3D1-3D2 comparisons were within the threshold of two repeat measurements. Thus it can be concluded that measurements were unaffected by tongue protrusion and there were no local variations in tissue structure. Consequently, such data types were combined in the data analysis. The similarity between configurations 3D1 and 3D2 is evidence of local homogeneity, which validates the assumptions made in the calculation of impedivity (eq. 1.8).

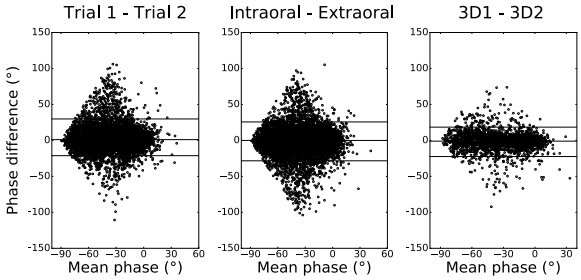

(a)

Measurement types		B-A: Bias(°)	B-A: 95% quantile range (°)	Mean NRMSE
Trial 1	Trial 2	0.9874	53.2	0.2137
Intraoral	Extraoral	-0.6660	54.07	0.2045
3D1	3D2	-1.9949	41.64	0.1439

(b)

Figure 2.7: (a) Bland-Altman plots showing the difference between measurements made for two repeat recordings, for measurements made intra- and extraorally, and for the two configurations 3D1 and 3D2. Horizontal lines plotted for 2.5th and 97.5th percentiles and the mean value. (b) Table summarising the Bland-Altman bias (mean value of phase difference) and 95% quantile range (difference between 97.5th and 2.5th percentiles), and the mean value of NRMSE metric between the two measurement types.

2.3.5 Spectral Patterns

In order to make an initial assessment of the disease-related spectral changes that are evident in the EIM tongue dataset, the median spectral patterns are presented across all electrode configurations. This is shown split up for the healthy cohort, and the ALS cohort separated into the four levels of symptom severity (Figure 2.8). From this, it is clear that there was a distinct progression of change when moving from healthy to more acute disease. There was a general trend of increased magnitude at the lower frequency end, as well as a positive shift in the centre frequency (the frequency where the phase minima occur). The degree of disease severity was also clearly correlated with the degree of deviation from the healthy spectral shape. Additionally, the asymptomatic patients (no symptom group) saw an observable shift from the healthy spectra in a number of the electrode configurations (particularly 3D1/2), suggesting that EIM does have the potential to detect the presence of disease earlier than other symptom markers.

The maximal splitting of the groups generally occurred at the low frequency end in the magnitude data but for mid frequencies in the phase data. The progression of change in the phase spectral shapes was slightly more complicated, with the value of the minimum phase initially becoming more negative when moving towards moderate disease, then tending to shift upwards towards a less negative value when moving to severe symptoms.

2.4 Discussion

Although outlier detection algorithms have not often been presented in EIM work, it is clear that some data will contain obvious artefacts (see figure 2.4) and must be removed from the dataset to prevent significant skewing of results. It is possible that these outliers could be removed manually, but the development of an algorithm is highly beneficial when the size of the dataset is large. The outlier removal algorithm was modified from the algorithm presented

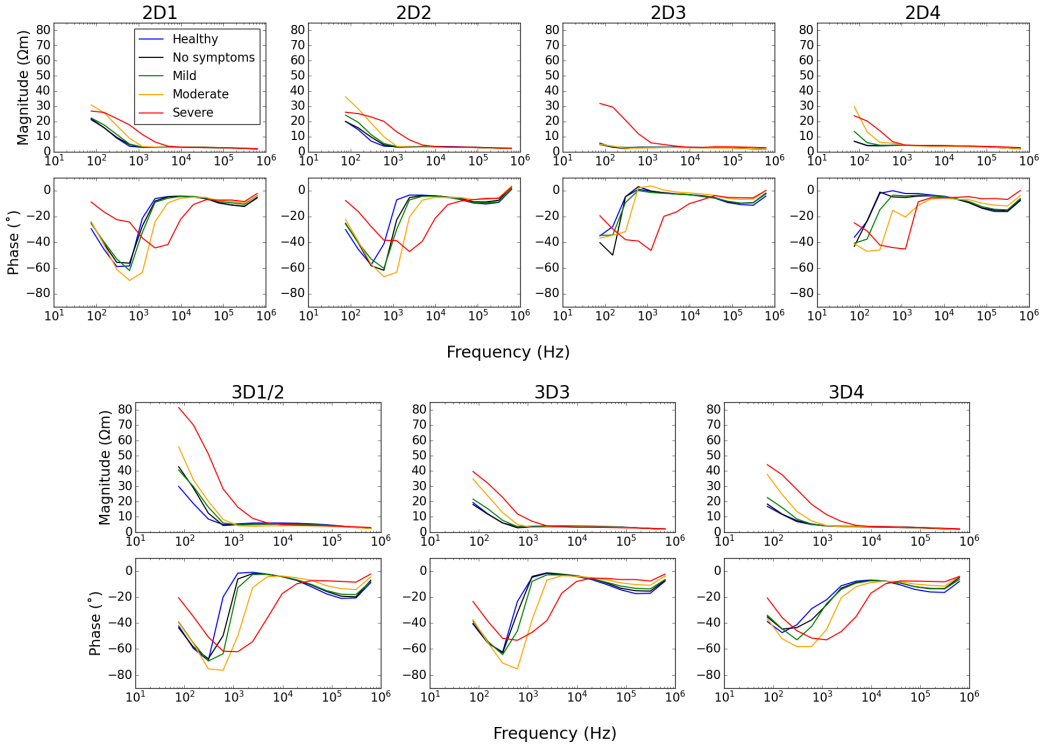

Figure 2.8: The median (volume independent) impedivity spectra for the healthy cohort (blue) and ALS cohort split into no (black), mild (green), moderate (yellow) and severe (red) symptoms, severity. Shown for each electrode configuration in turn presented for central placement data only.

in Alix et al. (2020), which used a root-mean-squared deviation to remove spectra that had significant deviation from the median magnitude spectral pattern. One drawback of this method was that the algorithm was only applied to the impedance magnitude data, thus some spectra that clearly had erroneous features within their phase pattern were not removed as outliers. Additionally, this method removed patient data in much larger quantities than healthy data, particularly in the severe symptom patient group where the proportion of spectra removed is nearly twice that within the healthy set. Furthermore, a total of 5 patient measurement visit sets were completely lost in outlier removal, while none were lost for healthy controls. We do expect that a small difference in the number of outliers for patients could arise (as seen in Table 2.5), due to it being harder for the clinician to maintain good electrode contact when patients have particularly severe bulbar symptoms. However, in the case of the algorithm used in Alix et al. (2020), the difference was so pronounced it indicates that some spectra were being removed due to disease-specific deviations in spectra. Clearly, this is far from ideal as crucial information from the dataset was being lost. In order to combat this the algorithm was changed, firstly to be applied to both the magnitude and the phase data. Secondly, the root-mean-squared deviation was calculated with respect to the severe patient median, which prevented disease-related, rather than artefact-specific outliers from being removed within the patient cohort.

An initial assessment of the tongue EIM dataset indicates successful data collection from the novel EIM tongue probe across the full cohort of participants; for all the different mea-

surement paradigms; and across the full spectrum of frequencies (76 Hz - 625 kHz). Two pairs of measurement types - both intraoral/extraoral and configurations 3D1/2 - were identified to output highly similar spectral information, within that of the similarity demonstrated between two analogous repeat measurements. Therefore these data types can be pooled in future analyses, which reduces the dimension of the dataset slightly to 21 spectra, or 588 data points per participant visit (3 placement positions; 7 independent electrode configurations; 14 frequencies; complex data output). Since a number of participants, mostly patients but also some healthy controls appeared to find extraoral recordings more difficult, this similarity indicates that the examiner can use whichever method is most comfortable for the participant. A further exploration of the differences between the different device placement positions on the tongue must be made. However, before making assessments on the lateral (left and right) data, work must be done to prove that this data is not dominated by edge effects.

First observation of the central placement EIM spectral patterns across different severities of disease found distinct directions of disease-related spectral shift (figure 2.8), suggesting that tongue EIM has significant potential as a sensitive biomarker for detecting bulbar disease in ALS. On an average group level, the direction of the shift demonstrated some variation with the minimum phase initially appearing more negative in moderate disease, but by the time severe symptoms set in this had shifted back to a much less negative value. This shift in the direction of the spectral pattern could be indicative of different stages of the disease progression, for example, acute denervation compared to chronic reinnervation. In order to validate this hypothesis, the spectral changes need to be assessed on an individual level over time and compared to the patient's clinical score as well as needle EMG findings.

Even when limiting the analysis to just central device placement, the dimension of the dataset is still large with 196 data points contained within the 7 electrode configuration spectra. The majority of previous work has demonstrated a splitting between healthy people and ALS patients in one upper surface 2D configuration, at a 50 kHz frequency. Looking at 50 kHz in the 2D1/2 spectra in figure 2.8, it is clear that fairly significant patient/healthy splitting is occurring, although there is also a clear overlap between some less severe patients and the healthy group. By using a larger range of frequencies and more configurations we would expect to gain information on different levels of disease splitting allowing us to improve the precision of disease prognosis evaluation. Additionally, incorporating all impedance data (not just phase) could give benefit, as there is also a distinct split between the groups emerging at the lower frequency end of the magnitude spectra. Clearly in order to incorporate these multiple levels, sophisticated dimensionality reduction analyses need to be employed.

One distinct change that occurs in disease is the shrinkage of muscle due to wasting (Carlson, 2014; Daroff and Aminoff, 2014). Therefore, one may hypothesise that the differences in the impedance spectral patterns observed between healthy participants and the patient groups of varying disease severities could be impacted by the size of the tongue. However, firstly the design of the tongue device means that the same volume of tissue is always recorded since the gap between the two electrode plates is fixed. Furthermore, the calculation of the impedivity (eq. 1.8) gives a volume independent output of the muscle properties. However, it must be noted that it is possible that participants with a larger tongue would experience increased compression of the tongue, which may affect the density/structure of the tissue and hence impact the underlying impedivity output. Furthermore, when a tongue has experienced significant wasting, a thinner volume can make it harder to maintain good contact with the electrodes. This is likely to be a contributing factor to the increase in the number of erroneous recordings seen within the severe cohort. A further exploration of these effects should be explored for future studies using this device. The final effect of depletion in tongue volume is the resulting reduction in the distance between the device electrodes and the tongue edge. The edge effects of impedance recordings

in this context are explored in the following section.

A final observation that can be made here is a comparison of the spectra between the electrode configurations. Larger impedance magnitude values were consistently seen in the 3D1/2 configuration, which measured vertically through the body of the tongue. This suggests that the conductivity across the plane of the tongue in both longitudinal (back to front) and transverse (left to right) directions is bigger than the conductivity vertically from top to bottom. While the tongue is made up of a complex arrangement of muscle fibres which run in multiple directions, including vertically (Sanders and Mu, 2013), there is an observable difference in the electrical properties of the muscle in the vertical direction. Comparing the 2D measurements, the severe patient groups gave very similar looking spectral patterns in all configurations. However, the shape of the spectra in the healthy cohort and milder ALS groups saw spectral differences in the measurements recorded on the upper tongue surface (2D1/2) compared to the lower tongue surface (2D3/4). Specifically, the centre frequency was reduced and the magnitude came down for the lower surface readings. The dorsal tongue has a partially keratinised epithelium, while the ventral tongue does not Di Fiore (2000), this could be contributing to the differences in the impedance outputs recorded on the upper and lower tongue surface. There was also more significant anisotropy seen in a comparison of the longitudinal vs transverse directions on the lower tongue in healthy participants and milder patients, compared to the severe disease cohort. This provides evidence of a reduction in muscle anisotropy and an increase in the homogeneity of the tongue composition in severe bulbar disease. More comprehensive modelling of this data could reveal more detail on the changes in the anisotropy and homogeneity of the electrical properties of the tongue for different levels of disease.

3 Chapter 3: Finite element modelling of the tongue

The majority of the work presented in this chapter has been published in Schooling et al. (2020).

3.1 Introduction

So far, tongue EIM recordings have only been reported for measurements made in the midline of the tongue (Alix et al., 2020; Shellikeri et al., 2015; Mcilduff et al., 2017; Pacheck et al., 2016); it is not known if lateral measurements are feasible or provide clinically useful information. While EIM electrodes can be carefully placed on limb muscles, for example, in relation to bony landmarks (Sanchez et al., 2016b), placement on the tongue is more difficult and could be subject to small rotations of the impedance device. Attempts to undertake recordings on either half of the tongue blade may also be undermined by the proximity of the electrodes to the tongue edge Hua et al. (1993); Scholz and Anderson (2000); Li et al. (2019), while additionally, the likelihood of device rotation is higher in this case. However, if possible, lateral recordings may provide additional diagnostic information, for example, by providing a more complete picture of the health of the muscle. Such recordings would also provide insight into disease pathophysiology, as although limb involvement in ALS is often asymmetrical (Devine et al., 2014), little is known about the presence/absence of bulbar disease asymmetry.

In this chapter, I demonstrated that lateral placement and electrode rotation had no significant effect on the impedance phase spectra. To establish this a finite element model of the tongue was optimised to achieve a simultaneous fit across multiple electrode configurations. The model was applied to patients with ALS exhibiting different severities of disease and to healthy controls. As a result the paper also develops a method for parameterising the multi-dimensional impedance dataset. The model parameters were then attributed to a lumped circuit LT-Spice model, which gave further insight into the underlying electrical changes that occur in disease.

Following the validation of lateral recordings an assessment of bulbar disease asymmetry was made by comparing measurements from the left and right sides. Additionally, a comparison of the spectral differences in central and lateral data was made. Finally, a comprehensive evaluation of the biomarker performance was undertaken comparing the central and lateral datasets, as well as an analysis of the performance using a combination of both datasets.

3.2 Methods

3.2.1 Building the FEM-based model

Capturing the detailed structure of the tongue is difficult due to a highly complicated muscle fibre arrangement, with fibres running in multiple directions (Gilbert and Napadow, 2005; Gaige et al., 2007). Here, a simplified tongue geometry was built from layers of tissue with varying electrical conductivity and anisotropy. The shape of the tissue was constructed to mimic that of a tongue MRI taken from Ong and Chong (2006), with a length of 78 mm and maximum breadth of 56.5 mm, which was reported for the average dimensions of an adult tongue (Hopkin, 1967). The muscle was surrounded by a 2 mm epithelium layer (Prestin et al., 2012), with dielectric spectra (3.9) taken from reported results for the dorsal and ventral mucosal layers (Lackovic and Stare, 2007; Richter et al., 2015). The geometry used is shown in figure 3.1.

The model was developed using the AC/DC module in Comsol Multiphysics software COMSOL (2023). Modelled local impedance measurements were produced using eight electrodes of 1.5 mm diameter in a cuboidal arrangement analogous to the novel tongue device. The conductivity of the electrodes was set to be much greater than that of the tissue. The finite element mesh was generated automatically with the Comsol software and consisted of 97,155 elements.

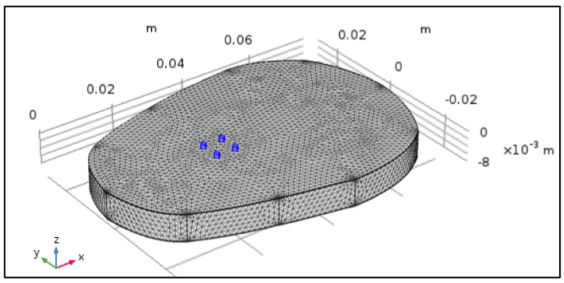

Figure 3.1: FEM tongue geometry and mesh built in Comsol Multiphysics®

Analysis shown in appendix, figure C2.1, demonstrates that this meshing gives numerically stable results. The model was run to generate spectra for each of the eight electrode configurations in turn, by passing current and reading voltage between different electrode pairs.

A frequency domain study was employed with the scalar electric potential as the dependent variable. Magnetic induction effects were assumed to be negligible since they are expected to be approximately 6 orders of magnitude smaller Senior (1960). The current flow in EIM is the combination of direct current and displacement current ($\bar{J}_{tot} = \bar{J}_c + \bar{J}_d$). Direct current flows due to moving charge particles and is defined as:

$$\bar{J}_c(x, y, z) = \sigma(z).\bar{E}(x, y, z), \tag{3.1}$$

where x y and z are the longitudinal, transverse and vertical coordinates of the local current; $\sigma(z)$ is the local conductivity of the tissue, which was assumed to be uniform over x and y but varied with z (different values between the layers of tissue); and $\bar{E}(x, y, z)$ is the local electric field.

An alternating current with amplitude, I_0 and frequency, ω (rad/s) was passed between a terminal electrode and ground electrode (where the electric potential was set to 0). The displacement current then arises from the changing field induced by this alternating current and is given by:

$$\bar{J}_d(x, y, z) = \mathcal{E}\frac{\partial \bar{E}(x, y, x)}{\partial t} = \mathcal{E}_0\mathcal{E}_r\frac{\partial \bar{E}(x, y, z)}{\partial t}, \tag{3.2}$$

where $\mathcal{E}$ is the permittivity ($\mathcal{E} = \mathcal{E}_0\mathcal{E}_r$), $\mathcal{E}_0$ is permittivity of free space (8.854×10^{-12}) and $\mathcal{E}_r$ is relative permittivity. The phasor representation of the electric field produced by an alternating current is given by:

$$\bar{E} = \bar{E}_0 e^{i\omega t} \tag{3.3}$$

and hence (3.2) becomes:

$$\bar{J}_d = i\omega\mathcal{E}_0\mathcal{E}_r\bar{E}. \tag{3.4}$$

For alternating current sources inside conductive media the equation of continuity is then solved:

$$Q = \nabla.\bar{J}_{tot}, \tag{3.5}$$

where Q is the total charge inside each element. To get a full description of an electromagnetics problem, boundary conditions must be specified at material interfaces. The boundary condition

implemented in Comsol, for interfaces between different media with electric field $\bar{E_1}$ and $\bar{E_2}$ and outward normal from medium two, $\bar{n_2}$ is given by:

$$\bar{n_2}.(\bar{E_1} - \bar{E_2}) = Q. \tag{3.6}$$

The electric field is related to the potential difference (V) through:

$$\bar{E} = -\nabla V \tag{3.7}$$

and hence the electrical potential at the electrode surfaces can be output by the FEM.

The local impedance (Z) between a set of electrode pairs at the frequency of excitation current signal was then calculated as:

$$Z = \frac{V_1 - V_2}{I_0} \tag{3.8}$$

where V_1 and V_2 are the potentials at the two electrodes respectively, as obtained from the FEM model.

3.2.2 Model parameterisation

The conductivity spectra for the tissue making up the main body of the tongue were set as the following simplified Cole-Cole equation:

$$\sigma(z \in \Phi_l) = \frac{1}{Z_1^{(l)} + \frac{Z_0^{(l)} - Z_1^{(l)}}{1 + i\frac{f}{F_c^{(l)}}}} \tag{3.9}$$

where j is the imaginary unit, f ($= \omega/2\pi$) is the frequency (Hz) and $Z_0^{(l)}$, $Z_1^{(l)}$ and $F_C^{(l)}$ are real valued free parameters, which depend on the specific layer of depth, Φ_l. The tongue muscle has anisotropic properties (Gaige et al., 2007), so different sets of parameters were input for the longitudinal, transverse and vertical directions of the tongue.

Since it is possible that fibres run in predominantly different directions at different depths (Benatar et al., 2016), the tongue body was split into three layers in order to allow enough geometrical complexity for the model to capture the details of the measurement spectral patterns. A total of 27 free parameters for conductivity properties were used, with an additional parameter representing the thickness of the middle layer.

To assess the agreement between the modelled and measured data the normalised root mean squared error (NRMSE) was employed. The NRMSE metric between the impedance measurement (θ, $|Z|$) and model estimate ($\hat{\theta}$, $|\hat{Z}|$) was calculated independently for phase and magnitude as:

$$NRMSE = \frac{\sqrt{\frac{\sum_{i=1}^{N_f}(\alpha_i - \hat{\alpha}_i)^2}{k}}}{\alpha_{max} - \alpha_{min}}, \tag{3.10}$$

where α represents θ or $|Z|$, N_f is the number of measurements in the set (14 frequencies per electrode configuration). Note that the calculation on impedance phase is not affected by phase flips since values are automatically constrained between -90° and 90°.

The parameter values were optimised to minimise the deviation between the model impedance output and the observed data (impedance spectral medians for each participant group). The optimisation process began with a preliminary exploration phase, where a comprehensive grid search was performed to cover a wide range of parameter values. This coarse-grained search

involved iteratively adjusting the parameters to obtain a rough approximation of the global minimum's location. Following this, an L-BFGS-B (limited-memory Broyden-Fletcher-Goldfarb-Shanno with bound constraint) (Byrd et al., 1995) optimiser was performed within a bound region around the identified area. L-BFGS-B is a variant of the BFGS method, which approximates the inverse Hessian matrix of the objective function, enabling efficient convergence towards the minimum. Moreover, L-BFGS-B incorporates the ability to handle bound constraints, allowing the optimisation process to respect predetermined limits on the parameter values (Byrd et al., 1995). This two pronged procedure provided a scientifically rigorous and computationally efficient means of determining the optimal parameter values for the model. By combining the broad exploration of the grid search with the focused refinement of the L-BFGS-B optimiser within the bounded region, the optimisation process was comprehensive and effective.

The patients were split into different disease categories due to differences in the appearance of spectra (see figure 2.8). This optimisation procedure was applied in turn to the median spectral shapes from healthy controls, patients with moderate disease and patients with severe disease. It was then possible to compare the model parameters between the different levels of disease to gain a deeper insight into the underlying disease-specific electrical changes that occurred within the muscle.

3.2.3 Lumped Circuit modelling

To gain further insight into the effect of the disease process from the external electrical measurements made, the system was reduced to a lumped circuit model, similar to that presented in Shiffman and Rutkove (2013a,b). The optimised model parameters describing the conductivity spectra of the tongue were fit to a lumped model of a balanced Pi network of four simplified Cole-Cole networks (figure 3.2). Four networks were chosen in order to sufficiently characterise the impedance spectra for the full frequency range. This network was simulated with the LT-Spice simulator using AC small-signal analysis. The NRMSE between the FEM cole-cole parameters and the LT-Spice model was optimised using a Quasi-Newton minimisation (Shanno, 1970). Each set of parameters (Z_0, Z_1, F_C) was then interpreted as intracellular resistance (RP), extracellular resistance (R) and capacitance (C).

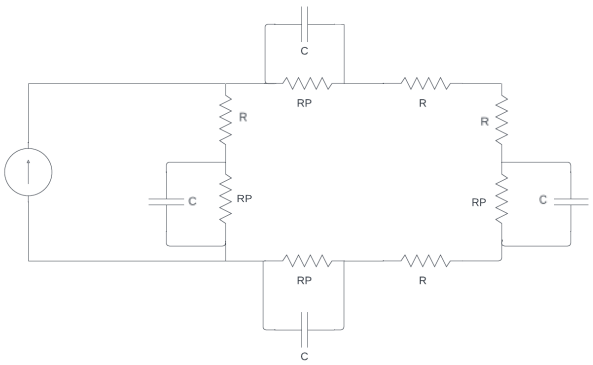

Figure 3.2: LT-spice 12 element Cole-Cole based circuit simulation. Contains resistors in series (R) and resistors in parallel (RP) with capacitors (C).

3.3 Results

3.3.1 Model fit

Separate models were generated for healthy controls, patients with moderate disease and patients with severe disease. Producing a simultaneous fit across all electrode configurations for both phase and magnitude was challenging due to the high number of parameters and variables involved. Despite this challenge, a high level of agreement between the observed data and FEM was achieved across all groups for both phase and magnitude (figure 3.3). The optimised parameter values are shown in table 3.1. It must be noted that the solution to this inverse model is not necessarily unique and interpretation of the optimised model parameters must be exercised with caution and an understanding of the limitations of the model.

		Severe Disease				Moderate Disease				Healthy			
Section	Direction	Z_0 (Ωm)	Z_1 (Ωm)	F_C (Hz)	Thickness (mm)	Z_0 (Ωm)	Z_1 (Ωm)	F_C (Hz)	Thickness (mm)	Z_0 (Ωm)	Z_1 (Ωm)	F_C (Hz)	Thickness (mm)
Upper	x	15.1	4	530		26.4	4.4	260		20.5	2.9	380	
	y	16.8	4.2	590	2.31	28.1	4.6	290	2.17	26.8	3.3	395	2.03
	z	6.2	4.8	1.7e5		7.1	4.5	1.4e5		7.5	4.3	1.1e5	
Middle	x	110	0.2	110		6.5	0.8	55		29	0.1	65	
	y	45	0.1	280	2.38	29	0.1	65	2.66	7.2	0.1	60	2.94
	z	210	0.2	200		235	1.5	60		180	0.1	35	
Lower	x	12.1	0.77	250		6.4	1.1	20		4.6	0.95	15	
	y	10.6	0.75	250	2.31	17.5	1.2	25	2.17	5.8	1.15	15	2.03
	z	12	9.6	1.7e5		6.1	3.5	1.4e5		9.2	4.4	1.1e5	

Table 3.1: Model parameters for the conductivity spectra in x, y and z directions and thickness of the upper, middle and lower sections of the tongue. For the model of severe disease, moderate disease and healthy tissue.

Visual assessment of the residual distributions of the FEM fit demonstrated a random distribution centred around 0 (appendix, figure C2.2). Calculation of the NRMSE also demonstrated a good fit (NRMSE$<$ 0.15 for all configurations), with the variation in the phase being around half of the average variation between two repeat measurements (see section 2.3.3 and figure 2.7). Therefore, the model was deemed to have sufficiently captured the underlying dielectric properties of the muscle in different stages of disease.

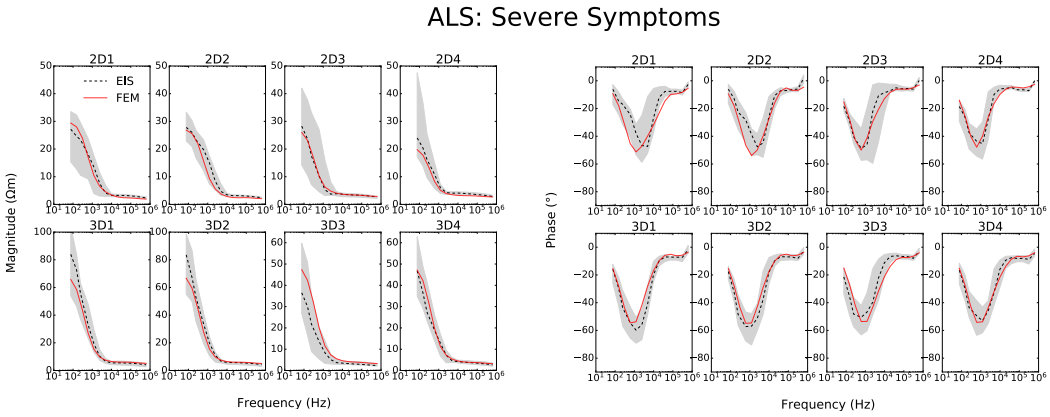

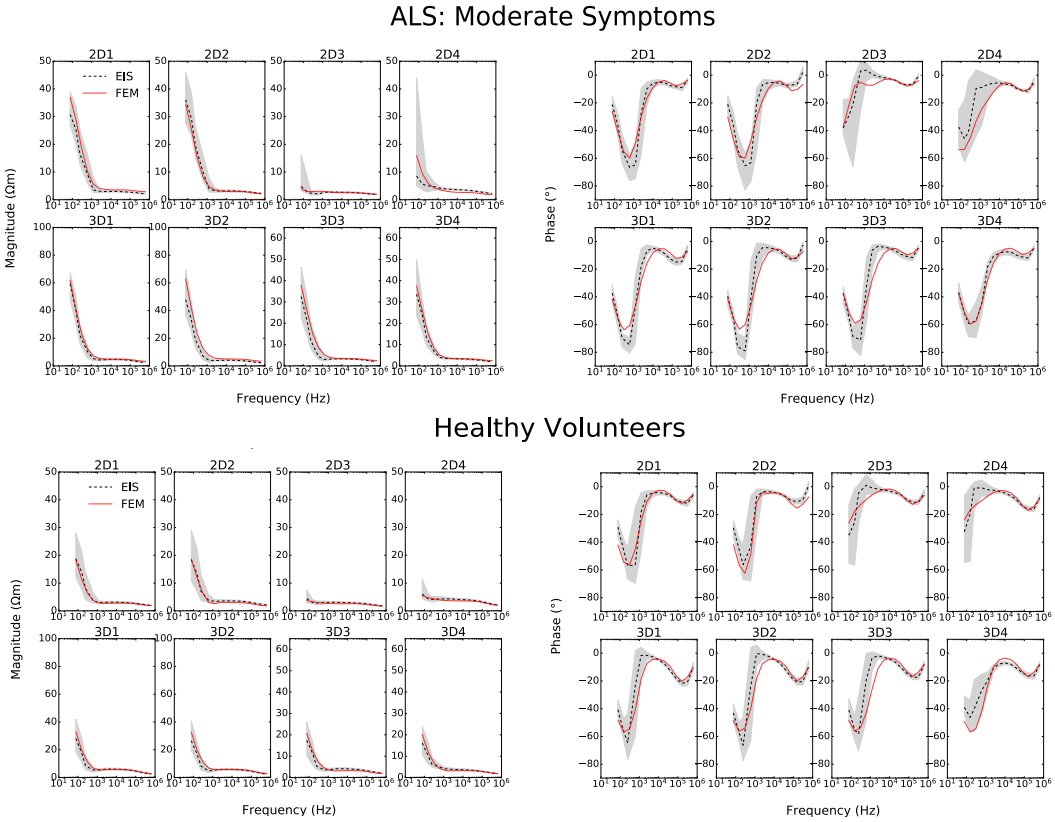

Figure 3.3: Data generated using Comsol (red line) compared to spectral distributions for human participants (dashed line: spectral median, shaded area: interquartile range). Magnitude and phase spectra presented for eight electrode configurations in severe symptom patients, moderate symptom patients, and healthy controls.

3.3.2 Physical interpretation of the model

Inspection of the model parameters for the three models (table 3.1) characterises the underlying disease changes to tongue properties and tissue anisotropy. Using LT-Spice simulations these were directly attributed to circuit parameters (figure 3.4). This gives a physical interpretation for deeper insights into the underlying dielectric changes that occur in disease.

A very good agreement (NRMSE < 0.005) was seen between Comsol and Spice, which demonstrated that the FEM tongue characteristics can accurately be reduced to a lumped model. The most explicit change seen was decreasing capacitance (and hence more negative reactance) with disease progression, mainly due to changes in the x/y directions in the middle and lower tongue sections. The overall effect on extracellular resistance was an increase with disease severity. The intracellular resistance also consistently increased in the lower tongue and the x/y directions of the middle tongue, while the direction of change seen in the upper tongue was less consistent. Overall, these results were in keeping with the known pathophysiology of muscle in ALS (see discussion).

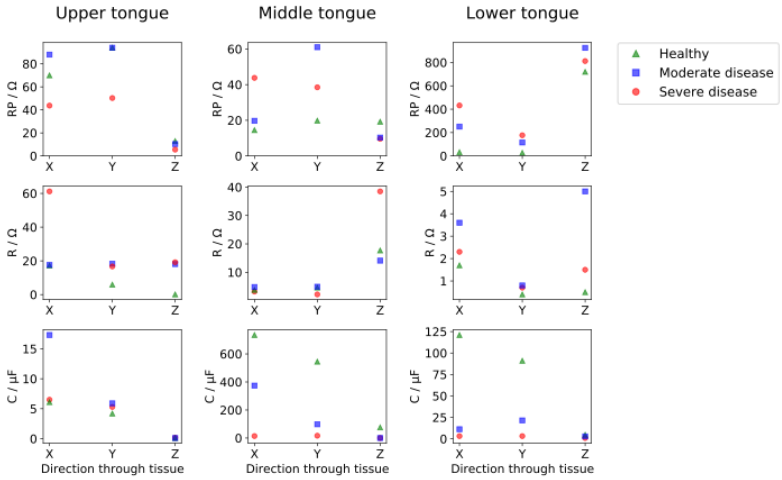

Figure 3.4: Model parameters interpreted as electrical circuit elements. Circuit parameter values RP, R and C for the three modelled disease states in the upper, middle and lower sections of tongue tissue. A general trend of increasing resistance and decreasing capacitance was observed when moving to more severe disease.

3.3.3 Lateral measurement feasibility assessment

To explore the efficacy of the lateral measurement data the significance of edge effects was explored. Generally, edge effects would be expected to occur when the electrodes were positioned close to the edge of the tongue surface. Additionally, when performing measurements with placement on the lateral sides of the tongue, it is likely that the device was slightly rotated, hence the effect of such a rotation was also investigated. If the data does not exhibit noticeable variations caused by edge effects or minor rotations of the electrode array, it can be concluded that lateral measurements represent viable data.

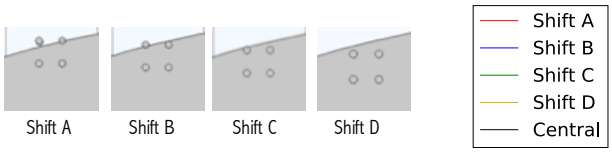

(a) Four electrode edge positions, labelled shift A-D. Starting from the extreme of one electrode pair having no contact with the tongue and moved inwards until all electrodes are within the tissue edge.

Using the optimised FEM-based models the effects of moving the electrodes closer to the edge of the tissue were investigated for both impedance magnitude and phase. Simulations were run for four edge positions (shift A-D as in figure 3.5a), starting with the extreme of one electrode pair having no contact with the tongue and moving until all electrodes are in full contact. Figure 3.6 shows that for edge measurements when there was at least partial contact with all electrodes (shift B-D), the edge effects were minimal, particularly in the phase spectra. In reality, if the electrodes do not have full contact the instrumentation would not produce reliable results with an open circuit electrode. Hence, the presence of artefacts would have a substantial impact on the impedance output, and the data would almost definitely be removed in the outlier removal procedure (4.5% of lateral measurements were removed as outliers, compared to 2.2% of central measurements). Therefore, the significant deviations seen for shift A were expected.

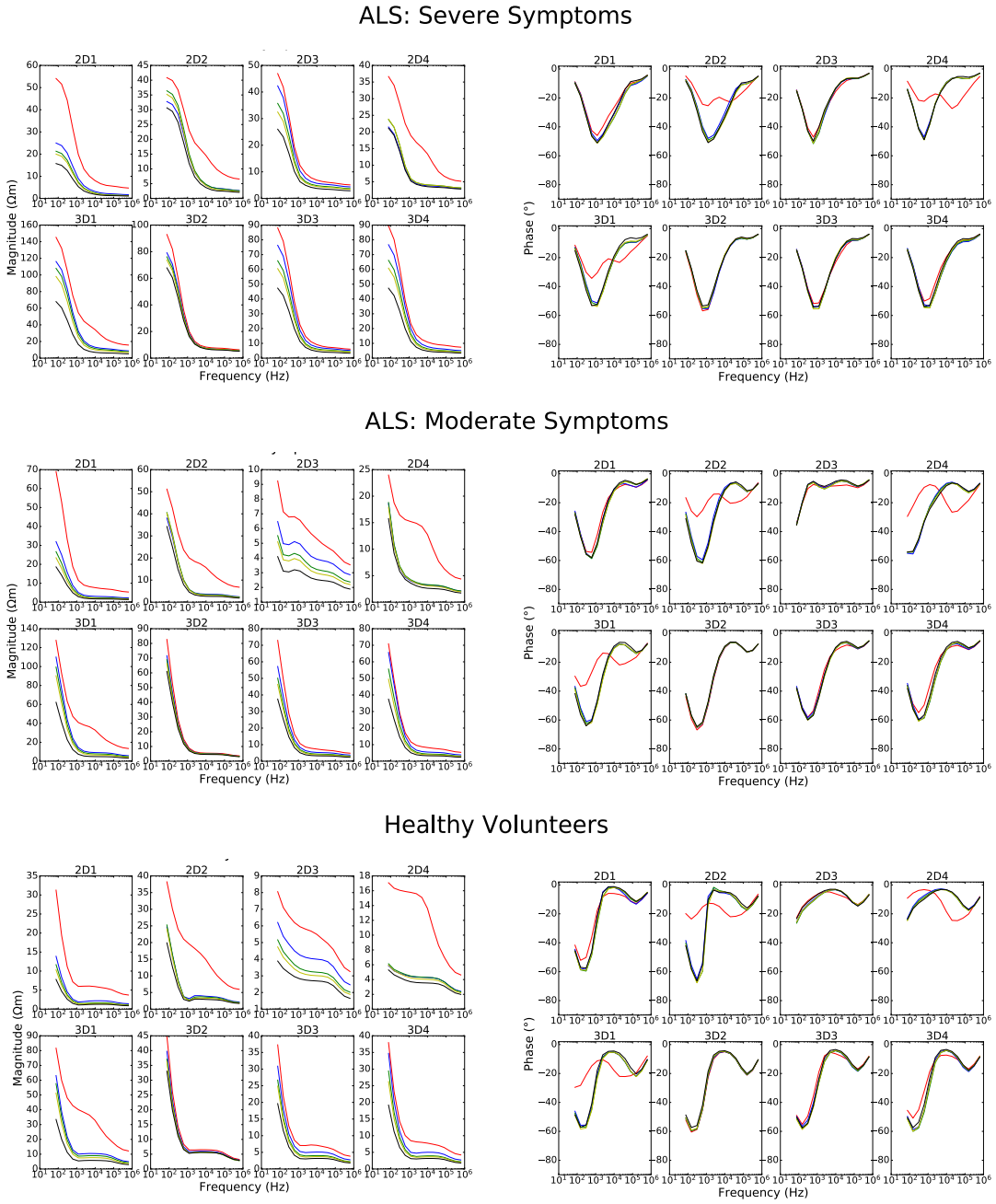

Figure 3.6: Modelled magnitude and phase spectra comparing central measurement (black line) to the measurements made at the four edge positions (red, blue, green and yellow lines for shifts A, B, C, D respectively). Shown for severe symptom, moderate symptom, and healthy control model.

The NRMSE values between the FEM central data and each level of shift to the tongue edge are presented in appendix, table C2.1. In the phase spectra for all three models, the deviation was smaller than the average deviation seen for repeat measurements, unless the electrode

contact is completely lost (shift A). In the magnitude spectra, the deviation was slightly more pronounced, but spectral deviation was negligible when full contact was maintained with the tongue surface (shift D).

Since the tongue muscle demonstrates anisotropy between the longitudinal and transverse directions, rotation of the electrode plates during device placement may impact the measured impedance spectra. To explore this, the FEM was utilised to simulate electrode plate rotations by 15°, 30° and 45° (figure 3.7, NRMSE values presented in appendix, table C2.2).

Minimal changes to either impedance magnitude or phase spectra were observed under electrode rotation. The only deviations greater than that of two repeat measurements were seen for the 45° rotation in configuration 2D3. Suggesting that there was potentially a higher level of anisotropy present on the tongue's lower surface. However, all other rotations found deviations significantly smaller than two repeats. Based on the stability of impedance spectra during measurements at the tongue edge and with electrode rotation, it was inferred that lateral measurements are a feasible approach. As long as all electrodes maintain in contact with the tongue surface and rotation of the device remains less than 45° the data output will be valid and robust.

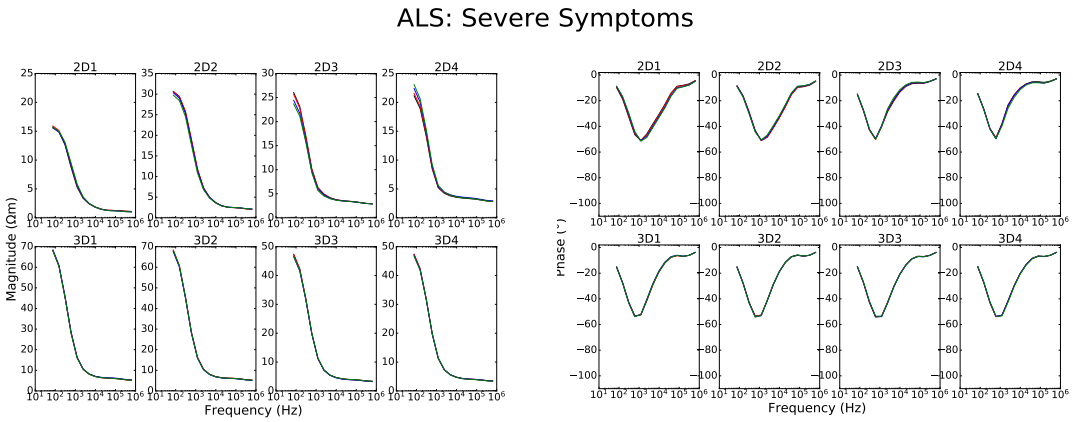

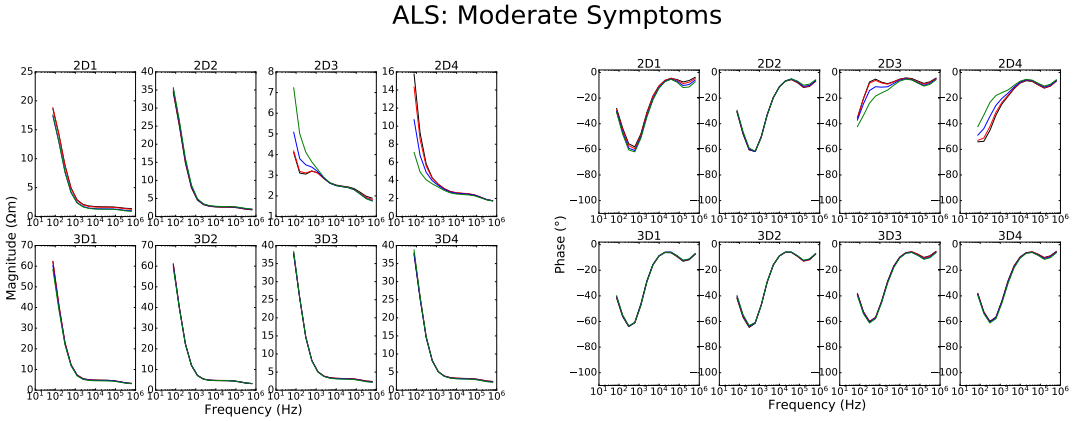

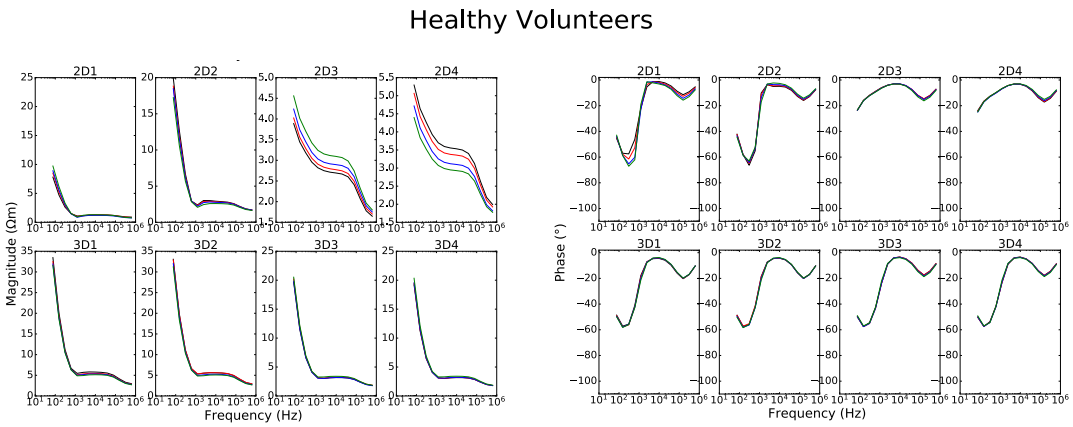

Figure 3.7: Modelled magnitude and phase spectra comparing no rotation (black line) to the rotated measurements (red, blue and green lines for 15°, 30° and 45° respectively). Shown for severe symptom, moderate symptom and healthy control model.

3.3.4 Tongue placement comparison in the measurement data

Once the lateral measurement data was deemed feasible to use, the left and right placement subsets of the tongue EIM dataset were then analysed. ALS disease progression often develops asymmetrically in the limbs (Devine et al., 2014), however, it has not been determined whether such asymmetry is present in bulbar disease. In order to make this assessment, the data recorded on the left and right sides of the tongue were compared.

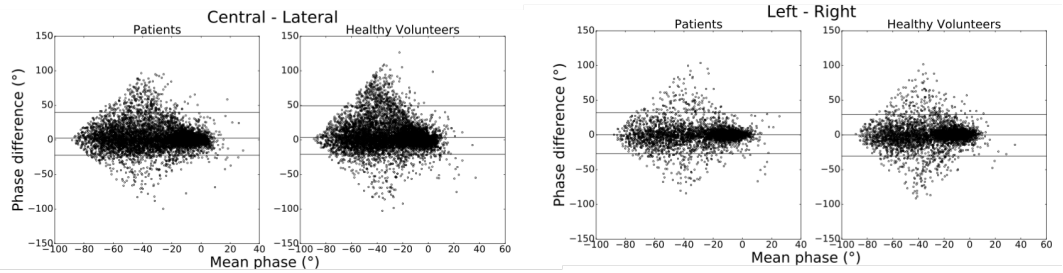

(a)

Measurement configurations		Disease	B-A: Bias(°)	B-A: 95% quantile range (°)	NRMSE mean
Left	Right	Patient	0.0251	59.23	0.2171
		Healthy	0.0159	59.67	0.2209
Central	Lateral	Patient	2.4048	62.1	0.2533
		Healthy	3.8367	69.75	0.3386
Trial 1	Trial 2	Pooled	0.9874	53.2	0.2137

(b)

Figure 3.8: (a) Bland-Altman plots showing the difference between measurements made at left and right sides of the tongue, and between measurements made in the centre and edges of the tongue. Horizontal lines plotted for 2.5th and 97.5th percentiles and the mean value. (b) Table summarising the Bland-Altman bias (mean value of phase difference) and 95% quantile range (difference between 97.5th and 2.5th percentiles), and the mean value of NRMSE metric between the two measurement configurations. Analysed separately for patient and healthy data. Initially the trial 1 vs trial 2 comparison, originally presented in section 2.3.4, is presented for context.

An evaluation of left compared to right placement is presented in figure 3.8, for both the healthy and patient cohort. Bland-Altman analysis revealed a high level of spectral similarity between the two sides of the tongue. The bias was smaller than that for two trial runs and the 95% quantile range and mean NRMSE are comparable (with a 10% deviation of the two trial comparison). This was the case for both ALS patients and healthy controls. Looking more specifically at the patients of varying disease severities, it is clear that there was no apparent asymmetry at any stage of disease, and no change as severity increased (appendix, table C3.1). This indicates that no asymmetry in bulbar disease was observed in tongue EIM, and the left and right measurements can be used interchangeably. From this point onward any data recorded on the tongue edge will simply be referred to as lateral measurement data.

On the other hand, observation of the comparison between lateral and central placements in figure 3.8, demonstrated a more distinct difference in the healthy and patient cohort. Here the bias was relatively high, suggesting that generally central measurements output a higher phase than lateral measurements. In addition, both the Bland-Altman range and the NRMSE exceed that of trial 1 - trial 2 comparison. For this reason, the central and lateral data were considered to be two independent datasets, with potentially different insights into disease.

3.3.5 Comparison of data performance

Thus far the only assessment of biomarker performance has been made on the central measurement subset of the dataset (Alix et al., 2020). Now that the lateral measurement data has been deemed valid to use, the performance of lateral and central recordings was assessed and compared.

To assess the prognostic performance of the raw EIM phase, each configuration was reduced to a combined L2-norm. This was done for the central and lateral data separately, as well as for a combined metric, which incorporates the frequency spectra from both placement positions. The Spearman rank for correlation between each of these L2 norm metrics and tongue strength is shown in table 3.2. The best overall performance was seen for the lateral dataset with 3D4. Overall, either the lateral or combined dataset consistently outperforms central data alone.

Configuration	Lateral	Central	Combined
2D1	**0.696**	0.462	0.638
2D2	**-0.583**	-0.525	-0.525
2D3	-0.578	0.487	**0.677**
2D4	-0.430	0.207	**-0.521**
3D1/2	0.584	0.587	**0.618**
3D3	0.546	0.549	**-0.684**
3D4	**0.721**	-0.535	-0.620

Table 3.2: Correlation between the configuration L2 norm and tongue strength. Spearman rank correlation coefficients, ρ, for all electrode configurations. The highest performing dataset ($|\rho|$ closest to 1) is shown in bold for each configuration.

In addition, classification analysis between patients and healthy controls was undertaken with 3-nearest neighbour and 4-fold cross-validation. Classification performance was assessed through sensitivity, specificity and the area under the receiver operating characteristics curve (AUROC). Feature selection was made through a wrapper algorithm forward selection approach. This involved building up features one by one using the AUROC as the evaluation criterion. The algorithm then selects the combination of features that gave the optimal results. A maximum of 8 features was implemented to reduce overfitting. Feature selection was applied to the central dataset, the lateral dataset and the combined central and lateral dataset, in turn.

For comparison of two AUROC values A_1 and A_2, the Z-score was calculated as:

$$\Xi = \frac{(A_1 - A_2)}{\sqrt{SE_1^2 + SE_2^2 - 2Covar[A_1, A_2]}}, \tag{3.11}$$

where SE_1 and SE_2 are the standard errors of each AUROC value, and $Covar[A_1, A_2]$ is the covariance of the two AUROCs. These were calculated using methods described in (Hanley and Hajian-Tilaki, 1997).

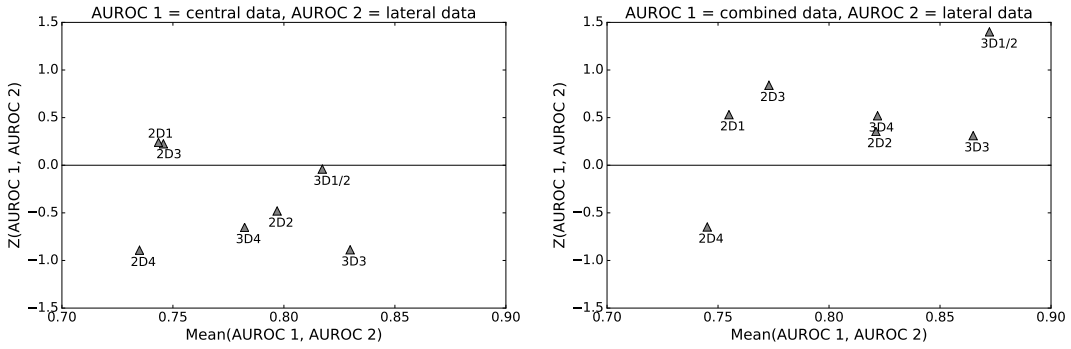

(a) (b)

Figure 3.9: Graphs showing the mean average of two AUROC values A1 and A2 against the comparative Z-score (12). Results for classification made on each electrode configuration individually. (a) The comparison of classification performance using either central data or lateral data. A negative Z value infers better performance for lateral measurements. (b) The classification performance with analysis made on both central and lateral data combined, compared to only lateral data. Positive Z value infers better performance for combined data analysis.

In these analyses, generally the lateral measurement AUROC outperformed those made on the centre of the tongue (figure 3.9a). Furthermore, the combined lateral and central dataset outperformed the lateral measurement only dataset (figure 3.9b), with optimal performance in 3D1/2, with AUROC=0.91. In addition, a comparison of left versus right lateral measurements revealed an identical performance ($\Xi = 0$).

Full details of classification performance and features selected for the central, lateral, and combined datasets are shown in appendix, table C4.1. Inspection of the features selected by the wrapper algorithm revealed a preponderance of frequencies in the top half of our frequency range. Comparing the performance of the different electrode configurations resulted in a general improvement for the 3D configurations over the 2D, as has been previously demonstrated by Alix et al. (2020).

3.4 Discussion

Previous FEM-based models of EIM have used impedance measurements of murine gastrocnemius muscle to obtain values for permittivity and conductivity (Pacheck et al., 2016; Jafarpoor et al., 2011, 2013). This has the advantage of obtaining and using information taken directly from muscle preparations but has the disadvantage of inputting results from muscle with a different distribution of fibre types and architectural structure to those in human subjects (Mathewson et al., 2012). Here, a large dataset of over 9000 spectra from eight electrode configurations was used to develop a 3-dimensional model optimised for different stages of disease. Despite the difference in approach, our results align well with previous studies. For example,

the small difference that was observed in the effect of recording on the muscle edge concurs with the conclusions of Pacheck et al., whose FEM modelling on tongue EIM indicated that there is limited flow of current away from the electrodes (Pacheck et al., 2016). Thus, despite the fact that identical tongue geometries were used for the patient and control models, both the results presented here and those of Pacheck et al., suggest that changes in tongue volume are unlikely to impact upon measured or modelled spectra.

Despite the fact that the optimised model output gave a satisfactory agreement between the model and the measured dataset, limitations with the model setup and geometry must be considered. As has been previously emphasised the structure of the tongue is highly complex, therefore the geometry setup using three isotopic layers of tissue to make up the main body of the tongue blade is unlikely to effectively capture the full extent of the complex tissue structure. Furthermore, the dielectric model parameters were not constrained to a physically realistic range. Looking to table 3.1 it is clear that the value of ZO is significantly higher in the midline layer compared to the other layers, however, such a disparity is unlikely to be plausible in reality. If stricter constraints had been introduced into the inverse modelling procedure the output parameters would be more robust and a unique solution may have been possible. Furthermore, the epithelial layer was characterised by dielectric properties taken from older studies in healthy tissue (Lackovic and Stare, 2007; Richter et al., 2015), however, more recent work has developed a more detailed understanding of the sensitivity of these dielectric properties to the level of keratinisation, as well as the impact of disease (Heath et al., 2022).

Edge effects have been reported in impedance imaging (Scholz and Anderson, 2000; Li et al., 2019). The FEM model employed in this study found phase values to be particularly robust to any edge effects. This implies that resistance and reactance are similarly affected by any edge effects and therefore become insensitive to changes in phase but not necessarily in magnitude. Phase is often employed as the measured impedance parameter since it is also deemed more resilient to changes in tissue size and effects of subcutaneous fat (Rutkove, 2009; Rutkove et al., 2007; Schwartz et al., 2015; Li et al., 2016b). However, a more detailed assessment of the results here finds that both the impedance phase and magnitude data are resilient to significant edge effects as long as all electrodes remain in good contact with the tongue surface. The outlier removal procedure applied to this dataset identified twice as much lateral data then central. Hence it is clear that lateral recordings are more likely to be subject to measurement error due to poor electrode contact. However, if recordings are performed effectively and the clinician ensures good contact throughout the measurement, all data within the lateral impedance dataset is viable to use.

One limitation of this work is the use of the central measurement data to optimise the FEM. However, the differences in central and lateral measurement spectra are small (figure 3.8) and much less prominent than the differences seen between the different patient groups. A future work could include generating models based on differing electrode placements in order to develop a more sophisticated 3D model, which incorporates non-homogeneity in all directions through the tongue.

Nonetheless, the application of FEM to Cole-Cole circuit simulation results in changes to model parameters that are in keeping with the known pathophysiology of ALS. For example, the capacitive element is differential to tissue permittivity and hence to cell membrane area within the tissue volume. Disease progression is associated with a loss of cell membranes and hence a reduction in the model capacitance is consistent with muscle cell atrophy. Increased extracellular resistance was also found and is in keeping with increases in extracellular connective tissue and fat known to occur in ALS (Rutkove, 2009). There are however, associated problems in attributing particular tissue properties directly to elements within the LT-Spice lumped parameter model, where the accuracy can be significantly affected by the approximations made

(McAdams and Jossinet, 1996). Overall, lumped parameter modelling involves simplifying complex biological systems into discrete elements. As a result, directly attributing tissue properties to model elements may not fully encompass the complexity of the biological system. It is important to acknowledge the limitations associated with such modelling approaches to ensure a comprehensive understanding of the system under investigation.

The results also provide insight into the pathophysiology of tongue disease in ALS as the asymmetry typically observed in limb muscles was not seen in the tongue. This was the case across all severities of disease, suggesting that there is not, for example, asymmetry early on which is lost as the disease progresses. In keeping with the present results, it seems apparent that clinically observable asymmetry of the tongue is not a feature of ALS. Cerebral hemispheric dominance has been suggested to be a driver of limb asymmetry (Henderson et al., 2019); interestingly, the hypoglossal nucleus receives bilateral cortical innervation which may limit any such effect in the tongue muscle (Urban et al., 1998; Chen et al., 1999). There do, however, appear to be differences in the impedance spectra obtained from the centre of the tongue versus the lateral portions. Histological studies show a central band of connective tissue, the lingual septum (Larsson et al., 1982), which may underlie such differences. It seems unlikely that the lingual septum will undergo any significant changes during ALS and thus changes observed in central tongue EIM measurements should still be dominated by muscle. In keeping with this, both our group and others have shown that central placement is sensitive to disease and correlates with ALS symptoms (Alix et al., 2020; Shellikeri et al., 2015; Mcilduff et al., 2017).

3D electrode configurations appear to provide a superior performance to 2D arrangements. The reason for this remains undetermined but perhaps relates to the 3D configurations assessing a relatively greater amount of tongue muscle. Regardless of the cause, this observation was preserved in both central and lateral placements. With regard to placement, classification performance across lateral and central measurements was high and correlation with tongue strength was observed in both datasets, suggesting pathology is occurring and detectable throughout the tongue. In general, however, lateral placement outperformed central placement. The underlying cause of the higher classification and tongue strength correlation from lateral measurements is unclear, although a purer assessment of muscle in lateral recordings (versus muscle and the lingual septum in central recordings) may be a contributing factor. Nonetheless, classification appears enhanced through the incorporation of both lateral and central measurements. Validation of such comparisons of the device placement should be further assessed in a larger study.

So far, data performance has only been assessed for each configuration in turn. Just as a combination of both central and lateral data appeared to enhance the biomarker potential of tongue EIM, combining multiple configurations into a more sophisticated multi-dimensional analysis is worth exploring. Although the L2 norm shows a fair performance, with significant correlations with tongue strength, it is a rather simple method of dimensionality reduction, and frequency specific information is lost. FEM modelling in tandem with lumped circuit modelling gives a detailed and comprehensive understanding of the physical changes that attribute specific impedance spectral shifts. However, this process while useful to apply to changes on a group level is far too computationally expensive to apply to each individual patient measurement set in turn. The next chapter moves on to the application and assessment of a more sophisticated dimensionality reduction procedure.

4 Chapter 4: Non-negative tensor factorisation in bulbar EIM

The majority of the work presented in this chapter has been published in Schooling et al. (2021) and Schooling et al. (2022).

4.1 Introduction

A key question in EIM research is how best to utilise the full spectrum of high-dimensional complex impedance data. Previous studies have reported a range of outputs for identifying disease-related change, often using a limited number of frequency outputs, even when a wide frequency spectrum has been collected. These include phase measurements at single frequencies (Shellikeri et al., 2015; Mcilduff et al., 2017; Rutkove et al., 2007) and phase ratios (Rutkove et al., 2017; Schwartz et al., 2015; Li et al., 2016b). More complete use of the frequency range has been attempted, either using reactance only measurements (Kapur et al., 2019) and multiple frequency phase values incorporated through machine learning algorithms including support vector machine (Srivastava et al., 2012). The tongue EIM data in this study includes a range of input frequencies, multiple electrode configurations and multiple device placement positions. The resulting data would hence be expected to achieve a more detailed assessment of muscle disease but are complex and high-dimensional. Having a simple quantitative output is key for progression in the development of EIM as an effective biomarker (Rutkove, 2015).

In ALS, quantitative measures of disease that change in line with the progression of disease are of increasing importance as several promising therapeutics reach clinical trials (Calabrese et al., 2021; Bald et al., 2021). While longitudinal EIM studies in ALS have used only a small amount of the available data, power analyses indicate that significant improvements in trial design can be achieved through limb EIM measurements (Rutkove et al., 2012a; Shefner et al., 2018). Bulbar disease monitoring in trials is often limited (Yunusova et al., 2019) and the most commonly assessed muscle, the tongue, provides additional challenges relating to the complexity of the myo-architecture (Gaige et al., 2007). Adding to this complexity are the contrasting effects that muscle changes in ALS would be expected to have on an impedance spectrum. The stages of atrophy tend to include denervation followed by reinnervation, which is then punctuated with further episodes of denervation and ultimately reinnervation failure. Hence, the muscle undergoes a variety of different changes throughout the progression. In preclinical studies that utilised sciatic nerve ligation, changes to impedance spectra in the acute setting were both short lived and different to those observed in a chronic setting (Carlson, 2014; Ahad et al., 2010). Later work with the SOD1G93A mouse model demonstrated resistance decreased in the pre-symptomatic stage and then increased in the symptomatic stage (Li et al., 2016b).

The tongue is an extraordinarily complex muscle, with fibres running through multiple planes (Gilbert and Napadow, 2005; Gaige et al., 2007). Thus, assessment of muscle impedance in a number of different directions using multiple frequencies should encapsulate maximal information. However, a potential problem lies in interpreting this large amount of data to give an objective measure of disease. Thus, decomposition of the data is required in order to draw out the most important features and facilitate interpretation/graphical representation. The previous analysis work (Chapter 3, Alix et al. (2020)) has used wrapper methods for feature selection in order to determine the specific frequencies to select for use in classification analysis. However, this has the disadvantage of being computationally expensive (Chandrashekar and Sahin, 2014), particularly when considering all dimensions in the dataset, as well as being more prone to overfitting (Loughrey and Cunningham, 2005).

This chapter presents the development of a novel methodology for the analysis of high-

dimensional EIM data. The procedure, which will be termed "tensor EIM", uses a combination of data preprocessing, non-negative tensor factorisation (NTF) and principal component analysis (PCA). This alternative methodology was performed on the same EIM tongue dataset. This approach involved computing a parts-based representation of the data, resulting in low-rank approximations. NTF is effective at exposing the latent structures in high-dimensional data and can extract the essential features (Chandrashekar and Sahin, 2014). The advantage of considering the data as contributions of different spectral shapes is the increased insight into the clinical interpretation of the spectral contributions between the different disease states. Here, the non-negativity constraint is key for providing physically interpretable outputs. Alternative dimensionality reduction techniques such as PCA, the L2 Euclidean norm and feature selection do not have the same physical interpretability. A further advantage to NTF is the capability of dealing with missing data for example, it has been demonstrated that a Parallel Factor Analysis (PARAFAC) model can be correctly determined even when up to 70% of the data are missing (Tomasi and Bro, 2005).

On the whole, the tensor EIM procedure aggregates and simplifies EIM data while minimising any loss of information. In this study, the aims were to assess if such an analysis could deliver features to discriminate between patients and healthy participants and to explore their correlation to patient symptoms and disease progression over time. It is expected that longitudinal changes in EIM spectra from individual patients will be complex due to the competing effects of acute and chronic denervation/reinnervation, hence multi-directional and multi-frequency information may improve the sensitivity to the multiple layers of disease progression.

Median spectra from patients and healthy controls have demonstrated clear differences in the overall spectral shapes (presented in Chapter 2, figure 2.8). Hence I hypothesise that tensor EIM will provide successful classification for an ALS diagnostic model and successful correlation with the severity of the disease. Results were compared to the performance of single frequency raw features, feature selection through wrapper methods, and the Euclidean L2 norm. Such methodologies have been previously applied to this dataset in the previous chapter, as well as in Alix et al. (2020). A detailed discussion of the limitations and benefits of these different analyses is also included. Overall, this chapter highlights the potential of tensor EIM as a valuable tool in monitoring neuromuscular diseases and improving the design of clinical trials for promising therapeutics.

4.2 Methods

4.2.1 Input EIM data

The high-dimensional EIM data were input into an NTF procedure, and the outputs were assessed for their ability to identify disease, assess prognosis and monitor changes over time. Participant datasets are often missing some measurement types due to measurement failure, or data removal following the outlier removal procedure (see section 2.3.2). To maximise the number of participants in the dimensionality reduction procedure, a subsection of data types were considered. Only the 3 three-dimensional electrode configurations (3D1/2, 3D3 and 3D4) were included as they consistently demonstrated improved performance for disease detection (as shown in Section 3.3.5, figure 3.9). The multiple dimensions of the dataset are made up of the different participants; multiple time points (when considering longitudinal change); the 3 electrode configurations, placements of the device (central and lateral); and the 14 frequencies of measurement for both resistance and reactance (giving 28 spectral points in total). This multi-dimensional breakdown of the data is shown in Figure 4.1.

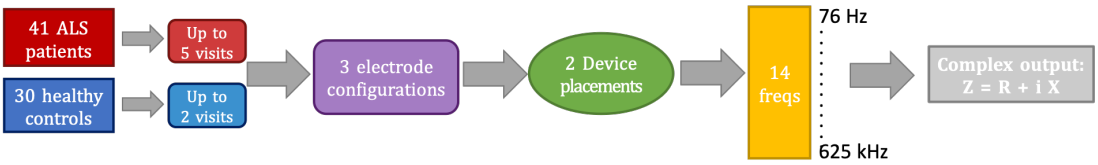

Figure 4.1: High-dimensional nature of the tongue EIM dataset. Each patient has up to 840 ($5 \times 3 \times 2 \times 14 \times 2$) data points, while each healthy control has up to 336 ($2 \times 3 \times 2 \times 14 \times 2$) data points.

The NTF can cope with some missing data, so each participant only had to have a subset of the measurement data available to be included in the analysis. While this means some spectra will be missing, it maximises the number of patients available, which was important as the sample size is already small. Overall, for either a central or lateral assessment each participant was required to have spectra available from at least 2 of the 3 electrode configurations for satisfactory reconstruction. Conversely, when the combined dataset was used each participant only required 3 spectra available out of the 6 measurement paradigms (3 configurations over 2 placements). For this reason, there were generally more participants available when assessing in a combined analysis. Furthermore, for a longitudinal analysis, a participant had to have available measurement data from at least 2 time points to be included. The participants available for different assessments are presented in table 4.1.

The data was initially factorised for the baseline visit in order to assess the diagnostic and prognostic power of the NTF outputs. This process was applied to the combined measurement set, which maximised the number of available patients (see table 4.1). Analysis was also repeated for the central and lateral datasets individually and no significant differences were found in the results. However, due to slightly different subsets of patients being available for each analysis, direct comparison was not possible. For brevity, only the combined placement assessment is presented here. Further, factorisation was applied to the full longitudinal dataset to assess the sensitivity of EIM to disease progression. Due to patient drop off over time, the sample size became particularly small in longitudinal assessment. Therefore, assessing the combined dataset was the optimal choice.

Time Point	**Patient**			**Healthy**		
	Central	Lateral:	Combined	Central	Lateral:	Combined
Baseline	33	29	34	28	27	30

(a)

Time Point	**Patient**			**Healthy**		
	Central	Lateral:	Combined	Central	Lateral:	Combined
Baseline	20	18	28	22	17	21
3 Months	19	16	26	-	-	-
6 Months	13	13	20	22	17	21
9 Months	11	11	14	-	-	-
12 Months	5	5	7	-	-	-

(b)

Table 4.1: The number of participants with enough measurement data available to use in the NTF factorisation. Split by patients and healthy across a central, lateral and combined analysis. (a) shows the baseline only analysis and (b) shows a longitudinal analysis where each participant is required to have data available on at least two time points to be included.

Before applying the tensor decomposition the original dataset was transformed. This must be done to meet the non-negativity requirement of NTF. Additionally, the data was normalised

to give an equal contribution from each frequency of the spectra.

The reactivity dataset, $\{\chi(f)\}$ is mostly negative with a small number of positive values in the lower frequency range. To transform the reactivity dataset all data were shifted by a set value at each frequency so that the maximum reactivity value becomes zero, and then divided by the median value at that frequency. This returns a normalised non-negative output. The resistivity dataset, $\{\rho(f)\}$ is by definition already non-negative, however for consistency the same transformation was applied here. All data were shifted so that the minimum resistivity value becomes zero, and subsequently divided by the median value at that frequency.

$$\rho^T(f_i) = \frac{\rho(f_i) - min(\{\rho(f_i)\})}{median(\{\rho(f_i)\})}, \qquad \chi^T(f_i) = \frac{\chi(f_i) - max(\{\chi(f_i)\}}{median(\{\chi(f_i)\}}. \tag{4.1}$$

The minimum, maximum and median values were calculated over the entire dataset at each frequency. Following the tensor factorisation, the inverse transformations were applied to the output modes. This returned complex impedivity spectra within a physically plausible data range.

4.2.2 Factorising the dataset

Non-negative tensor factorisation (NTF) is a process of approximating an N-dimensional tensor as the sum of R rank-1 tensors formed by the outer products of N vectors (Kolda, 2006; Kolda and Bader, 2009). For this analysis, the factorisation was applied for N=3 and N=4. These decompositions factorise the 3-dimensional data tensor, $\mathcal{T}$, as:

$$\mathcal{T} \approx \mathcal{T}^{'} = \sum_{\mathbf{r=1}}^{\mathbf{R}} \mathbf{a_r} \circ \mathbf{b_r} \circ \mathbf{c_r} \quad \mathbf{a} \in \mathbb{R}^{\mathbf{I}}, \mathbf{b} \in \mathbb{R}^{\mathbf{J}}, \mathbf{c} \in \mathbb{R}^{\mathbf{K}} \tag{4.2}$$

and the 4-dimensional tensor, $\mathcal{U}$, as:

$$\mathcal{U} \approx \mathcal{U}^{'} = \sum_{\mathbf{r=1}}^{\mathbf{R}} \mathbf{a_r} \circ \mathbf{b_r} \circ \mathbf{c_r} \circ \mathbf{d_r} \quad \mathbf{a} \in \mathbb{R}^{\mathbf{I}}, \mathbf{b} \in \mathbb{R}^{\mathbf{J}}, \mathbf{c} \in \mathbb{R}^{\mathbf{K}}, \mathbf{d} \in \mathbb{R}^{\mathbf{L}} \tag{4.3}$$

This process was undertaken for three scenarios:

1. A baseline assessment using either the combined placement measurements. Data was decomposed as a 3-dimensional tensor, where the dimensions describe the 28 spectral features (I=28); the 3 configurations over 2 placements (J=6); and the total number of participants (K=N_p).

2. A longitudinal assessment using the combined placement measurements. Data is decomposed as a 4-dimensional tensor where the dimensions describe the 28 spectral features (I=28); the 6 measurement paradigms (J=6); the total number of participants (K=N_p); the baseline and 6 month follow up (L=2).

3. A longitudinal assessment using the combined placement measurements. Data is decomposed as a 3-dimensional tensor, where the dimensions describe the 28 spectral features (I=28); the 6 measurement paradigms (J=6); and the total number of participants (K=$\sum_{n=1}^{N_p} V(n)$, where V(n) = number of time visits for participant n).

The tensor decompositions output R vectors, $\mathbf{a}_r$ (r=1,..R), each of length 28. These are the spectral modes, which represent the most common unique spectral patterns within the dataset. Additionally, $\mathbf{b}_r$ (r=1,..R) of length 6, represent the respective weighting of spectral mode r between the measurement paradigms, while $\mathbf{c}_r$ (r=1,..R) are the participant weightings with a length corresponding to the number of participants, these represent the respective weightings of spectral mode r for each individual participant. The participant weightings were used as features for assessing the diagnosis and prognosis of disease. By assessing how the values of the specific participant weightings vary between the healthy and patient groups, how they correlate with disease and how they change over time it was possible to identify the overall trend in the changes to the spectral patterns within the EIM data. Finally, for scenario 2, an additional R vectors $\mathbf{d}_r$ (r=1,..R) of length 2 represent the weighting of each spectral mode for baseline visit, and 6 month follow up.

To further reduce the data down to a single value per participant, principal component analysis was applied to the R participant weighting vectors, and the PC1 output was used as a single metric of disease assessment, termed the tensor EIM metric. In order to assess the contributions of each of the spectral shapes, the coefficients of PC1 were considered.

The tensor factorisations are approximated using CANDECOMP/PARAFAC (Carroll and Chan, 1970; Harshman et al., 1970) (or CP) decomposition via alternating least squares (Kolda and Bader, 2009). Considering a 3-dimensional factorisation, (4.2) can be written using the notation for the Kruskal Operator (Kruskal, 1977; Kolda, 2006):

$$T' = \sum_{r=1}^{R} \mathbf{a_r} \circ \mathbf{b_r} \circ \mathbf{c_r} = [\![\mathbf{A}, \mathbf{B}, \mathbf{C}]\!] \tag{4.4}$$

The goal was to compute a CP decomposition with R components that best approximates our original input tensor. This was done by minimising the reconstruction error, $\mathcal{E}$:

$$\mathcal{E} = \|T - T'\|, \qquad T' = \arg\min_{T'} \mathcal{E} \tag{4.5}$$

The alternating least squares procedure begins by initialising all the factor matrices with random values. Considering the third-order example the approach fixes $\mathbf{B}$ and $\mathbf{C}$ to solve for $\mathbf{A}$, then fixes $\mathbf{A}$ and $\mathbf{C}$ to solve for $\mathbf{B}$, then fixes $\mathbf{A}$ and $\mathbf{B}$ to solve for $\mathbf{C}$. This procedure was repeated until the convergence criteria were met, where the absolute difference between the current error and the previous error was less than 10^{-10}.

One issue that arises when performing such a tensor decomposition, is how one goes about choosing the number of rank-1 components, known as the rank, R of the reconstruction. Generally speaking, the value of R will be chosen to find the minimum value, which gives a satisfactory reconstruction accuracy in order to appropriately maximise the power of the dimensionality reduction. The value of R must first be chosen before the tensor decomposition can be optimised (Kolda and Bader, 2009), hence reconstructions for a number of different R values were computed to allow for an assessment of the optimal value. The rank choice was determined by comparing the error on the reconstructed data with the variability between repeat measurements. The frequency-dependent 95th percentile in resistance and reactance variability ($\mathcal{E}_R(f_i)$ and $\mathcal{E}_X(f_i)$, figure 4.2) were used as the acceptable variation at each frequency when assessing the acceptability of the reconstructed data.

For each reconstructed spectra the root mean squared deviation (RMSD) between the original data (R, X) and its reconstruction (R', X') were calculated, normalised by the 95th percentile variation:

$$RMSD = \sqrt{\frac{\sum_{i=1}^{14} \left(\frac{R(f_i) - R'(f_i)}{\mathcal{E}_R(f_i)}\right)^2 + \sum_{i=1}^{14} \left(\frac{X(f_i) - X'(f_i)}{\mathcal{E}_X(f_i)}\right)^2}{28}} \tag{4.6}$$

where $\{R(f), X(f)\}$ define the measured dataset, and $\{R^{'}(f), X^{'}(f)\}$ define the reconstructed dataset.

Acceptable variation for the reconstructed spectra was defined by RMSD$\leq$ 1. The probability, $\gamma(R)$ that a given reconstructed spectra will fall in the acceptable range for a given rank, R is characterised by the proportion of spectra to be acceptably reconstructed. The rank was selected as the lowest value satisfying $\gamma(R) = 1$, i.e. 100% of spectra reconstructed inside the acceptable range.

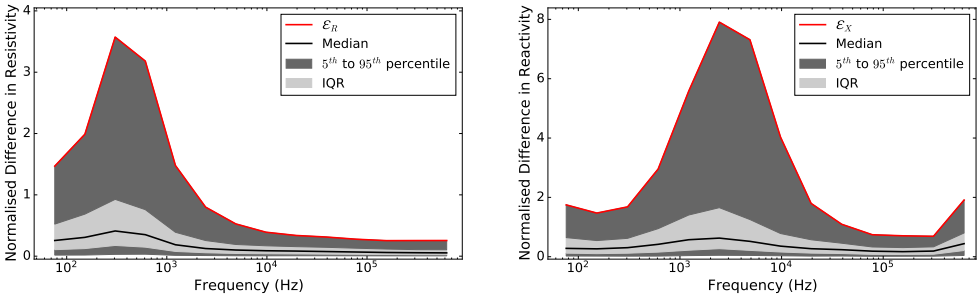

Figure 4.2: Variation between two repeat measurements on the same participant in resistivity and reactivity, normalised by the median at each frequency. The 95th percentile ($\mathcal{E}_R$ and $\mathcal{E}_X$) are used in the criteria for rank selection.

4.2.3 Analysis for assessing changes over time

The sensitivity of EIM metrics to disease progression was compared with other biomarkers of disease. Previous studies have looked at estimating sample size requirements in hypothetical clinical trials (Rutkove et al., 2012a; Shefner et al., 2018). This is a good technique for determining the sensitivity of a biomarker to disease changes because it allows researchers to determine the minimum sample size needed to detect a statistically significant difference in the biomarker between groups, which can help ensure the success and efficiency of future clinical trials. In order to explore a similar approach here the slopes of change of each biomarker ($\Delta x/\Delta t$) were calculated for each participant. Hence the mean slope was calculated for patients (μ_p) as well as for the healthy control group (μ_c), additionally, the standard deviation of slope over all participants was calculated (σ). From this Cohen's effect size (Cohen, 1988), δ, for each given biomarker was calculated as:

$$\delta = \frac{\mu_p - \mu_c}{\sigma} \tag{4.7}$$

For assessment of the ASLFRS-R, where there is clearly no healthy control group for comparison, this becomes:

$$\delta = \frac{\mu_p}{\sigma} \tag{4.8}$$

I thence determine an estimate for sample size, n, for a hypothetical clinical trial at 80% power ($\beta = 0.8$) and 5% significance level ($\alpha = 0.05$). This was calculated under the assumption of 50% and 20% treatment effects, where p = 0.5 or 0.2 is the expected proportion of patients to respond to a specific treatment. The sample size was calculated, using a two-tailed test, as:

$$n = 2 \times \left(\frac{(Z_{\alpha/2} + Z_\beta)}{p \times \delta} \right)^2 \tag{4.9}$$

(Hulley and Cummings, 2013), where Z is the standard normal distribution z-score. A two-tailed test was chosen as the treatment effect could be either beneficial or harmful, and such a clinical trial is designed to detect both possibilities.

An additional method for assessing the sensitivity of a biomarker to changes over time is using linear-mixed effects modelling using a compound symmetry covariance matrix, fitted using Restricted Maximum Likelihood. Assessment of change was made through the mixed model and using Mann-Whitney U tests in comparison to the healthy controls. Outcomes for four time points (baseline to 9 months) were assessed, due to significantly reduced patient numbers by 12 month follow up (see table 4.1).

4.3 Results

4.3.1 Patient identification

Tensor EIM was applied to quantify this difference in spectral shape between participants. Following the rank selection procedure a rank of 3 was selected, which gives a compression ratio of 19:1. The three spectral modes output from this decomposition are presented in figure 4.3a.

The contributions in the patient cohort and healthy cohort are assessed for the three spectral modes (c_1, c_2, c_3) as well as for the PC1 metric, termed *tensor EIM*, which is defined by $0.2 \times c_1 - 0.9 \times c_2 + 0.1 \times c_3$. Boxplots for these distributions are displayed in figure 4.3b.

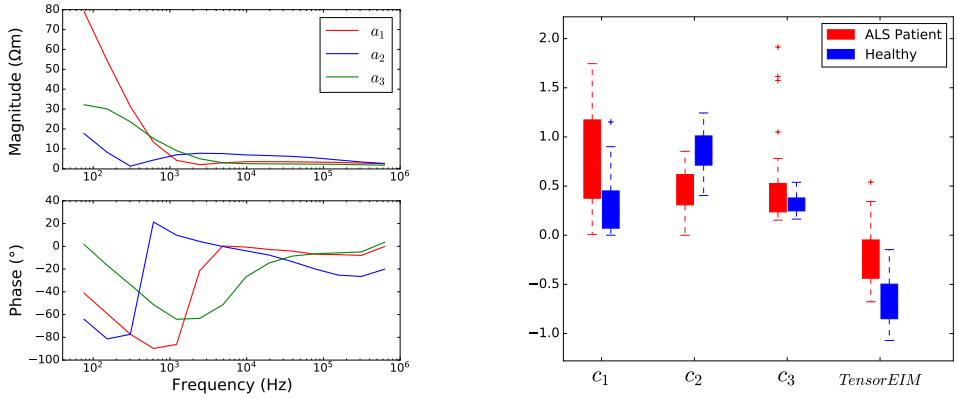

(a) (b)

Figure 4.3: (a) The three NTF spectral modes, a_1, a_2, a_3. (b) Boxplots showing each participant factor (c_1, c_2, c_3), which are a quantification of the contribution of each respective spectral mode in the individual's data, as well as the combined tensor EIM metric (a linear combination of the three factors). Presented for both the patient group (red) and the healthy group (blue). Crosses indicate data outliers.

It is clear that the first and third modes generally contribute most significantly in the patient cohort, while the second mode contributes most in the healthy cohort. This agrees with the general trend identified when the raw data median spectral patterns were assessed (figure 2.8). The significance of the difference between the healthy cohort and patients of varying disease severities for each metric was calculated using the Mann-Whitney U test, and the corresponding p-values are reported in table 4.2.

	Parameter	Mann-Whitney U test p-value		
		Patient v. Healthy	Mild v. Healthy	Severe v. Healthy
NTF Outputs	c_1	**<0.001**	0.009	**<0.001**
	c_2	**<0.001**	**<0.001**	**<0.001**
	c_3	0.20	0.165	0.002
	Tensor EIM	**<0.001**	**<0.001**	**<0.001**
Raw Data	L2 Norm	0.045	0.326	**<0.001**
	Best Single Freq* (3D4: f12)	**<0.001**	0.002	**<0.001**

*FDR correction applied

Table 4.2: Mann-Whitney U test p-value for separation between all patients and healthy participants as well as just mild patients and healthy participants. Shown for the three NTF modes, the combined tensor EIM and the raw data L2 norm and best single frequency.

These are compared to the raw data L2-norm and the best performing single frequency across all frequencies and electrode configurations (with FDR correction applied). The tensor EIM metric comprises all the spectral information and performs better than the previously used L2 norm. A single frequency separates the patient and healthy groups with similar high significance, however, NTF outputs increase sensitivity when comparing healthy with mild patients. Furthermore, a single frequency pertains to a significant reduction of information.

The patient diagnosis classification performance is summarised in table 4.3, which incorporates results from three classifiers (KNN, SVM, and RF). This was repeated for all tensor EIM features, all raw data features, and with wrapper feature selection applied to the raw data features. Performance was optimal when wrapper feature selection was applied. Yet when all features of the dataset were included, the tensor EIM process demonstrated an improvement (best with KNN, AUROC=0.78).

	Classifier	AUROC	Sensitivity	Specificity
All tensor EIM features	KNN	0.78	0.70	0.86
	SVM	0.76	0.73	0.79
	RF	0.76	0.73	0.79
All raw features	KNN	0.67	0.73	0.61
	SVM	0.67	0.64	0.71
	RF	0.76	0.73	0.79
Wrapper Feature Selection	KNN	0.84	0.89	0.79
	SVM	0.83	0.89	0.76
	RF	0.74	0.78	0.70

Table 4.3: Patient classification performance using three classifiers (KNN, SVF, RF) on tensor EIM features, all raw data features, and with wrapper feature selection applied. The features selected through the wrapper method are shown in appendix, table C4.2

EIM recordings from limb muscles generally began at approximately 10kHz due to electrode artefacts relating to keratinised skin (Martisnen et al., 1997). Mucosal surface recordings, like those from the tongue, are reported at lower frequencies, in ranges similar to those presented here (Murdoch et al., 2014; **?**; Ching et al., 2010; Lackovic and Stare, 2007). In order to assess the robustness of the low frequency EIM data, these analyses were repeated after removing the bottom two frequencies. These results are presented in appendix, figure C5.1. Comparing the NTF spectral modes to the full frequency range modes in figure 4.3a it is clear that the shapes of the spectra are completely maintained. The significance of splitting of the parameters between healthy and disease is also comparable with tensor EIM consistently giving highly significant p-values. The patient classification performance is also very similar (AUROC=0.77

truncated, 0.78 full range). Overall, this consistency in the pattern of spectral modes and general performance indicates that the lower power spectra are neither dominant nor unreliable.

4.3.2 Patient severity assessment

EIM can be used to help predict the severity of a patient's disease. This was assessed by looking at the ability of different data metrics to differentiate between the severe and mild patient cohort, as well as in the correlation performance with the overall symptom score.

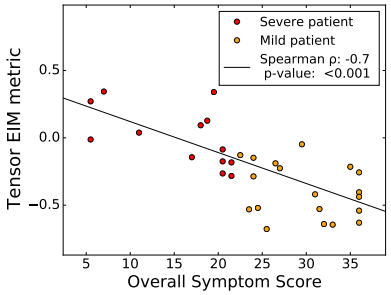

(a)

	Parameter	Spearman rank		MW U test
		ρ	p-value	p-value
NTF Outputs	c_1	-0.53	**0.001**	0.014
	c_2	0.66	**<0.001**	**<0.001**
	c_3	-0.51	**0.002**	**0.005**
	Tensor EIM	-0.70	**<0.001**	**<0.001**
Raw Data	L2 Norm	-0.47	**0.006**	0.015
	Best Single Freq* (3D1, f_{12})	-0.52	**0.001**	**0.006**

*FDR correction applied

(b)

Figure 4.4: (a) Scatter graph of Tensor EIM against overall symptom score shows significant correlation. (b) Spearman rank results for correlation with the overall symptom score. And Mann-Whitney U test p-value for separation between mild and severe patients. Shown for the three NTF modes, the combined tensor EIM and the raw data L2 norm and best single frequency.

Figure 4.4a demonstrates a highly significant correlation of the tensor EIM metric with patient symptoms. This was the best performance when compared to both the individual NTF factors and the raw data metrics (figure 4.4b). Correlation performance with the ALSFRS-R bulbar subscore is shown in table 4.4 and was similarly significant. Further, the Mann-Whitney U test significance values for the separation between severe and mild patients were highly significant for tensor EIM and individual factor c_2. These outperformed both the raw data L2 norm and the best single frequency.

	Parameter	Spearman rank	
		ρ	p-value
NTF Outputs	c_1	-0.36	0.040
	c_2	0.57	**0.006**
	c_3	-0.30	**0.094**
	Tensor EIM	-0.59	**<0.001**
Raw Data	L2 Norm	-0.46	**0.008**
	Best Single Freq* (3D1, f_{13})	-0.58	0.022

*FDR correction applied

Table 4.4: ALSFRS-R bulbar subscore correlations. Spearman rank results for the three NTF modes, the combined tensor EIM and the raw data L2 norm and best single frequency.

An analogous classification assessment to that presented in section 4.3.1 was made for the classification between mild and severe patients (table 4.5). Here, the best performance occurred for tensor EIM features (RF, AUROC=0.75). Again this analysis was repeated for the truncated frequency range as shown in appendix, figure C5.1. The results found comparable

performance in terms of correlation with symptoms (ρ=-0.66 truncated, -0.70 full range) as well as classification power between mild and severe patients (AUROC=0.73 truncated, 0.75 full range).

	Classifier	AUROC	Sensitivity	Specificity
All tensor EIM features	KNN	0.72	0.69	0.75
	SVM	0.64	0.38	0.9
	RF	0.75	0.69	0.80
All raw features	KNN	0.65	0.69	0.60
	SVM	0.67	0.54	0.80
	RF	0.66	0.46	0.85
Wrapper Feature Selection	KNN	0.72	0.60	0.84
	SVM	0.70	0.65	0.75
	RF	0.55	0.27	0.83

Table 4.5: Severe/mild patient classification performance using three classifiers (KNN, SVF, RF) on tensor EIM features, all raw data features and with wrapper feature selection applied.

4.3.3 Clinical interpretation

Two spectral modes can be identified from the tensor EIM metric, which can be interpreted as the ALS patient contribution and the healthy contribution, respectively. These were derived from the combination of spectral modes which contribute positively in the calculation of the tensor EIM metric (red spectra in figure 4.5), and the modes which contribute negatively (blue spectra in figure 4.5). On the whole, patients see a larger contribution from the red spectra in their decomposition, while healthy participants see a larger contribution from the blue. Likewise, the correlation seen in 4.4a demonstrates that as patient disease severity worsens, their contribution from the red spectra will increase and blue spectra will lessen. This shift in spectra, characterised predominantly by an increase in centre frequency with disease, is in clear agreement with the healthy and patient median spectral shapes (figure 2.8), as well as previous EIM analysis in ALS (Li et al., 2012, 2016b).

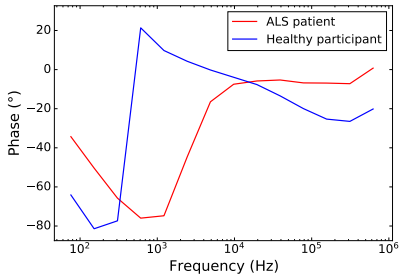

Figure 4.5: Spectral pattern which contributes most significantly in healthy participants (blue) and that which contributes most significantly in ALS patients (red), derived from the PC1 coefficients defining the tensor EIM metric.

In order to gain a clinical interpretation of what EIM data are measuring, these spectral patterns are fit to a lumped circuit model using the same method detailed in Section 3.2.3. Figure 4.6a shows this circuit, which was built in the LT-Spice simulator to represent a simplified muscle cell structure, where resistors in series represent extracellular space, and resistors in parallel with capacitors represent intracellular space and the cell membrane, respectively. Both

the healthy impedance spectra and the ALS impedance spectra were fit to this model, where the model fit and parameters are also presented in figure 4.6. The circuit parameter changes observed when moving from the healthy to diseased mode are characterised by a consistent increase in extracellular resistance and a decrease in intracellular resistance and capacitance. These changes are in keeping with the characterisation observed through FEM modelling (in Chapter 2) as well as the known effects of muscle atrophy.

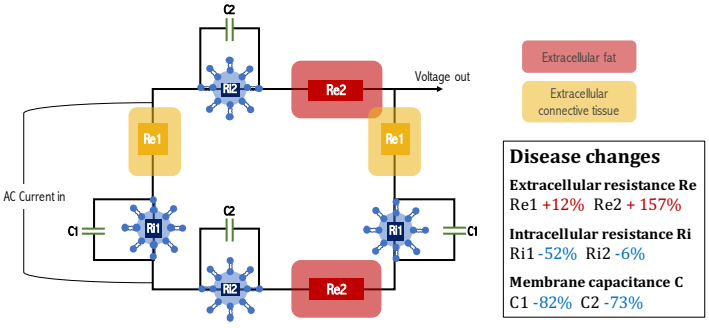

(a)

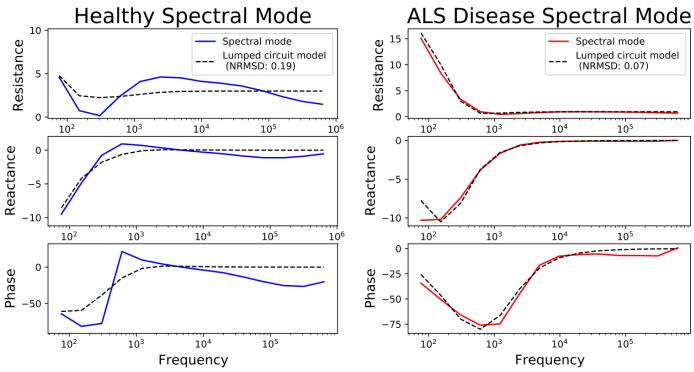

(b)

	Healthy	ALS	% Change
Re1	55.6	63	+12%
Ri1	13.3	6.4	-52%
C1	69.2	12.5	-82%
Re2	15.2	39	+57%
Ri2	16.2	15.2	-6%
C2	14.3	3.9	-73%

(c)

Figure 4.6: (a) Lumped circuit model representative of muscle, where extracellular resistors (Re) illustrate extracellular space remodelling, the intracellular resistors (Ri) are synonymous to internal cell resistance, and capacitors (C) describe the cell membrane. The two sub-circuits characterise different dispersion levels in the muscle impedance spectrum. The model was fit to the healthy and ALS patient spectral shapes (as in figure 4.5) and corresponding changes to the circuit parameters with disease progression are shown. (b) LT-Spice lumped circuit fit results for the healthy spectral pattern and ALS disease spectral pattern. (c) LT-Spice lumped circuit model optimised parameter values, and the respective change in value when moving from healthy to diseased spectra.

4.3.4 Longitudinal change with time

Longitudinal analysis was undertaken with a factorisation on the combined, central and lateral placement dataset. This decision was made to provide a maximum number of patients (see table 4.1), which allowed for more reliable and accurate statistical tests of change with time. All longitudinal data was used in the analysis for the sample size calculations, using Cohen's effect size (Cohen, 1988). For linear-mixed effects analysis data was included up to the 9 month follow up as patient drop off is significant by 12 months. The power of tensor EIM to detect disease changes over time was assessed and compared to the changes over time of alternative

EIM metrics as well as other biomarkers of bulbar disease; including the ALSFRS-R bulbar subscore, tongue strength, and the bulbar disease burden score (defined in Section 2.3.1, eq. 2.3).

The first stage of the analysis looked at exploring disease related EIM spectral changes at the group level, using the NTF approach scenario 2 (outlined in Section 4.2.2 above), which involves a 4-dimensional factorisation where the fourth dimension (vector $\mathbf{d}_r$) incorporates the two time points at baseline visit and the 6 month follow up. Here participants included must have measurement data available at both time points, giving a total of 21 Healthy controls and 28 patients included in each respective decomposition. From here the average spectral pattern ($\mathbf{Z}$) at time point (t) was calculated as:

$$\mathbf{Z}^t = \sum_{r=1}^{R} d_r(t)\,\mathbf{a}_r, \qquad t = 1, 2 \tag{4.10}$$

where $\mathbf{a}_r$ are the spectral modes. The rank of the decomposition was selected as R=2 and R=3 for the healthy and patient analyses respectively. The phase spectral group averages for baseline and 6 months are shown in figure 4.7. On average the ALS patient group demonstrated a spectral shift to the right over time. By contrast, healthy participant spectra were highly stable (complete overlap in the spectra at the two time points). Of note, the shift in the ALS patient spectra was in keeping with that associated with worsening disease severity identified in the baseline analysis (figure 4.5).

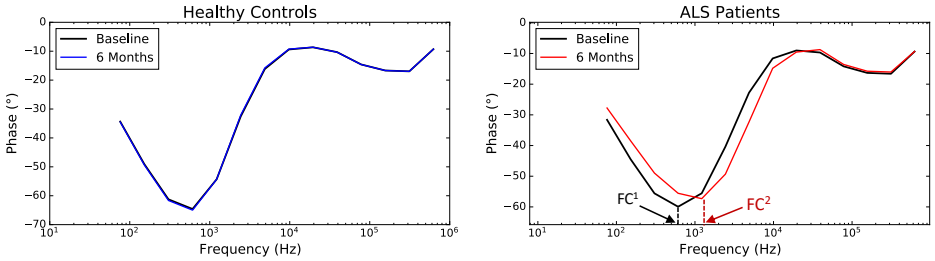

Figure 4.7: Group average in spectral change from baseline to 6 months for the healthy controls and ALS patient group. The healthy group is stable in time. The ALS patient group trend is a shift right in the spectra, characterised by an increase in centre frequency (Fc) from Fc^1 to Fc^2

However, when inspecting the raw spectra of individual patients, the change over time was often more complex. Some patients demonstrated consistent movement of the spectra to the right, while for others we observed transient shifts to the left, followed by spectral movement to the right. Figure 4.8 demonstrates an example of this multi-directional shift, where patient A presents a consistent increase in their centre frequency over time, conversely, patient B presents an initial shift to the left followed by later shifts to the left. Out of the 28 patients, 13 had a consistent shift to the right, while 15 patients had spectra which demonstrated movement to the left on at least one occasion.

In order to capture the effects of the more subtle spectral shifts on an individual level the 3-dimensional factorisation was applied to the full longitudinal dataset (scenario 3, section 4.2.2). Again, a rank of 3 was appropriate and the tensor EIM metric was calculated by applying a PCA. By definition, it was again possible to have a physical interpretation of this metric by identifying two spectral patterns, one which increases in contribution with the tensor EIM and one that decreases in contribution (figure 4.9a). The nature of this decomposition pulls out a similar pattern to the above analysis; overall an increase in tensor EIM represents a spectral

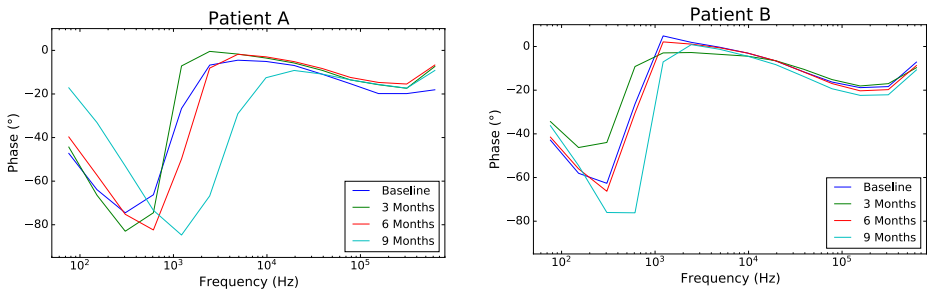

Figure 4.8: Two examples of individual patient change. Patient A presents consistent shifts to the right with time, while patient B presents an initial shift left followed by progression to the right.

shift to the right, hence a decrease signifies a shift left. The change in the tensor EIM metric (ΔT-EIM) was then used to quantify the direction of spectral change. Histograms of the change from baseline for all patients are shown at 3 months (n=26), 6 months (n=20) and 9 months (n=14) (figure 4.9b).

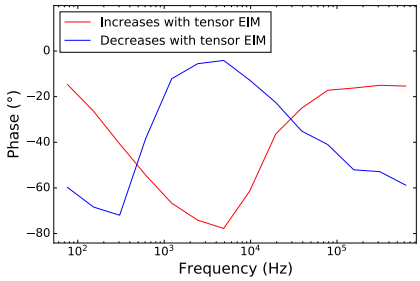

(a)

Month	3	6	9
Unchanged	10 (38%)	3 (15%)	2 (14%)
Negative shift	8 (31%)	6 (30%)	3 (21%)
Positive shift	8 (31%)	11 (55%)	9 (64%)

(b)

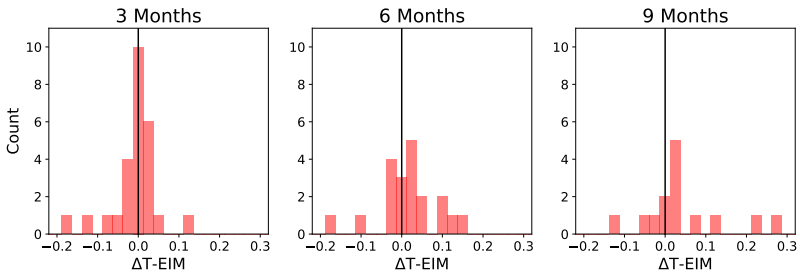

(c)

Figure 4.9: (a) A simple representation of how the tensor EIM metric is defined by two contrasting spectral patterns. A positive shift (ΔT-EIM$>$ 0) corresponds to the spectral shape in red, which shows a shift to the right. A negative shift in tensor EIM (ΔT-EIM$<$ 0) corresponds to the spectral shape moving left (blue). (b) A table summarising the number of patients whose spectra move in each direction or are unchanged after each time point. (c) Individual patient change in tensor EIM from baseline at three time intervals.

These reveal that, to begin with, spectra shifted in equal proportions in both directions. As time progressed, more spectra shifted in the positive direction (figure 4.9c), which corresponds to the overall spectral shape shifting to the right. These pronounced spectral shifts were not

observed for individual healthy participants. An assessment of the correlation between the tensor EIM and disease duration is shown in appendix, figure C5.2. This correlation is not statistically significant, likely impacted by the fact that the rate of disease progression is highly variable.

For further insight into these tensor EIM modes, lumped circuit modelling was again undertaken with the model shown in figure 4.6a. The impedance outputs of the circuit were fit to the T-EIM spectral modes with the model parameters shown in Table 4.6.

	Re1	Ri1	C1	Re2	Ri2	C2
Low centre frequency spectra	63	12.5	37	18	38	7.6
High centre frequency spectra	89	8	2.5	50	22	1.8
% Change for shift right	+41%	-36%	-93%	+178%	-42%	-76%

Table 4.6: Lumped circuit model used to parameterise spectral shapes, comprising resistors in parallel (Ri), in series (Re) and capacitors (C). Results of model when fit to the two tensor EIM spectra (Figure 4.9a) (low centre frequency/blue spectra and high centre frequency/red spectra). A shift to the right is characterised by an increase in extracellular resistance (Re) and a decrease in intracellular resistance (Ri) and capacitance (C).

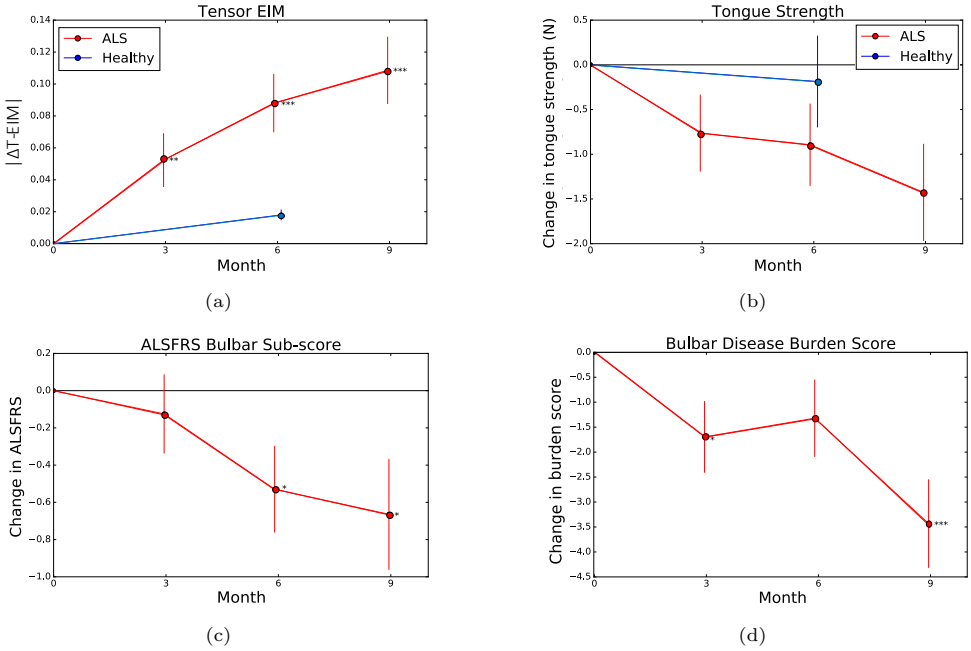

Figure 4.10: Linear mixed models showing the change in biomarker values with time. (a) Absolute change over time of tensor EIM (|ΔT-EIM|) in patients and healthy controls. (b) Change in tongue strength over time in patients and healthy controls. (c) Change in patient ALSFRS bulbar subscore. (d) Change in the patient bulbar disease burden score. The error bars represent one standard deviation and significant p-values are marked as * $p<0.05$, ** $p<0.01$, *** $p<0.001$.

It is clear that Δ T-EIM is detecting some disease changes, but the direction of these changes may be dependent on specific disease processes (for example, chronic versus acute changes, see discussion for details). In order to assess the overall sensitivity of tensor EIM for measuring disease progression, the absolute change in value from baseline (|Δ T-EIM|)was used in order to resolve the bidirectional change in spectral shape. Linear mixed modelling demonstrated

a significant change of tensor EIM over time, with greater than 1% significant change at 3 months, and greater than 0.1% significant change from 6 months onward (figure 4.10a).

Conversely, the other biomarkers; tongue strength, ALSFRS-R bulbar subscore and the overall bulbar disease burden score demonstrated more limited changes. Tongue strength is insignificant at all time points with large overlap with the healthy control group (figure 4.10b), the ALSFRS-R demonstrates a change within 5% significance from 6 months (figure 4.10c), and the bulbar disease burden score demonstrates a non-linear progression with a bigger change at the 3 month mark compared to 6 months, although does reach a highly significant change within 0.1% significance by 9 months (figure 4.10d).

	Effect Size	Sample size at 50% treatment effect	Sample size at 20% treatment effect
Tensor EIM	0.99	64	401
Median single frequency	0.48	274	1715
Range single frequency	0.28-0.85	87-802	545-5014
Bulbar Disease Burden Score	0.84	89	558
ALSFRS-R Bulbar subscore	0.46	298	1860
Tongue Strength	0.37	461	2881.

Table 4.7: Effect size and hypothetical clinical trial sample size estimation with 80% power and 0.05 significance level at 50% and 20% treatment effects. Calculated for tensor EIM; the median and range values for single frequency raw EIM data; bulbar disease burden score; ALSFRS-R; and tongue strength

To illustrate the potential of tensor EIM for the detection of bulbar disease, a hypothetical clinical trial sample size was calculated using 4.9 (table 4.7). Tensor EIM required the smallest sample size in comparison to other measures of symptoms. Trial size required when using raw data with a single frequency, as typically employed in EIM studies on ALS (Rutkove et al., 2012a; Shefner et al., 2018), has a large variation depending on the frequency and electrode configuration selected but the best performing single frequency did not surpass the performance of tensor EIM.

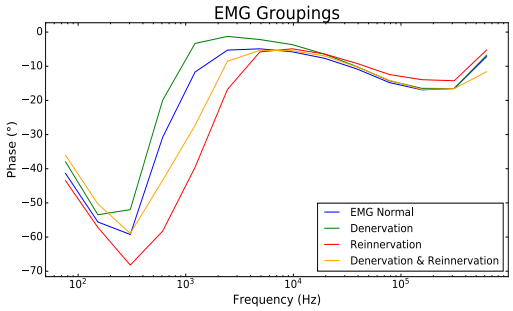

(a)

EMG finding	Number
Normal	6
Denervation	2
Reinnervation	3
Denervation & reinnervation	4

(b)

Figure 4.11: (a) Baseline median spectra median for 15 ALS patients with no clinical evidence of tongue atrophy. Patients are subdivided into those with normal tongue (genioglossus) EMG (blue), EMG evidence of acute denervation only (green), EMG findings of chronic denervation/reinnervation only (red), and both (yellow).

Since the spectral change with disease is multidimensional and complex, the potential effects of acute and chronic denervation were investigated. The baseline median spectra are presented for a subset of 15 ALS patients with no clinical signs of atrophy (clinical score=0, as in table 2.3) (figure 4.11). Such patients were chosen to try and minimise the persisting effects of chronic,

prominent disease. Using evidence from needle EMG of the genioglossus, these patients were split up into normal EMG; acute denervation; chronic denervation (or reinnervation); and both acute and chronic signs. Looking at the shift of the spectral shapes in comparison to normal EMG, it is clear that patients with signs of acute denervation presented a visual shift to the right (equivalent to an increase in the tensor EIM metric), while signs of reinnervation gave a visual shift the spectra to the left (equivalent to a decrease in the tensor EIM metric).

4.4 Discussion

The novel methodology outlined in this chapter has been proven to be a successful approach to analysing high-dimensional EIM data. The tensor EIM metric both separates patients from healthy participants and correlates well with clinical symptoms. Tensor EIM encapsulates all the information from the impedance dataset and captures the intrinsic symmetry of the impedance data, the compression ratio of 19:1 implies a high amount of redundancy and symmetry in the dataset. Hence, NTF can significantly reduce the dimensionality of the data without losing important information. Further, the capacity of NTF to deal with missing data makes it opportune for the use of analysis in clinical trials, where it is possible that some recordings will be unsuccessful.

While the classification performance of wrapper feature selection outperforms tensor EIM in the patient versus healthy classifier, it is important to consider the limitations of applying an exhaustive search feature selection on the dataset. These include it being a computationally expensive process and having a tendency for overfitting (Loughrey and Cunningham, 2005) or missing potentially insightful features. Despite using cross-validation to reduce overfitting, analysis of the features selected (see appendix, table C4.2) shows a large amount of inconsistency in the features, with most only appearing 25% of the time (i.e. in one of the four folds of the cross-validation). This suggests the feature selection is generally overfitting to each fold of the data and overall does not make a definitive decision on which features are best. Similarly, the selection of the best frequency for significance testing is also prone to overfitting, even when FDR correction is applied. By contrast, the tensor EIM process incorporates the information of the full dataset and consistently outperforms classification without the need for a feature selection process. In addition, unlike wrapper feature selection, tensor EIM is an unsupervised method, which identifies patterns in the dataset without bias.

The classification results that were presented at the end of chapter 2 (section 3.3.5, figure 3.9) also come from a wrapper based feature selection, so while it may appear that the potential for patient discrimination does not improve when using the tensor EIM framework, it is critical to understand that the methodology is much more robust and therefore likely to perform well on unseen data. It is possible to assess the performance of a wrapper selection approach on additional test data using nested cross-validation, where it is common to have two layers of cross-validation: one for the feature selection process and another for the evaluation of the classifier. While this would be interesting to assess, it is an unrealistic possibility here given the small sample size of the EIM dataset under analysis. Conducting an assessment on a potential future dataset to validate the performance of the wrapper selected features and classification model would be a valuable endeavour. Such an approach would facilitate a thorough comparison of the performance between feature selection and data factorised through the tensor EIM procedure while mitigating the potential effects of overfitting.

This analysis considers a high-dimensional EIM dataset over a broader range of frequencies than most previous limb studies (Rutkove et al., 2007, 2017; Schwartz et al., 2015). In the case of limb impedance recordings low frequency measurements can be unreliable and corrupted by artefacts since keratinised skin causes measurement errors below 10 kHz. However, on mucosal

surfaces such as the tongue, where there is limited keratinisation, low frequency impedance assessment has been implemented successfully (Murdoch et al., 2014; Sun et al., 2010; Ching et al., 2010; Lackovic and Stare, 2007). The use of low and high frequency EIM data in tandem has advantages such as capturing information on the sizes of both the intra-cellular and extra-cellular fluid spaces (Dittmar, 2003). The analysis has been repeated on a truncated frequency range using data $\geq$305 Hz, which successfully demonstrated that the low frequency data are reliable and do not dominate or skew results. Comparison of the performances between using the full frequency range and the truncated range (appendix, figures C5.1 and C5.1) suggests a small improvement when including the lowest frequencies. This could be tested on a larger patient cohort for validation, in order to make a full assessment of the additional value of including the low frequency data. In addition to the effects on performance, using a larger range of frequency inputs provides more information to improve the accuracy of lumped circuit models.

One considerable benefit to this type of analysis is the improved interpretability since the procedure details the contributions of different spectral shapes across the cohort, which can be fed into lumped circuit models. The consistent trend when moving from healthy to diseased spectra was identified as a shift in the centre frequency to the right, an increase in magnitude at low frequencies and a smaller phase at high frequencies. Using lumped circuit modelling these spectral changes are consistent with the histological changes associated with muscle atrophy and denervation. These include an increase in extracellular resistance due to remodelling of the extracellular space with connective tissue and fat (Jenkins et al., 2018), a reduction in membrane capacitance due to muscle cell atrophy (Al-Sarraj et al., 2014), and a smaller decrease in intracellular resistance due to increased cell membrane permeability and intracellular ionic content (Cisterna et al., 2020).

In ALS bulbar disease, a mixture of clinical signs related to both upper and lower motor neurone loss are typically seen (Tomik and Guiloff, 2008). At present, there are only a few studies which examine EIM changes in upper motor neurone conditions. EIM assessment in stroke patients demonstrates a reduction in phase at 50 kHz (Li et al., 2017b) and 100 kHz (Hu et al., 2019), this is in agreement with changes observed in ALS (Rutkove et al., 2007). Further, studies of stroke related skeletal muscle changes report myofibre atrophy, which includes a reduction in muscle area and volume, decreasing bilateral muscle fibre size and a reduction in the number of motor units (Sions et al., 2012; Hafer-Macko et al., 2008; Dalise et al., 2020). Additionally, fibre type changes are identified; with the number of type II fibres progressively decreasing (Sions et al., 2012; Hafer-Macko et al., 2008). This suggests that perhaps both upper and lower motor neurone degeneration cause similar changes to a patient's EIM, however further work is needed to assess these changes in the multi-frequency EIM spectral pattern.

When assessing the correlation of our impedance metrics with the overall symptom score it must be appreciated that current biomarkers for disease are subjective and lacking in sensitivity (Rutkove, 2015). So, while a perfect correlation is not expected, the optimal correlation found with tensor EIM is promising. When comparing the correlations with the overall symptom score (figure 4.4b) to the correlations with the ALSFRS-R bulbar subscore (table 4.4), it is clear that the overall bulbar disease burden score generally correlates better. Combining all known symptom information into one score should arrive at a more holistic appreciation of the disease state; the better correlation of EIM features with such a score offers encouragement that these are capturing a more complete representation of the disease state.

Moving on to consider tensor EIM as a measure for capturing ALS-related disease changes, it is clear that spectral shifts are complex in nature and vary in direction. Assessing longitudinal EIM data at the level of the whole spectrum, a complex and varied pattern of changes was observed. The overall spectral shift to the right (or increase in centre frequency) over time is

consistent with the progressive changes reported in mouse models of ALS (Li et al., 2016b, 2012), as well as in tongue and limb recordings from human patients (Mcilduff et al., 2017; Pacheck et al., 2016; Jafarpoor et al., 2011). Furthermore, transient spectral shifts in the opposite direction were observed, which is in keeping with work in animal models demonstrating that acute denervation can transiently shift impedance spectra in this fashion (Westgaard, 1975).

I have demonstrated for the first time in human ALS patients that the direction of spectral shift is complex and varied but we can only speculate as to what underpins this. Acute denervation results in extracellular oedema (Kamath et al., 2008; Carlson, 2014), which would act to reduce extracellular resistance and in turn shift spectral profiles to the left. Histological studies of muscle in ALS report myocyte hypertrophy (Jensen et al., 2016), which could, at least in theory, increase capacitance and also cause this spectral change. In contrast, authors of previous studies have attributed EIM changes in chronic settings to progressive myofibre atrophy (acting to reduce the overall tissue capacitance) and extracellular space remodelling (which would increase extracellular resistance). The circuit modelling based on dominant spectral patterns found changes in extracellular resistance and membrane capacitance, which is in agreement with these suggestions. It is therefore possible to hypothesise that the transient shift of spectra to the left relates to crescendos of denervation, while movement right represents the progression of chronic denervation-related changes. A preliminary stratification of EIM spectra by EMG findings promisingly matches with these, although the sample size is small. It is also necessary to take into account the limitations of these observations, including the fact that EMG was assessed in the genioglossus, while EIM was performed on the tongue blade. Additionally, tongue EMG is fraught with technical difficulties, including the small sampling area and difficulties in achieving muscle relaxation for spontaneous activity assessment. Further work relating EIM spectral patterns to EMG findings in other muscles may provide a better platform for testing this hypothesis.

An objective biomarker of bulbar disease would enhance ALS clinical trial design (Yunusova et al., 2019). The ability of tensor EIM to capture changes at the level of the whole EIM spectrum, across multiple electrode configurations and device placements likely underpins the reduced sample size requirements in the hypothetical clinical trial shown here. Previous studies on limb muscles utilising more limited spectral features have also shown that EIM assessment of limb muscles can capture disease progression and reduce sample size, perhaps due to the sensitivity of EIM to the effects of both acute denervation and chronic denervation (**?**). In the present work, possibly owing to the complex muscle fibre arrangement in the tongue, I have shown that tensor EIM can provide further improvements, with a sample size around four times smaller than that of the average single frequency. Even an exhaustive search for the best performing frequency does not perform as well as the tensor EIM method. This exhaustive search likely overfits the dataset (i.e. risks a type II error, where we fail to report a significant result due to noise and overemphasis on the wrong information).

4.5 Conclusions: biomarker potential of EIM in the tongue

Throughout the past three chapters, I have demonstrated that surface EIM of the tongue has significant potential as an effective biomarker in neurological diseases such as ALS. Data collected from a novel EIM tongue probe was found to be highly reproducible and provide information that distinguishes patients from healthy muscle and correlates well with the overall bulbar disease burden severity. Specifically, the integration of multi-frequency spectra obtained from 3D electrode configurations and multiple locations on the tongue appeared to provide the most comprehensive understanding of the disease. A detailed FEM model of the tongue was built, which captured the intricate characteristics of the anisotropic and non-homogeneous

nature of this complex muscle. By employing an optimisation procedure, model parameters were refined and impressive agreement was achieved with the multidimensional spectral patterns associated with healthy participants, ALS patients with moderate disease, and ALS patients with severe disease. Assessment of these parameters, with the aid of lumped circuit modelling, found that worsening disease can be attributed to an increase in intracellular resistance and a decrease in capacitance (associated with the cell membranes), which is in agreement with the known pathophysiological alterations in muscle structure caused by atrophy.

In addition, the FEM model offered validation for the use of data recorded from the lateral edges of the tongue. Insight from these lateral measurements was able to identify a lack of asymmetry present in bulbar ALS, due to negligible variation between spectra recorded from the left and right sides in patients of all levels of disease severity. Additionally, the combination of data recorded from both the lateral edge and central midline of the tongue appears to generally enhance the potential of EIM data to both identify patients as well as give prognostic evidence of disease severity. While the data observed on the left and right sides appear identical, interestingly the central and lateral regions of the tongue seemed to provide independent disease specific information, where incorporating both datasets improved performance. This suggests that it may be necessary to acquire recordings from multiple sites in order to capture the full details of the heterogeneous and complex structure of the tongue. When looking to a direct comparison of the performance of lateral versus central data, the performance of lateral measurements is generally superior. Overall, it will be important to further investigate the combined performance and discrepancies between central and lateral data in a larger cohort of patients.

Tensor EIM is a novel methodology, which has been designed to reduce high-dimensional EIM data down to a single score. This tensor EIM metric has a direct physical interpretation, where changes in the value can be attributed to specific directional shifts of the spectral patterns. When applied to the tongue EIM dataset, the procedure identifies the common spectral shapes in the healthy cohort and in patients, which allows the key spectral characteristics of disease to be determined. The approach has many benefits including reduced likelihood of overfitting, the ability to deal with missing data and physically interpretable outputs. I have shown that the features output from tensor EIM can yield high performance in disease classification and show a significant correlation with disease severity. Tensor EIM is also capable of capturing the complex spectral fingerprint of ALS disease progression in the tongue. Spectral change is described by a single tensor EIM metric, which can provide a simple measure for longitudinal studies. The overall trend of change with time is consistent with the spectral pattern associated with disease severity, however, individual short-term changes are complex and multi-directional, likely due to the complex nature of acute and chronic changes that affect the muscle at different stages of the disease. This approach enhances the potential of EIM as a biomarker in ALS, improving the capability for accurate diagnostic and prognostic measures, as well as improving the monitoring of disease progression in clinical trials. Future work to validate the association between changes in the tensor EIM metric with the effects of both acute and chronic denervation would be invaluable for increasing the biomarker potential of bulbar EIM.

5 Chapter 5: A first assessment of the high-dimensional limb EIM dataset

5.1 Introduction

A second EIM dataset was collected over the duration of this doctoral project. In this study, a newly developed novel EIM limb device was utilised, and multi-dimensional measurements were recorded from eight limb muscles in healthy participants, ALS patients and mimic/non-MND patients. The remainder of the thesis will focus on the analyses of this data.

This chapter commences with the introduction of the limb dataset. This includes a detailed description of the data collection methods, an outline of the additional disease specific data that were collected, and information regarding the characteristics and composition of the study cohort. The limb measurement set is much higher in dimension than previous studies, with recordings made over a large range of frequencies and multiple 2D and 3D electrode configurations. Initial analyses were undertaken to assess the validity of the EIM limb device outputs, including an assessment of a valid frequency range for the recordings taken on the surface of keratinised skin. Further to this, systematic calibration work was undertaken to evaluate the efficacy of a range of electrode configurations, which pertained to measurements in multiple directions through different volumes of the limb tissue. Finally, reproducibility analyses were made to assess the reliability of the limb EIM measurements.

The subcutaneous fat layer has previously been found to significantly contribute to EIM data measured in the limbs at a frequency of 50 kHz, for measurements made in both the longitudinal and transverse directions across the muscle (Sung et al., 2013; Li et al., 2016b). Some arguments have been made for the use of either reactance (Sung et al., 2013), or a two-frequency phase ratio in reducing this contribution (Schwartz et al., 2015; Li et al., 2016b; Rutkove et al., 2017). To explore this further, a thorough analysis of the correlation between the skin-subcutaneous fat thickness (S-SFT) and all features within the high-dimensional EIM dataset was undertaken. Furthermore, an evaluation was conducted to examine the possible influence of disease severity on the thickness of the SFL. Subsequently, the biomarker capability of the EIM data was evaluated, taking into account the potential impact of the SFL.

5.2 Methods

5.2.1 EIM data collection

The impedance measurements were recorded using a custom-made limb bioimpedance device developed by the Department of Clinical Engineering at Sheffield Teaching Hospitals NHS Foundation Trust (Healey et al., 2021). Like the tongue EIM system, this novel limb device also allows for measurements in both 2D and 3D electrode configurations. The device features an upper and lower electrode plate, each with eight, 7 mm diameter gold electrodes in a rectangular geometry (see figure 5.1). The device was gently placed onto the subject's limb, and secured using the clamping mechanism of the device to maintain good electrode-skin contact in order to minimise measurement artefacts. The separation between the two plates (z) can be varied to fit the size of the limb under measurement. Two devices were designed, one specifically for smaller muscles in the upper limbs, and one for larger muscles in the lower limbs. In reality, different devices were used for different muscles between participants depending on the size of their limbs. The range of plate separation is different for each device (figure 5.1b), however, the electrode plates used are geometrically identical.

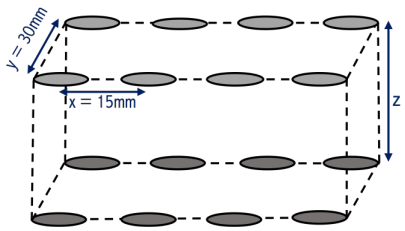

(a)

Device	z range
Upper limb	35-90 mm
Lower limb	60-115 mm

(b)

Figure 5.1: Novel limb bioimpedance probe. The electrodes in each plate are separated by 15mm in the longitudinal, x-direction and 30mm in the transverse, y-direction. The separation of the two plates, z, can be varied in 5mm increments from 35-90mm in the upper limb device and 60-115mm in the lower limb device.

The EIM spectra are measured across 18 different electrode configurations, this includes five 2D configurations on both the upper and lower plate, as well as eight 3D configurations with electrodes on both plates employed for the measurement. These electrode arrangements are presented in figure 5.2. The five, 2D configurations consist of recordings made parallel to the fibres ($2Da_{1/2}$, 2Db), transverse to the fibres (2Dc) and diagonally across the fibres (2Dd). $2Da_1$ and $2Da_2$ are geometrically equivalent arrangements and comprise all electrodes in parallel. Specifically, with the current injected longitudinally on the inner electrode pair and the voltage measured on the outer electrode pair. This is analogous to the configurations employed in a number of previous EIM studies (Rutkove, 2009; Schwartz et al., 2015; Li et al., 2016b; Rutkove et al., 2016, 2017). On the other hand, configurations 2Db, 2Dc, and 2Dd, are more novel and such electrode arrangements have not been presented in previous literature.

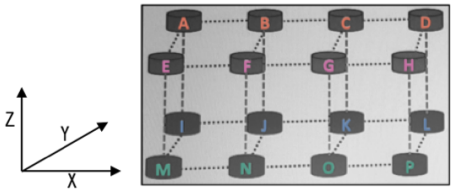

Configuration	Current in	Current out	Voltage +	Voltage -
2Da_1(U)	B	C	D	A
2Da_1(L)	J	K	L	I
2Da_2(U)	E	H	G	F
2Da_2(L)	M	P	O	N
2Db(U)	A	D	H	E
2Db(L)	I	L	P	M
2Dc(U)	A	E	H	D
2Dc(L)	I	M	P	L
2Dd(U)	A	F	H	C
2Dd(L)	I	N	P	L

Configuration	Current in	Current out	Voltage +	Voltage -
3Da_1	A	I	M	E
3Da_2	D	L	P	H
3Db_1	A	I	K	C
3Db_2	E	M	O	G
3Dc	G	O	I	A
3Dd	A	M	N	B
3De	A	N	O	B
3Df	A	H	P	I

Figure 5.2: Electrode configurations employed in the limb EIM measurements. The device was oriented so that the x and y directions were aligned longitudinally and transversely to the muscle fibres, respectively. There are five 2D electrode configurations, which are recorded on both the upper plate (U) and lower plate (L). There are eight 3D electrode configurations, however, there are two pairs ($3Da_{1/2}$ and $3Db_{1/2}$), which are geometrically identical but utilise electrodes which are shifted in the longitudinal/transverse direction and hence record through a different volume of tissue.

Additionally, 3D configurations have never before been applied to limb EIM measurements. These arrangements inject current vertically through the tissue, which is directly perpendicular to the electrode plates (3Da-3Dc) or diagonally through the tissue (3Dd, 3De). The final configuration, 3Df, injects the current on the upper plate and evaluates the voltage on the lower plate.

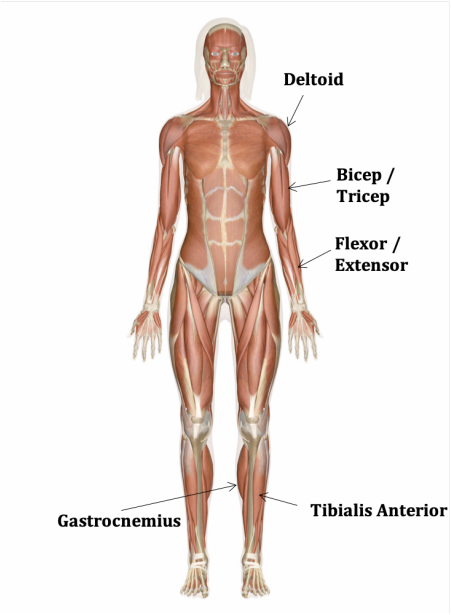

(a)

Placement	Upper plate	Lower plate
Upper arm	biceps	triceps
Forearms	extensors	flexors
Shoulder	anterior deltoid	posterior deltoid
Leg 1	lateral gastrocnemius	medial gastrocnemius
Leg 2	tibialis anterior	lateral gastrocnemius

(b)

Figure 5.3: The limb EIM device was recorded over five different placements on the body, incorporating eight different muscles. (a) Shows a diagram of different muscles that were investigated. (b) Gives the breakdown of each of the five placement sites, and the corresponding muscles that were recorded on using the upper and lower electrode plates.

EIM was recorded from five different placement sites on the body (figure 5.3). For each site, the device was placed so that the the long axis of the probe was aligned with the long axis of the muscle, with the upper and lower electrode plates oriented over the two muscles of interest (or a different aspect of the same muscle). Therefore, by investigating the 2D configurations each muscle can be assessed in turn, while the 3D configurations will produce impedance that is a superposition of tissue from both muscles. Overall, eight muscles are investigated: biceps, triceps, forearm flexors, forearm extensors, deltoid, lateral and medial gastrocnemius (commonly abbreviated as 'gastroc'), and the tibialis anterior (TA). Due to its size, the deltoid muscle was recorded on both the anterior and posterior sides. Recordings were taken on both the left and right sides of the body for all placements, giving a total of 10 placement sites per participant. Each measurement was repeated for 2 repeat trials in order for reproducibility to be assessed.

The limb device was programmed to measure on the same spectrum of 14 frequencies employed in the tongue study (76 Hz - 625 kHz). However, significant artefacts were expected to appear at lower frequencies ($< 6 - 10$ kHz) in surface impedance recorded on keratinised skin (Martisnen et al., 1997). Compared to the mucosal surface of the tongue, keratinised skin is thicker, rougher and less elastic resulting in uneven and poorer electrode contact, and hence increased chance of artefacts. To improve the quality of the recordings, each subject underwent

skin preparation prior to measurement. This involved exfoliating the skin with a standard skin preparation paste and wetting the skin with saline, which improves the electrode-skin contact. The data were assessed for artefacts, such as negative resistance values, in order to determine the viable range of frequencies that can be included in the analysis.

5.2.2 Additional data collection

Alongside the EIM measurements, numerous other data were measured in the participant cohort. The S-SFT thickness was measured using ultrasound with the Clarius L7 device. The ultrasound probe was placed over the belly of the muscle with the limb in a relaxed posture. With the probe orientated in the longitudinal plane of the muscle its parallel, fascicular structure could be appreciated and the superficial fascia visualised. Subcutaneous fat was apparent by its loculated nature, as the fat is hypoechoic and interspersed septations of connective tissue. The S-SFT was measured from the skin to the outside edge of the superficial fascial layer. The distance from the skin surface to the muscle was then determined through visual assessment of the image (see example in figure 5.4). This provided critical information to be included in the analysis since it is evident from previous works that the layer of subcutaneous fat can have a substantial impact on the surface impedance measurement (Jafarpoor et al., 2013; Sung et al., 2013; Schwartz et al., 2015; Li et al., 2016b; Rutkove et al., 2017). Gender is expected to have a significant effect on the S-SFT, while the impact of disease (if any) is unknown.

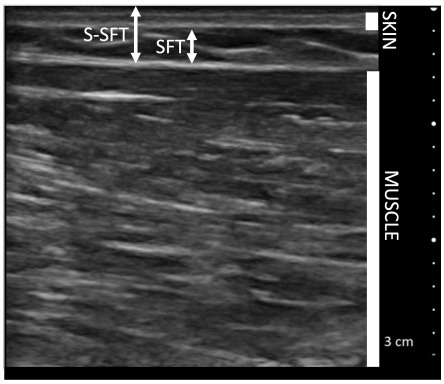

Figure 5.4: Ultrasound image of a limb showing the layers of skin, fat, and muscle. The thickness of the subcutaneous fat (SFT) and the skin-subcutaneous fat layer (S-SFT) are labelled.

Evaluation of muscle strength was performed using HHD (hand-held dynamometry). The strength assessments were conducted for the participants in a seated position for upper limb muscles and in a supine position for lower limb muscles. A standardised starting position, approximately midway between muscle flexion and extension, was employed for each muscle being tested. The HHD device was carefully positioned along the limb, and participants were instructed to gradually increase the force applied against the device. The maximum force reached during exertion, measured in newtons, was recorded. A single trial was conducted for all muscles on each side of the body. This was repeated if the examiner/participant felt that sub-maximal effort was captured.

For the ALS cohort, the ALSFRS-R was recorded. The full score is out of 48 but this incorporates bulbar and respiratory function, which are not directly related to degeneration within the limbs. For a more comprehensive comparison, the ALFRS-R is split into a limb, upper limb, and lower limb subscore. These are scored out of 24, 8, and 8 respectively, where

the categorisations are given in table 5.1

Subscore	Categories	Total score
Limb	Handwriting, cutting food, dressing/hygiene, turning in bed, walking, climbing stairs	24
Upper Limb	Handwriting, cutting food	8
Lower Limb	Walking, climbing stairs	8

Table 5.1: The categories used to calculate the ALSFRS-R subscores for assessing the functionality of the overall limbs, the upper limbs, and the lower limbs.

Finally, in all patients (ALS and non-MND) a comprehensive evaluation of each muscle was performed using needle EMG, where the motor unit potentials (MUPs) were assessed by an experienced clinician. Each muscle was categorised as having normal or abnormal MUPs, additionally, the abnormal EMG were categorised into myopathic and neurogenic muscle. Myopathy was defined as an EMG signal with low amplitude, short duration and polyphasic MUPs. While neurogenic muscle was determined by MUPs with increased duration and sometimes polyphasia.

5.2.3 Study cohort

The limb study data collection was undertaken between January 2021 and February 2023. Informed consent was obtained and the study was approved by Wales Research Ethics Committee 5 Bangor (reference 19/WA/0101). In total 98 participants were recruited for the study. This cohort was made up of 23 healthy participants and 75 patients, which included 28 ALS, 3 non-ALS MND, and 44 non-MND (table 5.2). The ALS group comprised 20 patients (71.4%) with limb onset disease, 5 patients (17.9%) with bulbar onset, 2 patients (7.1%) with respiratory onset and a final patient (3.6%) who had a genetic mutation known to cause the disease but who was asymptomatic at the time of testing.

MND

Diagnosis		Number
ALS	Limb onset	20
	Bulbar onset	5
	Respiratory onset	2
	Asymptomatic	1
PLS		2
PMA		1
Total		31

non-MND

Diagnosis		Number
Myopathy		9
Neuropathy	axonal	4
	demyelinating	3
	focal*	2
Benign cramp fasciculations (BCFS)		4
Spinal Condition**		12
	+ BCFS	3
	+ Parkinsons	1
Musculoskeletal		1
Idiopathic spastic paraparesis		1
Non-compressive myelopathy		1
Functional neurological disorder		1
Palatal myoclonus		1
Uncertain		1
Total		44

*sciatic and common peroneal

** including myeloradiculopathy and radiculopathy

Table 5.2: Break down of the patient diagnoses for the MND and non-MND subgroups.

The median total ALSFRS-R value is 39 (range: 26-48), and the median ALSFRS-R limb subscore is 19 (4-24). The non-MND group comprise a wide range of neurological diagnoses,

some of these are considered typical ALS mimics (myopathy, neuropathy, BCFS and some spinal conditions), while the remainder are more general neurological conditions.

Demographics of the participant cohort are presented in table 5.3. The three subgroups, healthy, MND and non-MND, were all age and gender matched, with non significant p-values shown between the three group pairings. Additionally, the duration of symptoms at the time of study is presented for the two patient groups. Here there was a significant difference between MND and non-MND, with the latter seeing generally longer duration of symptoms.

Measurement	Healthy N=23	MND N=31	non-MND N=44	P-value Healthy/MND	Healthy/non-MND	MND/non-MND
Mean age in years (range)	60 (46-85)	62 (40-83)	59 (30-80)	p=0.68	p=0.59	p = 0.31
Male: Female, n %	13:10 57:43	17:14 55:45	27:17 61:59	p=1.0	p=0.80	p=0.64
Mean symptom duration in months (range)		13.9 (2-60)	22.1 (3-72)			p=0.02

Table 5.3: Demographics of the participant cohort for each sub-group, including mean and range of age, the ratio of male to female, and the mean and range in symptom duration for the patient groups. A statistical t-test applied to age identified no statistical difference between each of the group pairings. A Fisher's test applied to the gender splitting identified no statistical difference between each of the group pairings. A t-test applied to the symptom duration in the MND and non-MND patient groups found a statistically significant (p=0.02) difference.

In addition, the difference between ALS and the non-MND group for muscle strength and EMG signs are presented in figure 5.5. The ALS group generally presented with weaker muscles. The data presented a significant difference between ALS and non-MND in all muscles but the gastrocnemius. Additionally, the ALS group saw a much larger percentage of limbs with abnormal EMG signs, indicative of a more prominent disease.

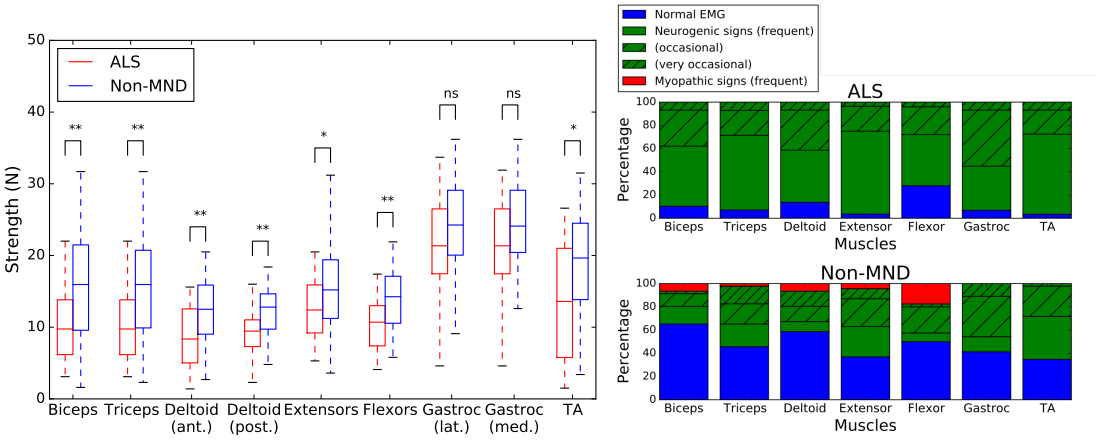

(a) (b)

Figure 5.5: (a) Boxplots showing muscle strength compared between the ALS and non-MND groups. Any significant differences in the groups are shown(FDR correct p-value < 0.05 *, < 0.01**) (b) The percentage split of EMG signs in each muscle for the ALS and non-MND groups. Blue shows normal EMG, and green shows neurogenic signs, where hatches signify if these signs were occasional or very occasional. Finally, red shows myopathic signs.

Overall, it is clear that in general, the ALS participants were presenting with more severe

symptoms in comparison to the non-MND group. This is representative of the rapid disease progression often seen in ALS, where despite having a generally shorter duration of disease progression the symptoms have progressed much faster. Overall, this is important to take into account when looking at comparisons of data between these two groups. Looking to the distribution of EMG signs, it is also clear that neurogenic signs were the least common occurrence, with only a small proportion present in the arm muscles of the non-MND group.

5.2.4 Device calibration

Initially, before calibrating the individual electrode configurations, a calibration of the hardware to correct for internal instrumentation error was determined. The purpose of this calibration was to characterise and correct any systematic errors or inconsistencies introduced by the instrumentation itself, such as amplifier gain variations, cable impedance, or other hardware-related factors. To complete this calibration, any test circuit can be used whose transfer impedance may be easily derived. Here the test circuit shown in figure 5.6a was employed, where the electrodes for current injection are connected at points A and C, while the voltage reading electrodes are connected at B and D. With this arrangement of resistors the expected transfer impedance is $Z_t = 666.\dot{6}\Omega$ (derived in appendix, B). Note that the 10 kΩ resistors, R5 and R6, simulate electrode impedances and they do not have an impact on the overall transfer impedance of the circuit. Any deviation from the expected transfer impedance recorded by the limb device indicates an instrumentation error. The calibration factor, F is defined as the correction relating the recorded impedance across the test circuit, Z_c, to the expected transfer impedance, Z_t:

$$Z_\mathrm{c}(f) = F(f) \cdot Z_t(f) \tag{5.1}$$

where all of the terms depend on the frequency, f. For the case of the test circuit chosen here, the calibration factor becomes:

$$F(f) = \frac{Z_\mathrm{c}(f)}{666.\dot{6}} \tag{5.2}$$

F must be calculated for each frequency, f, and is a complex number with real and imaginary parts. To determine a hardware correction for the instrumentation error, the corrected impedance, $Z_\mathrm{corrected}$ was determined from the measured impedance, Z_measured, simply as:

$$Z_\mathrm{corrected}(f) = \frac{Z_\mathrm{measured}(f)}{F(f)} \quad . \tag{5.3}$$

In order to calibrate the 2D configurations in the limb device, the top plate of the device was placed in a saline bath, so that the electrodes are just submerged in the solution. These saline solutions were prepared by combining water and sodium chloride, and the resulting conductivity was measured using an Orion Star™A322 conductivity meter. A titration method was used for solution preparation, where the experiment was repeated for a number of different concentrations of salt in a physiologically sensible range (0.1-2 S/m, agrees with biological tissue conductivities presented in Gabriel et al. (1996a,b)). The same method for determining cell constant as in section 2.2.2, was employed utilising the following equation:

$$K = \sigma \frac{R^2 + X^2}{R} \tag{5.4}$$

For calibration of the 3D configurations, a saline jelly was used, since both the upper and lower electrode plates need to be in contact for the recording. This was made by mixing up a saline solution in the above method, following which the solution was combined with gelatin

and poured into a mould to allow it to set (figure 5.6b). Although the conductivity of the liquid saline and gelatin can be measured with the conductivity meter, conductivity changes with temperature and the jelly clearly cools as it sets. Therefore, initially, the conductivity of the jelly was determined using the 2D electrode configurations using our predetermined knowledge of the 2D cell constants. Following this, the 3D configurations were measured and the cell constants for each were determined using equation 5.4 as above, again repeating the process for multiple levels of conductivity. Additionally, for 3D recordings, the cell constant, K, is dependent on the separation of the electrode plates. Therefore the jelly was sliced into different thicknesses, so recordings could be made to determine K at all separation distances, 30-115mm, in 5mm increments.

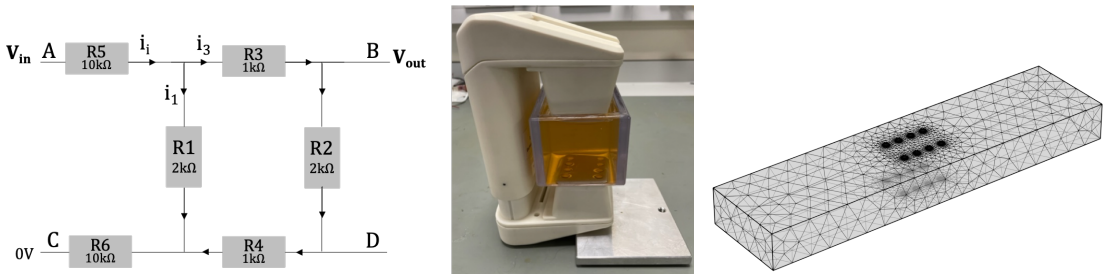

(a) (b) (c)

Figure 5.6: (a) Circuit used to measure the EIM device instrumentation error, incorporating 6 resistors with resistance 1, 2 or 10 kΩ. Current is connected across A-C and voltage is connected across B-D. Resistors R5 and R6 represent electrode impedances and do not affect the transfer impedance. The transfer impedance of this circuit is 666.6̇Ω (derived in appendix B). (b) Saline jelly used for the calibration of the 3D configurations. (c) FEM of limb EIM device recording in a saline bath.

To ascertain the validity of the computed cell constants, the values were compared to FEM generated data. Using Comsol, an FEM model of the limb EIM device was built, to take measurements on an isotropic and homogeneous material of constant conductivity, which mimics the saline bath/jelly (figure 5.6c). Using this model the relationship between the model transfer impedance and the input conductivity was used to determine the expected values of the cell constant for each configuration. In the model, the vertical plate separation was varied to determine the expected relationship between the cell constant and the separation. Some uncertainty was incorporated into the model, by varying the input conductivity by ±0.1 S/m and varying the electrode separation values by ±1 mm.

5.3 Results

5.3.1 Low frequency artefact assessment

As it was hypothesised that artefacts will occur in low impedance measurements on keratinised skin, the dataset was assessed to determine at which frequency the data starts to be free of significant artefacts. One obvious indicator of erroneous data is a negative output in the impedance resistance. Figure 5.7a presents the proportion of erroneous negative real data that was output from recordings at all frequencies in the full spectral range of 76 Hz - 625 kHz. Clearly, there are significant artefacts apparent at the lower frequency end. The first 7 frequencies, which range from 76 Hz to 4.88 kHz, show much larger proportions of negative data making up more than 5% of the data, and up to 45 % at a frequency of 610 Hz. The largest 7 frequencies (9.77-625 kHz) see much smaller proportions ($< 2.5\%$) and therefore appear to be

predominantly artefact free. From this assessment, it was decided that the first 7 frequencies of the spectra would be removed from the EIM dataset as they contain unreliable erroneous data. The analysis on the limb EIM dataset will focus on the spectra of 7 frequencies starting at 9.8 kHz.

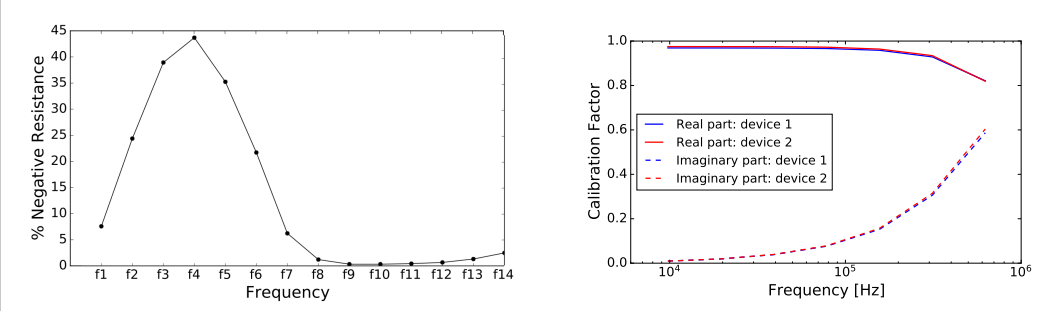

(a) (b)

Figure 5.7: (a) The proportion of data where resistance was negative for the full spectrum of 14 frequencies. (b) The complex calibration factor, F, as a function of frequency. Presented for the lower limb device (device 1, blue), and the upper limb device (device 2, red).

5.3.2 Configuration calibration and assessment

Firstly the calibration factor, F, was determined to account for internal instrumentation based errors. This was calculated for both the upper and lower limb devices separately. Figure 5.7b shows the real and imaginary components of F against frequency for both the upper and lower limb devices. There is very minimal discrepancy between the two devices, which indicates that the systematic errors are inherent to the instrumentation and not specific to one particular unit. From this, it was clear that the errors in the measurements were due to the hardware design itself. At the low frequencies the error was minimal with the calibration factor close to 1 in the real part and close to 0 in the imaginary part, while for increasing frequency this error begins to deviate significantly. Thus, applying the hardware calibration to the dataset was clearly an essential step to ensure accurate and reliable measurements.

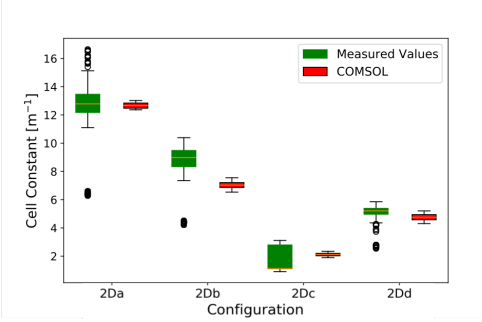

	Measured (IQR)	Comsol (error range)
2Da	12.8 (12.2-13.4)	12.7 (12.4-13.0)
2Db	8.9 (8.3-9.4)	7.0 (6.5-7.6)
2Dc	1.1 (1.2-2.8)	2.1 (1.9-2.3)
2Dd	5.2 (5.0-5.4)	4.8 (4.3-5.2)

Figure 5.8: Cell constants calculated for the four interdependent 2D electrode configurations. Measured values are determined using recordings in a saline bath with conductivity varied between 0.1 and 2 S/m. These measurements are validated with simulated data in Comsol.

Following the application of the calibration factor to all EIM recordings made with the device, the cell constants for the 2D configurations were determined and demonstrated suit-

able agreement with the Comsol FEM values (figure 5.8). The calculated cell constant values obtained from saline measurements exhibit a range, primarily due to various potential sources of random error. These sources include temperature fluctuations, potential impurities in the saline, and poor electrode-saline contact (i.e. air bubbles can form on the surface of the electrodes). Despite this, the fact that there is a suitable overlap between the measurement data and the FEM computed values suggests that the device instrumentation is successfully recording impedance data free of artefacts in the 2D configurations across a range of conductivity values. To calibrate the EIM dataset, the cell constants generated by Comsol are utilised, due to the FEM's inherent immunity to measurement error.

Additionally, figure 5.9 shows the cell constants determined for the six independent 3D configurations as a function of the plate separation. Here there is significantly less agreement between the values measured using the saline jelly compared with the FEM simulation. The first three 3D configurations (3Da-c) are arrangements of electrodes, which both inject current and read the voltage, directly through the medium perpendicular to the electrode plates (see figure 5.2). These configurations demonstrate minimal overlap with the model, and the deviation is more pronounced for jelly with larger thicknesses and smaller conductivity. This suggests that perhaps there is an inadequate signal of current for such measurements, and therefore measurement artefacts dominate.

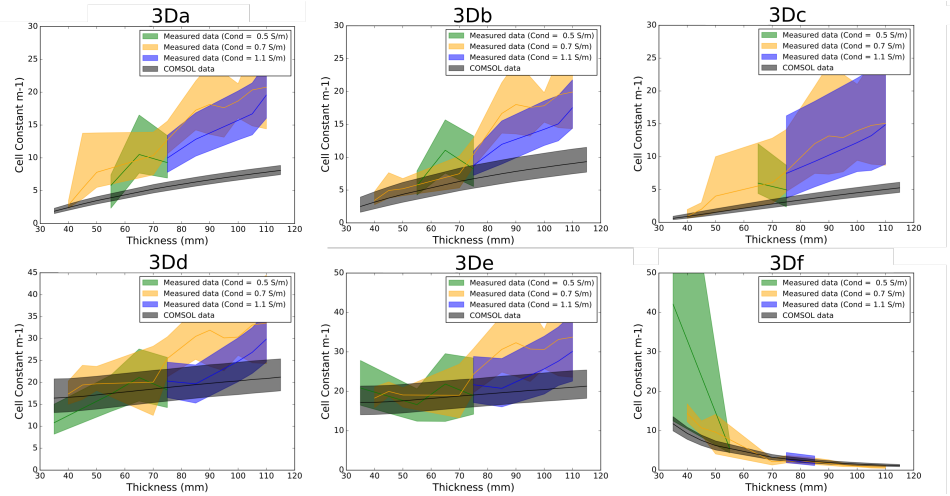

Figure 5.9: Cell constant determined as a function of the plate separation thickness. Shown for measured values using saline jelly of 0.5, 0.7 and 1.1 S/m, as well as for the FEM data generated using Comsol.

The next configurations 3Dd and 3De, inject current through the medium, but at an acute angle to the electrode plates (see figure 5.2). These give better agreement where significant overlap between measurements and the FEM data is seen at thicknesses up to approximately 70 mm. However, at larger plate separation more pronounced deviations begin to appear, which are again more amplified for the lower conductivity jelly. Configuration 3Df has a unique electrode setup, where the current injection and voltage measurement are undertaken with electrode pairs on opposite electrode plates. Therefore in a manner that resembles 2D configurations, the current is injected across the surface of the medium rather than directly through it (see figure 5.2). Interestingly, the agreement between the measurements and the model was best with this final configuration, where it was actually optimal for larger plate separations, > 70mm. Although larger deviations did arise at smaller separation for small conductivity ($\sigma = 0.5$ s/m).

Overall, the poor agreement between the measured and modelled data is concerning for the viability and reliability of the 3D configuration measurements in the limb device. Particularly as the electrical conductivity of biological tissue is generally small, where the muscle is expected to be in the range of 0.3-0.7 S/m, while skin and fat could be expected to see conductivity below 0.1 S/m. These findings suggest the presence of instrumentation issues that need to be addressed before relying on such 3D measurements for accurate analysis. For this reason, this project has focused analyses on the 2D configuration data.

5.3.3 Outlier removal

The dataset has been narrowed down to the subsection of 7 frequencies >9 kHz and the four independent 2D configurations. It is then necessary, for the same reasons as for tongue EIM, to consider outlier removal in order to identify and remove erroneous spectra from the dataset caused by measurement error. Here an analogous method is utilised, where first any spectra with a negative real part are removed. Secondly, spectra with a positive phase value at the highest frequency (625 kHz) were also removed, as this is not a characteristic feature of surface impedance measurements in the limbs, therefore such information indicates an unusual or erroneous response. Finally, a similar root-mean-squared deviation based outlier detection algorithm was applied to detect any remaining outlier spectra (see appendix A).

This varied slightly from the tongue EIM detection algorithm. Firstly, in the limb data, there was a less immediately obvious discrepancy between the spectral shapes of healthy and diseased participants. So for this reason the deviation of each spectra was calculated with respect to the overall data median shape without any issue with an overestimation in the proportion of data being removed within the severe patient cohort. Additionally, as previously discussed, the SFT has a significant effect on the EIM data, therefore as well as the algorithm being applied in turn to each independent electrode configuration, the data was also split up into different levels of S-SFT. Specifically, it was split in increments of 5mm ranging from 0 to 25 mm, which covered the full range of the dataset. The algorithm was then applied to each increment of data in turn.

Cohort	Negative resistance	Total Outliers
All Data	9.4 %	10.3 %
Healthy	8.4%	10.9%
ALS	6.6%	6.9 %
Non-MND	11.3%	11.8 %

Table 5.4: The proportion of outliers removed due to having negative resistance, and in total incorporating the root-mean-squared deviation based algorithm. Shown for the different participant groups within the dataset.

The identified outlier spectra are presented in figure 5.10, where it is visually clear that there were some obvious erroneous data that needed to be removed, while all the 'normal' looking spectral shapes remain within the dataset. The proportion of outliers removed in each of the participant groups is shown in table 5.4. Here, the proportion removed was fairly consistent between healthy participants and the two disease groups. The non-MND dataset contained the most outliers, but visually it is clear that there are more clear artefacts within this cohort. The proportion of outliers removed here was higher than for the tongue dataset since measurement artefacts are more likely when recording surface impedance on keratinised skin. In fact, the majority of the outlier detection comes from removing spectra with negative resistance, which makes up around 9% of the total dataset, the further set of outliers identified from the detection algorithm pertains to the remaining $\sim 1\%$ data removed.

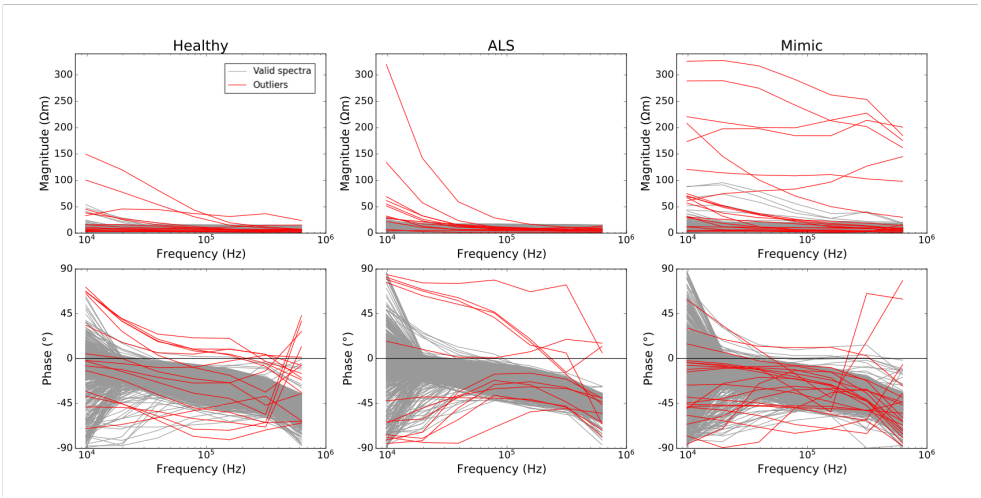

Figure 5.10: All recorded spectra (impedance magnitude and phase) shown for the healthy, ALS and non-MND patient cohort. Red spectra show the outlier spectra identified via the root-mean-squared deviation algorithm, and the grey spectra are the remaining data. Note this shows data for all the muscles and electrode configurations combined.

5.3.4 Reproducibility

In order to assess the test-retest reproducibility of the limb EIM measurement probe, ICC values were calculated for different subsets of the dataset (figure 5.11). On the whole, the dataset was found to be reproducible across all areas, with the ICC consistently exceeding 0.7.

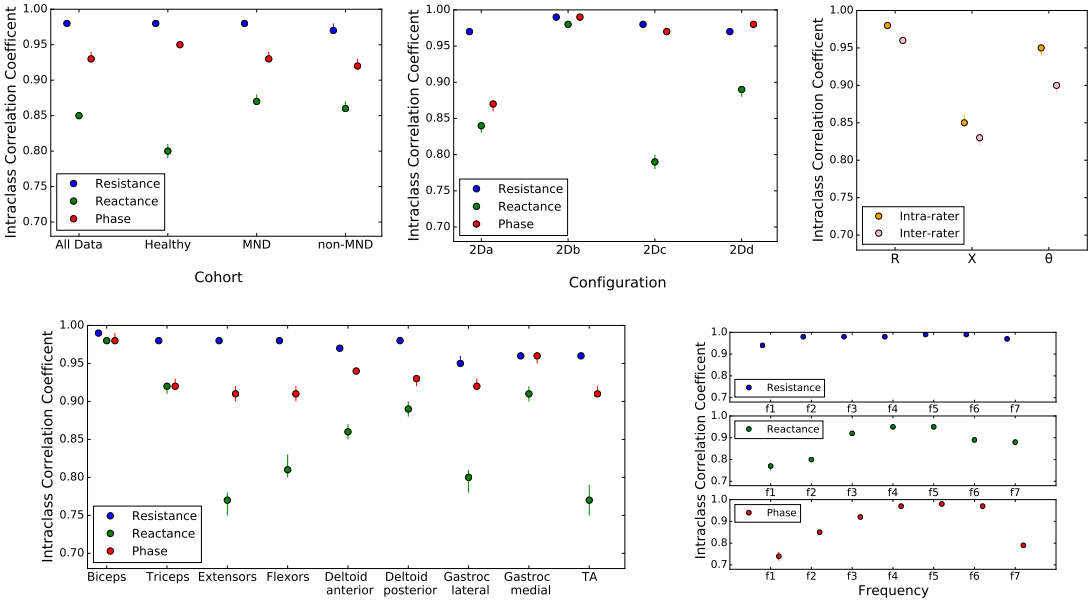

Figure 5.11: Intraclass correlation coefficients for different subsets of the data, presented for impedance resistance (R), reactance (X) and phase (θ). This data is also presented in the appendix, table D1.1.

The three metrics R, X and θ were compared, and it is clear that resistance is consistently highly reproducible (ICC$>$ 0.9), while reactance is marginally less so. Despite this for the chosen frequency range (which starts at 9.8 kHz), reactance still reports sufficient reproducibility. Looking at the overall trend with frequency the ICC increased in value over the spectrum with a maximal value seen for f5 (156.25 kHz). The ICC appeared to be highly comparable between the different cohorts within the participant group. In addition, all electrode configurations and muscles gave comparable and acceptable results, although specifically configuration 2Db and biceps saw impressive consistency between recordings. Finally, a comparison of the intra-rater (two recordings by the same experienced clinician) and inter-rater (experienced clinician versus medical student) gave comparable results, where the inter-rater performance was marginally reduced, but still with strong agreement.

5.3.5 Exploring the subcutaneous fat layer thickness

The thickness of the SFL was significantly affected by gender (see appendix, figure D2.1, table D2.2). Therefore the range of S-SFT for each muscle was compared between the healthy and patient subgroups for each gender in turn. Figure 5.12 demonstrates that there was some significant splitting in the S-SFL thickness when comparing healthy individuals to patients, where the overall trend was an increase in thickness with disease. Specifically, the SFL surrounding the forearm flexors, and sometimes the deltoids demonstrated a clear separation between the groups. This was also observed in the average thickness across all the muscles.

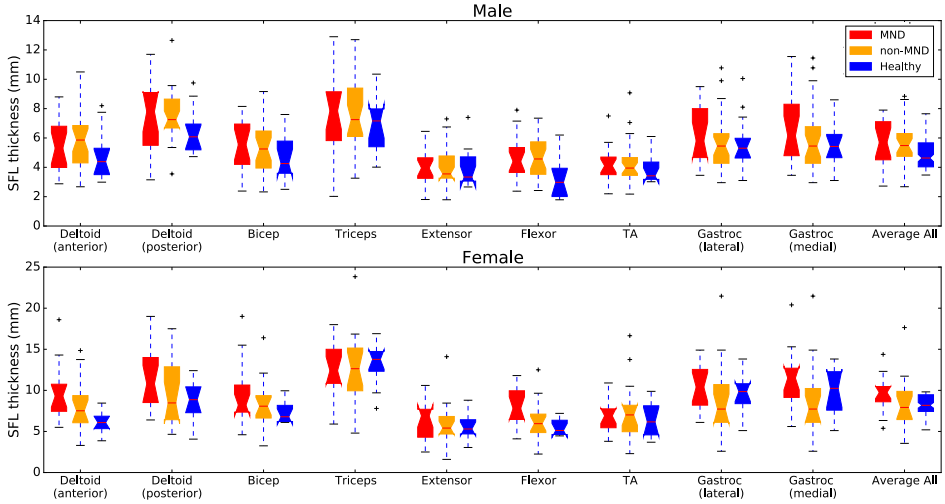

Split	Gender	Deltoid (anterior)	Deltoid (posterior)	Biceps	Triceps	Extensors	Flexors	TA	Gastroc (lateral)	Gastroc (medial)	Average all
Patient vs healthy	Male	ns	0.04	ns	ns	ns	0.007	ns	ns	ns	0.002
	Female	0.003	ns	ns	ns	ns	0.005	ns	ns	ns	0.005
MND vs healthy	Male	ns	ns	ns	ns	ns	0.02	ns	ns	ns	0.04
	Female	0.003	ns	ns	ns	ns	0.005	ns	ns	ns	0.005
non-MND vs healthy	Male	ns	0.03	ns	ns	ns	0.009	ns	ns	ns	0.006
	Female	ns	ns	ns	ns	ns	ns	ns	ns	ns	ns

ns=not significant

Figure 5.12: Boxplots of the S-SFT for each muscle shown for the three participant subgroups split by gender. A general trend of increased SFL thickness was seen in patients compared to the healthy participants. This data is also presented in appendix, table D2.1. The FDR-corrected p-values are presented for the Mann-Whitney U test performed on the SFL thickness for all patients compared to healthy; MND compared to healthy; non-MND compared to healthy.

To further investigate the potential impact disease has on the SFL, correlations were assessed between the S-SFT and both the ALSFRS-R and muscle strength for all patients. The thickness above each muscle, as well as the average cross-muscle thickness, were assessed in correlation with the limb; upper limb; and lower limb ALSFRS-R subscores (figure 5.13).

Muscle	ALSFRS-R subscores		
	Limb	Upper limb	Lower limb
Deltoid anterior	-0.53 **0.004**	-0.19 ns	0.32 0.01
Deltoid posterior	-0.57 **0.002**	-0.31 ns	-0.46 0.02
Biceps	-0.51 **0.007**	-0.08 ns	-0.45 0.02
Triceps	-0.35 ns	-0.14 ns	-0.26 ns
Extensors	-0.48 0.01	-0.25 ns	-0.47 0.01
Flexors	-0.69 **<0.001**	-0.26 ns	-0.63 **0.004**
TA	-0.52 **0.006**	-0.11 ns	-0.53 **0.004**
Gastroc lateral	-0.38 **0.05**	-0.13 ns	-0.37 0.05
Gastroc medial	-0.44 0.02	-0.19 ns	-0.41 0.03
Average	-0.55 **0.003**	-0.17 ns	-0.51 **0.006**

(a)

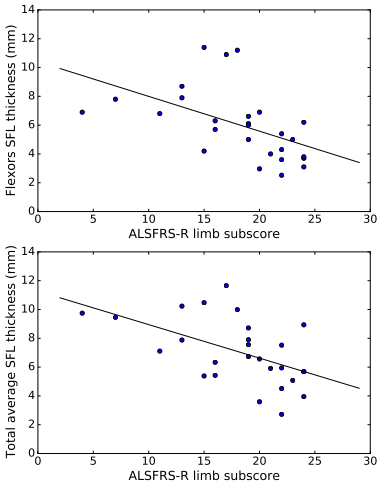

(b)

Figure 5.13: (a) Spearman rank correlation coefficient, and corresponding p-value, between the S-SFT and the ALSFRS-R subscores. Shown for the thickness surrounding each muscle, as well as the average thickness across all muscles. (b) Scatter plots of the ALSFR-R limb subscore against S-SFT on the flexors (the best performing correlation with p< 0.001), and against the total average thickness (p=0.003).

Muscle	Spearman rank (p-value)	
	Patients	Healthy
Deltoid	-0.19 ns	-0.52 ns
Biceps	-0.35 **0.004**	-0.69 0.01
Triceps	-0.34 **0.005**	-0.71 **0.009**
Extensors	-0.33 **0.007**	-0.53 ns
Flexors	-0.36 **0.003**	-0.65 0.02
TA	-0.36 **0.006**	-0.62 0.03
Gastroc	-0.13 **0.007**	-0.04 ns
Average	-0.45 **<0.001**	-0.71 0.01

(a)

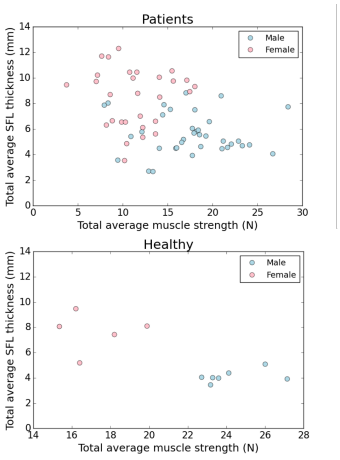

(b)

Figure 5.14: (a) Spearman rank correlation coefficient, and corresponding p-value, between the S-SFT and muscle strength for patients and healthy participants. Shown for each muscle, as well as the average thickness/strength across all muscles. (b) Scatter plots of the average limb strength against the average thickness for patients and healthy participants split by gender.

A trend of negative correlation was identified between the ALSFRS-R and the SFT, sug-

gesting that this thickness tends to increase with the severity of disease in ALS. All muscles apart from the triceps gave a statistically significant (FDR-corrected $p < 0.05$) correlation with both the overall limb and lower limb subscores. Interestingly, the upper limb subscore gave no statistically significant correlation. Figure 5.13b reveals this trend in a plot of the highest performing correlation of the limb subscore against the flexors S-SFT, as well as a plot of the limb subscore against the participant's average S-SFT.

Additionally, assessments of the correlations between the S-SFT and muscle strength were explored (figure 5.14). Again, a negative trend supports the theory that worsening disease appears to be associated with increasing fat thickness. However, when looking at this data split by gender it is clear that this effect is dominated by a gender effect, due to the general increased strength and reduced subcutaneous fat in the male cohort. Additionally, as the correlation is prevalent in both the healthy and diseased groups it may not be related to a specific disease etiology. It should also be noted that only a small number (12) of the healthy participants have data available for muscle strength testing.

5.3.6 How the subcutaneous fat layer effects EIM

On the whole, the SFL thickness certainly has some level of relationship with disease and the severity of symptoms. For this reason, it is crucial to exercise caution when evaluating the EIM data in order to properly account for the potential impact of the SFL. As a first stage of assessing this impact, correlation assessments were made between the thickness and the EIM dataset.

Significance	Resistance	Reactance	Phase	Magnitude
ns	14 5.6%	55 21.8%	5 2.0%	15 6.0%
<0.05	238 94.4%	197 78.2%	247 98%	237 94.0%
<0.01	234 92.9%	183 72.6%	243 96.4%	226 89.7%
<0.001	227 90.1%	168 66.7%	238 94.4%	221 87.7%

Table 5.5: Amount (and percentage) of significant and not significant (ns) results out of the 252 data dimensions. Testing the Spearman rank correlation between the S-SFT and EIM resistance, reactance, phase and magnitude, with FDR correction.

There are a total of 252 dimensions of the dataset that this was tested on (9 muscle sites, 4 independent electrode configurations, 7 frequencies). For each of the EIM metrics (R, X, θ and $|Z|$) a Spearman rank correlation assessment was made against the S-SFT. The proportion of features within the dataset that have a significant correlation is presented in table 5.5. Clearly, the majority of the EIM dataset gave a highly significant ($p< 0.001$) correlation with the contributing fat layer thickness. The strongest correlations were observed within the phase metric, although both resistance and magnitude saw a similar level. The reactance gave the least significance with 55 out of the 252 features demonstrating insignificant correlations, although that still leaves 197 features with a significant association.

To get further insight into how this correlation is impacted by the different measurements, figure 5.15 presents the range of Spearman ranks and corresponding p-values for each frequency, and each electrode configuration over the four impedance metrics. From this it is clear that the highest frequencies have the most consistent significant correlations with SFL, suggesting that the lower frequencies may be somewhat less dominated by the effects of the SFL layer. Looking to the different configurations, 2Da and 2Db (which record parallel to the muscle fibres) gave significant correlations for all features within resistance and magnitude, while conversely 2Dc

and 2Dd (which are perpendicular and diagonal to the fibres) gave significant correlations for all features within phase. Similar plots split by muscle are presented in the appendix, figure D3.1; however, no obvious discrepancies between the different muscles were observed.

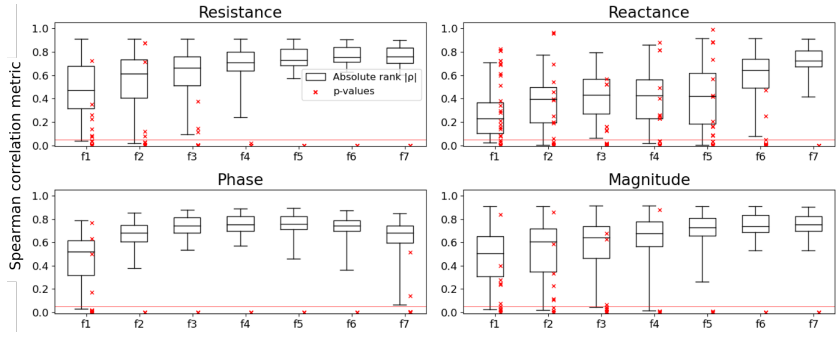

(a)

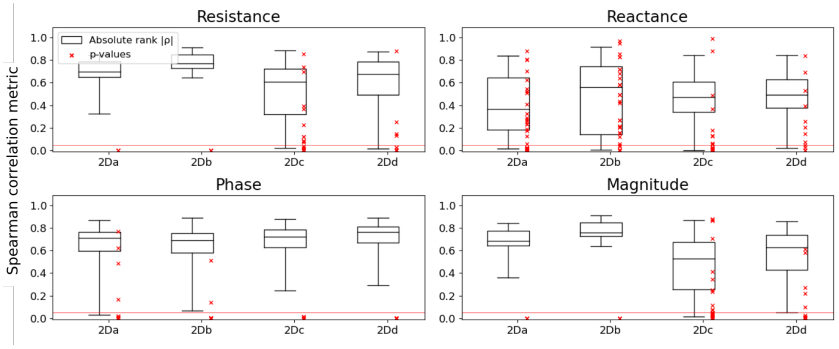

(b)

Figure 5.15: Boxplots showing the absolute value of the Spearman rank and corresponding p-values for correlation assessment between each of the EIM data features with S-SFT. (a) Split by frequency to assess how the significance of these correlations varies over the spectrum. (b) Split by electrode configuration.

A further investigation was made to explore if two-frequency ratios reduce the contribution of the SFL layer. As there are 7 frequencies of measurement, there are a total of 21 different two-frequency ratios that can be assessed. Table 5.6 shows a number of two-frequency phase and reactance ratios that were identified as substantially reducing the significance of association with the SFL. In comparison to table 5.5, there is now a large proportion of this EIM data that presents an insignificant correlation with the S-SFT.

		Significance for correlation with SFL			
Ratio	metric	ns	<0.05	<0.01	<0.001
19.5kHz/9.8kHz	X	24 (66.7%)	12 (33.3%)	6 (16.7%)	2 (5.6%)
39.0kHz/9.8kHz	θ	21 (58.3%)	15 (41.7%)	9 (25%)	8 (22.2%)
	X	26 (72.2%)	10 (27.8%)	3 (8.3%)	2 (5.6%)
78.1kHz/9.8kHz	θ	20 (55.6%)	16 (44.4%)	13 (36.1%)	7 (19.4%)
	X	24 (66.7%)	12 (33.3%)	10 (27.8%)	6 (16.7%)
156.3kHz/9.8kHz	θ	21 (58.3%)	15 (41.7%)	11 (30.6%)	9 (25%)
312.5kHz/9.8kHz	θ	20 (55.6%)	16 (44.4%)	13 (36.1%)	10 (27.8%)

Table 5.6: Amount of significant and not significant (ns) results for two-frequency ratios out of the 36 data dimensions. Testing the Spearman rank correlation between the S-SFT and EIM two-frequency ratio. Presented for the subset of data that significantly reduces the contribution of SFL.

5.3.7 Performance assessment

The findings thus far have revealed that there is a significant correlation between the SFL thickness and disease state, as well as between this thickness and the EIM features. The fundamental aim of this project is to assess the potential performance of EIM data as a biomarker for neurological conditions such as ALS (i.e. identify correlations with the disease state). Thus an assessment of the limb EIM biomarker performance was made, with the careful consideration of the impact of the contributing SFL.

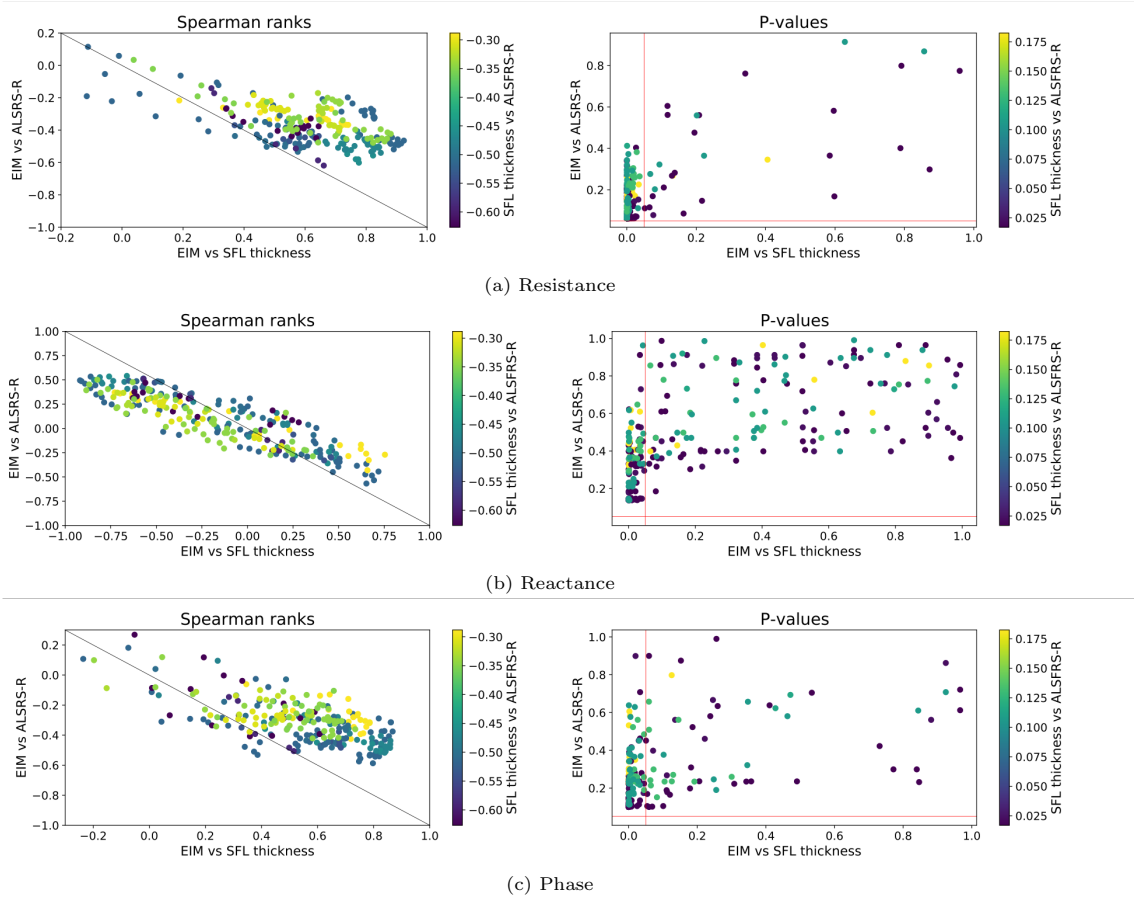

(a) Resistance

(b) Reactance

(c) Phase

Figure 5.16: Spearman correlation assessment between the 252 EIM metrics (7 frequencies, 4 configurations, nine muscle placements), the S-SFT, and the ALSFRS-R (limb subscore). Scatter plots show the Spearman rank and respective p-values (with FDR correction) from a correlation assessment on each metric in turn. The association between EIM and the S-SFT is plotted against the association between EIM and the ALSFRS-R, the colour map then shows the respective association with S-SFT and the ALSFRS-R. Shown for (a) EIM resistance, (b) EIM reactance and (c) EIM Phase.

An initial analysis of how the EIM features correlate with disease severity was performed. Using the subset of ALS patients, the ALSFRS-R limb subscore was assessed as a measure of disease severity. Figure 5.17 shows a comprehensive evaluation of how the correlation between each EIM metric within the high-dimensional dataset correlates with the S-SFT in comparison to its correlation with the ALSFRS-R. Additionally, the association between the respective S-SFT and the ALSFRS-R are shown as a colour map.

On the whole, while a few of the EIM features saw a reasonable correlation to the disease state ($|\rho| > 0.6$), after FDR correction no significant correlations were identified. For all three EIM metrics (R, X, and θ), there was an observable trend between the different correlation coefficients. The negative gradients seen in the scatter plots of the Spearman ranks determine that if an EIM metric has a stronger correlation with the S-SFT it was more likely to see a stronger correlation with the ALSFRS-R. This was particularly the case when the S-SFT saw a significant correlation with the ALSFRS-R (darker blue markers give a steeper gradient).

This same assessment was made for the reactance and phase two-frequency phase ratios (see appendix, figure D3.2 and D3.3). Here an analogous relationship was identified, with a clear trend between the correlation coefficients for SFL and the ALSFRS-R limb subscore. Despite the fact that these metrics gave reduced contribution from the SFL, the association with the disease state was not improved. In fact, there was only a single feature within the 78.1kHz/9.8kHz reactance that gave a significant correlation with the ALSFRS-R, and this feature also correlates significantly with the SFT. The remaining 6 two-frequency ratio datasets contained no features that significantly correlated with the ALSFRS-R.

In addition, the same assessment for the correlation with muscle strength is shown in figure 5.17. This assessment is split into male and female patient cohorts in order to remove the effect of gender. The association between the SFL and strength was insignificant for both genders, however, there was still a clear relationship identified between how EIM correlates with fat thickness and how it correlates with strength.

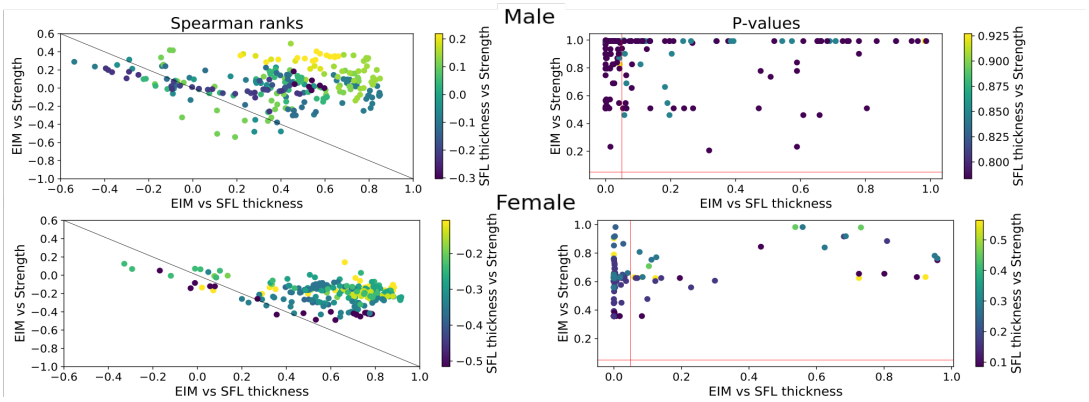

(a) Resistance

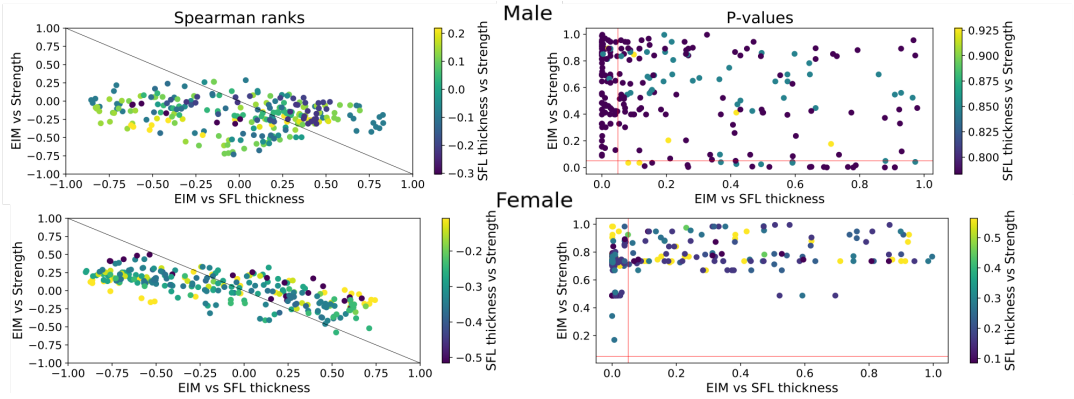

(b) Reactance

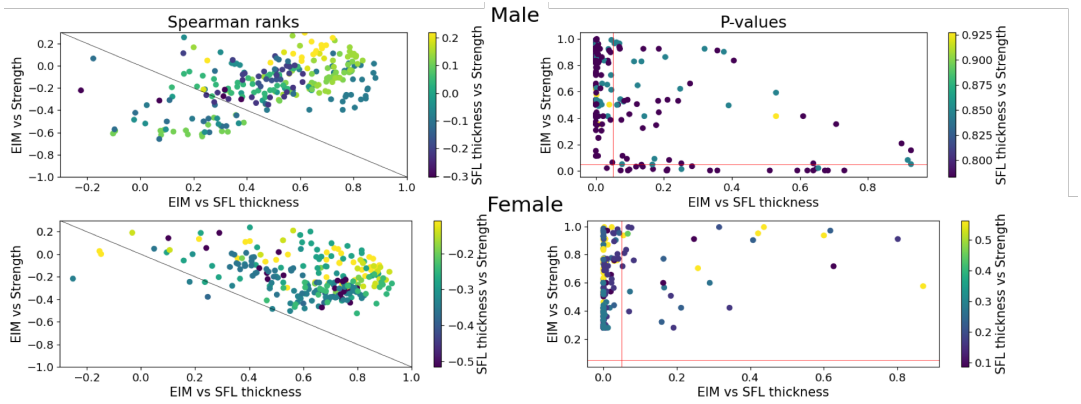

(c) Phase

Figure 5.17: Spearman correlation assessment between the 252 EIM metrics (7 frequencies, 4 configurations, nine muscle placements), the S-SFT, and the respective muscle strength. Scatter plots show the Spearman rank and respective p-values from a correlation assessment on each metric in turn. The association between EIM and the S-SFT is plotted against the association between EIM and the strength, the colour map then shows the respective association with S-SFT and strength. Shown for (a) EIM resistance, (b) EIM reactance and (c) EIM Phase, split by gender.

Interestingly, this association appears different in the male and female cohorts, where for females the features that have stronger correlations with strength tend to be those that also correlate well with the SFL. Conversely in males, the opposite effect was seen where features that strongly correlate with strength tend to be those that have minimal relationship with the SFL. In fact, the female cohort saw no features that correlated significantly with strength, while for male patients, there were a number of features that identified a significant correlation. For EIM reactance, 25 features correlate with <5% significance, and 12 correlate with <1% significance, while in the EIM phase, 24 features correlate with <5% significance, and 13 correlate with <1% significance. These specifically tended to be features that did not correlate with the S-SFT. Since the male cohort generally has a significantly thinner SFL, this suggests that the muscle-specific information within the limb EIM data may be more apparent for these participants.

In order to further investigate the presence of disease specific information within the limb EIM data, an assessment was made on the difference between both patients and healthy participants, as well as normal and abnormal muscle (determined through needle EMG). To test for any significant differences in the EIM, Mann-Whitney U tests were applied to each of the 252 EIM features with FDR correction applied. Figure5.18 shows the adjusted p-values for patient/healthy splitting compared to abnormal/normal splitting. Overall, all the resistance and phase features gave insignificant discrimination. However, 45 of the reactance features demonstrate <5% significance for separating patients from healthy muscle, with 10 of these giving <0.1% significance. Additionally, for separating abnormal from normal muscle, 7 reactance features demonstrate <5% significance, where this feature set overlaps with those that present significance in patients compared to healthy.

This was also repeated for the two-frequency ratios (see appendix, figure D3.4), however, the majority of this data exhibits no significance in group splitting. For example, no features were able to distinguish normal from abnormal muscle, and only 2 features within the reactance 19.5 kHz/9.8 kHz set and 2 features within the phase 39.0 kHz/9.8kHz set saw any significant discrimination between healthy participants and patients. Looking to the specific features that were identified as statistically meaningful, there were two that consistently reported significant values for correlation with strength (in males) and separation between both patients/healthy

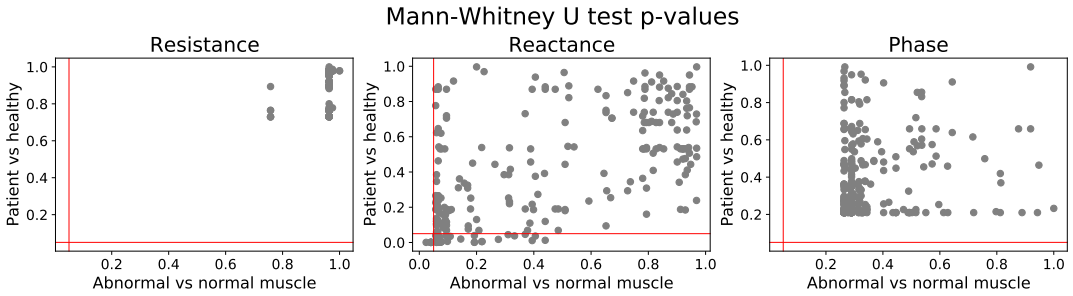

Figure 5.18: Mann-Whitney U test p-values for the discrimination between patients and healthy participants, against the p-values for the discrimination between abnormal and normal muscle. Shown for all EIM features across resistance, reactance and phase. The majority of features demonstrate no significant splitting.

participants and abnormal/normal muscle. Specifically, this was the EIM reactance recorded on the forearm extensors with configuration 2Db on frequencies 2 and 3. Furthermore, both of these features saw an insignificant correlation with the S-SFT. In summary, these findings indicate the presence of some relevant disease-related EIM features, though this information is largely concealed within the SFL-dominated data.

5.4 Discussion

An initial investigation of the measurement capabilities of the limb EIM probe has identified that both low frequency measurements (<9 kHz) and 3D configurations are not feasible to use. It is well documented in the domain of bioimpedance, that for keratinised skin, the epidermal Stratum Corneum layer, which consists mainly of dead skin cells, gives a large impedance in series with the viable skin, and thus dominates measurement at low frequencies (Martisnen et al., 1997; Martinsen et al., 1999). So, despite the undertaking of thorough skin prep, it is clear that the low frequency data recorded here is, as expected, dominated by artefacts with up to 45% of the spectra seeing the presence of negative resistance values. Three-dimensional EIM recordings have not previously been studied in the assessment of limb muscles. However, when testing the 3D configurations using saline jelly of known conductivity, the obtained impedance outputs did not align well with the expected values based on modelled data. This disagreement was more pronounced for larger plate separations, where artefacts appear to dominate the data. One explanation for this could be an inadequate amplitude of the injected current. Alternatively, there may be other more complex causes of measurement artefacts or instrument limitations at play. It is also possible that there could be some spatial variations in the conductivity of the saline jelly, where such non-uniformity could be contributing to the deviation between the measured and expected values. However, it is very unlikely that this would cause such pronounced deviations.

Overall, there are instrumentation issues that need to be addressed before the 3D configurations can be evaluated further. A detailed study has already been undertaken to validate the hardware performance of the EIM limb device in regard to mismatched electrode impedances (Healey et al., 2021). Further work is needed here to address how the hardware contributes to the deviation from expected impedance values, however, this is beyond the scope of this PhD. Furthermore, while 3D configurations have demonstrated excellent performance in EIM applications concerning the tongue, their applicability to limb assessments poses additional challenges. In the context of limb EIM measurements, 3D configurations involve the overlapping of two distinct muscles and the influence of underlying bone structures. Consequently, it

is plausible that 3D measurements may not exhibit comparable performance levels. Instead, 2D measurements, which isolate each distinct muscle, may potentially offer greater utility and effectiveness in assessing limb muscles. The impedance outputs obtained from the assessment of the 2D configurations exhibited a high level of agreement with the modelled data, which meant the cell constant for each configuration was determined.

A similar outlier removal procedure to that undertaken on the EIM tongue dataset was implemented here (appendix, A. Given that the thickness of the SFL exerts a significant influence on the data, the root-mean-squared deviation procedure was sequentially applied to subsets of the data with varying thicknesses, in 5mm increments. Furthermore, since there is a large overlap between the raw spectra of the different participant subgroups and levels of disease severity (due to the dominance of the SFL), the spectral deviations could be calculated with respect to the overall data median. Unlike the case of the tongue dataset, where this approach led to a large proportion of the severely diseased subset of data being misidentified as outlier spectra, here there is no notable disparity in the number of outliers identified between the healthy and diseased cohorts. In total 10.3% of the spectra were removed as outliers, the majority of which came from the presence of negative resistance values. This is clearly a significant loss to the dataset, and efforts to avoid artefactual measurements are crucial for the success of surface impedance recorded on limbs (or any area of keratinised skin) as a tool for monitoring disease.

It has been well documented that EIM of the limbs is highly reproducible (ICC>0.9) at the commonly utilised 50 kHz frequency (Rutkove et al., 2006; Martinez-Gonzalez et al., 2020). Here, an assessment over 7 frequencies (9.8-625 kHz) reported sufficient reproducibility, with ICC>0.7 in all cases, and ICC>0.9 for frequencies in the range 39-312.5kHz. In addition, this performance is well maintained between the different participant cohorts, indicating that even when disease introduces severe symptoms, measurements are still easy to reproduce. Reproducibility is also well maintained between the different electrode configurations and across the nine different muscle sites. Additionally, the intra-rater ICC for an experienced clinician is only marginally higher than an inter-rater ICC between an experienced clinician and a medical student. This suggests that recordings taken using the limb EIM probe are reliable and easy to reproduce even in inexperienced hands. Interestingly the resistance and phase data consistently outperform reactance in their ICC. This is not a trend that was observed in the tongue EIM dataset, which suggests that the layer of generally less conductive keratinised skin and subcutaneous fat has some impact on the reliability of reactance measurements. However, in the selected frequency range the reactance is still able to reproduce at a sufficient level.

When exploring the subcutaneous fat thickness levels between the different participant cohorts it is noteworthy that there are some significant differences in the thickness of the S-SFL when comparing healthy participants to patients. This is specifically observed in the deltoids and forearm flexors. Furthermore, when assessing the S-SFT in comparison to the ALSFRS-R limb subscore the outcome is of high correlation, with significant levels identified in all muscles but the triceps. These findings extend to the lower limb but not the upper limb subscore, which is likely due to the fact that the functionality related to walking/climbing stairs is more closely associated with disease severity. Further correlations are identified in relation to the S-SFT and muscle strength, although the prevalence of the gender effect is clearly a contributing factor to this. Overall, while it is well understood that following atrophy, fibrosis leads to an increase in the presence of intra-muscular fat (Rebolledo et al., 2019), the expected change to subcutaneous fat in ALS and other neurodegenerative diseases is less well understood. A number of studies report appetite loss and reductions in fat mass to correlate with disease progression (Ngo et al., 2019; Lee et al., 2021), while an additional study on adipose tissue distribution reports a reduction in subcutaneous fat thickness with worsening disease (Lindauer et al., 2013). These studies demonstrate the opposite trend to what was observed here, indicating the need for

further investigation to attain more definitive conclusions around the specific changes to SFL in disease. However, what is clear is that the thickness of the SFL is likely to undergo changes throughout the course of the disease, which highlights the importance of accounting for the contribution of the SFL when assessing the biomarker potential of limb EIM.

The SFL has been widely reported to dominate 50 kHz EIM data recorded in the limbs (Sung et al., 2013; Li et al., 2016b). It has been suggested that this dominance is reduced with the assessment of reactance data (Sung et al., 2013), or a two-frequency phase ratio (Schwartz et al., 2015; Li et al., 2016b; Rutkove et al., 2017). The assessment of our multi-dimensional limb EIM dataset found that, unsurprisingly the EIM data is highly correlated with the thickness of the S-SFL. This is the case for the majority of features within the impedance resistance, reactance, phase, and magnitude datasets. In agreement with previous reports, reactance does appear to demonstrate a reduced contribution from the SFL, with 55 of the 252 data points determined to have an insignificant association with the SFT. Given the widespread reporting of the two-frequency phase ratio, similar metrics were investigated within this dataset. Exploring all feasible frequency ratios revealed three reactance ratios and four phase ratios, which predominantly consisted of features showing insignificant associations with the SFL. Interestingly, each of these identified metrics were ratios of a given frequency with the smallest (9.8 kHz) frequency.

The correlations that have been identified so far suggest a potential causal relationship between EIM and the disease state, as the SFT has an influence on both factors. Therefore when moving on to the assessment of the capability of the EIM data in both identifying disease and correlating with disease prognosis, the contribution of the SFL was continually assessed. Overall, it is clear that the raw EIM data is dominated by fat, where the association between EIM and the S-SFT is generally much stronger compared to that between EIM and the disease severity. Almost all features, including the two-frequency phase/reactance ratios, exhibit little to no clinical significance. Following a comprehensive procedure of testing the performance of all the features in the high-dimensional set, with FDR correction accounted for, only a small number of features identify any level of significance in correlating with symptoms and differentiating disease states. Specifically, correlation with muscle strength is only identified in the male subset of the patient cohort for a small number of features. Additionally, two of these features (19.5kHz and 39kHz; 2Db; extensors) demonstrate significant ($p<0.05$) splitting between abnormal and normal muscle, as well as patients and healthy participants. The male participants, and the extensor muscle both exhibit the smallest fat thicknesses which is likely the reason why the EIM biomarker capability starts to demonstrate some level of potential here.

While previous studies have reported significant correlations for the 50 kHz EIM phase with both muscle strength and the ALSFRS-R (Rutkove et al., 2002, 2014; Offit et al., 2020), it is highly likely that the SFL is dominating this data. Since the S-SFT has been found to correlate with both of these disease specific biomarkers, it is very possible that these correlations are due to the effects of fat thickness changes rather than any muscle specific changes. Additionally, longitudinal studies in both ALS (Offit et al., 2020) and DMD (Rutkove et al., 2017; Kapur et al., 2019) report significant changes in limb EIM over disease progression. But again, since it is clear that the levels of the subcutaneous fat seem to change throughout neurodegenerative disease (as presented within our dataset and by Lindauer et al. (2013)), perhaps the longitudinal changes identified in EIM are majoritively capturing changes to the thickness of the SFL rather than structural changes to the muscle itself. I would hypothesise that all surface EIM data presented in the limbs so far are largely dominated by the impedance of the fat layer, with potential minimal contribution from muscle.

This bodes the question of whether EIM is really the appropriate name for such measure-

ments, where maybe impedance lipography would be more appropriate. In fact a large number of studies have now moved onto the investigation of needle EIM (Cardoner et al., 2021; Rutkove et al., 2023). This involves recording the impedance from a needle inserted into the muscle in order to entirely bypass the S-SFL. However, the non-invasive and pain-free nature of surface EIM offers distinct advantages over needle-based EIM techniques. In order to get a more detailed picture of the impedance of the limb muscles, an algorithm to remove the contribution of the dominating SFL and isolate the muscle impedance is required. Development of such an algorithm would be a notable feat, with the potential to gain a much more comprehensive picture of muscle structure through surface impedance measurements.

6 Chapter 6: Signal separation development to isolate the impedance signal from muscle.

6.1 Introduction

This chapter presents the development of an innovative methodology for the separation of the S-SFL and muscle impedance signals within the limb EIM dataset. Clearly, the dominance of subcutaneous fat in surface impedance measurements is extensive, meaning attempts to infer direct properties of the muscle state seem rather futile. FEM-based modelling was explored in order to gain a thorough understanding of how impedance signals superimpose when measuring over layers of materials with different potentially anisotropic dielectric properties. This approach was fine-tuned to accurately simulate surface EIM in a limb structure, encompassing multiple layers of skin, subcutaneous fat, and muscle.

The essential model parameters pertain to the dielectric properties of the respective biological materials. Initial insight into these values was gained from the extensive study undertaken by Gabriel et al. (1996a,b,c), although there are certain limitations to this study which have previously been discussed (section 1.3.5). Specifically, the range of values reported across the literature can vary by up to two orders of magnitude. Therefore in order to increase the accuracy of the modelled limb system, the input parameters were run through a detailed series of optimisations in order to find a close fit to our limb EIM measurement dataset. Furthermore, in order to validate the FEM-based work an ex vivo study was conducted to assess the properties of porcine tissue and explore the superposition of impedances from different biological tissues in comparison to modelled data.

Using our knowledge of the impedance system, with insights gained from this work and the trends within the measurement dataset, a comprehensive SFL removal procedure was determined. This algorithm transformed the EIM dataset, using knowledge of the participant's S-SFT, in order to remove the contribution of the S-SFL layer, ideally leaving behind the impedance of the isolated muscle. There are a number of assumptions and limitations to this methodology, which will be addressed. So while not perfect, the output of this procedure shows a clear reduction in the dominance of the SFL within the data. Following this, a detailed comparison was made in the biomarker performance of the EIM data before and after the SFL removal transformation.

6.2 Methods

6.2.1 Building an FEM limb model

A model of the limb system was constructed using Comsol Multiphysics®. As seen in figure 6.1, the geometry pertains to layers of muscle, subcutaneous fat and skin, with the gold circular electrodes placed on the skin surface. The geometry was oriented so that the x-direction aligns with the direction of the muscle fibres along the limb, the y-direction aligns perpendicularly across the limb and the z-direction represents the vertical axis connecting the upper and lower electrode plates. A skin thickness of 0.9 ± 0.3mm was used, based on values reported for the upper and lower extremity sites of interest (Lintzeri et al., 2022). The SFT was introduced as an independent variable with its value iteratively adjusted to encompass the range of SFT levels observed within the participant cohort (1.6-23.8mm). The total tissue thickness is known, based on the plate separation used for measurements (35-115 mm). Therefore, the input for the thickness of muscle can be directly inferred.

The electrodes have a diameter of 7mm and are separated by 15 mm in the x-direction and 30 mm in the y-direction. The rectangular array of electrodes is placed on the centre of the limb

arrangement. Since only 2D configuration data is under assessment, the model is simulated to record the impedance using the upper electrode array atop the limb geometry. Utilising the AC/DC module in Comsol different pairs of electrodes are employed to inject current and record the output voltage, which simulates each of the independent electrode configurations.

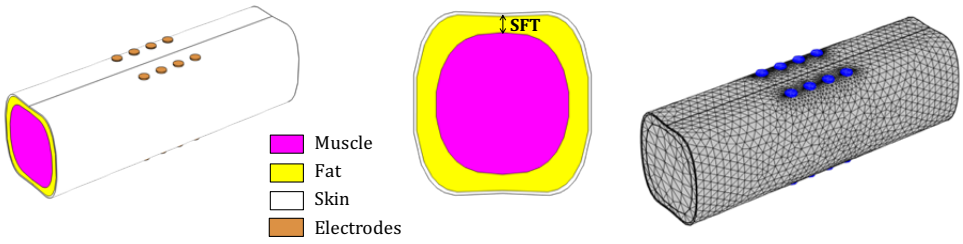

(a) (b)

Figure 6.1: (a) Model geometry of a limb consists of the skeletal muscle with a skin fat layer; 0.9 ± 0.3mm of skin and a varied thickness of subcutaneous fat. The parameter for skin fat thickness = SFT. Additionally, eight electrodes are placed on the upper and lower skin surface. (b) Schematic of the mesh used in the Comsol model.

The dielectric properties of the skin, fat, and muscle are model inputs that need to be determined. The skin and fat are both assumed to be isotropic, while the muscle is characterised as anisotropic with different dielectric properties parallel and transverse to the muscle fibres. This gives four dielectric spectra; $\mathcal{E}_S^*$, $\mathcal{E}_F^*$, $\mathcal{E}_{MT}^*$, $\mathcal{E}_{MP}^*$, for the skin, fat, transverse and parallel muscle, respectively. The complex dielectric spectrum of each tissue is described in terms of the Cole-Cole dispersion:

$$\mathcal{E}^*(\omega) = \mathcal{E}_\infty + \sum_{n=1}^{N} \frac{\Delta\mathcal{E}_n}{1 + (i\omega\tau_n)^{(1-\alpha_n)}} + \frac{\sigma_i}{i\omega\mathcal{E}_0} \tag{6.1}$$

where, ω is the angular frequency, $\mathcal{E}_0$, is the permittivity of free space, $\mathcal{E}_\infty$ is the tissue permittivity at large frequencies. This model describes the summation of N dispersions, where $\Delta\mathcal{E}_n$ is the magnitude of the n^{th} dispersion, τ_n is the time constant for the dispersion, and α_n is a measure of the broadening of the dispersion. This model was used for parameterisation of a large range of biological tissues in Gabriel et al. (1996c), where N=4 was found to appropriately model the dielectric behaviour of these tissues over a broad range of frequencies (Hz-GHz). The initial input parameters for the dielectric properties within the model were taken from the reported Cole-Cole dispersion parameters for muscle, skin, and fat (non-infiltrated) (Gabriel et al., 1996c). It must be noted that this work did not parameterise separate dielectric spectra for the transverse and parallel directions through muscle, thus the muscle is initially modelled as an isotropic material.

6.2.2 Ex vivo measurements in porcine tissue

An experiment to investigate the dielectric properties of ex vivo porcine tissue was undertaken (Home office project license number: PP1785781). Samples of tissue, which contained skin, fat and muscle were cut from the abdomen of the pig directly following euthanasia (figure 6.2).

Samples from three pigs were collected. The thickness of the layers of skin, fat, and muscle was measured using callipers.

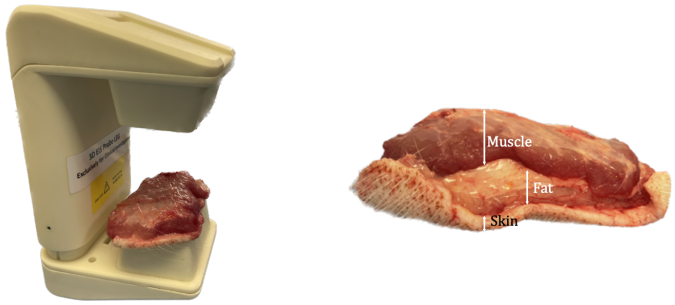

Figure 6.2: Photos showing the porcine tissue measured using the limb EIM device and the cross section of the tissue showing layers of skin, fat and muscle.

Impedance spectra of the tissue were recorded using the limb EIM probe. The measurements were conducted across various combinations, including the complete assemblage of skin, fat, and muscle (SFM); the combination of fat and muscle with skin removed (FM); solely the skin (S); solely the fat (F); and solely the muscle (M). All measurements were undertaken with 3 repeats on each porcine sample.

Additionally, in order to directly infer the 3D dielectric properties of each respective tissue, an impedance probe was built and designed to measure small cubes of each tissue. The design of this probe is shown in figure 6.3. Cubes of tissue were cut with a cross sectional area of $1cm^2$ and clamped in place with the device. The impedances were recorded by connecting the electrodes to the impedimed™device. In order to measure through all 3 dimensions the cube of tissue was rotated.

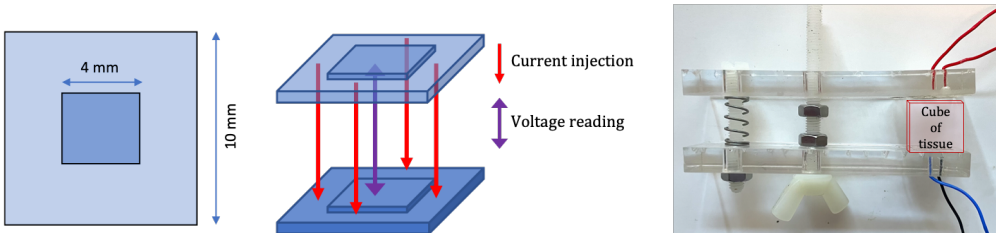

(a) (b) (c)

Figure 6.3: Impedance probe designed to directly measure the dielectric properties of cubes of tissue. The electrodes are made from silver/silver chloride (Ag/AgCl) in a 10mm square geometry, with a 4mm square in the middle as shown in (a). The outer inner electrodes inject current and the inner electrodes measure the voltage, which is visualised in (b). (c) Shows a photo of the probe, which is clamped onto a cube of tissue. The tissue was rotated to measure the dielectric properties in all three directions. Wires connected to each electrode are attached to the impedimed™device for impedance measurement.

From this impedance output, the dielectric properties can be directly inferred using eqs.1.9 and 1.10. Where the cell-constant (K) of the probe as a function of the electrode plate separation was determined using measurements in saline with validation from an FEM model. In order to reduce the impact of the electrode impedances, measurements were taken using two cubes of tissue with different thicknesses, t_1 and t_2. For each measurement, the impedance output can

be assumed to take the form:

$$Z1 = Z(t_1) + Z_e\,; \qquad Z2 = Z(t_2) + Z_e \tag{6.2}$$

where $Z(t_1)$, $Z(t_2)$ are the true impedances of the tissue with thickness t_1 and t_2, respectively. Additionally, Z_e is the electrode impedance. Hence by subtracting the two impedances, the electrode impedance will cancel out, leaving:

$$Z1 - Z2 = Z(t_1) - Z(t_2) = Z(t_1 - t_2) \tag{6.3}$$

and the dielectric properties can be determined using the cell constant for a plate separation of $t_1 - t_2$.

6.2.3 Optimising the model

Model optimisation was undertaken to determine the dielectric properties of the biological tissue in order to achieve the best fit with the measurement EIM dataset. This process was undertaken using the Optimization Module in Comsol (Multiphysics®, 2018). The main purpose of this optimisation was to maximise the accuracy of the dielectric properties of the subcutaneous fat. The model was optimised to fit the EIM dataset collected in healthy limbs, which was done in order to capture the dominance of changing fat thickness, without the effect of substantial changes occurring to the muscle due to disease. To achieve this fit, a two step optimisation procedure was undertaken, which is detailed in figure 6.4.

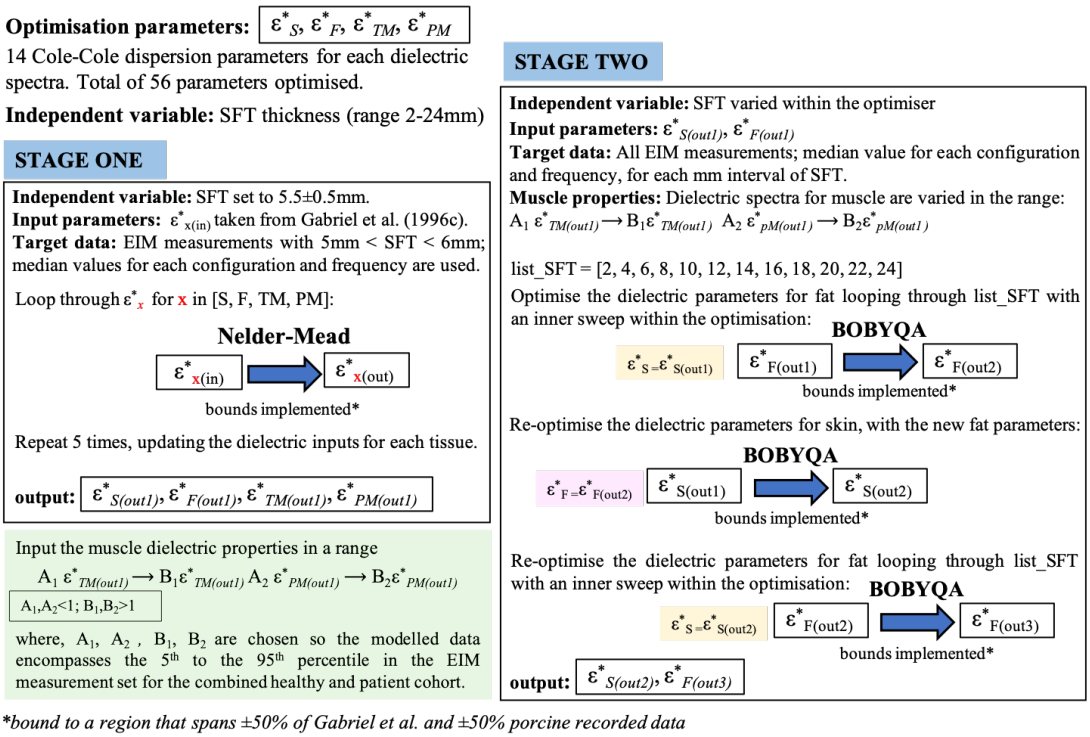

Figure 6.4: The optimisation follows a two stage procedure for determining the parameters that define the dielectric spectra for skin and fat. The limb EIM measurement set is the target data.

Firstly, employing a constant thickness for the SFL (5.5 ± 0.5mm) all model inputs (56 parameters) were fine-tuned in order to obtain an agreement for the general spectral shape with the EIM measurement dataset. This optimisation was undertaken using the method of moving asymptotes (MMA) solver (Svanberg, 1987), which was selected for its suitability to handle problems with large numbers of control variables (Multiphysics®, 2018). Model parameters were bound in a region that spans ±50% of the literature values taken from Gabriel et al. (1996c), and ±50% of the data recorded in porcine tissue. In this stage, a medium grained optimisation was undertaken, with parameter steps on the order of 5% of the median literature values. Following stage one, the optimised dielectric spectra for the muscle tissue were extended across a range in order for the model to encompass the EIM measurement data across all the participants in both the healthy and patient cohorts. This was implemented since it is well understood that muscle properties will differ between the varying levels of disease.

The next stage of the algorithm involved optimising the skin and subcutaneous fat properties across the full range of SFT values. This was done by performing a least-squares objective, with an inner sweep over thicknesses ranging from 2mm to 24mm. Here the bound optimisation by quadratic approximation (BOBYQA) solver was employed since a gradient free method was necessary when the geometry within the model is changed throughout the optimisation (Powell, 2009; Multiphysics®, 2018). By definition, such a solver allows bounds, and the parameters were again constrained within the region covering the Gabriel et al. (1996c) and ex vivo porcine data range. For the first two procedures, the same coarse grained optimisation was implemented, for the final procedure where the properties of the fat were re-optimised, a finer grained search with parameter steps on the order of 2% of the median literature values was implemented. The finalised model was then able to successfully capture the trends between the impedance values and SFT observed in the measurement EIM dataset.

6.2.4 Signal separation

In order to separate the surface impedance measurements into the impedance signal contribution from the muscle and that from the S-SFL, the combined impedance is modelled as a linear combination of the isolated signals:

$$Z_{\text{combined}} = aZ_{\text{muscle}} + bZ_{\text{S-SFL}} \tag{6.4}$$

where, Z_{combined}, Z_{muscle}, and $Z_{\text{S-SFL}}$ are the impedance spectral signals from the full limb structure, only the muscle, and only the skin-subcutaneous fat. The parameters a and b are the tissue mixing parameters, which define the contribution weight of the muscle and the S-SFL, respectively. These mixing parameters were determined for each electrode configuration and each value of SFT.

To ascertain the values of parameters a and b, FEM modelling was undertaken. Here a simplified cuboid geometry was utilised (figure 6.5), where the skin thickness remains constant, and the SFT was varied. Only 2D configurations in the upper electrode plate need to be tested, therefore the muscle and the SFT for the S-SFL only model are modelled with a large thickness (10cm), to prevent the current path from travelling through the whole cross-section of tissue. Hence, this yielded results comparable to those obtained from infinitely thick muscle.

The model was run for the three setups of tissue, when the muscle was incorporated this was looped over 100 different dielectric inputs for the anisotropic muscle. These inputs covered the pre-determined range of dielectric spectra, ascertained during the optimisation procedure. This was repeated for different values of SFT in 1mm intervals, from 1-24mm. For each configuration and SFT value, the tissue mixing parameters were chosen to optimally reconstruct the combined S-SFL-muscle signal across all 100 versions of the muscle. Following this, the transformation

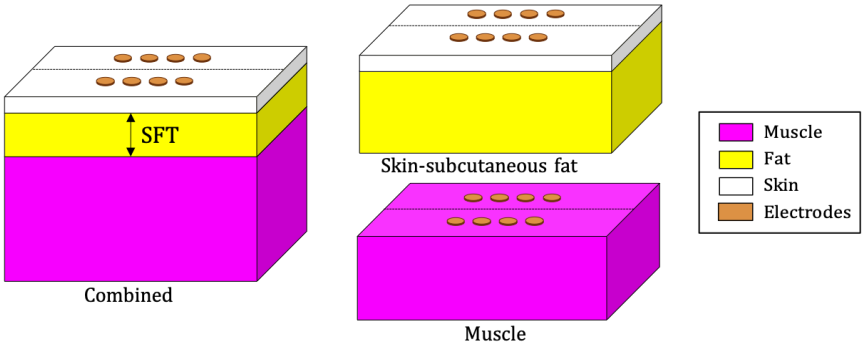

Figure 6.5: Simplified cuboid geometry utilised for FEM separation model. Model run for combined layers of skin-subcutaneous fat-muscle; just the skin-subcutaneous fat; just the muscle. The thickness of the skin was kept constant (0.9mm). In the combined model SFT was varied (1-24mm), in the skin-subcutaneous fat model SFT was set at 10cm. Additionally, the thickness of the muscle was set as 10cm.

to isolate the muscle signal from our EIM measurement set is given by:

$$Z_{\text{muscle}} = \frac{Z_{\text{combined}} - bZ_{\text{S-SFL}}}{a} \tag{6.5}$$

where $Z_{\text{S-SFL}}$ is the spectral output from the S-SFL model setup.

6.2.5 Classification

For assessment of the performance of the EIM datasets classification models were applied to each muscle feature set in turn. Firstly, a forward selection wrapper approach was utilised for feature selection on the high-dimensional data space. A maximum of 10 features were selected, in order to extract only the most relevant features and increase the efficiency of model training. An SVM classifier was selected for its capacity to effectively handle high-dimensional data while demonstrating resilience against overfitting (Salam et al., 2021). Additionally, cross-validation was applied to minimise overfitting. The classification was assessed for all patients versus healthy; ALS versus healthy; mimic patients versus healthy; ALS versus mimic patients; normal versus abnormal muscle; and ALS split by severity, with severe: limb ALSFRS-R<18, versus mild: limb ALSFRS-R≥18). Due to mismatches in the sample size of the different groups random oversampling was used. Cross-validation was applied using 5-fold, 4-fold, and 3-fold cross-validation depending on the relative sample size within the group. The size of each fold was constrained between 5 and 15 participants in each class, to maximise the number of folds for a more robust approach, while ensuring the size of the training data is not too small. The class sizes and chosen number of folds for each classification problem are presented in table 6.1.

Classification	Group 1	Group 2	Cross-validation
Patient / Healthy	75	22	5-fold
ALS / Healthy	28	22	4-fold
Non-MND / Healthy	44	22	4-fold
ALS / Non-MND	28	44	4-fold
Mild ALS / Severe ALS	15	13	3-fold
Abnormal / Normal	9-21	19-32	3-fold

Table 6.1: The sizes of each class and number of folds used for cross-validation in each of the 6 classification problems. Note that the class sizes for abnormal and normal muscles vary depending on the muscle site used.

In addition, classification was applied to the factorised NTF weightings, that were output during the tensor EIM procedure. Here, a Naive Bayes classifier was used, which is computationally efficient, robust to redundant features, and has good performance with small training sets (Zhang, 2004). All spectral weightings were input as features (3 or 4 depending on the muscle), hence all spectral information was preserved and biased feature selection was avoided. K-fold cross-validation and random oversampling were implemented in the same method described above.

6.3 Results

6.3.1 Porcine study

The dielectric spectra for the porcine dissected muscle, fat and skin are presented in figure 6.6, with a comparison to the data reported in Gabriel et al. (1996c) for human biological tissue. Measurements were taken in muscle for the directions transverse and parallel to the muscle fibres. There is a deviation between these two spectra, with a higher conductivity seen in the parallel direction, which is in agreement with what would be expected. Conversely, a comparison of the spectra obtained in transverse and parallel fat exhibited a significant overlap, providing confirmation of the isotropic nature of fat. In regards to skin, due to the size of the probe (figure 6.3) and the limited thickness of the skin, the dielectric properties were only measured in one direction. Looking at the data obtained in comparison to the spectra previously presented, there is reasonable agreement for both the muscle and skin. Interestingly, the conductivity and permittivity recorded in porcine fat are considerably higher than that reported by Gabriel et al. (1996c).

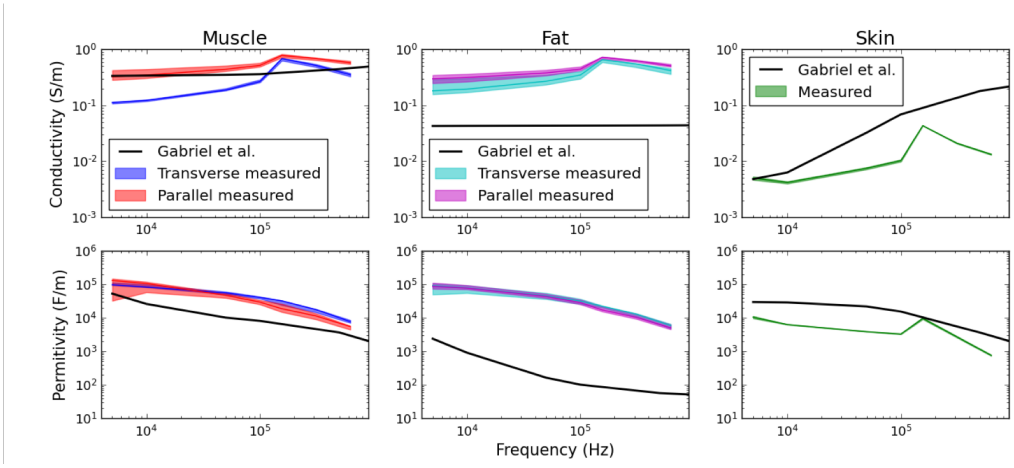

Figure 6.6: The dielectric spectra of porcine muscle, fat, and skin. Data was measured using the impedance probe detailed in figure 6.3, compared to data presented in Gabriel et al. (1996c).

Figure 6.7 shows the impedivity spectra recorded with the limb EIM device on the different layers of tissue (skin-fat-muscle; SFM, fat-muscle; FM, and each individual tissue; S, F, and M). These data were then reconstructed by inputting the dielectric properties of each spectrum into an FEM model in Comsol, using the known thicknesses of the layers for each of the porcine samples. In order to assess the effectiveness of the FEM model for reconstructing impedance spectra obtained from layers of different biological tissue, the measured and modelled porcine data were compared.

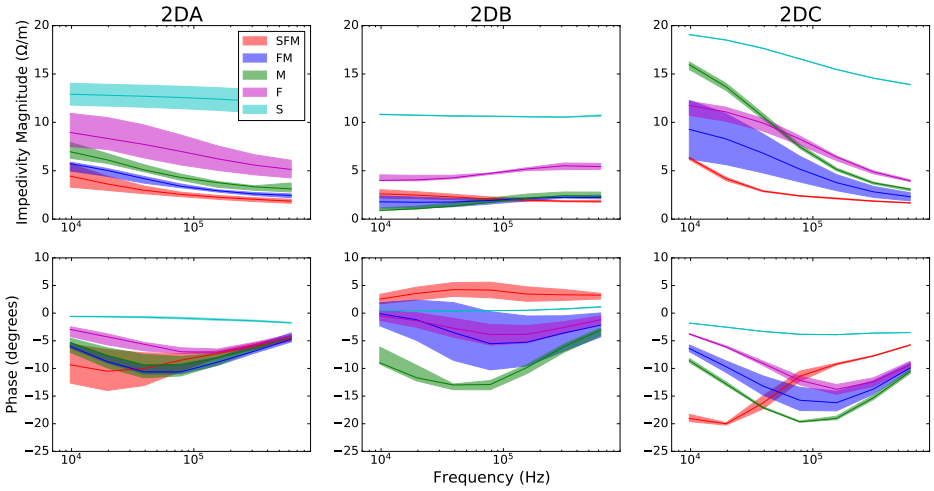

Figure 6.7: Impedivity spectra of porcine samples recorded using the limb EIM device. Shown for the combination of skin-fat-muscle (SFM), fat-muscle (F-M), skin (S), fat (F), muscle (M).

The deviation (NRMSE) between the measured and modelled data was calculated, and a comparison was made with the deviations observed between repeat measurements in the limb EIM dataset (figure 6.8). Overall, although the median deviation was consistently smaller when comparing repeat recordings, the maximum NRMSE for repeats always exceeded the maximum for the FEM model comparison. This was the case across all configurations in both the impedance resistance and reactance. Such a finding validates the procedure of using FEM modelling to reconstruct impedance measurements in biological tissue.

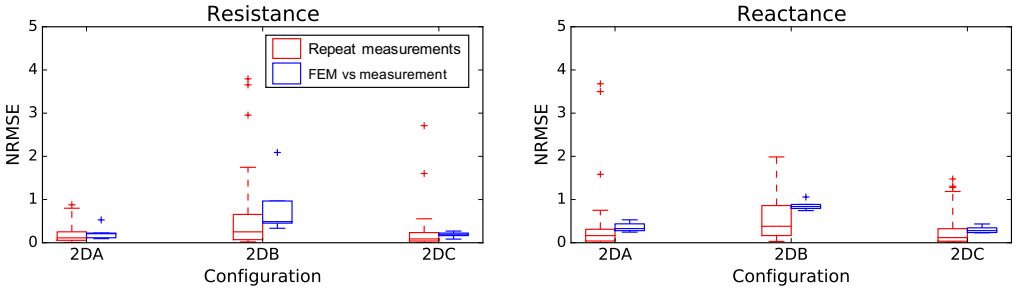

Figure 6.8: Boxplots showing NRMSE between repeat EIM measurements taken in porcine tissue samples (red), compared to that between the FEM model and the EIM measurements (blue).

6.3.2 Optimised FEM model

Following the multi stage optimisation procedure, the dielectric spectra for each of the biological tissues were determined. Figure 6.9 presents each optimised spectra in comparison to the ex vivo porcine data and that presented by Gabriel et al. (1996c). In order to encompass the different levels of disease state the dielectric spectra for muscle span a range. The dielectric spectra determined for fat lie in between the Gabriel et al. data and the porcine tissue data.

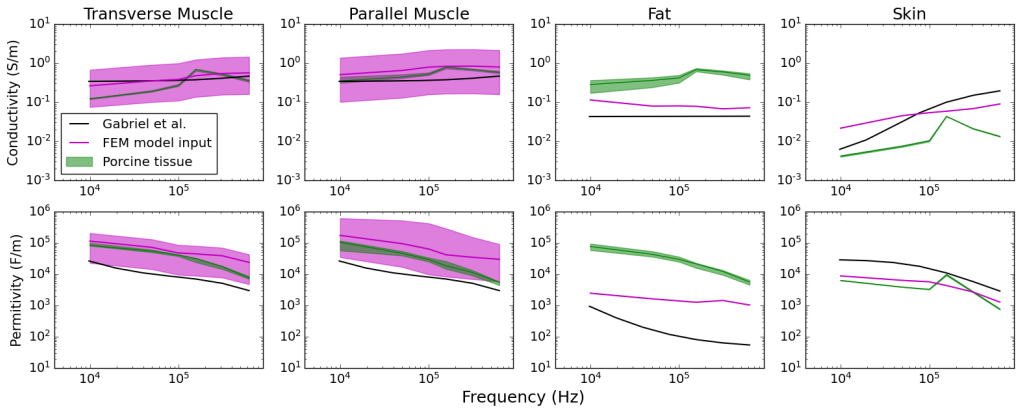

Figure 6.9: The optimised dielectric spectra FEM model input for each biological tissue (pink), compared to that recorded in porcine tissue (green) and that presented in Gabriel et al. (1996c) (black).

The optimised model demonstrated overlap with the measurement dataset, evidencing success of the optimisation procedure. The modelled spectral output in comparison to the measured EIM spectral 95% confidence interval is shown in figure 6.10, where the variability in the model output was a result of incorporating a range of input dielectric spectra for the muscle.

The success of the optimisation is evident through the impressive convergence between the model's characteristics and the target dataset across multiple levels of SFT. Additional visuals showing this data as a function of the SFT are presented in the appendix, figure D4.1, which further demonstrates how the model effectively captures the influence of changing fat thickness. Overall, the alignment between the model and the measurement dataset, in particular, the agreement in the trend with varying fat thickness (figure D4.1), indicate that the underlying dielectric properties of the fat have been very well characterised.

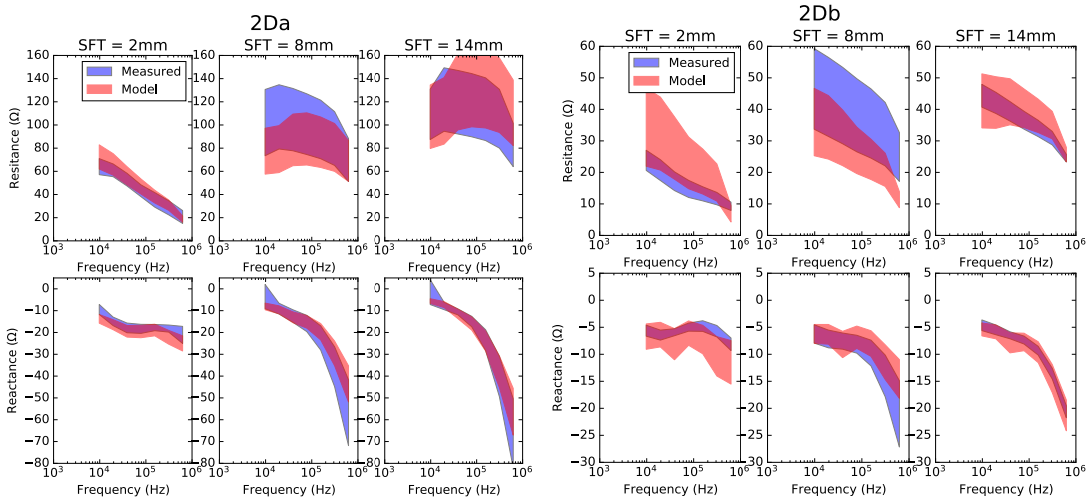

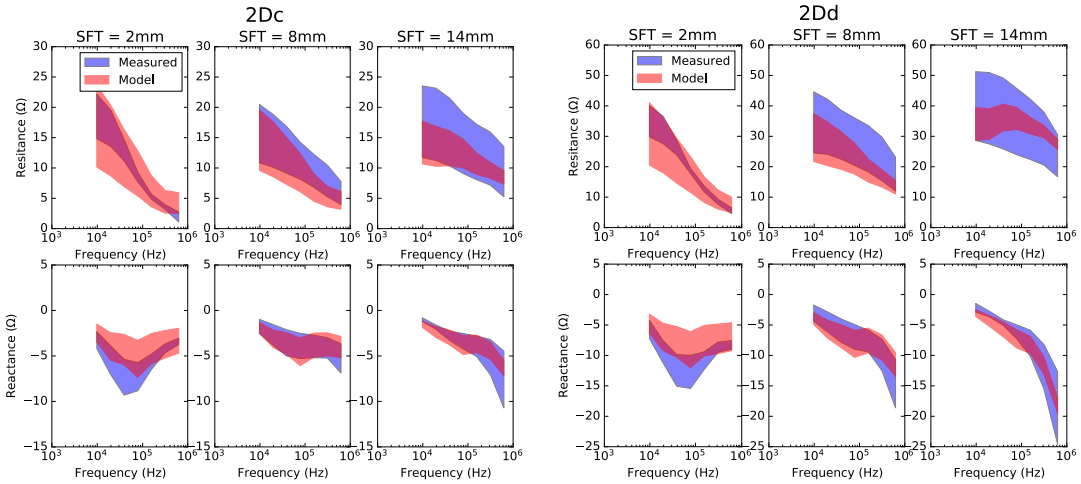

Figure 6.10: Optimised model output compared to the multi-participant EIM dataset 95% confidence interval. Spectral patterns for each electrode configuration are shown for three levels of SFT (2mm, 8mm, 14mm) to demonstrate how the model successfully captures the dependence on the amount of subcutaneous fat.

6.3.3 Assessing the signal separation

Through FEM modelling the values of the tissue mixing parameters (a and b) were determined for each electrode configuration as a function of fat thickness. These are shown in figure 6.11, where the contribution of fat clearly grows with the SFT, while the contribution of muscle decreases. Polynomial functions were employed to fit each distribution, enabling the determination of the mixing parameters across a continuous spectrum of SFT values.

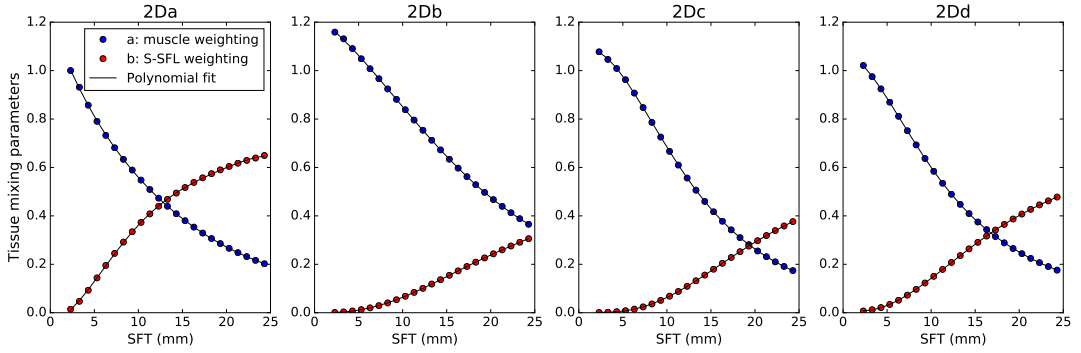

Figure 6.11: The tissue mixing parameters, a and b, as a function of SFT for each electrode configuration. Polynomial functions were fit to each parameter, so the mixing parameters could be determined for all SFT values across the participant cohort range.

To demonstrate the effectiveness of this signal separation procedure, a visual showing an example of the reconstructed muscle spectra in comparison to the actual muscle spectra is shown in figure 6.12. Although not perfect, the signal separation is able to proficiently reconstruct the muscle spectra with impressive agreement in the expected spectral pattern. To quantify the performance of these reconstructions, the difference between the true signal and the reconstructed signal was calculated using the NRMSE.

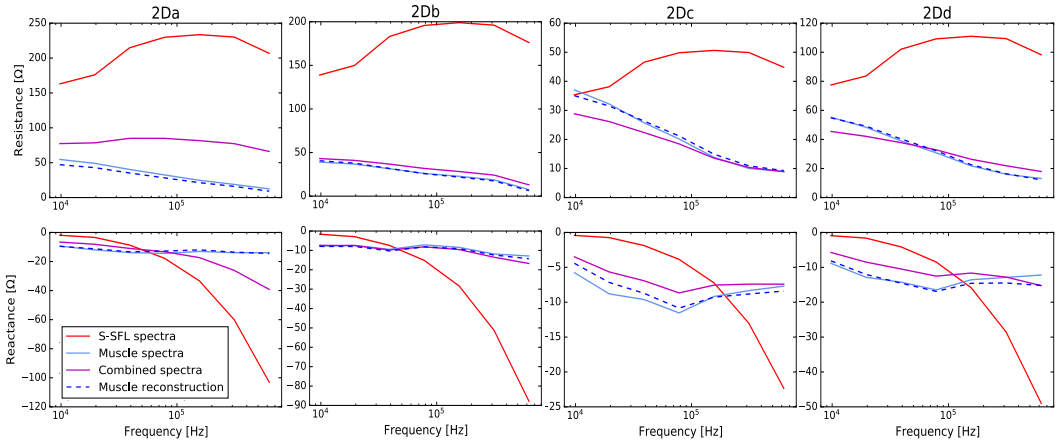

Figure 6.12: Example of signal separation with SFT=10mm. The reconstructed muscle spectra (dashed blue) is shown in comparison to the actual muscle spectra (light blue). Additionally, the S-SFL spectra (red) and combined spectra (pink) are shown.

Boxplots showing the range of NRMSE for each configuration and each value of SFT are presented in figure 6.13. This data was compared to the maximum observed NRMSE between repeat measurements in the limb EIM dataset at each configuration. It is clear that the reconstructions are more accurate within the resistance, furthermore, the reconstruction accuracy reduces as SFT increases. Up to an SFT of approximately 12 mm, the reconstructions exhibit sufficient accuracy, where deviations are less than the deviation between two repeat measurements, across all electrode configurations. For larger thicknesses, the error in some of the reactance data starts to exceed that observed for repeat measurements (particularly in 2Dc and 2Dd).

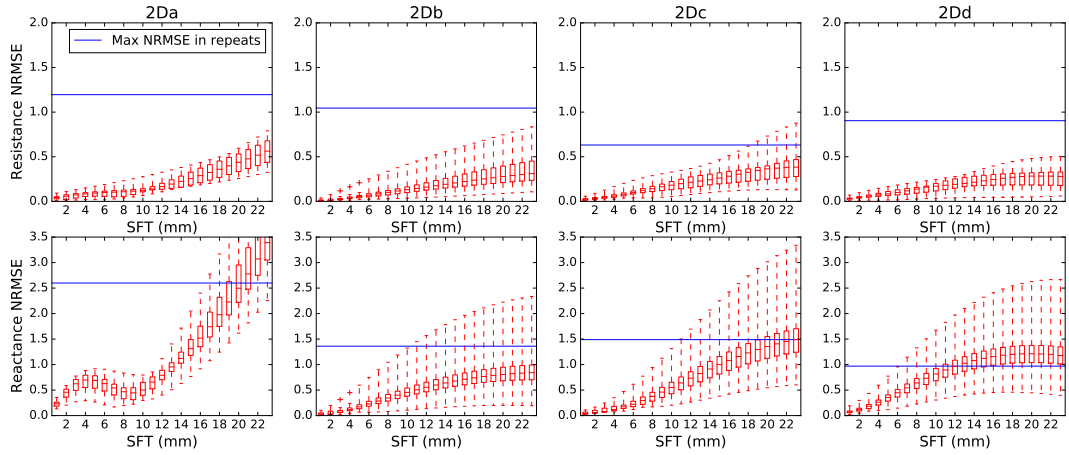

Figure 6.13: NRMSE for the deviation between the muscle reconstruction and the true muscle spectra. Shown for resistance and reactance for each configuration at each interval of SFT.

The transformation to separate the muscle spectra from the recorded EIM spectral data was applied to the limb EIM dataset. In order to further assess the effectiveness of the signal

separation, the data correlation with the SFT was assessed. The change in the absolute value of the Spearman rank for correlation between the EIM features and SFT is presented in figure 6.14. The majority of features see a reduction in the strength of correlation (change<0) across the impedance resistance, reactance, phase, and magnitude, for all muscles. This demonstrates the success of the signal separation since the dominance of the SFL is clearly being largely reduced.

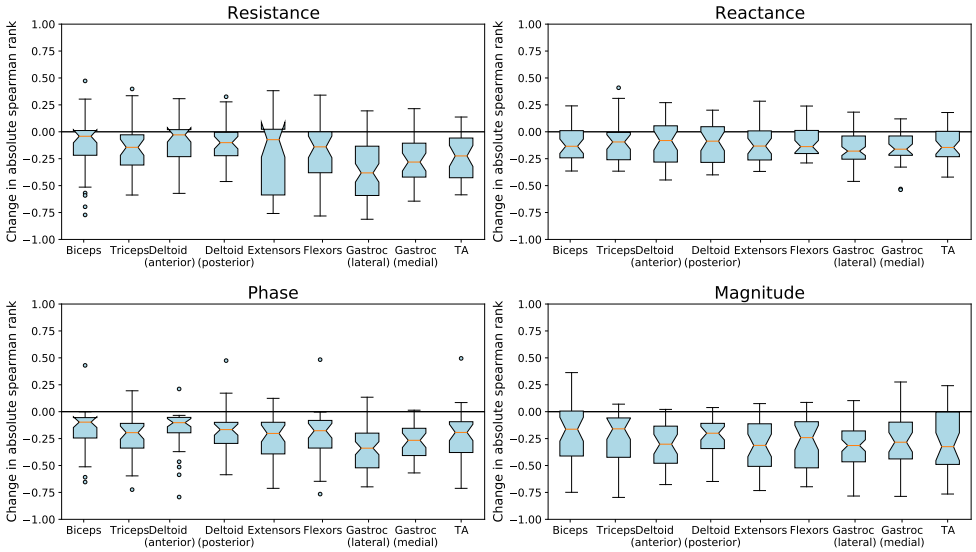

Figure 6.14: Assessment of the change in EIM correlation with SFT following the signal separation procedure. Change in the absolute value of the Spearman rank between the isolated EIM muscle signal features compared to the raw EIM data features ($|\rho_{\text{muscle}}| - |\rho_{\text{raw}}|$). A negative change represents a reduction in the strength of the correlation. Presented for the impedance resistance, reactance, phase, and magnitude, across all muscles.

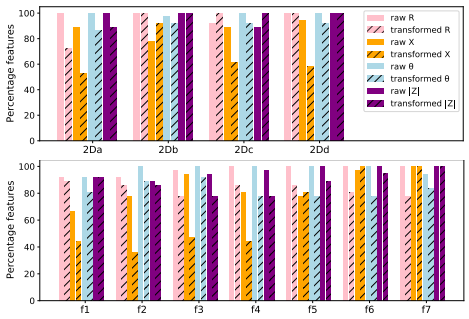

Figure 6.15: The percentage of features that exhibit a significant correlation (FDR-corrected p-value< 0.01) with SFT. Shown for the raw dataset (filled bars) and transformed dataset (hatched bars). Presented for all impedance metrics, split by electrode configurations and by frequency.

In addition, the significance of how the correlation with SFT changed was assessed. Figure 6.15 presents the percentage of the EIM features which exhibit a significant correlation (FDR-corrected p-value< 0.01) with SFT. This is shown for the raw EIM data and the transformed data following signal separation. It is clear that the dominance of the SFL was generally

reduced with maximal reduction in configuration 2Da, as well as for the lower frequencies (<156 kHz), particularly within the reactance. However, the contribution of the SFL was not entirely eliminated, with some of the features seeing a maintained or even increased correlation.

6.3.4 Biomarker performance of the isolated muscle EIM

Similar comparisons were made to assess how the signal separation procedure affected the EIM correlation with disease severity. Figure 6.16 presents an assessment of how the correlation of the EIM features with the ALSFRS-R limb subscore changes following the signal separation transformation. Comparison of the changes in the magnitude of the correlation ($|\rho|$) with the limb ALSFRS and the SFT are highly correlated (figure 6.16a). When the association with SFT was reduced, the association with the ALSFRS-R also decreased and vice-versa. Since the transformed EIM dataset generally saw reductions in the correlation with SFT, the same was found for ALSFRS-R correlations, indicating that the biomarker potential is actually worsening.

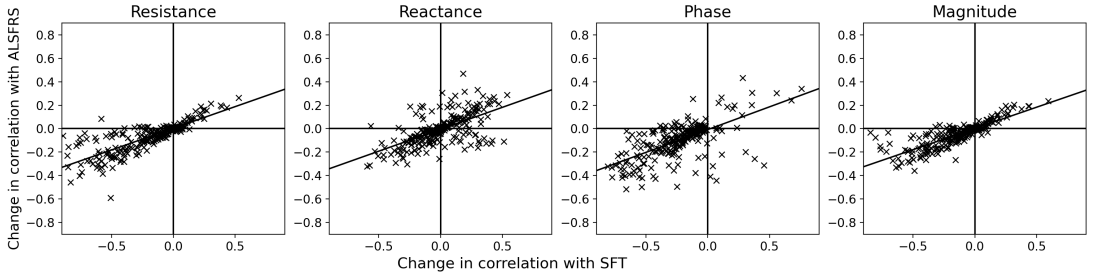

(a)

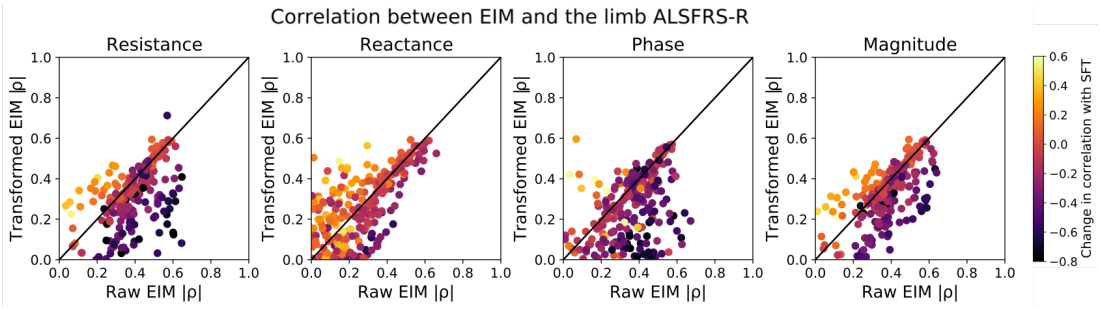

(b)

Figure 6.16: Assessment of how the correlation with the ALSFRS-R limb subscore changed following the signal separation transformation. (a) A scatter plot showing the change in the correlation with SFT against the change in correlation with the limb ALSFRS-R found a significant association between the two (best fit line plotted). (b) The absolute value of the Spearman rank for correlation between each EIM feature against limb ALSFRS-R, shown for the raw EIM data against the transformed EIM data. Features above the y=x line saw increased performance following transformation, and features below the line saw reduced performance. A single feature in the transformed EIM resistance data space found a significant correlation with the ALSFRS-R ($|\rho| = 0.71$, FDR-corrected p-value = 0.008).

This was further demonstrated by figure 6.16b, which shows a direct comparison of the correlation with the ALSFRS-R before and after signal separation. The colour of the plot represents how the association of each feature with SFT changed following the transformation. Generally, data above the line is more yellow (SFT association increased), while the data below the line is more purple (SFT association decreased). There is one feature outlying from this

trend, which is the transformed data point that demonstrated the most impressive correlation with the ALSFRS-R. Specifically, this is the resistance recorded on configuration 2Dc at the highest frequency (625 kHz) in the lateral gastrocnemius ($|\rho| = 0.71$, FDR-corrected p-value = 0.008). Converse to most of the data, this feature saw an increase in the magnitude of its correlation with the ALSFRS-R ($\Delta|\rho| = 0.14$), with a decrease in the association with SFT ($\Delta|\rho| = -0.60$). In fact, it is the only feature with a significant FDR-corrected p-value for correlation with the limb ALSFRS-R. A similar analysis of correlation with muscle strength can be seen in the appendix, figure D5.1, and demonstrated comparable results.

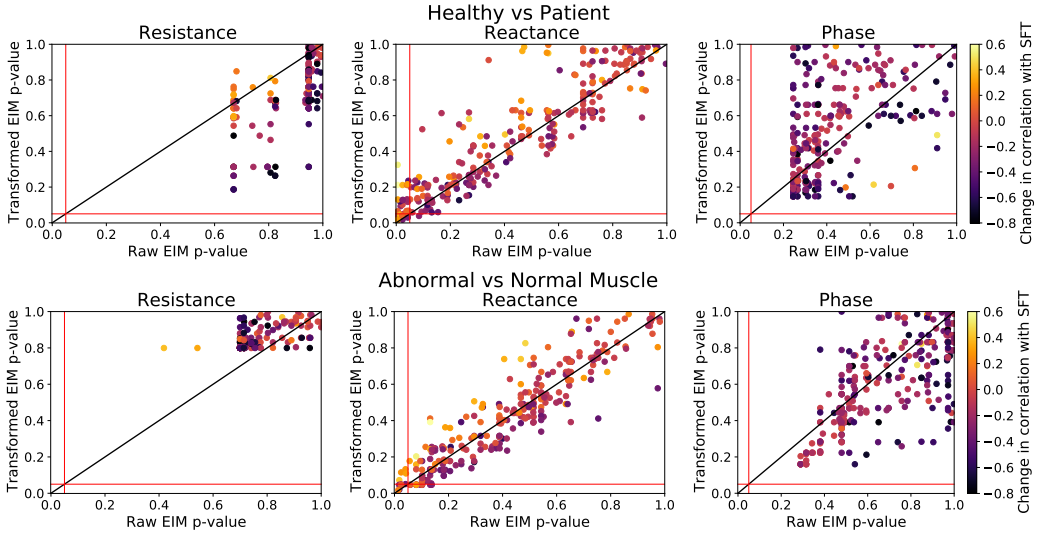

(a)

Test	Significance	Raw EIM	Transformed EIM
Patient vs Healthy	< 0.05	36 (14.3%)	20 (7.9%)
	< 0.01	18 (7.1%)	4 (1.6%)
	< 0.001	8 (3.2%)	0
Abnormal vs Normal muscle based on EMG	< 0.05	14 (5.6 %)	22 (8.3%)
	< 0.01	0	0
	< 0.001	0	0

(b)

Figure 6.17: Mann-Whitney U tests applied to each feature within the raw EIM dataset compared to the transformed EIM dataset. (a) Scatter plots of the FDR-corrected p-values for raw in comparison to transformed EIM. Shown for healthy/patient as well as normal/abnormal muscle discrimination. Features above the y=x line saw reduced discrimination performance following transformation, and features below the line saw increased performance. A colour map shows the change in the degree of correlation with SFT following transformation. (b) Table showing the proportion of reactance features with significant discrimination potential.

Additionally, the ability of the EIM features to separate different participant subgroups was assessed following the signal separation transformation. Figure 6.17 shows the FDR-corrected p-values for Mann-Whitney U tests between healthy participants and patients, and tests between abnormal and normal muscle in EMG findings. Scatter plots present how the significance of these tests changed following the signal separation. As with the raw EIM data no significant features were identified within the resistance or the phase transformed datasets. Interestingly, the majority of features saw an improved significance for healthy/patient separation within resistance and abnormal/normal separation within phase. On the other hand, the changes in significance for the reactance dataset were less pronounced, with most of the data points

clustered around the y=x line. In reactance, the significance of the performance looked to be more likely to improve if the correlation with SFT had reduced (darker purple points), and more likely to decline if this correlation had increased (lighter yellow points). Looking to the proportion of reactance features with significant p-values (figure 6.17b), the transformed data saw reduced features in patient/healthy separation but an increased number of features in abnormal/normal separation.

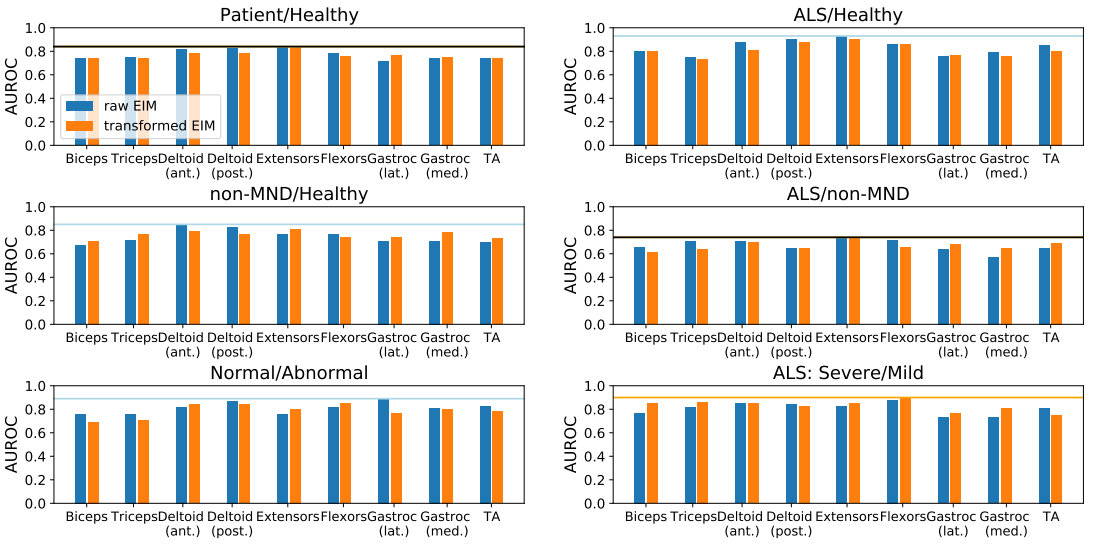

(a)

	Muscle	AUROC	Sensitivity	Specificity	Dataset	Features
Patient/ Healthy	Extensors	0.84	0.68	1.0	Raw	X: 2Da f2; 2Db f2; 2Dc f1; 2Dc f6
	Extensors	0.84	0.67	1.0	Transformed	X: 2Da f2; 2Db f1, f6; 2Dd f2
ALS/ Healthy	Extensors	0.93	0.86	1.0	Raw	X: 2Db f2; 2Dc f1
Mimic/ Healthy	Deltoid (anterior)	0.85	0.95	0.74	Raw	X: 2Da f3; 2Db f2; 2Dc f4
ALS/ Mimic	Extensors	0.74	0.75	0.73	Raw	X: 2Da f2, f4; 2Dc f1
	Extensors	0.74	0.79	0.69	Transformed	X: 2Da f2; 2Dc f1, f2, f4; 2Dd f1
Normal/ Abnormal	Gastroc (lateral)	0.89	0.90	0.89	Raw	X: 2Db f3; 2Dc f1
Severe/ Mild	Flexors	0.90	0.88	0.92	Transformed	R: 2Da f1, f2; 2Dc f5, X: 2Da f1

(b)

Figure 6.18: Classification AUROC results for each muscle on 6 different classification problems. Using support vector machine classifier, forward selection wrapper feature selection, with cross-validation applied. (a) Comparison of performance (AUROC) using the raw EIM dataset (blue) and the transformed EIM dataset (orange). The best AUROC for each problem is shown with a horizontal line (blue if raw data gave superior performance, orange if transformed data gave superior performance, and black if best performance was the same for both feature sets). (b) A table presenting the best performing muscle for each classification problem, showing the performance metrics and features selected.

In order to expand this assessment, classification models were applied to a number of classification problems, with performance compared between the raw and transformed feature sets. The classification was applied to each muscle in turn, across both the resistance and reactance, giving a total of 56 features (4 configurations, 7 frequencies, 2 impedance metrics) to select from. The AUROC values for both datasets, each muscle and each classification problem can be seen in figure 6.18. Additionally, a breakdown of the performance for each classification

is shown in appendix, figure D5.1. It is clear that the performance is relatively unchanged following signal separation, with some AUROC seeing small improvements and others seeing a decline.

The best performing muscle and dataset were identified for each classification problem; three had an optimal performance with the raw dataset, two had an unchanged best performance following transformation, and one had optimal performance for the transformed dataset. The most impressive result was seen for the classification of ALS and healthy (AUROC=0.93), with only 2 features selected to achieve this superior classification accuracy. While non-MND patients were more difficult to distinguish from healthy (AUROC=0.85). The lowest achieved performance was observed in ALS/non-MND classification (AUROC=0.74), which is expected to be a much harder problem due to overlaps in disease pathology. Only reactance features were selected in all problems apart from the severe/mild ALS classification. Here the optimal performance was seen with three resistance and one reactance features using the transformed feature set (AUROC=0.9). Looking to the muscles that saw the best performance, the extensors came up most frequently.

6.3.5 Tensor EIM framework

For additional assessment, the limb EIM dataset was factorised using the tensor EIM framework. This methodology followed the same procedure outlined in section 4.2.2, using NTF and PCA to reduce the high-dimensional data down to a single tensor EIM metric. This procedure was applied to each muscle in turn with 3-dimensional NTF employed, where the dimensions encapsulate the 14 impedance features (7 frequencies in R and X), the four electrode configurations, and each participant. The rank selection criteria determined a rank of 3 for all the arm muscles and a rank of 4 for the limb muscles. This process was applied to both the raw and transformed EIM datasets. The same spectral modes were implemented with each dataset so that a direct comparison of results could be made.

Table 6.2 presents the Spearman ranks for the correlation between tensor EIM with both SFT and the ALSFRS-R limb subscore. This assessment was repeated for each muscle in both the raw and transformed data. A highly significant correlation with the SFT was seen in many muscles, particularly the arm muscles. However, no correlation is observed in the gastrocnemius. Interestingly, after transformation, the forearm extensors and flexors, as well as the tibialis anterior, lose their significant correlation with SFT. In fact, almost all muscles show a decrease in the strength of the correlation with SFT, except for the medial gastrocnemius, which exhibits a slight increase but remains statistically insignificant.

A few muscles demonstrated significant correlation with the ALSFRS-R limb subscore, which includes the biceps, deltoids, extensors and flexors. For the majority of these cases, the association with SFT is also highly significant, hence the respective association with limb ALSFRS-R seems to be dependent on whether or not the SFT is also correlating. However, there is one outlier to this, in the transformed forearm extensors dataset where ALSFRS-R correlates but the SFT does not. Following the signal separation transformation, most muscles see a reduction in the strength of correlation with the ALSFRS-R, which is likely related to the reduced association with the subcutaneous fat (S-SFT and the limb ALSFRS-R are correlated, see figure 5.13).

Muscle	Correlation with SFT		Correlation with limb ALSFRS-R		Change in absolute correlation	
	Raw	Transformed	Raw	Transformed	with SFT	with ASLFRS-R
Biceps	-0.88 <0.001	-0.83 <0.001	0.48 0.009	0.50 0.007	-0.05	+0.02
Triceps	-0.76 <0.001	-0.72 <0.001	0.36 ns	0.38 ns	-0.04	+0.02
Deltoid (anterior)	0.82 <0.001	0.70 <0.001	-0.51 0.007	-0.46 0.02	-0.08	-0.05
Deltoid (posterior)	0.84 <0.001	0.56 0.007	-0.46 0.02	-0.21 ns	-0.28	-0.24
Extensors	0.67 <0.001	0.39 ns	-0.54 0.003	-0.48 0.01	-0.29	-0.06
Flexors	-0.56 0.008	-0.30 ns	0.43 0.04	0.37 ns	-0.26	-0.06
Gastroc (lateral)	0.38 ns	-0.16 ns	-0.2 ns	-0.15 ns	-0.22	-0.05
Gastroc (medial)	0.30 ns	0.35 ns	-0.22 ns	-0.19 ns	+0.05	-0.03
TA	-0.50 0.009	-0.26 ns	0.11 ns	0.03 ns	-0.24	-0.08

ns=not significant

Table 6.2: Spearman rank correlation and respective FDR-corrected p-values for correlation between tensor EIM and the SFT as well as the ALSFRS-R limb subscore. Presented for each muscle for the raw and transformed datasets. The final column shows how the strength of the correlation changed following data transformation.

The only muscle that saw a significant difference in the tensor EIM between healthy participants and patients was the anterior deltoids. Further assessment of the tensor EIM performance for this muscle was undertaken. Plots of the deltoid anterior tensor EIM against the limb ALSFRS-R and the S-SFT can be seen in the appendix, figure D5.2. Figure 6.19 shows the three spectral modes (a_1, a_2, a_3) that were used to factorise the anterior deltoid data. The tensor EIM was defined as a linear combination of these three spectra (using PCA), hence two spectral patterns were identified, one that increases with tensor EIM and the other that decreases with the tensor EIM.

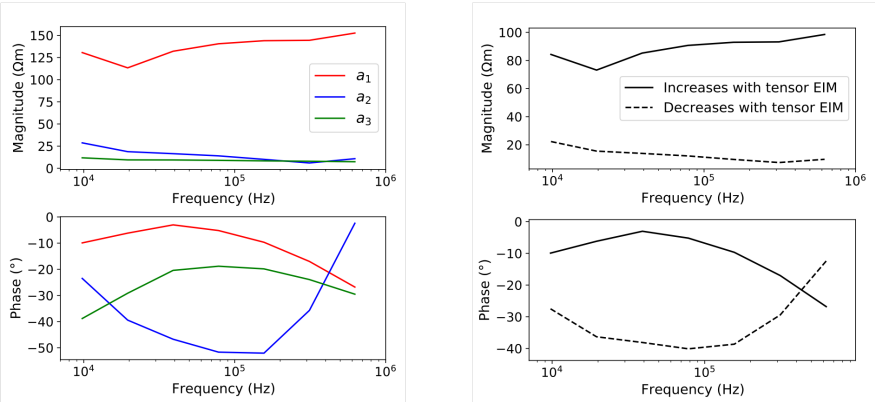

Figure 6.19: The spectral modes associated with the factorisation of the deltoid anterior data. As well as the spectra that aid the interpretability of the tensor EIM. One spectrum increases in contribution with tensor EIM (full line), and the other decreases in contribution with tensor EIM (dashed line).

Since the tensor EIM has a negative correlation with the ALSFRS-R limb subscore (table 6.2, this suggests that the metric increases with ALS disease severity. Looking to figure 6.19, this change can be understood as increasing impedance magnitude, and an increase in phase at all but the highest frequency. More specifically the phase sees a maxima rather than a minima

within the midline frequencies. Since the S-SFT reports significant positive correlations with the tensor EIM, then an increase in subcutaneous fat can also be attributed to this same change in spectral pattern.

Figure 6.20 shows the distribution of the tensor EIM for different participant subgroups. There was a significant difference identified between healthy and ALS, with the Mann-Whitney U p-value increasing in significance from p=0.03 to p< 0.001 when the dataset was transformed. Additionally, the transformed data saw a difference between ALS and non-MND (p=0.03) in the transformed dataset. No significant difference was seen when comparing the healthy to the non-MND group. Looking at ALS patients of different severities a significant difference with p=0.04 was maintained in the raw and transformed datasets. Additionally, the transformed dataset saw a significant difference between normal and abnormal muscle (p=0.02). Overall, all the significant changes are in agreement with the trend of increasing tensor EIM with disease state.

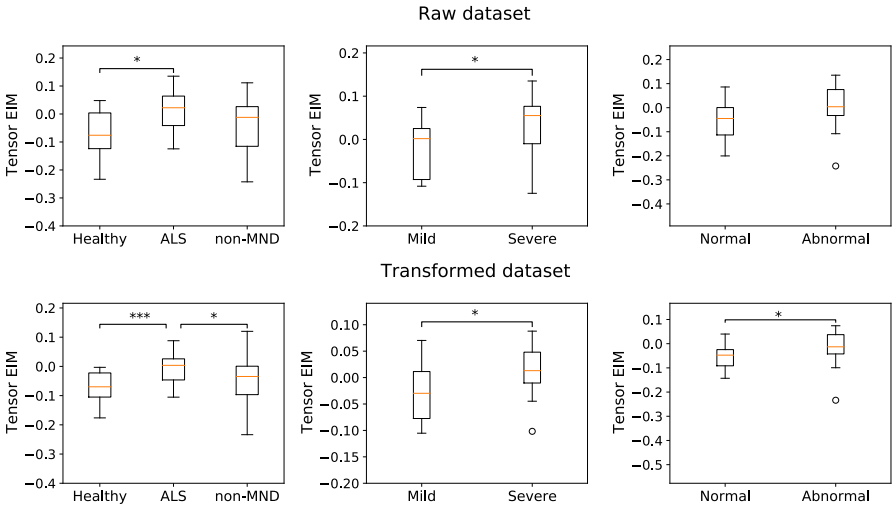

Figure 6.20: Distribution of tensor EIM in different participant groups (healthy, ALS, non-MND, mild ALS, severe ALS, normal EMG, abnormal EMG). Compared across raw and transformed datasets. Mann-Whitney U p-values are marked as * p<0.05, ** p<0.01, *** p<0.001.

Additionally, classification was applied using the NTF spectral weighting metrics. No feature selection was applied, rather all tensor weightings were incorporated into the model, meaning all information was preserved. A Naive Bayes classifier was used, with oversampling and cross-validation applied through the same approach as previously in described section 6.3.4. The same 6 classification problems were assessed, and the AUROC values for each muscle across the two datasets are presented in figure 6.21. In comparison to applying feature selection to the full high-dimensional dataset (figure 6.18), the performance of classification is generally reduced here. However, when comparing the results between the raw and transformed datasets, the latter saw a superior performance in all of the classification problems apart from the separation of ALS/non-MND. However, this specific classification generally performed poorly with most AUROC less than 60%. The posterior deltoid performed particularly well here, giving optimal performance for distinguishing healthy participants from all patients (AUROC=0.74); from ALS patients (AUROC=0.84); from non-MND patients (AUROC=0.69); and distinguishing normal from abnormal muscle (AUROC=0.72). The full set of classification metrics (AUROC, sensitivity, specificity) are presented in the appendix, figure D5.2.

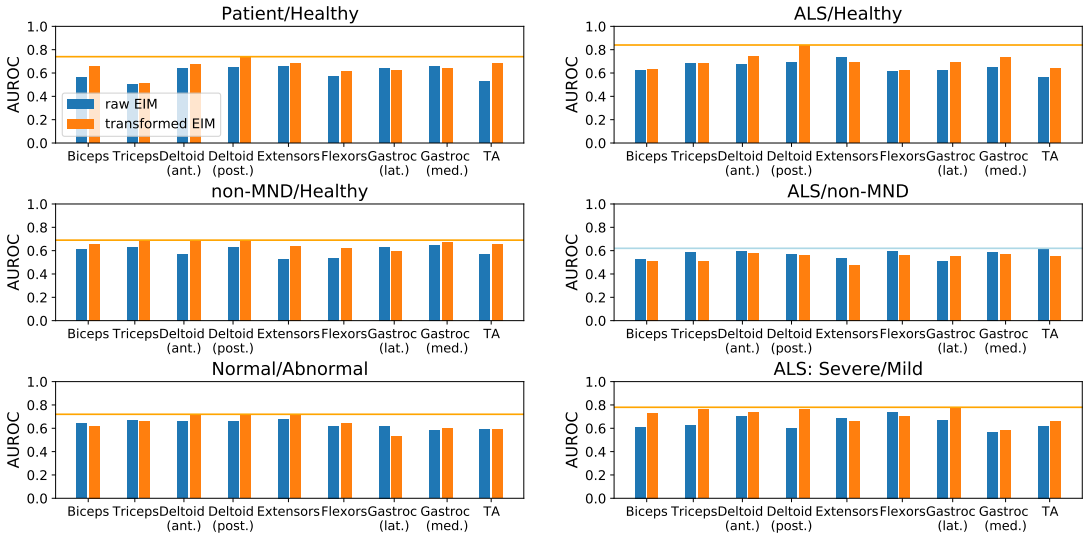

Figure 6.21: Classification AUROC results using the NTF metrics as features. Shown for each muscle on each different classification problem. Using Naive Bayes classifier with cross-validation applied.Comparison of performance (AUROC) using the raw tensor EIM dataset (blue) and the transformed tensor EIM dataset (orange). The best AUROC for each problem is shown with a horizontal line (blue if raw data gave superior performance, orange if transformed data gave superior performance).

Finally, an assessment of the difference between neurogenic and myopathic disease (based on EMG signs), was undertaken using the EIM framework. The number of patients who presented with signs of myopathy in their EMG assessment was limited, with only a handful (between 1 and 4) seen in each of the arm muscles, while none were seen in the leg muscles. The value of the tensor EIM was compared between the neurogenic and myopathic groups for each of the arm muscles in turn (figure 6.22), with the spectral interpretation of the tensor EIM also given. Overall, the myopathic group generally have a smaller value of tensor EIM observed in the biceps, triceps, and forearm extensors, and a bigger value in both deltoids and the forearm flexors. However, the spectral definitions of the tensor EIM were different for each muscle, hence in order to understand the spectral patterns the defining the metrics were noted.

Looking at the spectral patterns, the myopathic disease consistently followed the trend of having increased magnitude and increased phase (phase maxima rather than minima seen in the frequency range). Although, this is slightly different in the forearms, where magnitude tended to increase in the lower frequencies but decreased in the higher frequencies. Overall, the differentiation between the two groups looks to be more pronounced when looking to the transformed dataset. Due to the small sample sizes, none of these distributions see statistically significant separations thus these results must be interpreted as preliminary findings.

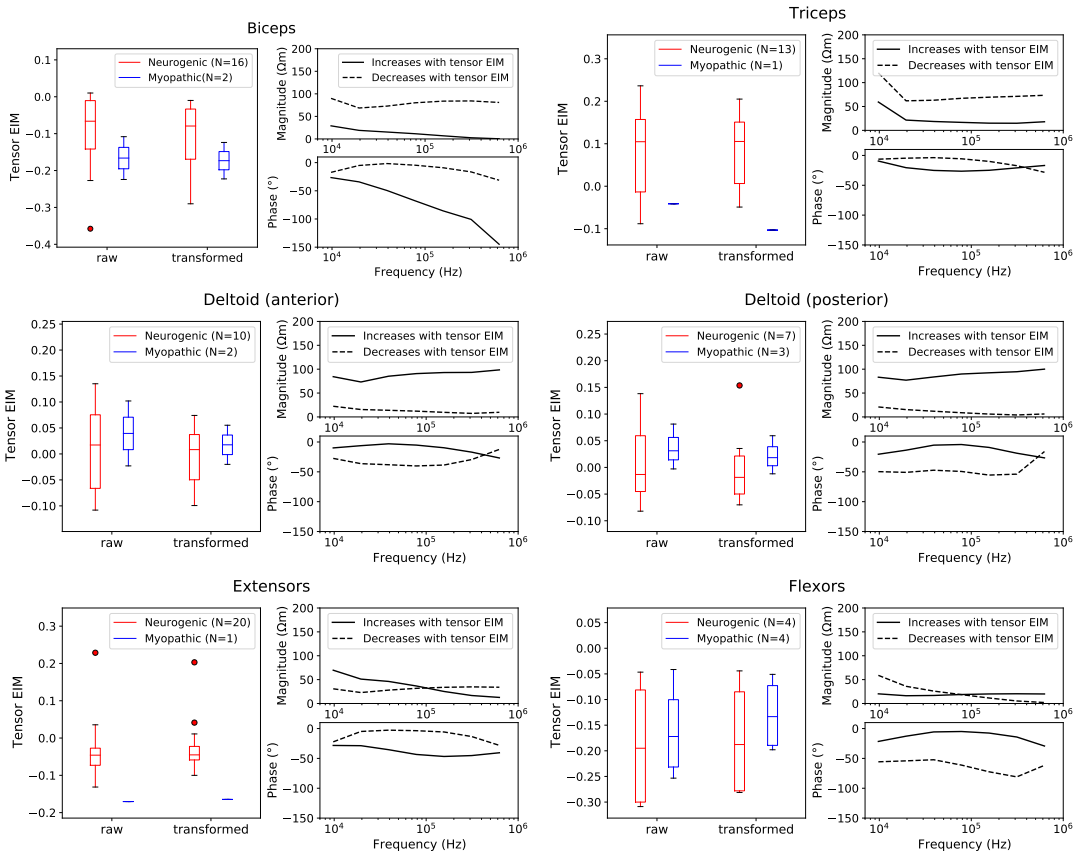

Figure 6.22: Tensor EIM for neurogenic and myopathic muscle shown for the raw and transformed datasets. Additionally, the spectra, which define tensor EIM are presented. Shown for each of the arm muscles in turn.

6.4 Discussion

The results presented in this chapter detail a comprehensive study of how the layer of subcutaneous fat contributes to the surface EIM measurements in the limbs. With the aid of the expected dielectric properties of biological tissue taken from previous literature and an ex vivo study in porcine tissue, a detailed FEM model of a human limb was built. A detailed and sophisticated optimisation algorithm was determined to refine the input parameters of the model in order to maximise the fit with the high-dimensional EIM measurement dataset. The preliminary stage of the optimisation involved determining the optimal values for 14 input parameters (cole-cole parameters for skin, fat, transverse muscle, and parallel muscle optimised in turn) to fit 56 EIM outputs (14 EIM spectral data points for each of the four electrode configurations). The second stage of the optimisation then involved determining the optimal value for 14 input parameters (cole-cole parameters for skin and fat in turn), to fit 672 EIM outputs (56 data across 12 different values of SFT). Overall, this was an extremely high-dimensional problem. Thus, in order to overcome the curse of dimensionality, bounds were implemented and the granularity of the optimisation grid-search space was carefully and appropriately adjusted throughout each stage of the optimisation to optimise the computational efficiency and maximise the parameter accuracy. Additionally, the input parameters were physically realistic (taken from Gabriel et al. (1996c)), which meant the initial values were already in proximity

to the optimal solution, so the computational effort and convergence time were significantly reduced.

Previous studies, which employed FEM models to investigate surface EIM in the limbs, used data from ex vivo mouse and rat gastrocnemius tissue to determine the dielectric inputs for muscle (Wang et al., 2011; Jafarpoor et al., 2011, 2013). However, there are limitations to this approach due to differences in the size of muscle fibres and architecture of the muscle (Mathewson et al., 2012). Conversely, porcine tissue is widely understood to be physiologically similar to human tissue with comparable biological responses and metabolic features (Spurlock and Gabler, 2008). Porcine models are argued to have a number of advantages compared to mouse models due to the closer anatomical size and similarity in genome structure (Selsby et al., 2015). One previous study used porcine skin, subcutaneous fat and muscle to model impedance measurements in the human abdomen (Wang et al., 2022). Furthermore, the dielectric properties of porcine skin have been found to be highly similar to human (Karacolak et al., 2012). Overall, porcine tissue is a promising candidate to estimate the dielectric properties of human tissue.

These same studies (Wang et al., 2011; Jafarpoor et al., 2011, 2013) additionally utilised the dataset presented in Gabriel et al. (1996b,c) for the dielectric properties of the skin and subcutaneous fat. Interestingly, when comparing the data from the study by Gabriel et al. (1996c) to the porcine dielectric properties that were recorded here, there were some pronounced differences. Particularly for fat, both the conductivity and permittivity were found to be between one and two orders of magnitude higher in the porcine tissue compared to that previously presented in humans. It is definitely probable that humans and pigs would see some differences in the dielectric properties of fat, but due to their anatomical similarities, such a pronounced difference would not be expected. In fact looking to the range of human data reported across the literature, as was presented in Gabriel et al. (1996a), there is a significant disagreement of up to four orders of magnitude in the dielectric spectra for fat. The observed variations could be attributed to a combination of factors including inter-subject variability, non-homogeneous properties of subcutaneous fat and variations across the body, as well as measurement errors. Since the primary objective of the FEM limb model is to understand and incorporate the impacts of the S-SFL, reaching an accurate estimate for the properties of the skin and fat was a crucial stage.

The final optimised model gave a good agreement with the measured dataset across all the EIM frequencies and configurations. In particular, the contribution of changing subcutaneous fat thickness was impressively characterised. The availability of the target impedance dataset, which was recorded over a healthy cohort with variation in their S-SFT (2-16mm), allowed for a very comprehensive understanding of how varying levels of fat are expected to impact the impedance spectra. The refined dielectric properties for fat and skin ultimately fell in between the spectral patterns recorded in the porcine tissue and those produced by Gabriel et al. (1996c). This is the first time such a model has been built and optimised in the field of surface impedance of the limbs. Future datasets could be utilised to enhance the model, where the inclusion of additional configurations of measurement would help increase the accuracy of the model optimisation. Overall, the use of such a model has the potential to be a highly useful tool for a deeper understanding of surface EIM measurements. For example, the relative contribution of the skin and subcutaneous fat for different electrode configuration setups can be assessed, with the objective of identifying configurations that exhibit minimal S-SFL contribution. Such efforts have previously been pursued (Jafarpoor et al., 2013), however, the FEM model parameters were not optimised to fit measured datasets, and hence the model developed here should be a much closer representation of real tissue. However, it must be noted that the FEM model has a number of limitations including a simplification of the limb geometry, assuming isotropic skin

and fat, and assuming homogeneity of all tissues. For this reason, despite a successful model agreement, the optimised parameters must be taken with caution.

Ultimately, the finalised model was used to determine how the combined S-SFL and muscle impedance signal can be separated in order to isolate the specific impedance properties of the muscle. Using both the FEM model and validation from measurement data in different layerings of porcine tissue it was found that the impedance signals can be modelled as combining as a linear sum. Using the refined dielectric properties of skin and fat it was then possible to use modelled data to predict the respective weightings for the S-SFL and the muscle at each level of SFT. This methodology was able to reconstruct the isolated muscle impedance spectra with impressive accuracy, especially for smaller SFL thicknesses (< 12mm).

When this reconstruction was applied to the measurement dataset, the transformed data exhibited an overall reduced correlation with the SFT across all muscles. This is evidence that the procedure is effectively removing at least some of the dominance of the fat layer. Particularly since the process of signal separation uses parameters that are directly dependent on the value of the SFT, any inaccuracies in the model could lead to an increase in the dependence on SFT. The dominance of fat was significantly mitigated in the reactance data for electrode configuration 2Da and frequency f2 (19.5 kHz), where the proportion of data exhibiting a significant correlation with SFT was reduced from 90% to 50%, and from 78% to 35%, respectively. Interestingly, this frequency and configuration combination were selected as a feature in all classification problems that gave optimal performance when using the transformed dataset. Furthermore, assessment of the tensor EIM metric found reductions in its association with SFT across the board, in fact, the tensor EIM for the forearm and leg muscles all presented an insignificant correlation with the SFT following the signal separation. While there has been one previous attempt to determine a method for signal separation to remove the contribution of the SFL (Kwon et al., 2019), their methodology has not been tested on a multi-participant dataset, therefore there is no evidence of a reduction in the correlation with SFT. Overall, the methodology presented here is the first time a procedure for signal separation in surface EIM data has successfully proven to be effective at removing the SFL dominance.

With clear evidence that the signal separation transformation had removed at least some of the dominance of the SFL a thorough comparison was made on the biomarker performance of the raw and transformed datasets. It was evident that as a general trend, the reduced correlation with SFT led to a reduced correlation with the ALSFRS-R, which is indicative of worsening biomarker performance. Since it is known that the SFT and ALSFRS-R have strong associations, perhaps the inclusion of the S-SFL is helpful for understanding disease severity to some level. However, none of the features within the raw EIM dataset saw a significant correlation with the ALSFRS-R when FDR correction was applied. In fact, the only feature that displayed significance was a transformed EIM feature, which gave optimal correlation with the ALSFRS ($|\rho|$=0.71, p< 0.01). This feature had seen a huge reduction in its association with SFT ($|\Delta|\rho| = -0.6$), thence this is suggestive that for this feature the signal separation had been successful in isolating the muscle and eliminating the SFL. Since this was only apparent in a single feature out of 252 it is possible that such a result could appear from random fluctuations, however, the combination of increasing association with disease and decreasing association with the SFL is certainly encouraging to see. In regards to the performance of the data to discriminate between different groups within the cohort, there wasn't a particularly noteworthy change when looking at the individual features within the high-dimensional dataset. In both the raw and transformed datasets the only impedance metric that found a significant difference in patients/healthy participants as well as normal/abnormal muscle was the reactance, which as we know has the least correlation with SFT. A comparison of the raw and transformed datasets saw a slight improvement within the raw data for separating patients/healthy but a slight

improvement within the transformed dataset for separating normal/abnormal. Generally, there was a more pronounced difference in the SFT for patients and healthy participants compared, with little disparity in fat thickness across normal and abnormal muscle, so this result makes sense.

Classification models applied with feature selection across the multi-dimensional data space achieved a promising performance across a range of different classification problems. Both the raw and transformed datasets performed well with AUROC > 0.9 in ALS/healthy classification; AUROC > 0.85 in normal/abnormal and severe mild classification; AUROC > 0.8 in patient/healthy and non-MND/healthy classification; AUROC>0.7 in ALS/non-MND classification. Generally, ALS was easier to identify as this group had more severe disease (see 5.5), additionally, differentiation between ALS and non-MND may well be due to the differences in levels of disease severity rather than inherent pathological differences between the diseases. Further assessment between these groups would be worthwhile, where assessing the difference between ALS and non-MND for only the subsets of patients with abnormal muscle (from EMG signs) would give more insight into any inherent disease-specific differences. Additionally, comparisons between the ALS group and the different subsets of diseases within the non-MND cohort would be of interest.

As has been emphasised throughout this thesis, there is always a likelihood of overfitting these models when wrapper feature selection is applied and sample sizes are small. The features that were selected were predominantly reactance. This again emphasises the preference for the use of reactance, which is both less dominated by the SFL and presents superior biomarker capabilities. However, the majority of previous studies in EIM of the limbs have only assessed phase (Rutkove et al., 2002, 2005, 2006, 2007; Garmirian et al., 2009; Rutkove et al., 2012a, 2014; Offit et al., 2020). Overall when the tensor decomposition features were used for classification, the transformed EIM notably tended to perform better than the raw EIM. While the classification performance here was not as impressive as with wrapper feature selection applied, this method has the advantage of being unsupervised with all spectral information maintained. Hence, results are more robust and overfitting is less likely.

The tensor EIM framework was utilised to reduce the high-dimensional dataset down to a single metric. The tensor EIM is defined by two spectral patterns one that increases in contribution with the metric and the other that decreases. With this framework, the spectral shift with disease could be understood as increasing magnitude and a shift to a much less negative phase. The physiological effects of atrophy can be understood as increases in the amount of connective tissue and fat, which in turn would be expected to increase resistance (Rutkove, 2009) as well as a reduction in the cell membrane capacitance (Al-Sarraj et al., 2014), which across a system of muscle cells with capacitance's in series, would lead to a reduction in X_C and hence reactance becoming less negative. Therefore the observed pattern changes are in agreement with what would be expected following atrophy. When comparing the differences in tensor EIM for neurogenic compared to myopathic disease signs, myopathic muscle tended to have a spectral shift analogous to that seen for worsening disease (increased magnitude and less negative phase). This trend was identified across all the muscles, which is an encouraging sign. However, the sample sizes were very small, especially in the myopathic groups, so further work is needed to validate these findings. Additionally, a previous study was able to identify differences in the anisotropy of limb EIM when comparing myopathic and neurogenic disease (Garmirian et al., 2009). These findings suggest that a combination of tensor EIM and anisotropy assessment may be helpful for a deeper understanding of these different categories of disease.

6.5 Conclusions: biomarker potential of EIM in the limbs

Throughout the final two analysis chapters I have explored the challenges and potential of surface EIM of the limbs as a potential biomarker for neurological diseases. In comparison to EIM of the tongue, there are a number of difficulties to overcome when assessing data recorded on the limbs. Specifically, only higher frequency EIM is possible due to the effects of recording on keratinised skin, and 3D configurations have proven difficult to assess due to larger volumes of less conductive tissue. However, the high frequency (> 9.8 kHz) and 2D configuration data were found to be highly reproducible.

Overall, the most prevalent challenge to overcome is the dominance of the layer of subcutaneous fat on measurements; where highly significant correlations were identified between EIM and SFT. Conversely, there was not much association found between EIM and the disease state. An additional complexity is apparent since there was a pattern of increasing SFT present with a worsening disease, with significant differences identified between healthy participants and patients, as well as a significant correlation with the ALSFRS-R. Overall this indicates the potential of a cause-and-effect association between EIM and the disease state since changes in SFT tend to affect both factors. Therefore, the main goal of this assessment was to gain a deeper understanding of how the SFL contributes, so that the signal could be characterised and separated in order to isolate the muscle specific impedance information.

An FEM model of a human limb was developed, and the input dielectric parameters were optimised with the measured EIM dataset used as the target data. The model gave a very impressive agreement with the measurement dataset. Specifically, the trends with the SFT were very well characterised, which suggests a high level of accuracy in the characteristics of fat. Overall this model gives credible insight into the contribution of the SFL in surface impedance.

With insights from the FEM model, as well as ex vivo measurements taken in porcine tissue the superposition of impedance signals from the S-SFL and muscle layer were modelled. Using this a rigorous signal separation process was developed, and was found to reduce the dominance of the SFL across the majority of the dataset. Following signal separation, the biomarker performance of the dataset improved in some areas and worsened in others. However, this is partially due to the causal relationship between EIM, and the disease state, where both have associations with the SFT. Overall, classification models found a good performance for the separation of the different patients with the healthy cohort, as well as separating patients of different severities and disease states (maximum AUROC=0.93 ALS/healthy, 0.90 severe/mild; 0.89 normal/abnormal). Additionally, the tensor EIM framework provided a single metric to represent the high-dimensional dataset, allowing for a deeper understanding of spectral shifts with disease states. The spectral shifts observed in diseased muscle were consistent with the expected changes in atrophy.

Clearly, EIM in the limbs has the potential to be an effective biomarker, with the ability to identify disease muscle and distinguish between differing levels of disease severity. Additionally, the data has shown promise for separating myopathic and neurogenic muscle. However, in order to fully establish the clinical utility of limb EIM, more work is necessary to validate these findings as well as to further develop and refine the methodology for removing the contribution of the SFL.

7 Chapter 7: Future work

7.1 Increasing sample size

It is challenging to recruit a large number of ALS patients for research studies, due to the rare nature of the disease. For this reason, the participant sample sizes tend to be small. In fact, previous studies on the biomarker potential of EIM had an extremely limited number, of between 1 and 11 ALS patients (Rutkove et al., 2002, 2005; Esper et al., 2006; Garmirian et al., 2009; Mcilduff et al., 2017). In order to maximise sample size multicentre research studies must be conducted over longer time periods. Some such studies in limb EIM have been completed (Rutkove et al. 2012a, Rutkove et al. 2014; N=60, 12 month study). However, the assessment only pertained to the 50 kHz impedance phase metric, which as noted earlier in this thesis is likely to be statistically biased and provide an incomplete and largely uninterpretable measure of muscle health. In order to validate the assessments of the multi-dimensional EIM datasets that have been presented in this work, it is crucial to repeat analyses on further datasets, where increased sample sizes would improve the robustness and statistical power of the results.

For example, in the study of the tongue dataset there appeared to be an improvement in the classification performance of the lateral compared to central measurement data, where incorporation of both feature sets gave optimal performance. However, there was a limited sample size, particularly when the requirement for data on both central and lateral measurements reduced this available sample size. Therefore, it was not possible to perform a statistically significant comparison between these two datasets. A larger study to undergo a comprehensive assessment of the biomarker capabilities of multiple tongue placement positions would be worthwhile. Furthermore, the use of a probe with an electrode array that covers a larger area of the tongue would mean multiple areas across the tongue could be studied in one placement. Additionally, a larger electrode array offers the possibility of employing additional electrode configurations.

As well as recruiting more participants for the study, the sample size within the dataset could also be increased if the number of spectra that end up being rejected due to the presence of artefacts were reduced. Possible reasons for artefacts include patient movement, poor or variable electrode contact, as well as external electrical interference such as radio transmissions. For this reason, it is important for the clinician to ensure they maintain good electrode contact throughout and do not move the device, the comfort of the patient should be ensured to minimise their likelihood of movement, and the study should be conducted in a room with no background interference signals. In some cases, the prevalence of more severe symptoms may hinder this, for example, if the patient presents with fasciculations in the muscle. If this is the case the clinician must proceed with extra caution. Additionally, when measurements are undertaken in the limbs or any area of keratinised skin, thorough skin preparation is crucial to minimise artefacts. These techniques were employed during measurements for the collection of both datasets studied in this thesis, however, data were still lost due to artefacts. In the tongue dataset, 3.1% of the data was lost in outlier removal, for the central and lateral measurement datasets, 2.2% and 4.5% of these were lost, respectively, since poor contact was more likely when the device was placed on the tongue edge. For the limb dataset artefacts were even more prevalent, with 10.3% of the data lost in outlier removal. Clearly, artefactual spectra are not uncommon to see, even with best efforts made to minimise their prevalence. For future work, the outlier identification procedures could be implemented into the software of the EIM device measurement stage. By doing this the clinician would be notified if a measurement contained spectral artefacts, which would prompt them to repeat the measurement. Furthermore, since it has now been widely evidenced that EIM gives impressive reproducibility, repeat measurements would not be needed if no artefacts were present, which would increase the efficiency of the study.

All the classification models presented in this thesis would benefit from validation with data collected in an additional study cohort. Since the data is very high-dimensional and sample sizes are relatively small, the chances of overfitting are potentially high (even with cross-validation), in particular when wrapper based feature selection was employed. Assessment of the model performance on unseen data will determine the degree to which these models may or may not have overfit the dataset. Furthermore, if an additional study had increased participant numbers, it would be possible to implement a more robust methodology involving nested cross-validation. This process involves an outer cross-validation, where the data is split into k folds, as well as an inner cross-validation for feature selection (He et al., 2020). Adaptations of this methodology are also possible and include consensus nested cross-validation (Parvandeh et al., 2020), as well as repeated double cross-validation (Filzmoser et al., 2009). These techniques would allow for a more reliable and rigorous assessment of the relevant features, as well as identification of the more redundant features. Furthermore, with increases in sample size, an even more extensive number of features could be comprehensively assessed.

The work presented here has introduced a novel methodology for the assessment of high-dimensional EIM data, termed tensor EIM. This technique has proven to be very effective at providing a single metric, which shows much promise as an effective biomarker of disease, as well as providing a comprehensive interpretation of how changes in the metric relate to directional shifts in the EIM spectral pattern. In order to demonstrate that tensor EIM is a robust and generalisable tool, and increase the statistical power of the findings, this methodology should be applied to further datasets, with an increased sample size. Collaborating with other research institutions, medical centres, and organisations worldwide would help gather diverse datasets and facilitate the validation of Tensor EIM across different populations. This would facilitate the future adoption of Tensor EIM as a standard biomarker tool.

The longitudinal assessment of tensor EIM in the tongue demonstrated potential as a sensitive tool for monitoring disease progression. However, although patients were seen up to 12 months from baseline where possible, results are only presented up to 9 months, due to a significant patient drop off by the 12 month mark. As ALS is so relentlessly progressive by nature, it is important for even more patients to be recruited for longitudinal studies, in order to account for patient death throughout the study period. Assessment of the longitudinal change of tensor EIM saw complex multi-directional changes in individuals. This was hypothesised to be due to different stages of disease, where the direction of spectral change is expected to be different in acute compared to chronic denervation. Some preliminary data presented in comparison to EMG findings validated this hypothesis, but further assessment is needed in a larger number of patients with both acute and chronic signs of disease confirmed through EMG.

Furthermore, the limb EIM research study project did not involve a longitudinal assessment of patients (due to delays caused by the Covid-19 pandemic). Therefore, future work to assess the changes of EIM in the limbs is an obvious next stage of analysis. A number of previous studies have presented assessments of how limb EIM changes with time, and found promising results (Rutkove et al., 2007, 2012a; Schwartz et al., 2015; Rutkove et al., 2017; Shefner et al., 2018; Kapur et al., 2019; Offit et al., 2020). However, none of this analysis involved any attempts to remove the contribution of the SFL. From my analysis, it is clear that SFL dominates EIM signals, where additionally the thickness of the SFL has shown a significant correlation with the severity of the disease. It is therefore possible that the previous studies may have been capturing changes in the SFT rather than changes to the fundamental structure of the muscle. A future longitudinal study, where both EIM and SFT are measured longitudinally in a large cohort of patients is crucial for further understanding of the biomarker potential of EIM in the limbs. The work presented here also gave a preliminary understanding of the spectral differences that one may expect to occur in myopathic compared to neurogenic muscle, however, the patient

numbers were very small and this assessment needs to be validated on a larger cohort. With a larger sample size, it would be possible to undertake a deeper analysis with a more complex tensor decomposition to investigate the spectral shifts for these different types of disease.

Overall, in order to promote further progression of this research a multicentre research study with access to a larger cohort of patients is necessary. Moreover, artefact assessment should be undertaken at the time of collection to maximise data. This is a crucial next stage for validation of the results presented in this thesis, as well as an avenue for investigating further measurement types and refining analyses.

7.2 Signal separation

A sophisticated signal separation procedure has been presented and shown to effectively reduce the dominance of the SFL across most features in the dataset. Overall, while this approach demonstrated some improvements to the biomarker potential of the dataset, there was clearly still a remaining contribution of the SFL signal in the transformed dataset. To improve the viability of surface limb EIM, future work will be necessary to refine this methodology, as well as to explore different analysis techniques for signal separation.

The signal separation procedure was based on a number of assumptions, including consistent dielectric properties for skin and fan across all participants of all disease states. Additionally, both the fat and the skin were assumed to be isotropic in nature, and the effect of bone was neglected in the model. The FEM model was also optimised for a generic limb utilising the measurement data collected from all muscle sites simultaneously. It is possible that by undertaking a more rigorous process of building a separate model for each muscle, one may capture intricate differences between the muscles, such as disparities in the properties of fat seen at different locations on the body. In order to account for the properties of fat changing throughout the disease, different models could be fit for subsets of patients at different levels of disease severity. However, this could be difficult to accurately model, since it is possible that there would be significant discrepancies in the dielectric properties of the muscle between different patients, even if they are presenting a similar degree of symptoms.

Another option would be to optimise an FEM model for each participant in turn. This would be based on the assumption that the properties of the fat are consistent across one person's body, but would account for the potential for significant inter-participant differences. Performing optimisation on each participant in turn could be computationally expensive. However, if the parameters are effectively initialised and constrained it could be possible. While the instrumentation of the limb device appeared to struggle with 3D configurations, such measurement paradigms may describe additional disease relevant information, as was demonstrated in the tongue study. If an updated instrumentation design can be used for viably measuring in a 3D plane, additional configurations could be incorporated into the model. This would increase the size of the target dataset providing the optimisation with more information to achieve a more accurate fit. However, with the use of 3D configurations, it would be necessary to incorporate the bone into the model and include two separate muscles with potentially differing properties.

In order to improve our understanding of the dielectric properties of fat, an ex vivo study in postmortem human tissue could be extremely valuable. This would allow for a more comprehensive understanding of the true dielectric properties of the SFL in humans. Such a study would allow for an assessment of the isotropic nature of both skin and subcutaneous fat. Additionally, it would be advantageous to assess the homogeneity of the properties of the SFL at different positions on the body, as well as a comparison between different human subjects. Further insight into the differences in the dielectric properties of the SFL when comparing healthy individuals to patients affected by neurodegenerative diseases such as ALS would be

very useful. Access to such data would be invaluable for enhancing the accuracy of the limb FEM model, although there will be postmortem changes that occur to subcutaneous tissue that need to be considered (Van Grinsven et al., 2017). Furthermore, access to additional limb EIM datasets would be necessary to further validate the performance of the optimised model.

Analysis of FEM modelled data supports the hypothesis that the combined skin, fat and muscle impedance signal can be decomposed as a linear combination of the S-SFL as well as that of the muscle. Where the specific coefficients pertaining to the contribution of the skin-subcutaneous fat, and the muscle varies for each configuration. Based on this decomposition it would be theoretically possible to remove the signal of the S-SFL without knowing what the expected signal is, with the use of two electrode configurations. Specifically, if two configurations were utilised which pertain to the same geometry but cover a different area of tissue, then the combined signals would be given by:

$$\begin{aligned} Z^1_{\text{combined}} &= a_1 Z_{\text{S-SFL}} + b_1 Z_{\text{muscle}} \\ Z^2_{\text{combined}} &= a_2 Z_{\text{S-SFL}} + b_2 Z_{\text{muscle}} \end{aligned} \tag{7.1}$$

Therefore, if the mixing coefficients a_1, b_1, a_2, and b_2, were determined via FEM modelling, then the two combined signals could be used to calculate the signal of the isolated muscle as:

$$Z_{\text{muscle}} = \frac{a_1 a_2}{b_1 a_2 - b_2 a_1} \left(\frac{Z^1_{\text{combined}}}{a_1} - \frac{Z^2_{\text{combined}}}{a_2} \right). \tag{7.2}$$

such an approach would provide a simple and effective method for removing the S-SFL signal where inter-participant differences in the properties of fat, potential anisotropy in the fat, as well as non-homogeneity of the fat across the body, would no longer become an issue. Although this approach does assume local homogeneity of the skin, the fat and the muscle. The values of the coefficients for the relative contribution of S-SFL and muscle will have some dependence on the property of the fat itself, which would introduce some error into the reconstruction, however, these variations are likely to be relatively small.

Additional analyses for separating the signal of the skin-subcutaneous fat could be pursued with the use of NMF or NTF. Specifically, the EIM dataset could be decomposed with one of the spectral modes being set as the impedance signal analogous to that expected from the skin-subcutaneous fat. Furthermore, the specific weighting of that mode would be forced to have proportionality to the SFT. With this implemented, the remaining modes of the decomposition should then theoretically pertain to the muscle specific information. Likewise, regression techniques could be employed for a more detailed understanding of how the EIM data is dominated by the S-SFL by assessing its performance for predicting the thickness of the subcutaneous fat. Additionally, covariate adjustments could be made in regression modelling in order to account for the influence of the thickness of the subcutaneous fat in the modelling.

7.3 Additional data comparison and combination

While EIM stands on its own as a promising biomarker for ALS and other neurodegenerative diseases, its capacity could be further expanded by using EIM in tandem with additional measurement data. For example, recent work has presented the development of a device that records EIM and surface EMG signals simultaneously (Vavrinskỳ et al., 2018; Ngo et al., 2022), both of which can provide disease relevant information about the muscle. Moreover, electrophysiology biomarkers such as MUNIX/MUNE could provide useful insights when used alongside EIM, where the process of acute denervation can be directly assessed with the motor unit number. Henceforth, the spectral shifts in EIM following significant acute denervation can be more directly understood. Clearly, needle EMG is also crucial for providing important information

pertaining to the disease state including signs of acute denervation, chronic reinnervation, myopathic disease, and neurogenic disease. Additionally, ultrasound data has also shown promise in detecting disease progression for neurodegenerative disease (Zaidman et al., 2017), and combining this information with EIM spectral data could give a more detailed picture of disease. Overall a multivariate regression analysis could be utilised to incorporate multiple types of data to predict the severity and state of the disease.

The most recent advancement for EIM is the development of needle EIM, where the impedance is recorded from a needle which is inserted into the muscle (Cardoner et al., 2021; Luo et al., 2023; Rutkove et al., 2023). Such a methodology is beneficial as it directly measures the muscle without the contribution of the S-SFL, however, it is clearly a significantly more invasive procedure than surface EIM measurements. Needle EIM has thus far been shown to be both reproducible as well as effective at directly determining the dielectric properties of the muscle (Cardoner et al., 2021; Luo et al., 2023). Potentially, a study that utilised needle EIM in tandem with surface EIM could be used to test and refine the methodology for signal separation. If accurate and efficient signal separation could be implemented, then the invasive nature of needle EIM may not be necessary.

8 Conclusion

In conclusion, this work has found that tongue EIM emerges as a promising application of EIS. The characterisation of tongue tissue using multiple electrode configurations and frequencies, facilitated by the tensor EIM framework, adds value providing a comprehensive picture of the muscle health. Tongue EIM shows significant potential as a biomarker, demonstrating diagnostic capabilities and exhibiting strong correlations with disease severity. Furthermore, tongue EIM captures complex changes over time, enhancing its utility in monitoring disease progression and treatment efficacy. Overall, the objectives of the project outlined at the start of the thesis have been successfully completed, culminating in the validation of hypotheses i-vi in regards to tongue EIM as a biomarker for bulbar disease.

Conversely, the application of EIM in the limbs presents distinct challenges due to the confounding influence of fat tissue. However, SFL measurements have also shown apparent correlations with disease, which may be an underlying factor in previous findings related to the biomarker potential of EIM in the limbs. Overall, the clear dominance of subcutaneous fat in surface EIM measurements suggests that without appropriate signal separation, these measurements are primarily related to impedance lipography. As set out in the objectives, the main focus of the limb study involved a comprehensive assessment of the effect of this dominant subcutaneous fat layer, with the development of a methodology for separating the muscle signal. It was found that while it is possible to mitigate the contributions of subcutaneous fat through appropriate techniques, further research is necessary to address the complexities of this problem. This work has served to substantiate hypothesis vii, presenting strong evidence of a high correlation between limb EIM and fat thickness, with the use of FEM modelling to capture this effect. Preliminary work in signal separation has contributed to the assessment of hypothesis viii, however, additional efforts are needed to refine this work and comprehensively assess the level of muscle specific information that can be revealed. Overall, these advancements in EIM offer valuable prospects for non-invasive diagnostics and monitoring of diseases.

References

M. A. Ahad, P. Narayanaswami, and S. B. Kasselman, L. J. an Rutkove. The effect of subacute denervation on the electrical anisotropy of skeletal muscle: Implications for clinical diagnostic testing. *Clinical Neurophysiology*, 121(6):882–86, 2010.

J.-H. Ahn, S. Kim, J.-H. Oh, and S. Choi. Multiple nonnegative-matrix factorization of dynamic pet images. In *Proceedings of Asian Conference on Computer Vision*, pages 1009–1013. Citeseer, 2004.

M. Akmal, S. Zubair, M. Jochumsen, E. N. Kamavuako, and I. K. Niazi. A tensor-based method for completion of missing electromyography data. *IEEE access*, 7:104710–104720, 2019. ISSN 2169-3536.

A. Al-Chalabi, O. Hardiman, M. C. Kiernan, et al. Amyotrophic lateral sclerosis: moving towards a new classification system. *The Lancet Neurology*, 15(11):1182–1194, 2016. ISSN 1474-4422.

S. Al-Sarraj, A. King, M. Cleveland, P.-F. Pradat, A. Corse, J. D. Rothstein, P. N. Leigh, B. Abila, S. Bates, J. Wurthner, and V. Meininger. Mitochondrial abnormalities and low grade inflammation are present in the skeletal muscle of a minority of patients with amyotrophic lateral sclerosis; an observational myopathology study. *Acta neuropathologica communications*, 2(1):165–165, 2014. ISSN 2051-5960.

J. Alix, M. Plesia, S. Hool, C. Coldicott, I.and Kendall, P. Shaw, R. Mead, and J. Day. Fiber optic raman spectroscopy for the evaluation of disease state in duchenne muscular dystrophy: An assessment using the mdx model and human muscle. 2022a.

J. Alix, M. Plesia, G. Lloyd, A. Dudgeon, C. Kendall, C. Hewamadduma, M. Hadjivassiliou, C. McDermott, G. Gorman, R. Taylor, P. Shaw, and J. Day. Rapid identification of human muscle disease with fibre optic raman spectroscopy. 2022b.

J. Alix, M. Plesia, C. Schooling, A. Dudgeon, C. Kendall, V. Kadirkamanathan, C. McDermott, G. Gorman, R. Taylor, R. Mead, P. Shaw, and J. Day. Non-negative matrix factorisation of raman spectra finds common patterns relating to neuromuscular disease across differing equipment configurations, preclinical models and human tissue. 2022c.

J. J. Alix, H. E. Mcdonough, B. Sonbas, S. J. French, D. G. Rao, V. Kadirkamanathan, C. J. Mcdermott, T. J. Healey, and P. J. Shaw. Multi-dimensional electrical impedance myography of the tongue as a potential biomarker for amyotrophic lateral sclerosis. *Clinical Neurophysiology*, 131(4):799–808, 2020. ISSN 1388-2457.

J. J. P. Alix, M. Plesia, G. R. Lloyd, A. P. Dudgeon, C. A. Kendall, C. J. McDermott, G. S. Gorman, R. W. Taylor, P. J. Shaw, and J. C. Day. The application of raman spectroscopy to the diagnosis of mitochondrial muscle disease: A preliminary comparison between fibre optic probe and microscope formats. *Journal of Raman spectroscopy*, 53(2):172–181, 2022d. ISSN 0377-0486.

J. J. P. Alix, N. S. Verber, C. N. Schooling, V. Kadirkamanathan, M. R. Turner, A. Malaspina, J. C. C. Day, and P. J. Shaw. Label-free fibre optic raman spectroscopy with bounded simplex-structured matrix factorization for the serial study of serum in amyotrophic lateral sclerosis. *Analyst (London)*, 147(22):5113–512, 2022e. ISSN 0003-2654.

P. M. Andersen, S. Abrahams, G. D. Borasio, et al. Efns guidelines on the clinical management of amyotrophic lateral sclerosis (mals) – revised report of an efns task force. *European Journal of Neurology*, 19(3):360–375, 2012.

D. Andreuccetti, R. Fossi, and P. C. An internet resource for the calculation of the dielectric properties of body tissues in the frequency range 10 hz-100 ghz. *Based on data published by C.Gabriel et al. in 1996. IFAC-CNR, Florence (Italy)*, 1997. URL http://niremf.ifac.cnr.it/tissprop/.

D. Anumba, V. Stern, J. Healey, S. Dixon, and B. Brown. The value of cervical electrical impedance spectroscopy to predict spontaneous preterm delivery in asymptomatic women: the ecclippx prospective cohort study. *Ultrasound in Obstetrics & Gynecology*, 2020.

P. Aram, L. Shen, J. A. Pugh, S. Vaidyanathan, and V. Kadirkamanathan. An efficient tof-sims image analysis with spatial correlation and alternating non-negativity-constrained least squares. *Bioinformatics*, 31(5):753–760, 2015. ISSN 1367-4803.

T. Aridegbe, R. Kandler, S. J. Walters, et al. The natural history of motor neuron disease: Assessing the impact of specialist care. *Amyotrophic Lateral Sclerosis and Frontotemporal Degeneration*, 14(1):13–19, 2013. doi: 10.3109/17482968.2012.690419. URL https://doi.org/10.3109/17482968.2012.690419.

E. M. Bald, C. S. Nance, and J. L. Schultz. Melatonin may slow disease progression in amyotrophic lateral sclerosis: Findings from the pooled resource open-access als clinic trials database. *Muscle & nerve*, 63(4):572–576, 2021. ISSN 0148-639X.

R. H. Baloh, W. Rakowicz, R. Gardner, et al. Frequent atrophic groups with mixed-type myofibers is distinctive to motor neuron syndromes. *Muscle & Nerve: Official Journal of the American Association of Electrodiagnostic Medicine*, 36(1):107–110, 2007.

R. Bayford. Bioimpedance tomography (electrical impedance tomography). *The Annual Review of Biomedical Engineering*, 8(1):63–91, 2006. ISSN 1523-9829.

M. Benatar, K. Boylan, A. Jeromin, S. B. Rutkove, J. Berry, N. Atassi, and L. Bruijn. Als biomarkers for therapy development: State of the field and future directions. *Muscle & nerve*, 53(2):169–182, 2016.

Y. Benjamini and Y. Hochberg. Controlling the false discovery rate: a practical and powerful approach to multiple testing. *Journal of the Royal statistical society: series B (Methodological)*, 57(1):289–300, 1995.

C. M. Bishop. *Pattern Recognition and Machine Learning*. Springer, 2006.

J. M. Bland and D. G. Altman. Measuring agreement in method comparison studies. *Statistical Methods in Medical Research*, 8(2):135–160, 1999. doi: 10.1177/096228029900800204. URL https://doi.org/10.1177/096228029900800204. PMID: 10501650.

V. Bolón-Canedo, N. Sánchez-Maroño, and A. Alonso-Betanzos. *Feature selection for high-dimensional data*. Springer, 2015.

S. C. Bourke, M. Tomlinson, T. L. Williams, et al. Effects of non-invasive ventilation on survival and quality of life in patients with amyotrophic lateral sclerosis: a randomised controlled trial. *Lancet Neurology*, 5(2):140–147, 2006. ISSN 1474-4422.

L. Breiman. Random forests. *Machine learning*, 45:5–32, 2001.

R. G. Brereton. *Chemometrics: data analysis for the laboratory and chemical plant*. John Wiley & Sons, 2003.

R. Bro. Multiway analysis in the food industry. models, algorithms and applications. *Ph.D. dissertation, University of Amsterdam, Amsterdam*, 08 2001.

K. Brodlie, D. Duke, and K. Joy. Transfer functions for imaging spectroscopy data using principal component analysis. 2005.

T. Brody. *Clinical trials [electronic resource] : study design, endpoints and biomarkers, drug safety, FDA and ICH guidelines*. Academic Press, London, 1st ed. edition, 2012. ISBN 1-283-32021-5.

P. Bühlmann, M. Kalisch, and L. Meier. High-dimensional statistics with a view toward applications in biology. *Annual Review of Statistics and Its Application*, 1:255–278, 2014.

R. H. Byrd, P. Lu, J. Nocedal, and C. Zhu. A limited memory algorithm for bound constrained optimization. *SIAM Journal on scientific computing*, 16(5):1190–1208, 1995.

S. Byrne, C. Walsh, C. Lynch, et al. Rate of familial amyotrophic lateral sclerosis: a systematic review and meta-analysis. *Journal of Neurology, Neurosurgery & Psychiatry*, 82(6):623, 2011. ISSN 0022-3050. URL http://jnnp.bmj.com/content/82/6/623.full.pdf.

E. J. Calabrese, V. Calabrese, and J. Giordano. Demonstrated hormetic mechanisms putatively subserve riluzole-induced effects in neuroprotection against amyotrophic lateral sclerosis (als): Implications for research and clinical practice. *Ageing research reviews*, 67:101273, 2021. ISSN 1568-1637.

M. M. d. M. Cardoner, H. Kwon, H. V. G. Pulido, J. Nagy, S. Rutkove, and B. Sanchez. Modeling and reproducibility of twin concentric electrical impedance myography. *IEEE transactions on biomedical engineering*, 68(10):3068–3077, 2021. ISSN 0018-9294.

B. M. Carlson. The biology of long-term denervated skeletal muscle. *European journal of translational myology*, 24(1), 2014. ISSN 2037-7452.

J. D. Carroll and J. J. Chan. Analysis of individual differences in multidimensional scaling via an n-way generalization of "eckart-young" decomposition. *Psychometrika*, 35:293–319, 1970.

G. C. Cawley and N. L. Talbot. On over-fitting in model selection and subsequent selection bias in performance evaluation. *Journal of Machine Learning Research*, 11(Jul):2079–2107, 2010.

J. M. Cedarbaum, N. Stambler, E. Malta, et al. The alsfrs-r: a revised als functional rating scale that incorporates assessments of respiratory function. *Journal of the Neurological Sciences*, 169(1-2):13–21, 1999. ISSN 0022-510X.

G. Chandrashekar and F. Sahin. A survey on feature selection methods. *Computers & electrical engineering*, 40(1):16–28, 2014. ISSN 0045-7906.

C. H. Chen, T. Wu, and N. S. Chu. Bilateral cortical representation of the intrinsic lingual muscles. *Neurology*, 52(2):411–413, 1999. ISSN 0028-3878.

K.-S. Cheng, Y.-L. Su, L.-C. Kuo, T.-H. Yang, C.-L. Lee, W. Chen, and S.-H. Liu. Muscle mass measurement using machine learning algorithms with electrical impedance myography. *Sensors (Basel, Switzerland)*, 22(8):3087, 2022. ISSN 1424-8220.

C. T.-S. Ching, T.-P. Sun, S.-H. Huang, C.-S. Hsiao, C.-H. Chang, S.-Y. Huang, Y.-J. Chen, C.-S. Cheng, H.-L. Shieh, and C.-Y. Chen. A preliminary study of the use of bioimpedance in the screening of squamous tongue cancer. *International journal of nanomedicine*, 5(default): 213–220, 2010. ISSN 1178-2013.

A. Chiò, S. Battistini, A. Calvo, et al. Genetic counselling in als: facts, uncertainties and clinical suggestions. *Journal of Neurology, Neurosurgery & Psychiatry*, 85(5):478, 2014. ISSN 0022-3050. URL http://jnnp.bmj.com/content/85/5/478.full.pdf.

A. Chiò, J., A. Calvo, D., L. Mazzini, D., et al. Extensive genetics of als: A population-based study in italy. *Neurology*, 79(19):1983–1989, 2012. ISSN 0028-3878.

A. Cichocki and A.-H. Phan. Fast local algorithms for large scale nonnegative matrix and tensor factorizations. *IEICE transactions on fundamentals of electronics, communications and computer sciences*, 92(3):708–721, 2009.

A. Cichocki and R. Zdunek. Regularized alternating least squares algorithms for non-negative matrix/tensor factorization. In *Advances in Neural Networks – ISNN 2007*, volume 4493 of *Lecture Notes in Computer Science*, pages 793–802, Berlin, Heidelberg, 2007. Springer Berlin Heidelberg. ISBN 3540723943.

A. Cichocki, R. Zdunek, A. H. Phan, and S.-I. Amari. *Nonnegative matrix and tensor factorizations*. Wiley-Blackwell, Hoboken, NJ, Sept. 2009.

B. A. Cisterna, A. A. Vargas, C. Puebla, P. Fernández, R. Escamilla, C. F. Lagos, M. F. Matus, C. Vilos, L. A. Cea, E. Barnafi, H. Gaete, D. F. Escobar, C. P. Cardozo, and J. C. Sáez. Active acetylcholine receptors prevent the atrophy of skeletal muscles and favor reinnervation. *Nature communications*, 11(1):1073–1073, 2020. ISSN 2041-1723.

J. Cohen. *Statistical power analysis for the behavioral sciences*. Routledge, 2nd edition, 1988.

K. S. Cole and R. H. Cole. Dispersion and absorption in dielectrics i. alternating current characteristics. *The Journal of Chemical Physics*, 9(4):341–351, Apr. 1941. doi: 10.1063/1.1750906. URL https://doi.org/10.1063/1.1750906.

A. COMSOL. Comsol multiphysics® v. 6.1. www.comsol.com., 2023. URL https://www.comsol.com/comsol-multiphysics.

D. R. Cox. Regression models and life-tables. *Journal of the Royal Statistical Society. Series B, Methodological*, 34(2):187–220, 1972. ISSN 0035-9246.

P. Cunningham and S. J. Delany. k-nearest neighbour classifiers. 2007.

A. Czaplinski, A. A. Yen, and S. H. Appel. Forced vital capacity (fvc) as an indicator of survival and disease progression in an als clinic population. *Journal of Neurology, Neurosurgery & Psychiatry*, 77(3):390, 2006. ISSN 0022-3050. URL http://jnnp.bmj.com/content/77/3/390.full.pdf.

S. Dalise, V. Azzollini, and C. Chisari. Brain and muscle: How central nervous system disorders can modify the skeletal muscle. *Diagnostics (Basel)*, 10(12):1047, 2020. ISSN 2075-4418.

R. B. Daroff and M. J. Aminoff. *Encyclopedia of the neurological sciences*. Academic press, 2014.

M. de Carvalho and M. Swash. Lower motor neuron dysfunction in als. *Clinical Neurophysiology*, 127(7):2670–2681, 2016.

M. de Carvalho, R. Dengler, A. Eisen, et al. Electrodiagnostic criteria for diagnosis of als. *Clinical Neurophysiology*, 119(3):497–503, 2008. ISSN 1388-2457.

J. O. Deasy. Multiple local minima in radiotherapy optimization problems with dose–volume constraints. *Medical physics (Lancaster)*, 24(7):1157–1161, 1997. ISSN 0094-2405.

E. Debie and K. Shafi. Implications of the curse of dimensionality for supervised learning classifier systems: theoretical and empirical analyses. *Pattern Analysis and Applications*, 22: 519–536, 2019.

M. Devine, M. Kiernan, K. Pannek, S. Rose, P. McCombe, and R. Henderson. 28.: Asymmetry of motor dysfunction in amyotrophic lateral sclerosis: The effect of limb dominance. *Journal of clinical neuroscience*, 21(11):2042–2042, 2014. ISSN 0967-5868.

M. S. H. Di Fiore. *Di fiore's atlas of histology: With functional correlations*. Lippincott Williams and Wilkins, Philadelphia, PA, 9 edition, Apr. 2000.

C. Ding, T. Li, and M. I. Jordan. Nonnegative matrix factorization for combinatorial optimization: Spectral clustering, graph matching, and clique finding. In *2008 Eighth IEEE International Conference on Data Mining*, pages 183–192. IEEE, 2008.

M. Dittmar. Reliability and variability of bioimpedance measures in normal adults: Effects of age, gender, and body mass. *American journal of physical anthropology*, 122(4):361–370, 2003. ISSN 0002-9483.

C. P. Douglass, R. H. Kandler, P. J. Shaw, et al. An evaluation of neurophysiological criteria used in the diagnosis of motor neuron disease. *Journal of Neurology, Neurosurgery & Psychiatry*, 81(6):646, 2010. ISSN 0022-3050. URL http://jnnp.bmj.com/content/81/6/646.full.pdf.

F. Duck. Electrical properties of tissue in phys. prop. tissues, 1990.

A. Ebied, L. Spyrou, E. Kinney-Lang, and J. Escudero. On the use of higher-order tensors to model muscle synergies. 2020.

M. Elamin, P. Bede, S. Byrne, et al. Cognitive changes predict functional decline in als: A population-based longitudinal study. *Neurology*, 80(17):1590–1597, 2013. ISSN 0028-3878.

G. J. Esper, C. A. Shiffman, R. Aaron, et al. Assessing neuromuscular disease with multifrequency electrical impedance myography. *Muscle & Nerve*, 34(5):595–602, 2006. ISSN 0148-639X.

A. Farinha, S. Kellogg, K. Dickinson, and T. Davison. Skin impedance reduction for electrophysiology measurements using ultrasonic skin permeation: initial report and comparison to current methods. *Biomedical Instrumentation & Technology*, 40(1):72–77, 2006.

A. Field. *Discovering statistics using IBM SPSS statistics*. sage, 2013.

P. Filzmoser, B. Liebmann, and K. Varmuza. Repeated double cross validation. *Journal of Chemometrics: A Journal of the Chemometrics Society*, 23(4):160–171, 2009.

B. Frenay and M. Verleysen. Classification in the presence of label noise: A survey. *IEEE transaction on neural networks and learning systems*, 25(5):845–869, 2014. ISSN 2162-237X.

C. Gabriel, S. Gabriel, and E. Corthout. The dielectric properties of biological tissues: I. literature survey. *Physics in medicine & biology*, 41(11):2231–2249, 1996a. ISSN 0031-9155.

S. Gabriel, R. W. Lau, and C. Gabriel. The dielectric properties of biological tissues: II. measurements in the frequency range 10 hz to 20 GHz. *Physics in Medicine and Biology*, 41(11):2251–2269, nov 1996b. doi: 10.1088/0031-9155/41/11/002. URL https://doi.org/10.1088%2F0031-9155%2F41%2F11%2F002.

S. Gabriel, R. W. Lau, and C. Gabriel. The dielectric properties of biological tissues: Iii. parametric models for the dielectric spectrum of tissues. *Physics in medicine & biology*, 41 (11):2271–2293, 1996c. ISSN 0031-9155.

T. A. Gaige, T. Benner, R. Wang, V. J. Wedeen, and R. J. Gilbert. Three dimensional myoarchitecture of the human tongue determined in vivo by diffusion tensor imaging with tractography. *Journal of Magnetic Resonance Imaging: An Official Journal of the International Society for Magnetic Resonance in Medicine*, 26(3):654–661, 2007.

A. Gallina, S. J. Garland, and J. M. Wakeling. Identification of regional activation by factorization of high-density surface emg signals: A comparison of principal component analysis and non-negative matrix factorization. *Journal of electromyography and kinesiology*, 41:116–123, 2018. ISSN 1050-6411.

W. Gao, L. Zhou, S. Liu, Y. Guan, H. Gao, and J. Hu. Machine learning algorithms for rapid estimation of holocellulose content of poplar clones based on raman spectroscopy. *Carbohydrate Polymers*, 292:119635, 2022.

L. P. Garmirian, A. B. Chin, and S. B. Rutkove. Discriminating neurogenic from myopathic disease via measurement of muscle anisotropy. *Muscle & Nerve*, 39(1):16–24, Jan. 2009. doi: 10.1002/mus.21115.

M. Gaweł. Electrodiagnostics: Mune and munix as methods of estimating the number of motor units–biomarkers in lower motor neurone disease. *Neurologia i neurochirurgia polska*, 53(4): 251–257, 2019.

T. R. Geisbush, N. Visyak, L. Madabusi, S. B. Rutkove, and B. T. Darras. Inter-session reliability of electrical impedance myography in children in a clinical trial setting. *Clinical neurophysiology*, 126(9):1790–1796, 2015. ISSN 1388-2457.

A. Gerzhik, A. Kobelev, P. Luzhnov, and I. Sergeev. Calibration method for precision electrical impedance measurement system. In *2020 Ural Symposium on Biomedical Engineering, Radioelectronics and Information Technology (USBEREIT)*, pages 0016–0019. IEEE, 2020.

R. J. Gilbert and V. J. Napadow. Three-dimensional muscular architecture of the human tongue determined in vivo with diffusion tensor magnetic resonance imaging. *Dysphagia*, 20(1):1–7, 2005.

C. L. Gooch, T. J. Doherty, K. M. Chan, et al. Motor unit number estimation: A technology and literature review. *Muscle & Nerve*, 50(6):884–893, 2014. ISSN 0148-639X.

S. A. Goutman, O. Hardiman, A. Al-Chalabi, A. Chió, M. G. Savelieff, M. C. Kiernan, and E. L. Feldman. Recent advances in the diagnosis and prognosis of amyotrophic lateral sclerosis. *The Lancet Neurology*, 2022.

S. Greenland, S. J. Senn, K. J. Rothman, J. B. Carlin, C. Poole, S. N. Goodman, and D. G. Altman. Statistical tests, p values, confidence intervals, and power: a guide to misinterpretations. *European journal of epidemiology*, 31:337–350, 2016.

I. Guyon and A. Elisseeff. An introduction to variable and feature selection. *Journal of machine learning research*, 3(Mar):1157–1182, 2003.

C. E. Hafer-Macko, A. S. Ryan, F. M. Ivey, and R. F. Macko. Skeletal muscle changes after hemiparetic stroke and potential beneficial effects of exercise intervention strategies. *Journal of rehabilitation research and development*, 45(2):261–272, 2008. ISSN 0748-7711.

D. Halliday, R. Resnick, and J. Walker. *WIE Fundamentals of Physics Extended, Sixth Edition,*. Wiley, July 2000. ISBN 0471392227. URL https://www.xarg.org/ref/a/0471392227/.

J. A. Hanley and K. O. Hajian-Tilaki. Sampling variability of nonparametric estimates of the areas under receiver operating characteristic curves: an update. *Academic radiology*, 4(1): 49–58, 1997.

O. Hardiman, L. H. van den Berg, and M. C. Kiernan. Clinical diagnosis and management of amyotrophic lateral sclerosis. *Nature Reviews Neurology*, 7(11):639–649, Oct. 2011. doi: 10.1038/nrneurol.2011.153. URL https://doi.org/10.1038/nrneurol.2011.153.

O. Hardiman, A. Al-Chalabi, A. Chio, et al. Amyotrophic lateral sclerosis. *Nature Reviews Disease Primers*, 3(1), 2017. ISSN Nature Reviews Disease Primers.

R. A. Harshman and M. E. Lundy. Parafac: Parallel factor analysis. *Computational Statistics & Data Analysis*, 18(1):39–72, 1994.

R. A. Harshman et al. Foundations of the parafac procedure: Models and conditions for an" explanatory" multimodal factor analysis. 1970.

T. Hastie, R. Tibshirani, J. H. Friedman, and J. H. Friedman. *The elements of statistical learning: data mining, inference, and prediction*, volume 2. Springer, 2009.

D. M. Hawkins. The problem of overfitting. *Journal of chemical information and computer sciences*, 44(1):1–12, 2004.

J. He, P. Chalise, et al. Nested and repeated cross validation for classification model with high-dimensional data. *Revista Colombiana de Estadística*, 43(1):103–125, 2020.

T. J. Healey, E. R. Billinge, J. J. Alix, V. Kadirkamanathan, and C. R. Kemp. Circuit architecture for electrical impedance spectroscopy instrumentation to address electrode impedance mismatch in clinical devices. *IEEE Sensors Journal*, 21(20):22258–22269, 2021.

J. P. Heath, K. D. Hunter, C. Murdoch, and D. C. Walker. Computational modelling for electrical impedance spectroscopy-based diagnosis of oral potential malignant disorders (opmd). *Sensors*, 22(15):5913, Aug. 2022. ISSN 1424-8220. doi: 10.3390/s22155913. URL http://dx.doi.org/10.3390/s22155913.

R. D. Henderson, F. C. Garton, M. C. Kiernan, M. R. Turner, and A. Eisen. Human cerebral evolution and the clinical syndrome of amyotrophic lateral sclerosis. *Journal of Neurology, Neurosurgery & Psychiatry*, 90(5):570, 2019. ISSN 0022-3050. URL https://jnnp.bmj.com/content/90/5/570.full.pdf.

B. Hentze, T. Muders, H. Luepschen, E. Maripuu, G. Hedenstierna, C. Putensen, M. Walter, and S. Leonhardt. Regional lung ventilation and perfusion by electrical impedance tomography compared to single-photon emission computed tomography. *Physiological measurement*, 39(6):065004–065004, 2018. ISSN 0967-3334.

E. Hobson and C. McDermott. Supportive and symptomatic management of amyotrophic lateral sclerosis. *Nature Review Neurology*, 12:526–38, 2016.

D. Holder. Brief introduction to bioimpedance. *Series in Medical Physics and Biomedical Engineering Electrical Impedance Tomography*, page 411–422, 2004. doi: 10.1201/9781420034462. axa.

G. Hopkin. Neonatal and adult tongue dimensions. *The Angle Orthodontist*, 37(2):132–133, 1967.

E. Hosseini-Asl, J. M. Zurada, and A. El-Baz. Lung segmentation based on nonnegative matrix factorization. In *2014 IEEE International Conference on Image Processing (ICIP)*, pages 877–881. IEEE, 2014.

C. Hu, H. Hu, X. Mai, W. L. A. Lo, and L. Li. Correlation between muscle structures and electrical properties of the tibialis anterior in subacute stroke survivors: A pilot study. *Frontiers in neuroscience*, 13:1270–1270, 2019. ISSN 1662-4548.

P. Hua, E. Woo, J. Webster, and W. Tompkins. Finite element modeling of electrode-skin contact impedance in electrical impedance tomography. *IEEE transactions on biomedical engineering*, 40(4):335–343, 1993. ISSN 0018-9294.

S. B. Hulley and S. R. Cummings. *Designing Clinical Research*. Wolters Kluwer Health, 4th edition, 2013.

W. Huynh, N. G. Simon, J. Grosskreutz, M. R. Turner, S. Vucic, and M. C. Kiernan. Assessment of the upper motor neuron in amyotrophic lateral sclerosis. *Clinical Neurophysiology*, 127(7): 2643–2660, 2016.

J. Iwanaga and R. S. Tubbs. *Anatomy of the Oral Cavity*, page 47–105. Springer International Publishing, 2021. ISBN 9783030783273. doi: 10.1007/978-3-030-78327-3_3. URL http://dx.doi.org/10.1007/978-3-030-78327-3_3.

M. Jafarpoor, A. J. Spieker, J. Li, M. Sung, B. T. Darras, and S. B. Rutkove. Assessing electrical impedance alterations in spinal muscular atrophy via the finite element method. *2011 Annual International Conference of the IEEE Engineering in Medicine and Biology Society*, pages 1871–1874, 2011. ISSN 1094-687X.

M. Jafarpoor, J. Li, J. K. White, and S. B. Rutkove. Optimizing electrode configuration for electrical impedance measurements of muscle via the finite element method. *IEEE transactions on biomedical engineering*, 60(5):1446–1452, 2013. ISSN 0018-9294.

T. M. Jenkins, J. J. P. Alix, R. H. Kandler, et al. The role of cranial and thoracic electromyography within diagnostic criteria for amyotrophic lateral sclerosis. *Muscle & Nerve*, 54(3): 378–385, 2016. ISSN 0148-639X.

T. M. Jenkins, J. J. P. Alix, C. David, et al. Imaging muscle as a potential biomarker of denervation in motor neuron disease. *Journal of Neurology, Neurosurgery & Psychiatry*, 89 (3):248, 2018. ISSN 0022-3050. URL http://jnnp.bmj.com/content/89/3/248.full.pdf.

L. Jensen, L. H. Jørgensen, R. D. Bech, U. Frandsen, and H. D. Schrøder. Skeletal muscle remodelling as a function of disease progression in amyotrophic lateral sclerosis. *BioMed research international*, 2016:5930621–12, 2016. ISSN 2314-6133.

N. Jiang, K. B. Englehart, and P. A. Parker. Extracting simultaneous and proportional neural control information for multiple-dof prostheses from the surface electromyographic signal. *IEEE transactions on biomedical engineering*, 56(4):1070–1080, 2009. ISSN 0018-9294.

I. Jolliffe. Principal component analysis. *Encyclopedia of statistics in behavioral science*, 2005.

A. K. Jonscher. Dielectric relaxation in solids. *Journal of Physics D: Applied Physics*, 32(14): R57, 1999.

S. Kamath, N. Venkatanarasimha, M. Walsh, et al. Mri appearance of muscle denervation. *Skeletal Radiology*, 37(5):397–404, 2008. ISSN 0364-2348.

K. Kapur, J. A. Nagy, R. S. Taylor, B. Sanchez, and S. B. Rutkove. Estimating myofiber size with electrical impedance myography: a study in amyotrophic lateral sclerosis mice: Eim estimates myofiber size. *Muscle & nerve*, 58(5):713–717, 2018. ISSN 0148-639X.

K. Kapur, B. Sanchez, A. Pacheck, B. Darras, S. B. Rutkove, and R. Selukar. Functional mixed-effects modeling of longitudinal duchenne muscular dystrophy electrical impedance myography data using state-space approach. *IEEE transactions on biomedical engineering*, 66(6):1761–1768, 2019. ISSN 0018-9294.

T. Karacolak, R. Cooper, E. S. Unlu, and E. Topsakal. Dielectric properties of porcine skin tissue and in vivo testing of implantable antennas using pigs as model animals. *IEEE antennas and wireless propagation letters*, 11:1686–1689, 2012. ISSN 1536-1225.

P. Kaufmann, L.P., G. Levy, L., J. Thompson, H., et al. The alsfrsr predicts survival time in an als clinic population. *Neurology*, 64(1):38–43, 2005. ISSN 0028-3878.

M. G. M. G. Kendall and A. Stuart. *The advanced theory of statistics*, volume 2: Interference and Relationship. Griffin, London, 4th ed. edition, 1979. ISBN 0852642555.

S. Khan, A. Mahara, E. S. Hyams, A. R. Schned, and R. J. Halter. Prostate cancer detection using composite impedance metric. *IEEE transactions on medical imaging*, 35(12):2513–2523, 2016. ISSN 0278-0062.

M. Kiernan. New criteria for als diagnosis. *Journal of the neurological sciences*, 429:117997, 2021. ISSN 0022-510X.

M. C. Kiernan, S. Vucic, B. C. Cheah, et al. Amyotrophic lateral sclerosis. *The Lancet*, 377 (9769):942–955, 2011. ISSN 0140-6736.

Y. Kim, S. Stapornchaisit, M. Miyakoshi, N. Yoshimura, and Y. Koike. The effect of ica and non-negative matrix factorization analysis for emg signals recorded from multi-channel emg sensors. *Frontiers in neuroscience*, 14:600804–600804, 2020. ISSN 1662-4548.

T. G. Kolda. Multilinear operators for higher-order decompositions. Technical report, Sandia National Laboratories (SNL), Albuquerque, NM, and Livermore, CA, 2006.

T. G. Kolda and B. W. Bader. Tensor decompositions and applications. *SIAM review*, 51(3): 455–500, 2009.

C. Krarup. Lower motor neuron involvement examined by quantitative electromyography in amyotrophic lateral sclerosis. *Clinical Neurophysiology*, 122(2):414–422, 2011. ISSN 1388-2457. URL http://search.proquest.com/docview/954612667/.

J. B. Kruskal. Three-way arrays: rank and uniqueness of trilinear decompositions, with application to arithmetic complexity and statistics. *Linear algebra and its applications*, 18(2): 95–138, 1977. ISSN 0024-3795.

T. Kwan, M. Kazamel, K. Thoenes, Y. Si, N. Jiang, and P. H. King. Wnt antagonist frzb is a muscle biomarker of denervation atrophy in amyotrophic lateral sclerosis. *Scientific reports*, 10(1):16679, 2020.

H. Kwon, W. Q. Malik, S. B. Rutkove, et al. Separation of subcutaneous fat from muscle in surface electrical impedance myography measurements using model component analysis. *IEEE Transactions on Biomedical Engineering*, 66(2):354–364, Feb 2019. ISSN 1558-2531. doi: 10.1109/TBME.2018.2839977.

I. Lackovic and Z. Stare. Low-frequency dielectric properties of the oral mucosa. In *13th International Conference on Electrical Bioimpedance and the 8th Conference on Electrical Impedance Tomography*, pages 154–157. Springer, 2007.

S. G. Larsson, A. Mancuso, and W. Hanafee. Computed tomography of the tongue and floor of the mouth. *Radiology*, 143(2):493–500, 1982.

J. Lederer. *Fundamentals of high-dimensional statistics*. Springer, 2022.

D. Lee and H. S. Seung. Algorithms for non-negative matrix factorization. *Advances in neural information processing systems*, 13, 2000.

I. Lee, M. Kazamel, T. McPherson, J. McAdam, M. Bamman, A. Amara, D. L. Smith Jr, and P. H. King. Fat mass loss correlates with faster disease progression in amyotrophic lateral sclerosis patients: Exploring the utility of dual-energy x-ray absorptiometry in a prospective study. *PLoS One*, 16(5):e0251087, 2021.

J. S. Lee, D. D. Lee, S. Choi, and D. S. Lee. Application of nonnegative matrix factorization to dynamic positron emission tomography. In *3rd International Conference on Independent Component Analysis and Blind Signal Separation*, pages 556–562, 2001.

J. Li, W. L. Staats, A. Spieker, M. Sung, and S. B. Rutkove. A technique for performing electrical impedance myography in the mouse hind limb: data in normal and als sod1 g93a animals. *PloS one*, 7(9):e45004–e45004, 2012. ISSN 1932-6203.

J. Li, M. Sung, and S. B. Rutkove. Electrophysiologic biomarkers for assessing disease progression and the effect of riluzole in sod1 g93a als mice. *PloS one*, 8(6):e65976, 2013. ISSN 1932-6203.

J. Li, A. Pacheck, B. Sanchez, and S. B. Rutkove. Single and modeled multifrequency electrical impedance myography parameters and their relationship to force production in the als sod1g93a mouse. *Amyotrophic lateral sclerosis and frontotemporal degeneration*, 17(5-6): 397–403, 2016a. ISSN 2167-8421.

J. Li, Z. Ji, B. Liu, and X. s. D. Shi. Influence of the measuring probe structure on the electric-field edge effect in electrical impedance scanning. *Journal of Medical Imaging and Health Informatics*, 9(1):47–52, 2019.

J. Li, R. Wang, and L. Pan. An enhanced emg-driven musculoskeletal model based on non-negative matrix factorization. *Biomedical signal processing and control*, 79:104178, 2023. ISSN 1746-8094.

L. Li, X. Li, H. Hu, H. Shin, and P. Zhou. The effect of subcutaneous fat on electrical impedance myography: Electrode configuration and multi-frequency analyses. *PLOS ONE*, 11(5):e0156154, May 2016b. doi: 10.1371/journal.pone.0156154. URL https://doi.org/10.1371/journal.pone.0156154.

L. Li, H. Shin, A. Stampas, X. Li, and P. Zhou. Electrical impedance myography changes after incomplete cervical spinal cord injury: An examination of hand muscles. *Clinical neurophysiology*, 128(11):2242–2247, 2017a. ISSN 1388-2457.

X. Li, L. Li, H. Shin, S. Li, and P. Zhou. Electrical impedance myography for evaluating paretic muscle changes after stroke. *IEEE Transactions on Neural Systems and Rehabilitation Engineering*, 25(11):2113–2121, 2017b.

H. Lin, H. J. Lee, N. Tague, J.-B. Lugagne, C. Zong, F. Deng, J. Shin, L. Tian, W. Wong, M. J. Dunlop, et al. Microsecond fingerprint stimulated raman spectroscopic imaging by ultrafast tuning and spatial-spectral learning. *Nature communications*, 12(1):3052, 2021.

E. Lindauer, L. Dupuis, H.-P. Müller, H. Neumann, A. C. Ludolph, and J. Kassubek. Adipose tissue distribution predicts survival in amyotrophic lateral sclerosis. *PloS one*, 8(6):e67783, 2013.

D. Lintzeri, N. Karimian, U. Blume-Peytavi, and J. Kottner. Epidermal thickness in healthy humans: a systematic review and meta-analysis. *Journal of the European Academy of Dermatology and Venereology*, 36(8):1191–1200, 2022. ISSN 0926-9959.

W. Liu, F. Peng, S. Feng, J. You, Z. Chen, J. Wu, K. Yuan, and D. Ye. Semantic feature extraction for brain ct image clustering using nonnegative matrix factorization. *Lecture Notes in Computer Science*, 4901:41–48, 2007.

J. Loughrey and P. Cunningham. Overfitting in wrapper-based feature subset selection: The harder you try the worse it gets. In *Research and Development in Intelligent Systems XXI: Proceedings of AI-2004, the Twenty-fourth SGAI International Conference on Innovative Techniques and Applications of Artificial Intelligence*, pages 33–43. Springer, 2005.

C. Lungu, A. W. Tarulli, D. Tarsy, P. Mongiovi, V. G. Vanderhorst, and S. B. Rutkove. Quantifying muscle asymmetries in cervical dystonia with electrical impedance: A preliminary assessment. *Clinical neurophysiology*, 122(5):1027–1031, 2011. ISSN 1388-2457.

X. Luo and B. Sanchez. In silico muscle volume conduction study validates in vivo measurement of tongue volume conduction properties using a user tongue array depressor. *Physiological measurement*, 42(4):45009, 2021. ISSN 0967-3334.

X. Luo, H. V. Gutierrez Pulido, S. Rutkove, and B. Sanchez. A bioimpedance-based device to assess the volume conduction properties of the tongue in neurological disorders affecting bulbar function. *IEEE open journal of engineering in medicine and biology*, 2:278–285, 2021a. ISSN 2644-1276.

X. Luo, H. V. Gutierrez Pulido, S. B. Rutkove, and B. Sanchez. In vivo muscle conduction study of the tongue using a multi-electrode tongue depressor. *Clinical neurophysiology*, 132 (2):683–687, 2021b. ISSN 1388-2457.

X. Luo, S. Wang, S. B. Rutkove, and B. Sanchez. Nonhomogeneous volume conduction effects affecting needle electromyography: an analytical and simulation study. *Physiological measurement*, 42(11):115005, 2021c. ISSN 0967-3334.

X. Luo, J. Shi, A. Marin Llobet, S. B. Rutkove, and B. Sanchez. Electrical impedance myography method of measuring anisotropic tongue tissue. *Physiological measurement*, 2023. ISSN 0967-3334.

J. Malmivuo and R. Plonsey. *Bioelectromagnetism : principles and applications of bioelectric and biomagnetic fields*. Oxford University Press, New York ; Oxford, 1995. ISBN 0195058232.

M. Martinez-Gonzalez, J. Montilla-Herrador, J. A. García-Vidal, P. Escolar-Reina, M. Gacto-Sánchez, and F. Medina-Mirapeix. Intra- and inter-rater reliability of electrical impedance myography using adhesive electrodes in healthy volunteers. *Journal of electromyography and kinesiology*, 55:102456–102456, 2020. ISSN 1050-6411.

O. G. Martinsen and S. Grimnes. *Bioimpedance and bioelectricity basics*. Academic press, 2011.

O. G. Martinsen, S. Grimnes, and E. Haug. Measuring depth depends on frequency in electrical skin impedance measurements. *Skin research and technology*, 5(3):179–181, 1999.

O. G. Martisnen, S. Grimnes, and O. Sveen. Dielectric properties of some keratinised tissues. part 1 : Stratum corneum and nail in situ. *Medical & biological engineering & computing*, 35 (3):172–176, 1997. ISSN 0140-0118.

P. Masrori and P. Van Damme. Amyotrophic lateral sclerosis: a clinical review. *European journal of neurology*, 27(10):1918–1929, 2020.

M. A. Mathewson, M. A. Chapman, E. R. Hentzen, J. Fridén, and R. L. Lieber. Anatomical, architectural, and biochemical diversity of the murine forelimb muscles. *Journal of anatomy*, 221(5):443–451, 2012. ISSN 0021-8782.

E. McAdams and J. Jossinet. Problems in equivalent circuit modelling of the electrical properties of biological tissues. *Bioelectrochemistry and Bioenergetics*, 40(2):147–152, 1996. ISSN 0302-4598.

A. J. Mccomas, P. R. Fawcett, M. J. Campbell, and R. E. Sica. Electrophysiological estimation of the number of motor units within a human muscle. *Journal of neurology, neurosurgery, and psychiatry*, 34(2):121–131, 1971. ISSN 0022-3050. URL http://search.proquest.com/docview/74942205/.

C. Mcilduff, S. Yim, A. Pacheck, T. Geisbush, A. Mijailovic, and S. B. Rutkove. An improved electrical impedance myography (eim) tongue array for use in clinical trials. *Clinical neurophysiology*, 127(1):932–935, 2015. ISSN 1388-2457.

C. E. Mcilduff, S. J. Yim, A. K. Pacheck, and S. B. Rutkove. Optimizing electrical impedance myography of the tongue in amyotrophic lateral sclerosis. *Muscle & Nerve*, 55(4):539–543, 2017. doi: 10.1002/mus.25375. URL https://onlinelibrary.wiley.com/doi/abs/10.1002/mus.25375.

C. F. Mela and P. K. Kopalle. The impact of collinearity on regression analysis: the asymmetric effect of negative and positive correlations. *Applied Economics*, 34(6):667–677, 2002.

R. Menke, F. Agosta, J. Grosskreutz, et al. Neuroimaging endpoints in amyotrophic lateral sclerosis. *Neurotherapeutics*, 14(1):11–23, 2017. ISSN 1933-7213.

S. Millecamps, S. Boillée, I. Le Ber, et al. Phenotype difference between als patients with expanded repeats in c9orf72 and patients with mutations in other als-related genes. *Journal of Medical Genetics*, 49(4):258, 2012. ISSN 0022-2593. URL http://jmg.bmj.com/content/49/4/258.full.pdf.

R. K. Morgan, S. Mcnally, M. Alexander, et al. Use of sniff nasal-inspiratory force to predict survival in amyotrophic lateral sclerosis. *American journal of respiratory and critical care medicine*, 171(3):269–274, 2005. ISSN 1073-449X. URL http://search.proquest.com/docview/67373505/.

V. Mozhaeva, D. Kudryavtsev, K. Prokhorov, Y. Utkin, S. Gudkov, S. Garnov, I. Kasheverov, and V. Tsetlin. Toxins' classification through raman spectroscopy with principal component analysis. *Spectrochimica acta. Part A, Molecular and biomolecular spectroscopy*, 278:121276, 2022. ISSN 1386-1425.

C. Multiphysics®. Optimization module user's guide. *COMSOL Multiphysics*, 2018.

C. Murdoch, B. H. Brown, V. Hearnden, P. M. Speight, K. D'Apice, A. M. Hegarty, J. A. Tidy, T. J. Healey, P. E. Highfield, and M. H. Thornhill. Use of electrical impedance spectroscopy to detect malignant and potentially malignant oral lesions. *International journal of nanomedicine*, 9(Issue 1):4521–4532, 2014. ISSN 1178-2013.

E. K. Murphy, A. Mahara, S. Khan, E. S. Hyams, A. R. Schned, J. Pettus, and R. J. Halter. Comparative study of separation between ex vivo prostatic malignant and benign tissue using electrical impedance spectroscopy and electrical impedance tomography. *Physiological measurement*, 38(6):1242–1261, 2017. ISSN 0967-3334.

E. K. Murphy, J. Skinner, M. Martucci, S. B. Rutkove, and R. J. Halter. Toward electrical impedance tomography coupled ultrasound imaging for assessing muscle health. *IEEE transactions on medical imaging*, 38(6):1409–1419, 2018a.

E. K. Murphy, X. Wu, and R. J. Halter. Fused-data transrectal eit for prostate cancer imaging. *Physiological measurement*, 39(5):054005–054005, 2018b. ISSN 0967-3334.

J. A. Nagy, C. Semple, P. Lo, and S. B. Rutkove. Assessing the therapeutic impact of resveratrol in als sod1-g93a mice with electrical impedance myography. *Frontiers in neurology*, 13: 1059743–1059743, 2022. ISSN 1664-2295.

C. Ngo, C. Munoz, M. Lueken, A. Hülkenberg, C. Bollheimer, A. Briko, A. Kobelev, S. Shchukin, and S. Leonhardt. A wearable, multi-frequency device to measure muscle activity combining simultaneous electromyography and electrical impedance myography. *Sensors*, 22(5):1941, 2022.

S. T. Ngo, R. P. van Eijk, V. Chachay, L. H. Van Den Berg, P. A. McCombe, R. D. Henderson, and F. J. Steyn. Loss of appetite is associated with a loss of weight and fat mass in patients with amyotrophic lateral sclerosis. *Amyotrophic Lateral Sclerosis and Frontotemporal Degeneration*, 20(7-8):497–505, 2019.

D. Nion and L. De Lathauwer. An enhanced line search scheme for complex-valued tensor decompositions. application in ds-cdma. *Signal Processing*, 88(3):749–755, 2008.

M. Noshiro, T. Morimoto, H. Nagao, and H. Matsuda. Electrical impedance in the lower limbs of patients with duchenne muscular dystrophy: a preliminary study. *Medical and Biological Engineering and Computing*, 31:97–102, 1993.

J. Nyboer, M. M. Kreider, and L. Hannapel. Electrical impedance plethysmography: A physical and physiologic approach to peripheral vascular study. *Circulation*, 2(6):811–821, 1950.

M. B. Offit, T. Wu, M. K. Floeter, and T. J. Lehky. Electrical impedance myography (eim) in a natural history study of c9orf72 mutation carriers. *Amyotrophic lateral sclerosis and frontotemporal degeneration*, 21(5-6):445–451, 2020. ISSN 2167-8421.

O. T. Ogunnika, M. Scharfstein, R. C. Cooper, H. Ma, J. L. Dawson, and S. B. Rutkove. A handheld electrical impedance myography probe for the assessment of neuromuscular disease. *2008 30th Annual International Conference of the IEEE Engineering in Medicine and Biology Society*, pages 3566–3569, 2008. ISSN 1094-687X.

O. T. Ogunnika, S. B. Rutkove, H. Ma, P. M. Fogerson, M. Scharfstein, R. C. Cooper, and J. L. Dawson. A portable system for the assessment of neuromuscular diseases with electrical impedance myography. *Journal of medical engineering & technology*, 34(7-8):377–385, 2010. ISSN 0309-1902.

C. K. Ong and V. F. Chong. Imaging of tongue carcinoma. *Cancer Imaging*, 6(1):186, 2006.

A. Pacheck, A. Mijailovic, S. Yim, et al. Tongue electrical impedance in amyotrophic lateral sclerosis modeled using the finite element method. *Clinical Neurophysiology*, 127(3):1886–1890, Mar. 2016. doi: 10.1016/j.clinph.2015.11.046. URL https://doi.org/10.1016/j.clinph.2015.11.046.

M. Pagani, Consuelo, A. Chiò, Consuelo, M. Valentini, Consuelo, et al. Functional pattern of brain fdg-pet in amyotrophic lateral sclerosis. *Neurology*, 83(12):1067–1074, 2014. ISSN 0028-3878.

X. Pan, X. Yang, W. Ma, W. He, Z. L. Vasic, M. Cifrek, and Y. Gao. A study of handgrip force prediction scheme based on electrical impedance myography. *IEEE journal of electromagnetics, RF and microwaves in medicine and biology*, 7(1):90, 2023. ISSN 2469-7249.

S. R. Pandeya, J. A. Nagy, D. Riveros, C. Semple, R. S. Taylor, M. Mortreux, B. Sanchez, K. Kapur, and S. B. Rutkove. Estimating myofiber cross-sectional area and connective tissue deposition with electrical impedance myography: A study in d2-mdx mice. *Muscle & nerve*, 63(6):941–950, 2021. ISSN 0148-639X.

S. R. Pandeya, J. A. Nagy, D. Riveros, C. Semple, R. S. Taylor, A. Hu, B. Sanchez, and S. B. Rutkove. Using machine learning algorithms to enhance the diagnostic performance of electrical impedance myography. *Muscle & nerve*, 66(3):354–361, 2022. ISSN 0148-639X.

S. Parvandeh, H.-W. Yeh, M. P. Paulus, and B. A. McKinney. Consensus features nested cross-validation. *Bioinformatics*, 36(10):3093–3098, 2020.

F. Pedregosa, G. Varoquaux, A. Gramfort, V. Michel, B. Thirion, O. Grisel, M. Blondel, P. Prettenhofer, R. Weiss, V. Dubourg, J. Vanderplas, A. Passos, D. Cournapeau, M. Brucher, M. Perrot, and E. Duchesnay. Scikit-learn: Machine learning in Python. *Journal of Machine Learning Research*, 12:2825–2830, 2011.

J. Phukan, M. Elamin, P. Bede, et al. The syndrome of cognitive impairment in amyotrophic lateral sclerosis: a population-based study. *Journal of Neurology, Neurosurgery & Psychiatry*, 83(1):102, 2012. ISSN 0022-3050. URL http://jnnp.bmj.com/content/83/1/102.full.pdf.

W. Pinto, R. Debona, P. Nunes, A. Assis, C. Lopes, T. Bortholin, R. Dias, F. Naylor, M. Chieia, P. Souza, and A. Oliveira. Atypical motor neuron disease variants: Still a diagnostic challenge in neurology. *Revue neurologique*, 175(4):221–232, 2019. ISSN 0035-3787.

M. Plesia, O. Stevens, G. Lloyd, C. Kendall, I. Coldicott, A. Kennerley, G. Miller, P. Shaw, R. Mead, J. Day, and J. Alix. In vivo fiber optic raman spectroscopy of muscle in preclinical models of amyotrophic lateral sclerosis and duchenne muscular dystrophy. 2021.

K. Poesen, M., M. De Schaepdryver, G., B. Stubendorff, W., et al. Neurofilament markers for als correlate with extent of upper and lower motor neuron disease. *Neurology*, 88(24): 2302–2309, 2017. ISSN 0028-3878.

A. L. Pomerantsev and O. Y. Rodionova. Multiclass partial least squares discriminant analysis: Taking the right way-a critical tutorial: Pls-da: A critical tutorial. *Journal of chemometrics*, 32(8):e3030, 2018. ISSN 0886-9383.

M. J. Powell. The bobyqa algorithm for bound constrained optimization without derivatives. *Cambridge NA Report NA2009/06, University of Cambridge, Cambridge*, 26, 2009.

S. Prestin, S. I. Rothschild, C. S. Betz, and M. Kraft. Measurement of epithelial thickness within the oral cavity using optical coherence tomography. *Head & neck*, 34(12):1777–1781, 2012.

K. Pugdahl, J.-P. Camdessanché, B. Cengiz, M. de Carvalho, R. Liguori, C. Rossatto, M. O. Santos, V. Vacchiano, and B. Johnsen. Gold coast diagnostic criteria increase sensitivity in amyotrophic lateral sclerosis. *Clinical Neurophysiology*, 132(12):3183–3189, 2021.

S. Qiu, J. Feng, R. Xu, J. Xu, K. Wang, F. He, H. Qi, X. Zhao, P. Zhou, L. Zhang, et al. A stimulus artifact removal technique for semg signal processing during functional electrical stimulation. *IEEE Transactions on Biomedical Engineering*, 62(8):1959–1968, 2015.

A. Radunovic, D. Annane, M. Rafiq, et al. Mechanical ventilation for amyotrophic lateral sclerosis/motor neuron disease. *Cochrane Database of Systematic Reviews*, (10), 2017. ISSN 1465-1858. doi: 10.1002/14651858.CD004427.pub4. URL https://doi.org//10.1002/14651858.CD004427.pub4.

H. S. R. Rajula, G. Verlato, M. Manchia, N. Antonucci, and V. Fanos. Comparison of conventional statistical methods with machine learning in medicine: diagnosis, drug development, and treatment. *Medicina*, 56(9):455, 2020.

J. E. B. Randles. Kinetics of rapid electrode reactions. *Discussions of the Faraday Society*, 1: 11, 1947. ISSN 0366-9033.

D. L. Rebolledo, D. González, J. Faundez-Contreras, O. Contreras, C. P. Vio, J. E. Murphy-Ullrich, K. E. Lipson, and E. Brandan. Denervation-induced skeletal muscle fibrosis is mediated by ctgf/ccn2 independently of tgf-β. *Matrix Biology*, 82:20–37, 2019.

I. Richter, I. Alajbeg, V. VUČIĆEVIĆ BORAS, A. ANDABAK ROGULJ, and V. Brailo. Mapping electrical impedance spectra of the healthy oral mucosa: A pilot study. *Acta stomatologica Croatica*, 49(4):331–339, 2015.

B. Roy, S. B. Rutkove, and R. J. Nowak. Electrical impedance myography as a biomarker of inclusion body myositis: A cross-sectional study. *Clinical neurophysiology*, 131(2):368–371, 2020. ISSN 1388-2457.

S. Rutkove. Clinical measures of disease progression in amyotrophic lateral sclerosis. *Neurotherapeutics*, 12(2):384–393, 2015. ISSN 1933-7213.

S. Rutkove and B. Darras. Electrical impedance myography for the assessment of children with muscular dystrophy: A preliminary study. *Journal of Physics: Conference Series*, 434(1): 12069–4, 2013. ISSN 1742-6588.

S. B. Rutkove. Electrical impedance myography: Background, current state, and future directions. *Muscle & Nerve*, 40(6):936–946, 2009. ISSN 0148-639X.

S. B. Rutkove, R. Aaron, and C. A. Shiffman. Localized bioimpedance analysis in the evaluation of neuromuscular disease. *Muscle & Nerve*, 25(3):390–397, 2002. ISSN 0148-639X.

S. B. Rutkove, R. A. Partida, G. J. Esper, et al. Electrode position and size in electrical impedance myography. *Clinical Neurophysiology*, 116(2):290–299, 2005. ISSN 1388-2457.

S. B. Rutkove, K. S. Lee, C. A. Shiffman, and R. Aaron. Test–retest reproducibility of 50 khz linear-electrical impedance myography. *Clinical neurophysiology*, 117(6):1244–1248, 2006. ISSN 1388-2457.

S. B. Rutkove, H. Zhang, D. A. Schoenfeld, E. M. Raynor, et al. Electrical impedance myography to assess outcome in amyotrophic lateral sclerosis clinical trials. *Clinical Neurophysiology*, 118(11):2413–2418, 2007. ISSN 1388-2457.

S. B. Rutkove, J. M. Shefner, M. Gregas, H. Butler, J. Caracciolo, C. Lin, P. M. Fogerson, P. Mongiovi, and B. T. Darras. Characterizing spinal muscular atrophy with electrical impedance myography. *Muscle & nerve*, 42(6):915–921, 2010. ISSN 0148-639X.

S. B. Rutkove, J. B. Caress, M. S. Cartwright, et al. Electrical impedance myography as a biomarker to assess als progression. *Amyotrophic Lateral Sclerosis*, 13(5):439–445, 2012a. ISSN 1748-2968. URL http://www.tandfonline.com/doi/abs/10.3109/17482968.2012.688837.

S. B. Rutkove, M. C. Gregas, and B. T. Darras. Electrical impedance myography in spinal muscular atrophy: A longitudinal study: Eim in sma. *Muscle & nerve*, 45(5):642–647, 2012b. ISSN 0148-639X.

S. B. Rutkove, J. B. Caress, M. S. Cartwright, et al. Electrical impedance myography correlates with standard measures of als severity. *Muscle & Nerve*, 49(3):441–443, 2014. ISSN 0148-639X.

S. B. Rutkove, J. S. Wu, C. Zaidman, et al. Loss of electrical anisotropy is an unrecognized feature of dystrophic muscle that may serve as a convenient index of disease status. *Clinical Neurophysiology*, 127(12):3546–3551, Dec. 2016. doi: 10.1016/j.clinph.2016.09.017. URL https://doi.org/10.1016/j.clinph.2016.09.017.

S. B. Rutkove, K. Kapur, C. M. Zaidman, J. S. Wu, et al. Electrical impedance myography for assessment of duchenne muscular dystrophy. *Annals of Neurology*, 81(5):622–632, 2017. ISSN 0364-5134.

S. B. Rutkove, S. Callegari, H. Concepcion, T. Mourey, J. Widrick, J. A. Nagy, and A. K. Nath. Electrical impedance myography detects age-related skeletal muscle atrophy in adult zebrafish. *Scientific Reports*, 13(1):7191, 2023.

M. A. Salam, A. T. Azar, M. S. Elgendy, and K. M. Fouad. The effect of different dimensionality reduction techniques on machine learning overfitting problem. *International journal of advanced computer science & applications*, 12(4):641–655, 2021. ISSN 2158-107X.

R. Salzer. *Infrared and Raman spectroscopic imaging*. Wiley-VCH, Weinheim, Germany, second, completely revised and updated edition. edition, 2014. ISBN 3-527-67815-8.

B. Sanchez and S. Rutkove. Electrical impedance myography and its applications in neuromuscular disorders. *Neurotherapeutics*, 14(1):107–118, 2017. ISSN 1933-7213.

B. Sanchez, J. Li, R. Bragos, and S. B. Rutkove. Differentiation of the intracellular structure of slow- versus fast-twitch muscle fibers through evaluation of the dielectric properties of tissue. *Physics in medicine & biology*, 59(10):2369–2380, 2014. ISSN 0031-9155.

B. Sanchez, J. Li, T. Geisbush, R. B. Bardia, and S. B. Rutkove. Impedance alterations in healthy and diseased mice during electrically induced muscle contraction. *Crop and pasture science*, 63(8):1602–1612, 2016a. ISSN 0018-9294.

B. Sanchez, A. Pacheck, and S. B. Rutkove. Guidelines to electrode positioning for human and animal electrical impedance myography research. *Scientific reports*, 6(1):32615–32615, 2016b. ISSN 2045-2322.

B. Sanchez, S. R. Iyer, J. Li, K. Kapur, S. Xu, S. B. Rutkove, and R. M. Lovering. Non-invasive assessment of muscle injury in healthy and dystrophic animals with electrical impedance myography. *Muscle & nerve*, 56(6):E85–E94, 2017. ISSN 0148-639X.

B. Sanchez, O. G. Martinsen, T. J. Freeborn, and C. M. Furse. Electrical impedance myography: A critical review and outlook. *Clinical neurophysiology*, 132(2):338–344, 2021. ISSN 1388-2457.

I. Sanders and L. Mu. A three-dimensional atlas of human tongue muscles. *The Anatomical Record*, 296(7):1102–14, 2013.

N. Sauwen, M. Acou, S. Van Cauter, D. Sima, J. Veraart, F. Maes, U. Himmelreich, E. Achten, and S. Van Huffel. Comparison of unsupervised classification methods for brain tumor segmentation using multi-parametric mri. *NeuroImage clinical*, 12(C):753–764, 2016. ISSN 2213-1582.

B. Scholz and R. Anderson. On electrical impedance scanning—principles and simulations. *Electromedica*, 68:35–44, 2000.

C. N. Schooling, T. Jamie Healey, H. E. McDonough, S. J. French, C. J. McDermott, P. J. Shaw, V. Kadirkamanathan, and J. J. P. Alix. Modelling and analysis of electrical impedance myography of the lateral tongue. *Physiological measurement*, 41(12):125008–125008, 2020. ISSN 0967-3334.

C. N. Schooling, T. Jamie Healey, H. E. McDonough, S. J. French, C. J. McDermott, P. J. Shaw, V. Kadirkamanathan, and J. J. P. Alix. Tensor electrical impedance myography identifies clinically relevant features in amyotrophic lateral sclerosis. *Physiological measurement*, 42 (10):105004, 2021. ISSN 0967-3334.

C. N. Schooling, T. Healey, H. E. McDonough, S. J. French, C. J. McDermott, P. J. Shaw, V. Kadirkamanathan, and J. J. Alix. Tensor electrical impedance myography identifies bulbar disease progression in amyotrophic lateral sclerosis. *Clinical neurophysiology*, 139:69–75, 2022. ISSN 1388-2457.

H. Schwan. Electrical properties of tissues and cell suspensions: mechanisms and models. In *Proceedings of 16th Annual International Conference of the IEEE Engineering in Medicine and Biology Society*, volume 1, pages A70–A71 vol.1. IEEE, 1994. ISBN 9780780320505.

S. Schwartz, T. R. Geisbush, A. Mijailovic, et al. Optimizing electrical impedance myography measurements by using a multifrequency ratio: A study in duchenne muscular dystrophy. *Clinical Neurophysiology*, 126(1):202–208, Jan. 2015. doi: 10.1016/j.clinph.2014.05.007. URL https://doi.org/10.1016/j.clinph.2014.05.007.

J. T. Selsby, J. W. Ross, D. Nonneman, and K. Hollinger. Porcine models of muscular dystrophy. *ILAR journal*, 56(1):116–126, 2015. ISSN 1084-2020.

C. Semple, D. Riveros, D.-M. Sung, J. A. Nagy, S. B. Rutkove, and M. Mortreux. Using electrical impedance myography as a biomarker of muscle deconditioning in rats exposed to micro- and partial-gravity analogs. *Frontiers in physiology*, 11:557796–557796, 2020. ISSN 1664-042X.

T. Senior. Impedance boundary conditions for imperfectly conducting surfaces. *Applied Scientific Research, Section B*, 8(1):418–436, 1960.

S. Sennfält, U. Kläppe, S. Thams, K. Samuelsson, R. Press, F. Fang, and C. Ingre. The path to diagnosis in als: delay, referrals, alternate diagnoses, and clinical progression. *Amyotrophic lateral sclerosis and frontotemporal degeneration*, 24(1-2):45–53, 2023. ISSN 2167-8421.

D. F. Shanno. Conditioning of quasi-newton methods for function minimization. *Mathematics of computation*, 24(111):647–656, 1970. ISSN 0025-5718.

J. Shefner. Strength testing in motor neuron diseases. *Neurotherapeutics*, 14(1):154–160, 2017. ISSN 1933-7213.

J. M. Shefner, S. B. Rutkove, J. B. Caress, M. Benatar, W. S. David, M. S. Cartwright, E. A. Macklin, and J. L. Bohorquez. Reducing sample size requirements for future als clinical trials with a dedicated electrical impedance myography system. *Amyotrophic lateral sclerosis and frontotemporal degeneration*, 19(7-8), 2018.

J. M. Shefner, A. Al-Chalabi, M. R. Baker, L.-Y. Cui, M. de Carvalho, A. Eisen, J. Grosskreutz, O. Hardiman, R. Henderson, J. M. Matamala, H. Mitsumoto, W. Paulus, N. Simon, M. Swash, K. Talbot, M. R. Turner, Y. Ugawa, L. H. van Den Berg, R. Verdugo, S. Vucic, R. Kaji, D. Burke, and M. C. Kiernan. A proposal for new diagnostic criteria for als. *Clinical neurophysiology : official journal of the International Federation of Clinical Neurophysiology*, 2020. ISSN 13882457. URL http://search.proquest.com/docview/2401111474/.

S. Shellikeri, Y. Yunusova, J. R. Green, et al. Electrical impedance myography in the evaluation of the tongue musculature in amyotrophic lateral sclerosis. *Muscle & Nerve*, 52(4):584–591, June 2015. doi: 10.1002/mus.24565. URL https://doi.org/10.1002/mus.24565.

C. A. Shiffman and S. B. Rutkove. Circuit modeling of the electrical impedance: I. neuromuscular disease. *Physiological measurement*, 34(2):203–221, 2013a. ISSN 0967-3334.

C. A. Shiffman and S. B. Rutkove. Circuit modeling of the electrical impedance: ii. normal subjects and system reproducibility. *Physiological Measurement*, 34(2):223–235, 2013b. ISSN 0967-3334.

C. A. Shiffman, H. Kashuri, and R. Aaron. Electrical impedance myography at frequencies up to 2 mhz. *Physiological Measurement*, 29(6):S345–S363, 2008. ISSN 0967-3334.

J. M. Sions, C. M. Tyrell, B. A. Knarr, A. Jancosko, and S. A. Binder-Macleod. Age- and stroke-related skeletal muscle changes: a review for the geriatric clinician. *Journal of geriatric physical therapy (2001)*, 35(3):155–161, 2012. ISSN 1539-8412.

J. Song, D. Kim, Y. Han, and J.-Y. Chung. Comparative analysis of the kernel types in generalized autocalibrating partially parallel acquisition algorithms for accelerated three-dimensional magnetic resonance spectroscopic imaging data. *International Journal of Imaging Systems and Technology*, 32(1):163–177, 2022.

M. E. Spurlock and N. K. Gabler. Development of porcine models of obesity and the metabolic syndrome. *The Journal of nutrition*, 138(2):397–402, 2008. ISSN 0022-3166.

T. Srivastava, B. T. Darras, J. S. Wu, and S. B. Rutkove. Machine learning algorithms to classify spinal muscular atrophy subtypes. *Neurology*, 79(4):358–364, 2012. ISSN 0028-3878.

T.-P. Sun, C. T.-S. Ching, C.-S. Cheng, S.-H. Huang, Y.-J. Chen, C.-S. Hsiao, C.-H. Chang, S.-Y. Huang, H.-L. Shieh, W.-H. Liu, C.-M. Liu, and C.-Y. Chen. The use of bioimpedance in the detection/screening of tongue cancer. *Cancer epidemiology*, 34(2):207–211, 2010. ISSN 1877-7821.

M. Sung, A. J. Spieker, P. Narayanaswami, et al. The effect of subcutaneous fat on electrical impedance myography when using a handheld electrode array: The case for measuring reactance. *Clinical Neurophysiology*, 124(2):400–404, 2013. ISSN 1388-2457.

K. Svanberg. The method of moving asymptotes—a new method for structural optimization. *International journal for numerical methods in engineering*, 24(2):359–373, 1987.

H. Tankisi, C. S.-Z. Nielsen, J. Howells, B. Cengiz, G. Samusyte, M. Koltzenburg, J. U. Blicher, A. T. Møller, K. Pugdahl, A. Fuglsang-Frederiksen, et al. Early diagnosis of amyotrophic lateral sclerosis by threshold tracking and conventional transcranial magnetic stimulation. *European Journal of Neurology*, 28(9):3030–3039, 2021.

A. Tarulli, G. Esper, K. Lee, R. Aaron, C. Shiffman, and S. Rutkove. Electrical impedance myography in the bedside assessment of inflammatory myopathy. *Neurology*, 65(3):451–452, 2005.

A. Tarulli, A. Chin, K. Lee, and S. Rutkove. Impact of skin-subcutaneous fat layer thickness on electrical impedance myography measurements: An initial assessment. *Clinical neurophysiology*, 118(11):2393–2397, 2007. ISSN 1388-2457.

A. W. Tarulli, N. Duggal, G. J. Esper, L. P. Garmirian, P. M. Fogerson, C. H. Lin, and S. B. Rutkove. Electrical impedance myography in the assessment of disuse atrophy. *Archives of physical medicine and rehabilitation*, 90(10):1806–1810, 2009.

G. Tomasi and R. Bro. Parafac and missing values. *Chemometrics and intelligent laboratory systems*, 75(2):163–180, 2005. ISSN 0169-7439.

B. Tomik and R. Guiloff. Dysarthria in amyotrophic lateral sclerosis: A review. *Amyotrophic lateral sclerosis*, pages 1–12, 2008. ISSN 1748-2968.

M. R. Turner and K. Talbot. Mimics and chameleons in motor neurone disease. *Practical Neurology*, 13(3):153–164, 2013. ISSN 1474-7758. doi: 10.1136/practneurol-2013-000557. URL https://pn.bmj.com/content/13/3/153.

P. Turner, Martin R, P. Kiernan, Matthew C, F. Leigh, P Nigel, and D. Talbot, Kevin. Biomarkers in amyotrophic lateral sclerosis. *Lancet neurology*, 8(1):94–109, 2009. ISSN 1474-4422.

P. Urban, T. Vogt, and H. Hopf. Corticobulbar tract involvement in amyotrophic lateral sclerosis. a transcranial magnetic stimulation study. *Brain*, 121(6):1099–1108, 1998. ISSN 1460-2156.

L. Van Der Maaten, E. Postma, J. Van den Herik, et al. Dimensionality reduction: a comparative. *J Mach Learn Res*, 10(66-71):13, 2009.

M. A. Van Es, O. Hardiman, A. Chio, A. Al-Chalabi, R. J. Pasterkamp, J. H. Veldink, and L. H. Van den Berg. Amyotrophic lateral sclerosis. *The Lancet*, 390(10107):2084–2098, 2017.

T. Van Grinsven, S. Lafebre, B. Kubat, and W. Klein. Postmortem changes in musculoskeletal and subcutaneous tissue. *Journal of Forensic Radiology and Imaging*, 10:29–36, 2017.

E. Vavrinskỳ, H. Svobodova, M. Donoval, M. Daricek, M. Kopani, P. Miklovic, F. Horinek, and P. Telek. Application of single wireless holter to simultaneous emg, mmg and eim measurement of human muscles activity. *Lékař a technika-Clinician and Technology*, 48(2): 52–58, 2018.

N. S. Verber, S. R. Shepheard, M. Sassani, H. E. Mcdonough, et al. Biomarkers in motor neuron disease: A state of the art review. *Frontiers in neurology*, 10:291–291, 2019. ISSN 1664-2295. URL http://search.proquest.com/docview/2211944522/.

E. d. Vries, L. Alic, R. M. Schols, K. S. Emanuel, F. P. Wieringa, N. D. Bouvy, and G. J. M. Tuijthof. Near-infrared spectral similarity between ex vivo porcine and in vivo human tissue. *Life (Basel, Switzerland)*, 13(2):357, 2023. ISSN 2075-1729.

S. Vucic and M. Kiernan. Transcranial magnetic stimulation for the assessment of neurodegenerative disease. *Neurotherapeutics*, 14(1):91–106, 2017. ISSN 1933-7213.

S. Vucic and M. C. Kiernan. Novel threshold tracking techniques suggest that cortical hyperexcitability is an early feature of motor neuron disease. *Brain*, 129(9):2436–2446, 2006.

Y. B. Wah, N. Ibrahim, H. A. Hamid, S. Abdul-Rahman, and S. Fong. Feature selection methods: Case of filter and wrapper approaches for maximising classification accuracy. *Pertanika Journal of Science & Technology*, 26(1), 2018.

L. L. Wang, M. Ahad, A. McEwan, J. Li, M. Jafarpoor, and S. B. Rutkove. Assessment of alterations in the electrical impedance of muscle after experimental nerve injury via finite-element analysis. *IEEE transactions on biomedical engineering*, 58(6):1585–1591, 2011. ISSN 0018-9294.

M. Wang, P. Ma, L. Cai, C. Fan, X. Wang, H. Zheng, and E. Li. Investigation of localizing precise human abdomen models for wireless capsule endoscopy antenna design. *IEEE transactions on antennas and propagation*, 70(2):1367–1379, 2022. ISSN 0018-926X.

R. H. Westgaard. Influence of activity on the passive electrical properties of denervated soleus muscle fibres in the rat. *The Journal of Physiology*, 251(3), 1975.

R. G. Whittaker. The fundamentals of electromyography. *Practical Neurology*, 12(3):187, 2012. ISSN 1474-7758. URL http://pn.bmj.com/content/12/3/187.full.pdf.

L. C. Wijesekera and P. Nigel Leigh. Amyotrophic lateral sclerosis. *Orphanet journal of rare diseases*, 4:1–22, 2009.

D. Williams, N. G. Mandal, and A. Sharma. Electricity and magnetism. *Anaesthesia & Intensive Care Medicine*, 12(9):423–425, 2011. ISSN 1472-0299.

G. Wohlfart. Collateral regeneration from residual motor nerve fibers in amyotrophic lateral sclerosis. *Neurology*, 7(2):124–124, 1957. ISSN 0028-3878. doi: 10.1212/WNL.7.2.124. URL https://n.neurology.org/content/7/2/124.

Y. Xie, P. & Song. Multi-domain feature extraction from surface emg signals using nonnegative tensor factorization. *IEEE International Conference on Bioinformatics and Biomedicine*, pages 322–325, 2014.

B. Yakimov, A. Venets, J. Schleusener, V. Fadeev, J. Lademann, E. Shirshin, and M. Darvin. Blind source separation of molecular components of the human skin: In vivo: Non-negative matrix factorization of raman microspectroscopy data. *Analyst (London)*, 146(10):3185–3196, 2021. ISSN 0003-2654.

W. Youn and J. Kim. Estimation of elbow flexion force during isometric muscle contraction from mechanomyography and electromyography. *Medical & biological engineering & computing*, 48:1149–1157, 2010.

Y. Yunusova, E. K. Plowman, J. R. Green, C. Barnett, and P. Bede. Clinical measures of bulbar dysfunction in als. *Frontiers in neurology*, 10:106–106, 2019. ISSN 1664-2295.

C. M. Zaidman, J. S. Wu, K. Kapur, A. Pasternak, L. Madabusi, S. Yim, A. Pacheck, H. Szelag, T. Harrington, B. T. Darras, et al. Quantitative muscle ultrasound detects disease progression in duchenne muscular dystrophy. *Annals of neurology*, 81(5):633–640, 2017.

H. Zhang. The optimality of naive bayes.

A Outlier removal algorithm

1. All impedance spectra with a negative real part ($R < 0$) at any frequency
2. Additional conditions are implemented to identify spectra that deviate from the characteristic features you would physiologically expect and represent physically unrealistic values.
   (a) **For the tongue EIM data.** All spectra with impedance phase $> 30°$ at frequencies 76 Hz or 625 kHz are removed.
   (b) **For the limb EIM data.** All spectra with impedance phase $> 0°$ at 625 kHz are removed.
3. Root-mean-squared deviation based algorithm is applied to both the impedance magnitude data and the impedance phase data in turn.

Tongue EIM algorithm:
Calculate the 'severe patient' median and quartiles, using data from the patients presenting with severe symptoms. Repeat this for each configuration (c) and frequency (j) returning: $Q1_p^{cj}$, $Q2_p^{cj}$, $Q3_p^{cj}$.

$$J_c^i = \sqrt{\frac{1}{14}\sum_{j=1}^{14}\left(\frac{Z_c^i(f_j) - Q2_p^{cj}}{Q3_p^{cj} - Q1_p^{cj}}\right)^2} \tag{A.1}$$

For the variable J_c^i calculate the lower quartile ($Q1[J_c^i]$), upper quartile ($Q3[J_c^i]$) and MedCouple ($MC[J_c^i]$). Then define a threshold (T_c) for each configuration (c):

$$T_c = Q3[J_c^i] + A * (Qc[J_c^i] - Q1[J_c^i]) * e^{4*MC[J_c^i]} \tag{A.2}$$

Hence if

$$J_c^i \geq T_c \tag{A.3}$$

the full set of measurements i in configuration c is removed as outlier data.

Limb EIM algorithm:
Split participants up into five levels of S-SFT: [0-5mm]; [5-10mm]; [10-15mm]; [20-25mm]; [25-30mm]. For each S-SFL subset, calculate the data median and quartiles, for each configuration (c) and frequency (j) returning: $Q1_p^{cj}$, $Q2_p^{cj}$, $Q3_p^{cj}$.

$$J_c^i = \sqrt{\frac{1}{14}\sum_{j=1}^{14}\left(\frac{Z_c^i(f_j) - Q2_p^{cj}}{Q3_p^{cj} - Q1_p^{cj}}\right)^2} \tag{A.4}$$

For the variable J_c^i calculate the lower quartile ($Q1[J_c^i]$), upper quartile ($Q3[J_c^i]$) and MedCouple ($MC[J_c^i]$). Then define a threshold (T_c) for each configuration (c):

$$T_c = Q3[J_c^i] + A * (Qc[J_c^i] - Q1[J_c^i]) * e^{4*MC[J_c^i]} \tag{A.5}$$

Hence if

$$J_c^i \geq T_c \tag{A.6}$$

the full set of measurements i in configuration c is removed as outlier data in this S-SFL subset.

The parameter A is optimised, so the algorithm only removes data with obvious visual artefacts. For the bulbar EIM dataset A=3, for the limb EIM dataset A=5.

B Derive transfer impedance of test circuit

Here the transfer impedance, Z_t, for the test circuit shown in figure B.1 is derived. In this circuit, the injected current flow is from node A to node C. The output voltage is taken as the potential difference between B and D. The current injected into the circuit is $\mathrm{i_i}$, this splits into i_1 through R1, and i_3 through R3, R2, and R4.

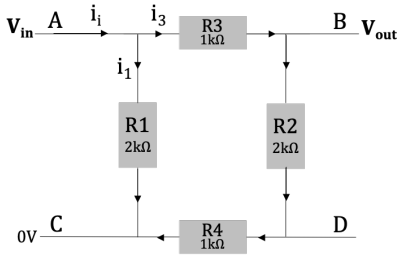

Figure B.1: Test circuit used to determine the instrumentation calibration of the limb device (detailed in Section B.1).

Since R2, R3, R4 are in series, with R1 in parallel to them, the total resistance in the circuit, R_T is given by:

$$\frac{1}{R_T} = \frac{1}{R1} + \frac{1}{R3 + R2 + R4}\,. \tag{B.1}$$

Through ohms law, the current injected into the circuit can be given by:

$$\mathrm{i_i} = \frac{V_{in}}{R_T} = V_{in}\left(\frac{1}{R1} + \frac{1}{R3 + R2 + R4}\right) = V_{in}\left(\frac{R1 + R2 + R3 + R4}{R1(R2 + R3 + R4)}\right) \tag{B.2}$$

rearranging this for input voltage gives:

$$V_{in} = \mathrm{i_i}\left(\frac{R1(R3 + R2 + R4)}{R1 + R2 + R3 + R4}\right). \tag{B.3}$$

The output voltage is the potential difference across B and D, thence is given by:

$$V_{out} = \mathrm{i}_3 R2 \tag{B.4}$$

where the current i_3 can be defined by:

$$\mathrm{i}_3 = \frac{V_{in}}{R3 + R2 + R4} \tag{B.5}$$

subbing B.5 into B.4 gives:

$$V_{out} = V_{in}\frac{R2}{R3 + R2 + R4} \tag{B.6}$$

thence subbing B.3 into B.6 produces:

$$V_{out} = \mathrm{i_i}\frac{R2}{R3 + R2 + R4} \times \frac{R1(R3 + R2 + R4)}{R1 + R2 + R3 + R4} = \mathrm{i_i}\left(\frac{R1R2}{R1 + R2 + R3 + R4}\right). \tag{B.7}$$

Therefore, the transfer impedance, Z_t for this circuit is given by:

$$Z_t = \frac{R1R2}{R1 + R2 + R3 + R4} \tag{B.8}$$

subbing in the values R1=R2=2 kΩ, and R3=R4=1 kΩ, gives the output:

$$Z_t = \frac{4\,M\Omega}{6\,k\Omega} = \frac{2000}{3}\,\Omega = 666.\dot{6}\,\Omega\,. \tag{B.9}$$

C Tongue EIM: figures and tables

C.1 ICC values

Group	R	X	θ
All Data	0.85	0.84	0.83
Healthy	0.84	0.84	0.80
All Patients	0.86	0.84	0.85
Mild ALS	0.83	0.84	0.83
Moderate ALS	0.89	0.87	0.89
Severe ALS	0.85	0.78	0.87

Measurement	R	X	θ
Intraoral	0.86	0.86	0.84
Extraoral	0.84	0.81	0.81
Central	0.85	0.81	0.83
Left	0.85	0.84	0.84
Right	0.85	0.85	0.82

	f1	f2	f3	f4	f5	f6	f7	f8	f9	f10	f11	f12	f13	f14
R	0.77	0.78	0.79	0.79	0.80	0.78	0.78	0.83	0.85	0.85	0.83	0.80	0.76	0.73
X	0.72	0.73	0.74	0.76	0.79	0.82	0.82	0.76	0.70	0.77	0.83	0.84	0.77	0.71
θ	0.79	0.77	0.79	0.82	0.85	0.88	0.90	0.90	0.83	0.81	0.89	0.91	0.88	0.86

Table C1.1: ICC values calculated for different subsets of the EIM tongue dataset.

C.2 Tongue FEM

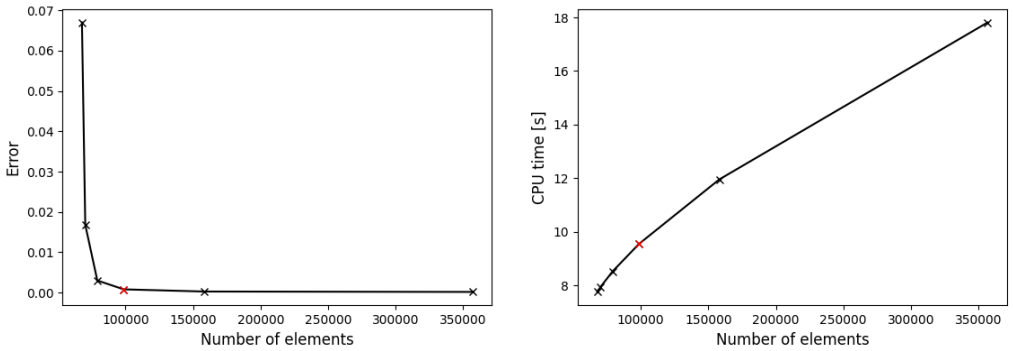

Figure C2.1: Numerical assessment of the model, showing the error against the number of mesh elements and the CPU time (for the computation of a single electrode configuration impedance spectra) against the number of mesh elements. The chosen number of elements (97,155) is shown in red. It is clear that this solution is numerically stable, and there is limited improvement in model accuracy to be gained without a substantial increase to the computational cost.

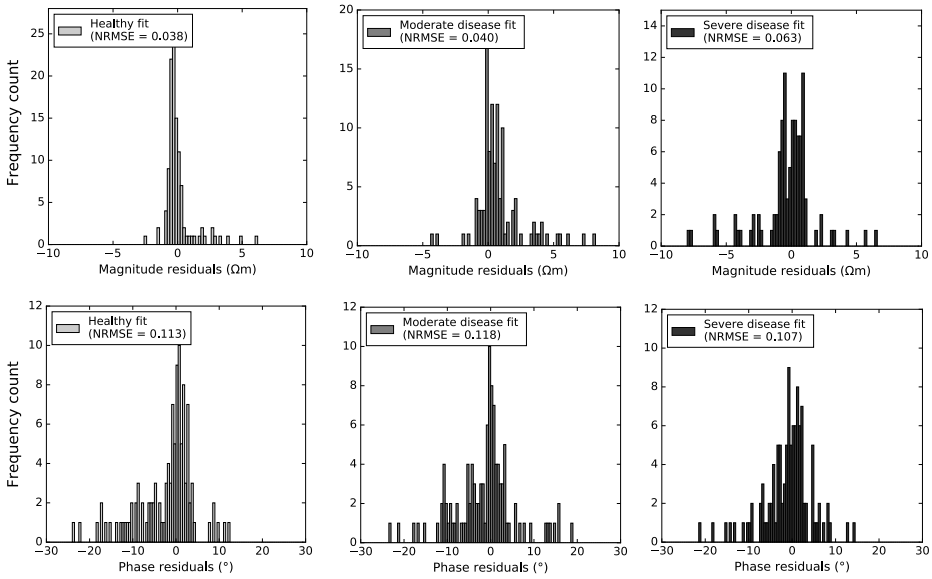

Figure C2.2: Residual plots for the FEM tongue model fit to the median impedance phase and magnitude spectra for healthy controls (light grey), moderate symptom patients (dark grey) and severe symptom patients (black). All residual plots demonstrate random errors centred around zero.

	Severe Disease				Moderate Disease				Healthy			
	Magnitude NRMSE											
Shift	A	B	C	D	A	B	C	D	A	B	C	D
2D1	**1.272**	**0.310**	0.183	0.139	**1.113**	**0.301**	0.178	0.105	**1.25**	**0.304**	0.186	0.119
2D2	**0.325**	0.057	0.112	0.085	**0.394**	0.061	0.082	0.074	**0.714**	0.100	0.104	0.078
2D3	**0.398**	**0.307**	0.182	0.122	**1.404**	**0.714**	**0.395**	0.245	**1.279**	**0.640**	**0.302**	0.195
2D4	**0.574**	0.016	0.065	0.067	**0.612**	0.070	0.079	0.055	**2.81**	0.191	0.208	0.142
3D1	**0.638**	**0.360**	**0.295**	0.218	**0.559**	**0.298**	0.229	0.169	**0.949**	**0.343**	**0.273**	0.195
3D2	0.160	0.076	0.055	0.038	0.122	0.062	0.046	0.031	0.125	0.070	0.041	0.033
3D3	**0.405**	**0.291**	0.183	0.129	**0.361**	0.203	0.126	0.087	**0.365**	0.223	.133	0.097
3D4	**0.425**	**0.304**	0.191	0.135	**0.356**	**0.294**	0.185	0.120	**0.424**	**0.300**	0.191	0.130
	Phase NRMSE											
2D1	0.067	0.032	0.039	0.034	0.051	0.026	0.024	0.020	0.082	0.022	0.033	0.027
2D2	**0.298**	0.049	0.027	0.023	**0.334**	0.045	0.025	0.019	**0.338**	0.027	0.029	0.028
2D3	0.033	0.032	0.030	0.020	0.066	0.021	0.030	0.029	0.072	0.054	0.078	0.064
2D4	**0.316**	0.021	0.015	0.013	**0.380**	0.032	0.023	0.014	**0.502**	0.060	0.037	0.026
3D1	**0.234**	0.050	0.045	0.032	**0.297**	0.039	0.035	0.032	0.043	0.031	0.030	0.022
3D2	0.032	0.015	0.017	0.016	0.042	0.021	0.012	0.011	0.055	0.024	0.025	0.022
3D3	0.032	0.015	0.017	0.016	0.042	0.021	0.012	0.011	0.055	0.024	0.025	0.022
3D4	0.046	0.039	0.033	0.024	0.068	0.036	0.037	0.029	0.085	0.036	0.050	0.039

Table C2.1: NRMSE between central impedance spectra and spectra for shift A, B, C, D (see Fig. 5a). Shown for all electrode configurations for impedance magnitude and phase. NRMSE is shown in bold if the value is greater than two repeat measurement average deviation (0.2137 for phase, 0.2471 for magnitude).

	Severe Disease			Moderate Disease			Healthy		
	Magnitude NRMSE								
Rotation	45°	30°	15°	45°	30°	15°	45°	30°	15°
2D1	0.020	0.012	0.011	0.041	0.040	0.006	0.097	0.058	0.035
2D2	0.023	0.010	0.002	0.022	0.014	0.007	0.054	0.029	0.021
2D3	0.041	0.028	0.007	**0.468**	0.160	0.021	0.188	0.098	0.040
2D4	0.043	0.028	0.010	0.188	0.109	0.031	0.183	0.127	0.051
3D1	0.003	0.004	0.001	0.021	0.010	0.002	0.027	0.021	0.014
3D2	0.003	0.003	0.003	0.008	0.004	0.003	0.026	0.016	0.002
3D3	0.005	0.007	0.001	0.008	0.004	0.003	0.020	0.004	0.012
3D4	0.005	0.004	0.001	0.012	0.004	0.006	0.025	0.007	0.006
	Phase NRMSE								
2D1	0.045	0.031	0.005	0.064	0.044	0.018	0.100	0.083	0.039
2D2	0.026	0.015	0.004	0.021	0.011	0.006	0.043	0.024	0.012
2D3	0.026	0.015	0.008	**0.240**	0.098	0.018	0.037	0.015	0.006
2D4	0.021	0.010	0.008	0.209	0.102	0.028	0.049	0.031	0.012
3D1	0.008	0.011	0.003	0.015	0.009	0.008	0.024	0.015	0.010
3D2	0.007	0.006	0.003	0.017	0.011	0.007	0.018	0.011	0.005
3D3	0.007	0.005	0.002	0.022	0.012	0.003	0.017	0.009	0.006
3D4	0.007	0.004	0.002	0.025	0.013	0.006	0.016	0.007	0.004

Table C2.2: NRMSE between central impedance spectra and spectra for rotations of 45°, 30° and 15°. Shown for all electrode configurations for impedance magnitude and phase. NRMSE shown in bold if value is greater than two repeat measurement average deviation (0.2137 for phase, 0.2471 for magnitude).

C.3 Tongue disease asymmetry

Symptoms	**B-A: Bias(°)**	**B-A: data range (°)**	**NRMSE mean**
None	1.1187	55.21	0.2195
Mild	-0.3454	63.28	0.2866
Moderate	0.7829	51.95	0.1842
Severe	0.8679	54.00	0.2494

Table C3.1: Asymmetry analysis at different symptom severities. The difference between left and right measurements is quantified through Bland-Altman (B-A) analysis (columns 1 and 2) and the NRMSE metric (column 3). Variation in the left and right spectra neither increases nor decreases with disease.

C.4 Tongue EIM classification

C.4.1 Device placement performance comparison

Lateral data classification

	Features	AUROC	Sen.	Spec.
2D1	f9, f12, f13	0.74	0.69	0.79
2D2	f10, f12	0.81	0.84	0.79
2D3	f1, f11	0.73	0.71	0.76
2D4	f3, f6, f11, f12, f13, f14	0.77	0.75	0.79
3D1/2	f9, f10, f12, f14	0.82	0.71	0.92
3D3	f3, f5, f9, f10, f11, f12, f13, f14	0.86	0.90	0.81
3D4	f8, f11, f13, f14	0.81	0.81	0.8

(a)

Central data classification

	Features	AUROC	Sen.	Spec.
2D1	f11, f12	0.75	0.79	0.71
2D2	f9, f12, f13	0.78	0.74	0.82
2D3	f5, f6, f7, f8, f9, f12, f13, f14	0.75	0.59	0.92
2D4	f1, f12, f14	0.70	0.5	0.90
3D1/2	f2, f5, f9, f10, f11, f12	0.82	0.79	0.85
3D3	f10, f11, f13	0.80	0.79	0.81
3D4	f6, f12, f13	0.76	0.75	0.77

(c)

Combined data classification

	Features	AUROC	Sen.	Spec.
2D1	C: f8 L: f11, f12	0.77	0.76	0.79
2D2	C: f8 L: f10	0.83	0.84	0.82
2D3	C: f4, f9 L: f1, f9	0.79	0.71	0.88
2D4	C: f1, f3 L: f12, f14	0.72	0.44	1.0
3D1/2	C: f1, f11, f13 L: f9, f13	0.91	0.89	0.92
3D3	C: f11, f13 L: f12	0.87	0.90	0.85
3D4	C: f9, f11, f12, f13 L: f14	0.84	0.88	0.8

(b)

Table C4.1: Classification performance comparison between (a) lateral data, (b) central data, and (c) both data types combined. For each electrode configuration 3-nearest neighbour, 4-fold cross-validation with forward selection wrapper method algorithm applied to select a maximum of 8 features.

C.4.2 Features selected in nested wrapper

Classifier	Frequency	Features
KNN	25%	**3D1**: f_{10}, f_{12}, **3D3**: f_9, **3D4**: f_7
	50%	**3D4**: f_{13}
	75%	**3D4**: f_{12}
SVM	25%	**3D1**: f_6, f_8, **3D3**: f_{12}, **3D4**: f_1, f_6, f_8, f_{14}
	50%	**3D1**: f_7, f_{12}, **3D4**: f_{12}, f_{13}
RF	25%	**3D1**: f_1, f_3, f_7, f_{11}, f_{14}, **3D3**: f_{12}, **3D4**: f_{11}
	50%	**3D1**: f_6, **3D3**: f_{13}, **3D4**: f_{12}

(a)

Classifier	Frequency	Features
KNN	25%	**3D1**: f_{11}, **3D3**: f_7, f_{11}
	50%	**3D1**: f_{10}, **3D4**: f_7
SVM	25%	**3D1**: f_1, f_2, **3D3**: f_5, f_{12}, **3D4**: f_5, f_7, f_8, f_9
	50%	**3D1**: f_{10}
RF	25%	**3D1**: f_3, f_8, f_{10}, f_{12} **3D3**: f_6, f_{14}, **3D4**: f_3 f_4, f_7

(b)

Table C4.2: Features selected in nested wrapper. (a) For classification between ALS and healthy. (b) For classification between mild and severe disease. The frequency gives the proportion of times each feature was selected in the four-fold cross-validation.

C.5 NTF Results for a Truncated Frequency Range

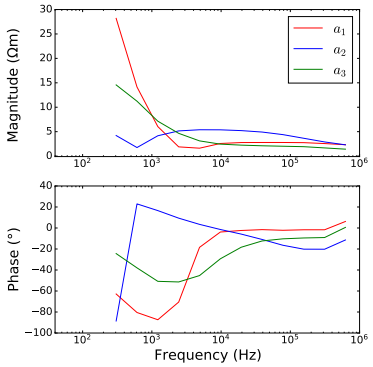

(a)

Parameter	Mann-Whitney U test p-value		
	All Patients	Mild	Severe
c1	**<0.001**	**0.002**	**<0.001**
c2	**<0.001**	**<0.001**	**<0.001**
c3	0.02	0.01	0.23
Tensor EIM	**<0.001**	**<0.001**	**<0.001**

(b)

Classifier	AUROC	Sensitivity	Specificity
KNN	0.77	0.79	0.75
SVM	0.75	0.77	0.75
RF	0.70	0.76	0.64

(c)

Figure C5.1: Diagnostic tensor EIM results using truncated frequency range starting at 305 Hz. (a) The three NTF spectral modes. (b) Mann-Whitney U significance test results comparing patients with healthy participants for the three modes and the combined tensor EIM. (c) Patient versus healthy classification performance with all NTF features applied to the three different classifiers.

Metric	Spearman correlation		MW U test
	ρ	p-value	p-value
c1	-0.56	**0.001**	0.012
c2	0.54	**0.001**	**0.001**
c3	0.04	0.82	0.36
Tensor EIM	-0.66	< 0.001	$<$**0.001**

Classifier	AUROC	Sensitivity	Specificity
KNN	0.64	0.39	0.90
SVM	0.68	0.46	0.90
RF	0.73	0.62	0.85

Table C5.1: Prognostic tensor EIM results using truncated frequency range starting at 305 Hz. (a) Correlation performance with overall symptom score. (b) Mild versus severe classification performance with all NTF features applied to the three different classifiers.

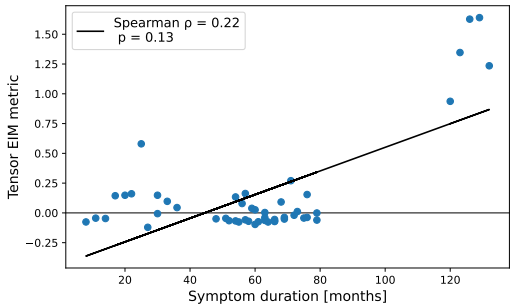

Figure C5.2: Correlation between the tensor EIM and patient's symptom duration in months. A mild positive correlation is observed, which demonstrates a general trend of higher tensor EIM for longer disease. This is not significant due to a large variation in the rate of disease change.

D Limb EIM: figures and tables

D.1 ICC values

Group	R	X	θ
All Data	0.98	0.85	0.93
Healthy	0.98	0.80	0.95
MND	0.98	0.87	0.93
non-MND	0.97	0.86	0.92

Config	R	X	θ
2Da	0.97	0.84	0.87
2Db	0.99	0.98	0.99
2Dc	0.98	0.79	0.97
3Dd	0.97	0.89	0.98

Rater	R	X	θ
intra	0.98	0.85	0.95
inter	0.96	0.83	0.90

Muscle	R	X	θ
Biceps	0.99	0.98	0.98
Triceps	0.98	0.92	0.92
Extensors	0.98	0.77	0.91
Flexors	0.98	0.81	0.91
Deltoid anterior	0.97	0.86	0.94
Deltoid posterior	0.98	0.89	0.93
Lateral gastrocnemius	0.95	0.80	0.92
Medial gastrocnemius	0.96	0.91	0.96
Tibialis anterior	0.96	0.77	0.91

Frequency	R	X	θ
f1	0.94	0.77	0.74
f2	0.98	0.80	0.85
f3	0.98	0.92	0.92
f4	0.98	0.95	0.97
f5	0.99	0.95	0.98
f6	0.99	0.89	0.97
f7	0.97	0.88	0.79

Table D1.1: ICC values calculated for different subsets of the EIM limb dataset.

D.2 S-SFT data

Subgroup	Gender	Deltoid (anterior)	Deltoid (posterior)	Biceps	Triceps	Extensors	Flexors	TA	Gastroc (lateral)	Gastroc (medial)	Average all
Healthy	Male	4.4	6.1	4.3	7.2	3.3	3.0	3.4	5.3	5.4	4.6
		3.0-8.2	4.7-9.8	2.5-7.6	4.0-10.4	2.7-7.4	1.8-6.2	3.0-6.1	3.1-10.1	3.1-8.6	3.5-7.6
	Female	6.1	8.9	6.8	13.8	5.3	5.1	6.2	9.9	10.2	8.2
		3.9-8.5	4.1-12.4	6.1-10.0	7.8-16.9	3.1-8.8	4.5-7.2	3.7-9.9	5.1-13.8	5.1-13.8	5.2-9.8
MND	Male	5.3	7.8	5.6	7.9	4.0	4.4	4.1	5.8	6.15	5.7
		2.9-8.8	3.1-11.7	2.4-8.2	2.0-12.9	1.8-6.5	2.4-7.9	2.2-7.5	3.5-9.5	3.5-11.6	2.7-7.9
	Female	9.3	10.8	8.2	12.4	6.9	7.8	6.9	10.4	11.5	9.7
		5.5-18.6	6.4-19.0	4.6-19.0	5.9-18.0	2.5-10.6	4.1-11.8	3.8-10.9	6.1-14.9	5.6-20.4	5.4-14.4
non-MND	Male	5.9	7.3	5.3	7.3	3.6	4.6	4.0	5.4	5.4	5.5
		2.7-10.5	3.6-12.6	2.3-9.2	3.3-12.7	1.8-7.3	2.4-7.4	2.2-9.1	3.0-10.8	3.0-11.5	2.7-8.8
	Female	7.5	8.5	8.1	12.6	5.4	5.9	7.0	7.7	7.7	7.9
		3.3-14.9	4.7-17.5	3.3-16.4	4.8-23.8	1.6-14.1	2.3-12.5	2.3-16.7	2.6-21.5	2.6-21.5	3.6-17.6

Table D2.1: SFL thickness median and range for each muscle placement, for the three participant subgroup split by gender. All measurements are in mm.

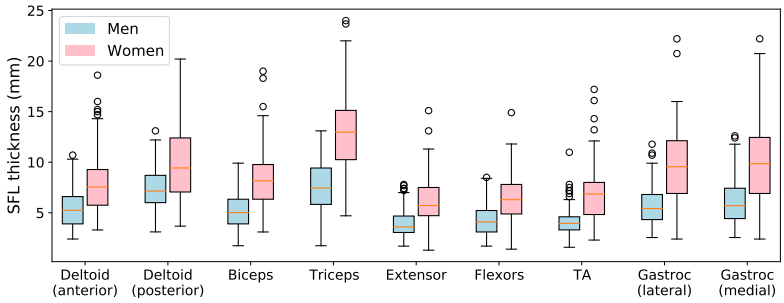

Figure D2.1: Boxplots showing SFL thickness split by gender for each muscle.

Subgroup	Deltoid (anterior)	Deltoid (posterior)	Biceps	Triceps	Extensors	Flexors	TA	Gastroc (lateral)	Gastroc (medial)	Average all
Healthy	0.04	0.02	0.003	<0.001	0.02	0.001	0.003	0.002	0.003	<0.001
MND	<0.001	0.004	<0.001	<0.001	0.005	<0.001	<0.001	<0.001	<0.001	<0.001
Non-MND	0.03	ns	0.01	<0.001	0.007	0.01	0.001	0.005	0.02	0.001

ns=not significant

Table D2.2: Mann-Whitney-U p-values with FDR correction for the difference in S-SFT between genders. A significant difference is found in all but one muscle across the three participant subgroups.

D.3 EIM correlation with S-SFT

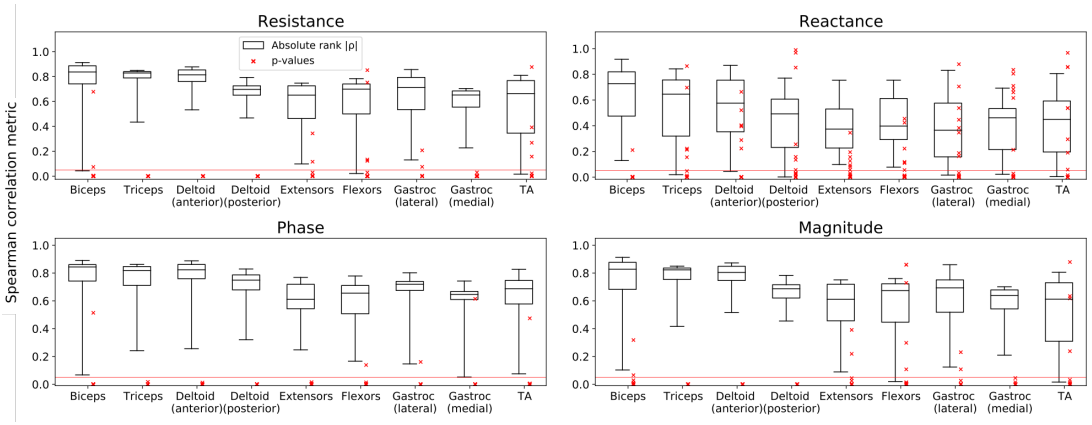

Figure D3.1: Boxplots showing the absolute value of the Spearman rank and corresponding p-values for correlation assessment between each of the EIM data features with S-SFT. Split by each muscle site.

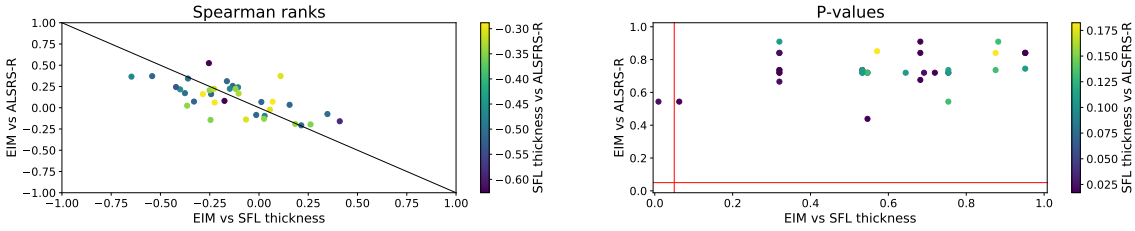

(a) Reactance; 19.5 kHz/9.8 kHz

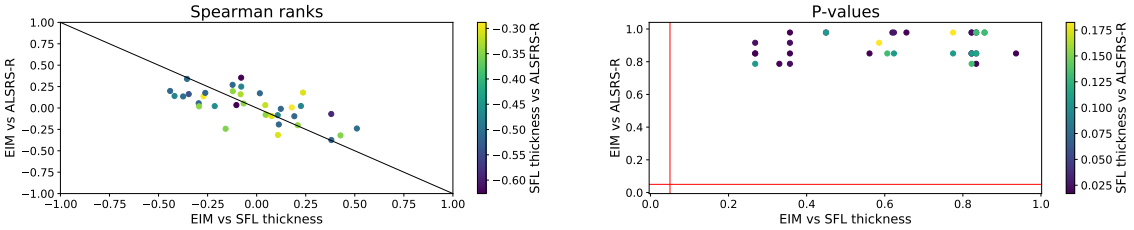

(b) Reactance; 39.0 kHz/9.8 kHz

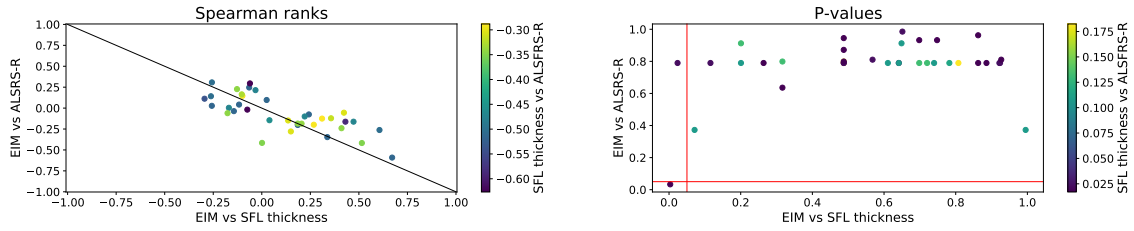

(c) Reactance; 78.1 kHz/9.8 kHz

Figure D3.2: Spearman correlation assessment for different reactance frequency ratios. Association between the 36 EIM reactances (4 configurations, 9 muscle placements), the S-SFT, and the ALSFRS-R (limb subscore). Scatter plots show the Spearman rank and respective p-values (with FDR correction) from a correlation assessment on each metric in turn. The association between EIM and the S-SFT is plotted against the association between EIM and the ALSFRS-R, the colour map then shows the respective association with S-SFT and the ALSFRS-R.

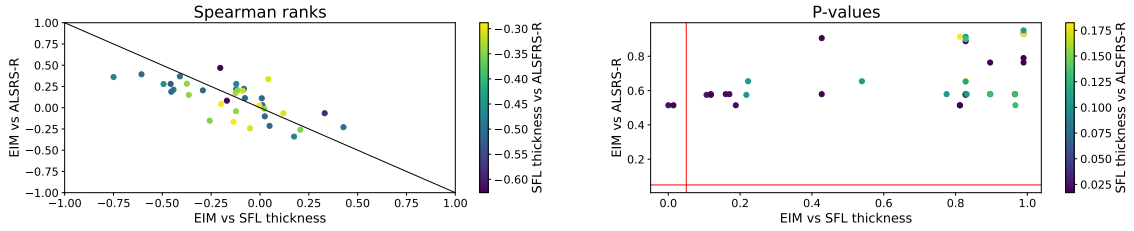

(a) Phase; 39.0 kHz/9.8 kHz

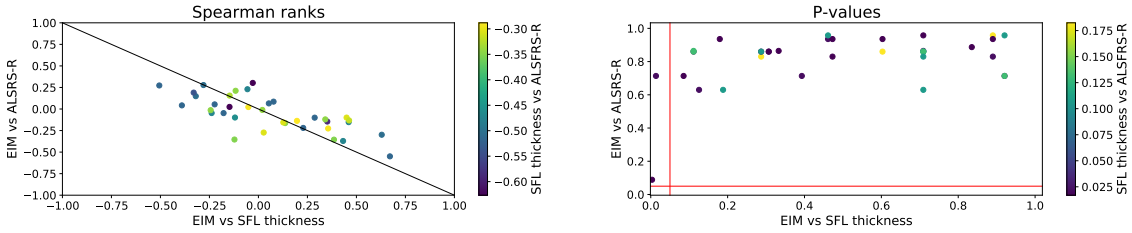

(b) Phase; 156.3 kHz/9.8 kHz

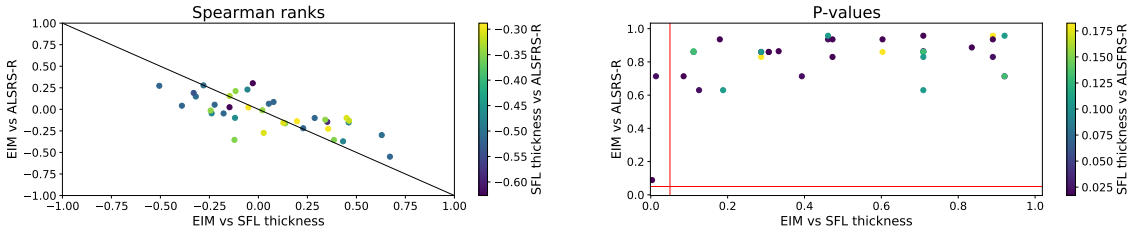

(c) Phase; 312.5 kHz/9.8 kHz

Figure D3.3: Spearman correlation assessment for different phase frequency ratios. Association between the 36 EIM phases (4 configurations, 9 muscle placements), the S-SFT, and the ALSFRS-R (limb subscore). Scatter plots show the Spearman rank and respective p-values (with FDR correction) from a correlation assessment on each metric in turn. The association between EIM and the S-SFT is plotted against the association between EIM and the ALSFRS-R, the colour map then shows the respective association with S-SFT and the ALSFRS-R.

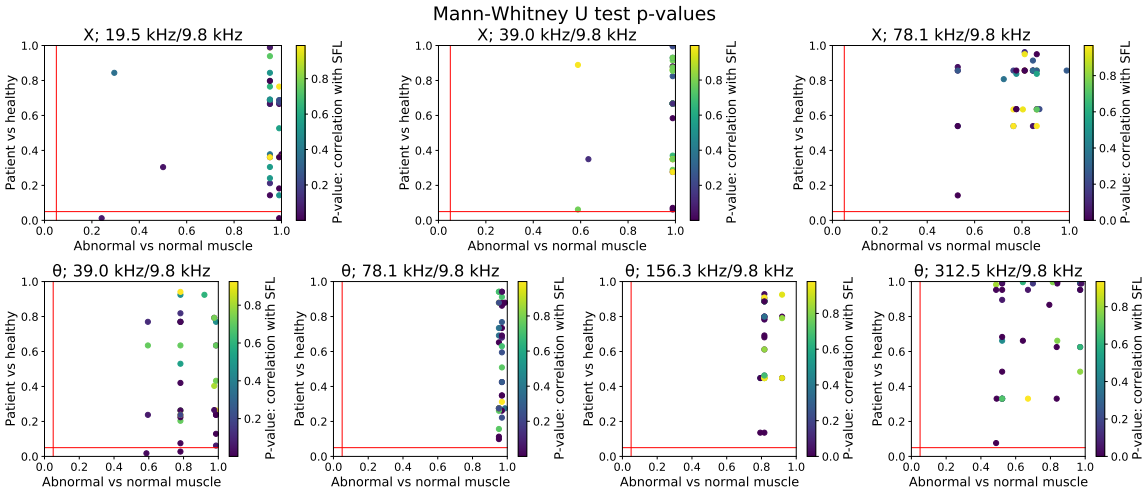

Figure D3.4: Mann-Whitney U test p-values for the discrimination between patients and healthy participants, against the p-values for discrimination against normal and abnormal muscle. Shown for all EIM features across different two-frequency ratios in the reactance and phase impedance sets.

D.4 FEM limb model

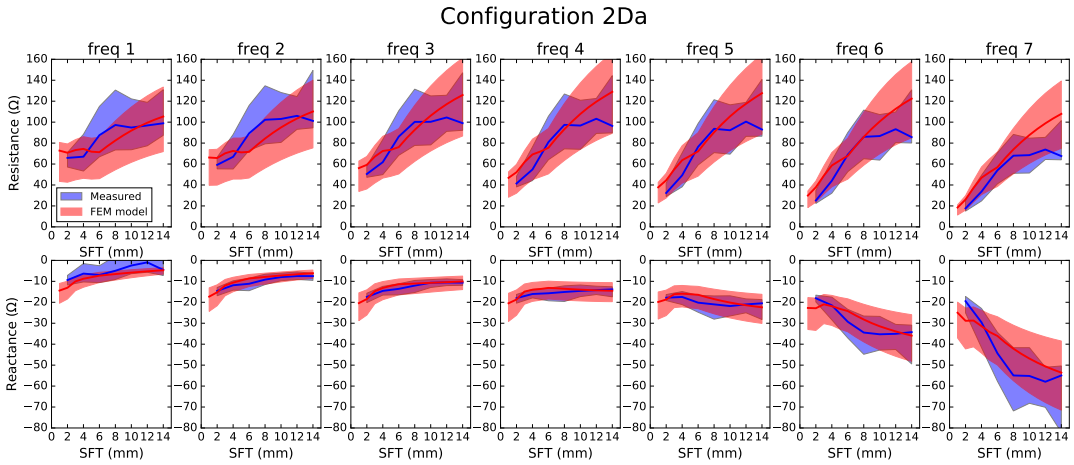

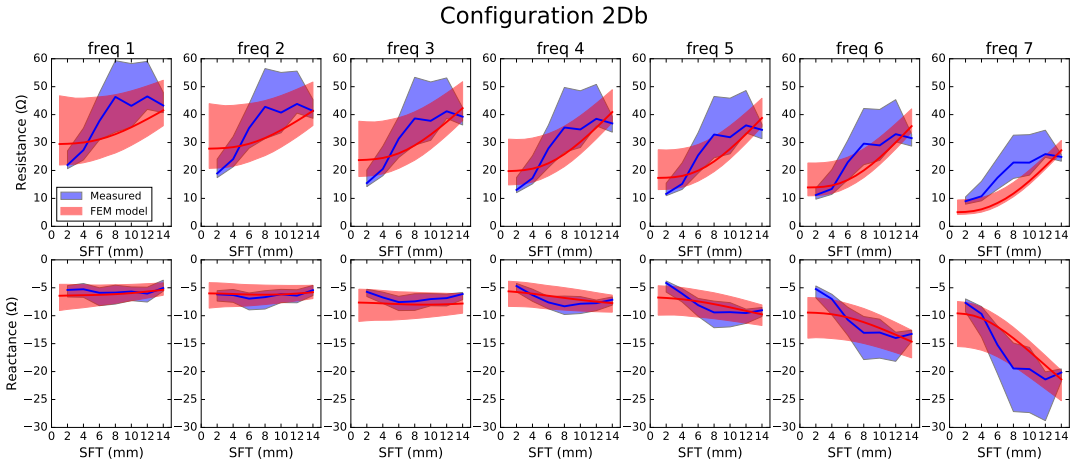

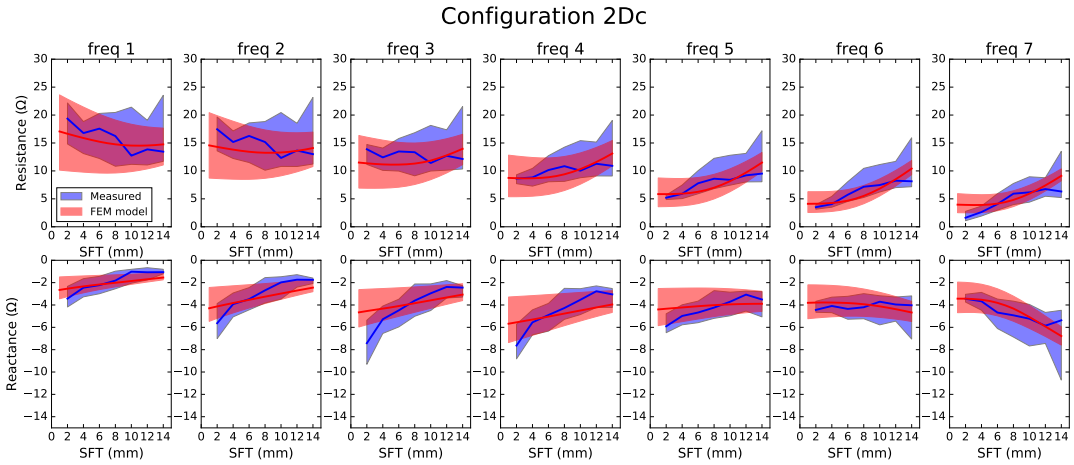

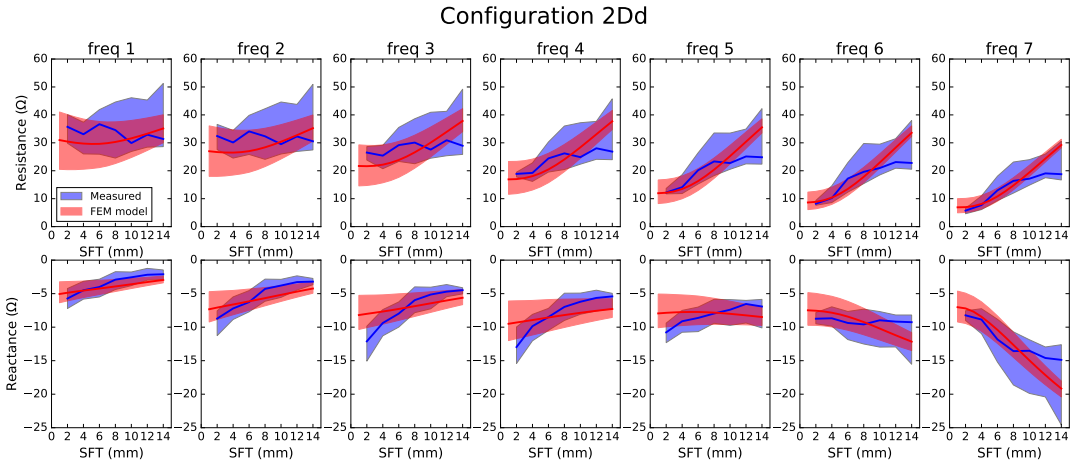

Figure D4.1: Optimised FEM limb model output in comparison to the measured EIM dataset. Shown for each frequency and electrode configuration as a function of SFT.

D.5 Muscle signal separation assessment

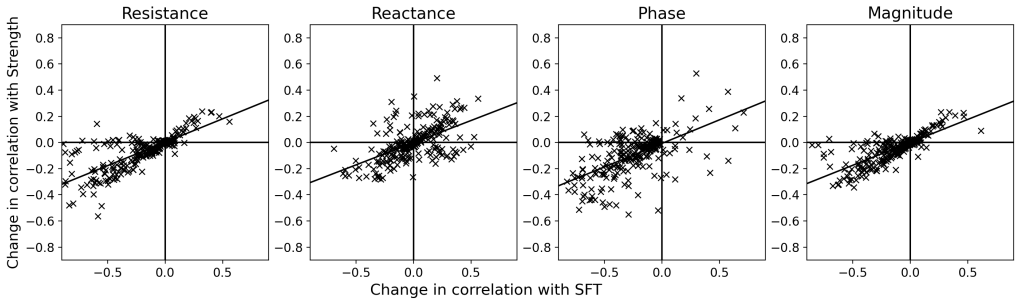

(a)

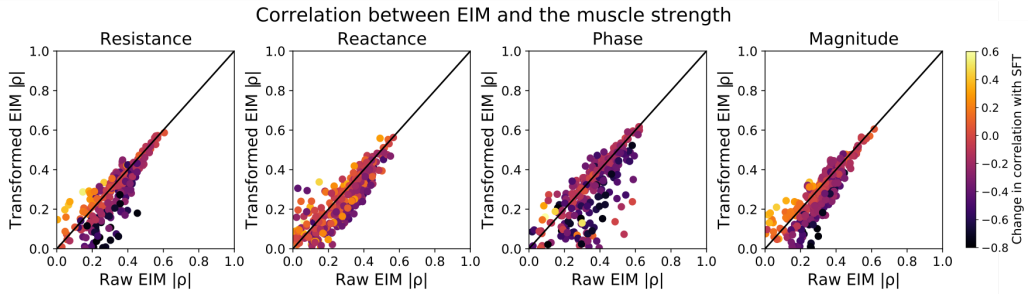

(b)

Figure D5.1: Assessment of how the correlation with the muscle strength changed following the signal separation transformation. (a) Scatter plot showing the change in the correlation with SFT against the change in correlation the muscle strength shows a significant association between the two (best fit line plotted). (b) The absolute value of the Spearman rank for correlation between each EIM feature against muscle strength, shown for the raw EIM data against the transformed EIM data. Features above the y=x line saw increased performance following transformation, and features below the line saw reduced performance.

Classification	Muscle	Raw EIM feature set			Transformed EIM feature set		
		AUROC	Sens.	Spec.	AUROC	Sens.	Spec.
Patient/Healthy	Biceps	0.74	0.65	0.82	0.74	0.57	0.91
	Triceps	0.75	0.54	0.95	0.74	0.58	0.91
	Deltoid (anterior)	0.82	0.69	0.95	0.78	0.61	0.95
	Deltoid (posterior)	0.83	0.70	0.95	0.78	0.61	0.95
	Extensors	0.84	0.68	1.0	0.84	0.67	1.0
	Flexors	0.78	0.61	0.95	0.76	0.56	0.95
	Gastroc (lateral)	0.72	0.54	0.91	0.77	0.72	0.82
	Gastroc (medial)	0.74	0.76	0.72	0.75	0.64	0.86
	TA	0.74	0.76	0.72	0.74	0.62	0.86
ALS/Healthy	Biceps	0.80	0.69	0.91	0.80	0.66	0.95
	Triceps	0.75	0.63	0.86	0.73	0.56	0.90
	Deltoid (anterior)	0.88	0.75	1.0	0.81	0.71	0.91
	Deltoid (posterior)	0.90	0.88	0.91	0.88	0.85	0.91
	Extensors	0.93	0.86	1.0	0.90	0.79	1.0
	Flexors	0.86	0.86	0.86	0.86	0.91	0.81
	Gastroc (lateral)	0.76	0.61	0.91	0.77	0.71	0.82
	Gastroc (medial)	0.79	0.68	0.91	0.76	0.61	0.91
	TA	0.85	0.88	0.82	0.80	0.73	0.8 6
Mimic/Healthy	Biceps	0.67	0.91	0.43	0.71	0.86	0.57
	Triceps	0.72	0.81	0.63	0.77	0.81	0.74
	Deltoid (anterior)	0.85	0.95	0.74	0.79	0.82	0.76
	Deltoid (posterior)	0.83	0.95	0.70	0.77	0.95	0.58
	Extensors	0.77	0.95	0.58	0.81	0.95	0.67
	Flexors	0.77	1.0	0.54	0.74	1.0	0.49
	Gastroc (lateral)	0.71	0.82	0.61	0.74	0.82	0.65
	Gastroc (medial)	0.71	0.77	0.64	0.78	0.91	0.64
	TA	0.70	0.91	0.49	0.73	0.91	0.56
ALS/Mimic	Biceps	0.66	0.76	0.56	0.61	0.55	0.67
	Triceps	0.72	0.74	0.71	0.64	0.39	0.89
	Deltoid (anterior)	0.71	0.86	0.56	0.70	0.68	0.71
	Deltoid (posterior)	0.65	0.58	0.72	0.65	0.69	0.60
	Extensors	0.74	0.75	0.73	0.74	0.79	0.69
	Flexors	0.72	0.68	0.76	0.66	0.55	0.78
	Gastroc (lateral)	0.64	0.93	0.35	0.68	0.68	0.68
	Gastroc (medial)	0.57	0.89	0.23	0.65	0.61	0.69
	TA	0.65	0.65	0.65	0.69	0.58	0.81
Normal/Abnormal	Biceps	0.76	0.90	0.60	0.69	0.76	0.61
	Triceps	0.76	0.75	0.77	0.71	0.58	0.85
	Deltoid (anterior)	0.82	0.76	0.87	0.84	0.88	0.80
	Deltoid (posterior)	0.87	0.82	0.92	0.84	0.76	0.92
	Extensors	0.76	0.67	0.85	0.80	0.89	0.70
	Flexors	0.82	0.89	0.75	0.85	0.78	0.92
	Gastroc (lateral)	0.89	0.90	0.89	0.77	0.60	0.94
	Gastroc (medial)	0.81	0.85	0.77	0.80	0.69	0.91
	TA	0.83	0.88	0.79	0.78	0.88	0.68
ALS Severe/Mild	Biceps	0.77	0.54	1.0	0.85	0.69	1.0
	Triceps	0.82	0.80	0.83	0.86	0.80	0.92
	Deltoid (anterior)	0.85	0.69	1.0	0.85	0.69	1.0
	Deltoid (posterior)	0.84	0.75	0.92	0.83	0.67	1.0
	Extensors	0.83	0.67	1.0	0.85	0.83	0.87
	Flexors	0.88	0.75	1.0	0.90	0.88	0.92
	Gastroc (lateral)	0.73	0.54	0.93	0.77	0.62	0.93
	Gastroc (medial)	0.73	0.54	0.93	0.81	0.77	0.86
	TA	0.81	1.0	0.62	0.75	0.58	0.92

Table D5.1: Table showing the classification performance metrics for each muscle on 6 different classification problems. Presented for the assessment of both the raw and transformed EIM feature set. Analysed using support vector machine classifier, forward selection wrapper feature selection, with cross-validation applied.

Classification	Muscle	Raw tensor EIM metrics			Transformed tensor EIM metrics		
		AUROC	Sens.	Spec.	AUROC	Sens.	Spec.
Patient/Healthy	Biceps	0.56	0.48	0.64	0.66	0.6	0.73
	Triceps	0.5	0.57	0.43	0.51	0.41	0.62
	Deltoid (anterior)	0.64	0.59	0.68	0.67	0.47	0.86
	Deltoid (posterior)	0.65	0.43	0.86	0.74	0.58	0.91
	Extensors	0.66	0.5	0.82	0.68	0.5	0.86
	Flexors	0.57	0.33	0.81	0.61	0.37	0.86
	Gastroc (lateral)	0.64	0.38	0.91	0.62	0.32	0.91
	Gastroc (medial)	0.66	0.41	0.91	0.64	0.46	0.82
	TA	0.53	0.47	0.59	0.68	0.44	0.91
ALS/Healthy	Biceps	0.62	0.55	0.68	0.63	0.48	0.77
	Triceps	0.68	0.7	0.67	0.68	0.7	0.67
	Deltoid (anterior)	0.67	0.75	0.59	0.74	0.61	0.86
	Deltoid (posterior)	0.69	0.46	0.91	0.84	0.81	0.86
	Extensors	0.73	0.68	0.77	0.69	0.57	0.8
	Flexors	0.61	0.65	0.57	0.62	0.52	0.71
	Gastroc (lateral)	0.62	0.46	0.77	0.69	0.57	0.82
	Gastroc (medial)	0.65	0.54	0.77	0.73	0.64	0.82
	TA	0.56	0.54	0.59	0.64	0.46	0.82
non-MND/Healthy	Biceps	0.61	0.59	0.64	0.66	0.63	0.6
	Triceps	0.63	0.74	0.52	0.68	0.74	0.62
	Deltoid (anterior)	0.57	0.28	0.86	0.68	0.5	0.86
	Deltoid (posterior)	0.63	0.53	0.73	0.69	0.47	0.91
	Extensors	0.53	0.24	0.82	0.64	0.41	0.86
	Flexors	0.54	0.46	0.62	0.62	0.49	0.76
	Gastroc (lateral)	0.63	0.35	0.91	0.6	0.28	0.91
	Gastroc (medial)	0.65	0.43	0.86	0.67	0.48	0.86
	TA	0.57	0.59	0.55	0.66	0.45	0.86
ALS/non-MND	Biceps	0.53	0.43	0.62	0.51	0.54	0.48
	Triceps	0.59	0.61	0.57	0.51	0.42	0.61
	Deltoid (anterior)	0.6	0.37	0.82	0.58	0.37	0.79
	Deltoid (posterior)	0.57	0.56	0.58	0.56	0.63	0.5
	Extensors	0.54	0.54	0.54	0.48	0.11	0.86
	Flexors	0.6	0.32	0.87	0.56	0.22	0.91
	Gastroc (lateral)	0.51	0.46	0.57	0.55	0.78	0.32
	Gastroc (medial)	0.59	0.29	0.89	0.57	0.17	0.96
	TA	0.62	0.5	0.75	0.55	0.27	0.82
Normal/Abnormal	Biceps	0.64	0.72	0.55	0.62	0.67	0.58
	Triceps	0.67	0.71	0.63	0.66	0.79	0.53
	Deltoid (anterior)	0.66	0.75	0.58	0.72	0.67	0.77
	Deltoid (posterior)	0.66	0.6	0.72	0.72	0.6	0.84
	Extensors	0.68	0.67	0.7	0.71	0.76	0.65
	Flexors	0.62	0.5	0.75	0.64	0.62	0.65
	Gastroc (lateral)	0.62	1.0	0.25	0.53	0.33	0.72
	Gastroc (medial)	0.58	0.88	0.28	0.6	1.0	0.21
	TA	0.59	0.65	0.52	0.59	0.4	0.78
ALS Severe/Mild	Biceps	0.61	0.62	0.6	0.73	0.72	0.74
	Triceps	0.63	0.6	0.67	0.76	0.6	0.92
	Deltoid (anterior)	0.7	0.69	0.71	0.74	0.62	0.86
	Deltoid (posterior)	0.6	0.58	0.62	0.76	0.75	0.77
	Extensors	0.69	0.58	0.8	0.66	0.58	0.73
	Flexors	0.74	0.56	0.92	0.7	0.56	0.852
	Gastroc (lateral)	0.67	0.56	0.78	0.78	0.78	0.78
	Gastroc (medial)	0.57	0.38	0.76	0.58	0.38	0.79
	TA	0.62	0.46	0.79	0.66	0.46	0.86

Table D5.2: Table showing the classification performance metrics for each muscle on 6 different classification problems. Presented for the assessment of both the raw and transformed tensor EIM metrics. Analysed using Naive Bayes classifier, with cross-validation applied.

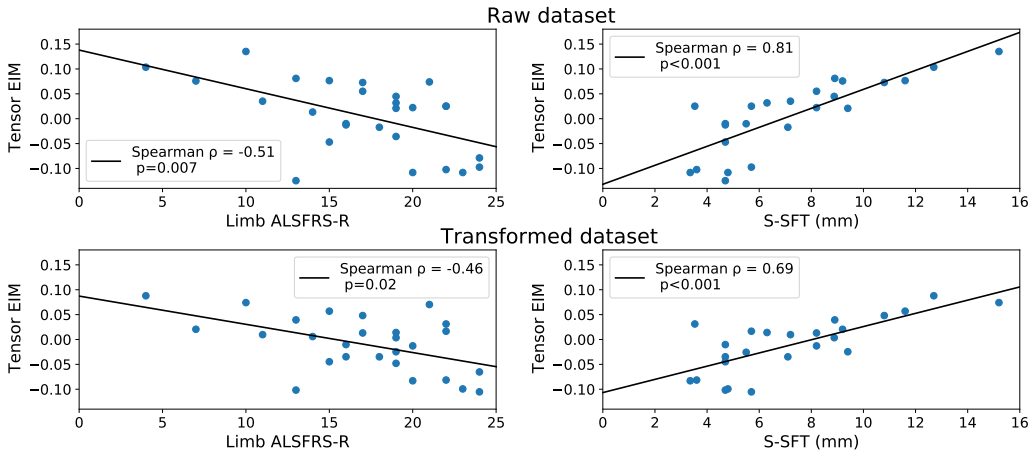

Figure D5.2: Anterior deltoid tensor EIM plotted against the limb ALSFRS-R and the S-SFT with Spearman rank correlation coefficients shown. Presented for both the raw and transformed EIM datasets.